Title

Source versus process-driven geochemical variations of mafic lavas from different tectonic regimes

Author

Durkin, Kathryn

Publication Date

2020

UNIVERSITY OF CALIFORNIA SAN DIEGO

Source versus process-driven geochemical variations of mafic lavas from different tectonic regimes

A dissertation submitted in partial satisfaction of the
requirements for the degree
Doctor of Philosophy

in

Earth Sciences

by

Kathryn Elaine Durkin

Committee in charge:

Professor Paterno Castillo, Chair
Professor James Day
Professor Arnold Rheingold
Professor Dave Stegman
Professor Emily Van Allen

2020

The dissertation of Kathryn Elaine Durkin is approved, and it is acceptable in quality and form for publication on microfilm and electronically:

Chair

University of California San Diego

2019

EPIGRAPH

It is good to have an end to journey toward; but it is the journey that matters, in the end.

Ursula K. Le Guin, The Left Hand of Darkness

TABLE OF CONTENTS

LIST OF FIGURES

LIST OF TABLES

ACKNOWLEDGEMENTS

It has been an honor to share this journey with the welcoming community of astonishing students and mentors at SIO as well as friends and family. I can't adequately thank everyone for their support, light and grace through these years. My most heartfelt and deepest thanks.

Pat, I can't thank you enough for both your patience and kindness, as well as your willingness to help me navigate (and push me) through the times I got in my own way. Thank you for your guidance. To my committee; James, Emily, Dave and Arnie, you have inspired me to produce better quality work from your feedback. James, thank you for your encouragement, help and mentorship, especially in these last months. Thank you, Emily, for organizing our inter-lab group discussions and challenging me to practice presentation skills. I also need to thank my teaching mentors, Cheryl, Geoff, James, Erilynn and the rest of the ETC and GTC cohort for the opportunities to teach/TA at UCSD. Your support helped me explore my teaching style and philosophy and articulate a lifelong passion. To the administrative and other, unsung heroes of SIO - Gilbert, Josh Reeves, Maureen, Cups/PinPoint café (yes, I really did need all that coffee), lab managers and custodians - thank you for putting up with my inconvenient drop-ins and gracefully helping all of us navigate the frustrations of being a graduate student.

To my extended labmates, friends, SIO 2014 cohort and family- I couldn't have done this without you. It has been a true privilege to have met and worked with you. Thank you for the hope, reality checks and necessary hugs you gave me along this journey. To the past and present members of the SIGL lab – thank you for including me in lab meetings, labwork and as a friend. To the Chin-Castillo-Aarons group – our discussions and practice presenting have been invaluable. To the Na Casino and Pfizer softball team, thank you for the ability to burn off some steam. To Art and Jenny, thank you for opening your hearts and home to me and the rest of

Team Miller; it's meant so much to me to have you as a surrogate set of parents at UCSD. To the SIO 2014 cohort and friends who have become family; Dillon, Shelby, Reuben, Catherine, Alfredo, Bia, Gui, Charlotte, JD, little PJ, Keelan, Olavo, Paul, Taylor, Wes, Isa, Rishi, Alyssa, Beverly, Georgie, Carrie, Momme, Mike E., Hunter, Emma, Radiance, Stephen, Sarah M., Emily W., Jasmeet, Marine, Emilie, Sherly, Tim, Dave, Pete, Kori, Twin and Sis – there is no other way to say it; I love you, thank you for everything. To Jackie, Wayne and Michael, thank you for welcoming me into your family, I am the lucky one. To my parents, your unconditional love and support in the highs and lows of these last six years have been my lifeline. Alan, you believed in me more than I did in myself, spoke both welcome and hard truths and helped me grow as a scientist and a human being. I cannot be more grateful or more excited to continue this journey together.

Chapter 2, in full, is a reproduction of material as it appears in Durkin, K., Castillo, P.R., Straub, S.M., Abe, N., Tamura, Y., An origin of the along-arc compositional variation in the Izu-Bonin arc system, *Geoscience Frontiers,* 2020. The dissertation author was the primary investigator and author of this work.

Chapter 3, in full, is a reproduction of material that is in preparation for submission to Geochemistry, Geophysics, Geosystems as Durkin, K., Castillo, P.R., Straub, S.M., Mallick, S., Saal, A., Muller, J. K., Widespread contamination of the Pacific upper mantle during the Mid-Cretaceous. The dissertation author was the primary investigator and author of this work.

Chapter 4, in full, is material that is in preparation for submission to Earth Planetary Science Letters as Durkin, K., Day, J. M. D., Panter, K., Xu, J., Juda, N., Castillo, P. R., Causes of isotopic variations across an ocean-continental transition, Ross Sea Embayment, Antarctica. The dissertation author was the primary investigator and author of this work.

VITA

2008-2012	Bachelor of Arts in Geoscience, Smith College
2014-2020	Graduate Student Researcher, Scripps Institution of Oceanography
2016	Master of Science in Earth Sciences, University of California San Diego
2020	Doctor of Philosophy in Earth Sciences, University of California San Diego

PUBLICATIONS

Durkin, K., Castillo, P.R., Straub, S.M., Abe, N., Tamura, Y., 2020. Geoscience Frontiers An origin of the along-arc compositional variation in the Izu-Bonin arc system. Geoscience Frontiers. https://doi.org/10.1016/j.gsf.2019.12.004

ABSTRACT OF THE DISSERTATION

Source versus process-driven geochemical variations of mafic lavas from different tectonic regimes

by

Kathryn Elaine Durkin

Doctor of Philosophy in Earth Sciences

University of California San Diego, 2020

Professor Paterno R. Castillo, Chair

Understanding the geochemical evolution between the source and resultant magmas is an important step in refining our understanding of plate tectonics. Primitive, mafic lavas are generally considered the most likely to preserve mantle source characteristics as these melts have been the least modified by geochemical effects of magmatic and secondary processes. Such processes (e.g. partial melting, fractional crystallization and contamination through assimilation of crustal material) exert geochemical controls on the composition and evolution of such magmas.

The primary aim of this thesis is to study geochemical source signatures of magmas from a variety of tectonic settings and the processes that have affected such magmas. Major chapters of this thesis explore the generation and transfer of the geochemical signature of Pacific altered oceanic crust (AOC) subducting into the Izu-Bonin trench, the effects of Pacific oceanic plateau formation on the upper mantle source of the Pacific-Izanagi mid-ocean ridge basalts during the Mid-Cretaceous and the generation of compositionally similar alkalic lavas on both continental and oceanic crust in the West Antarctic Rift System (WARS). I used a variety of geochemical measurements, including major and trace element and Sr-Nd-Pb-Hf-Os isotope analyses to analyze two unique sets of samples to illuminate the geochemical mantle source-primary melt-erupted volcanic evolution at a convergent margin, an established mid-ocean ridge setting and a rift zone.

The samples studied in Chapters 2 and 3 were dredged AOC from an along-arc transect. They have a Pacific-type Pb-isotope signature and show a progressive trace element and radiogenic isotope enrichment from older crust in the south to younger, northern crust. This observation indicates that the previously documented Indian-type Pb-isotope signature of Izu-Bonin arc lavas is not directly sourced from the subducting material and that the Indian-type mantle wedge has a greater than anticipated role in the generation of the Pb-isotopic signature of the associated arc lavas. Chapter 3 focuses on this same suite of transect samples but addresses the unanticipated geochemical enrichment trend from the older northern crust to the younger southern crust. This compositional trend likely results from contamination of the Pacific upper mantle due to the eruption of the Ontong-Java, Manihiki and Hikurangi plateaus in a massive magmatic pulse centered around 125 Ma. Chapter 4, on the other hand, uses an ocean-continent transect of alkalic lavas from the West Antarctic rift system (WARS) to assess the effects and degree of crustal contamination in WARS lavas. My findings indicate a similar mantle source for these lavas with variable degrees of crustal contamination that are most evident in the continental samples. This result emphasizes the pervasive nature of crustal contamination, especially in continental settings.

Chapter 1

Introduction

The geochemistry of volcanic rocks represents the culmination of a series of complex interactions beginning from partial melting to produce an initial melt composition and subsequent differentiation processes during magma ascent and cooling such as crustal assimilation and fractional crystallization (AFC) processes. Each process has its own effect on melt composition, that can obfuscate the original composition and geochemical characteristics of the initial magma. However, in order to understand the nature of the source of a magma, it is imperative to unravel the geochemical processes that acted on a magma as it evolved. The principal aim of this thesis is to further refine our understanding of magma generation and subsequent evolution at plate margins. Chapters 2 and 3 investigate established convergent and divergent margins, and Chapter 4 studies an incipient rift setting.

Chapter 2 of this thesis aims to constrain the origin of the latitudinal compositional variation of Izu-Bonin arc lavas younger than 42Ma. It is widely accepted that there is a geochemical link between subducting slabs and arc lavas in convergent plate margins (e.g. McCulloch and Gamble, 1991; Elliott et al., 1997; Bryant et al., 2003; Elliott, 2003). The Izu-Bonin Marianas (IBM) arc system exhibits a well-documented latitudinal geochemical variation of arc lavas in its northern, Izu-Bonin section (e.g. Taylor and Nesbitt, 1998; Straub et al., 2004; Ishizuka et al., 2007). Izu-Bonin is unique as an oceanic-oceanic convergence zone involving subduction of the old Pacific Plate with a lithologically uniform and relatively thin (~400m) pelagic sediment cover. Thus, of the two primary geochemical inputs coming from the subducting plate, sediments and altered oceanic crust (AOC), sediments can be ruled out as a source for the arc lava geochemical variation due to their uniform cover and homogeneity. Compared to prior investigations of Izu-Bonin that relied on spot samples of the Pacific AOC input and their role in the genesis of arc lava output, my study involves a more in-depth analysis of AOC samples collected over a wide (~7o) latitudinal range. We study the cycling of aqueous fluid-mobile elements and geochemical signatures from the subducting Pacific Plate into the arc volcanics using a full suite of geochemical measurements including major elements, trace elements and Sr-Nd-Pb isotopic measurements to model the generation of a subduction component and its subsequent mixing and generation of a hypothetical average Izu-Bonin arc lava.

Chapter 3 builds upon the previous chapter by collecting Hf isotope data on the AOC samples to further constrain the range of global MORB Hf isotopes and the effects (if any) that alteration may produce in this isotope system. The Hf isotopic composition of AOC helps to study the petrogenesis of Pacific oceanic crust produced at an established mid-ocean ridge and the potential influence that massive secondary volcanism during the Cretaceous may have had on the geochemistry of that section of crust. Although Hf and Nd isotopic ratios are closely coupled in both mantle and terrestrial scales (Blichert-Toft and Albarède, 1998; John et al., 2004), Hf isotopes have a narrower range than Nd isotopes in mid-ocean ridge basalts (MORB) compared to ocean island basalts (OIB) that are typically associated with mantle plumes (Nowell et al., 1998; Chauvel and Blichert-Toft, 2001; Salters et al., 2011). As a result, plume influence in the generation of Pacific AOC may be more visible in the combined Hf-Nd isotope investigation. One such possible plume influence is the Mid-Cretaceous volcanic event (Janney and Castillo, 1996, 1997; Madrigal et al., 2016).

The question of source versus process is especially relevant when considering the generation of lavas during the evolution of the West Antarctic Rift System (WARS) in the northwest Ross Sea (NWRS). The WARS has not produced a fully mature divergent margin like a mid-ocean ridge setting but has produced a region of geochemically similar alkalic lavas that originated in both oceanic and continental crust. This alkalic magmatism is debated to be the result of either mantle plumes or extensional forces that facilitate decompression melting of metasomatized lithospheric mantle (White and Hofmann, 1982; Zindler and Hart, 1986; White et al., 1987; Chauvel et al., 1992; Finn et al., 2005; Panter, 2006; Martin et al., 2013; Aviado et al., 2015). This debate has recently been renewed by (Panter et al., 2018) using preliminary analyses of samples dredged from Adare Basin Seamounts (ABS) in conjunction with published data from the WARS to create a geochemical transect between continental intraplate volcanics and oceanic intraplate volcanics. This chapter extends the preliminary work done by Panter et al. (2018) using pre-existing O isotopes and expanded Pb-Nd-Sr and especially Os isotope data set. The expansion of data from the ocean-continent transect initiated by Panter et al. (2018) is a unique opportunity to study the influence of oceanic versus continental lithospheric contributions, e.g. crustal assimilation and/or thickness, and their role in the production of alkalic lavas in the WARS.

References

Aviado, K.B., Rilling-Hall, S., Bryce, J.G., Mukasa, S.B., 2015. Submarine and subaerial lavas in the west Antarctic Rift System: Temporal record of shifting magma source components from the lithosphere and asthenosphere. Geochemistry Geophysics Geosystems 16, 4344–4361. https://doi.org/10.1002/2015GC006076

Blichert-Toft, J., Albarède, F., 1998. The Lu–Hf isotope geochemistry of chondrites and the evolution of the mantle–crust system. Earth and Planetary Science Letters 154, 349. https://doi.org/10.1016/S0012-821X(97)00198-2

Bryant, C.J., Arculus, R.J., Eggins, S.M., 2003. The geochemical evolution of the Izu-Bonin arc system: a perspective from tephras recovered by deep-sea drilling. Geochemistry, Geophysics, Geosystems 4. https://doi.org/10.1029/2002GC000427

Chauvel, C., Blichert-Toft, J., 2001. A hafnium isotope and trace element perspective on melting of the depleted mantle. Earth and Planetary Science Letters 190, 137–151. https://doi.org/10.1016/S0012-821X(01)00379-X

Chauvel, C., Hofmann, A.W., Vidal, P., 1992. HIMU-EM: The French Polynesian connection. Earth and Planetary Science Letters 110, 99–119. https://doi.org/10.1016/0012-821X(92)90042-T

Elliott, T., 2003. Tracers of the slab. Inside the Subduction Factory. 23–45. https://doi.org/10.1029/138gm03

Elliott, T., Plank, T., Zindler, A., White, W., Bourdon, B., 1997. Element transport from slab to volcanic front at the Mariana arc. Journal of Geophysical Research 102, 14991–15019.

Finn, C.A., Müller, R.D., Panter, K.S., 2005. A Cenozoic diffuse alkaline magmatic province (DAMP) in the southwest Pacific without rift or plume origin. Geochemistry, Geophysics, Geosystems 6. https://doi.org/10.1029/2004GC000723

Ishizuka, O., Taylor, R.N., Yuasa, M., Milton, J.A., Nesbitt, R.W., Uto, K., Sakamoto, I., 2007. Processes controlling along-arc isotopic variation of the southern Izu-Bonin arc. Geochemistry, Geophysics, Geosystems 8. https://doi.org/10.1029/2006GC001475

Janney, P.E., Castillo, P.R., 1997. Geochemistry of Mesozoic Pacific mid-ocean ridge basalt: constraints on mantle generation and the evolution of the Pacific upper mantle. Journal of Geophysical Research 102, 5207–5229.

Janney, P.E., Castillo, P.R., 1996. Basalts from the Central Pacific Basin: evidence for the origin of Cretaceous igneous complexes in the Jurassic western Pacific. Journal of Geophysical Research 101, 2875–2893. https://doi.org/10.1029/95JB03119

John, T., Scherer, E.E., Haase, K., Schenk, V., 2004. Trace element fractionation during fluid-induced eclogitization in a subducting slab: Trace element and Lu-Hf-Sm-Nd isotope systematics. Earth and Planetary Science Letters 227, 441–456. https://doi.org/10.1016/j.epsl.2004.09.009

Madrigal, P., Gazel, E., Flores, K.E., Bizimis, M., Jicha, B., 2016. Record of massive upwellings from the Pacific large low shear velocity province. Nature Communications 7, 13309.

Martin, A.P., Cooper, A.F., Price, R.C., 2013. Petrogenesis of Cenozoic, alkalic volcanic lineages at Mount Morning, West Antarctica and their entrained lithospheric mantle xenoliths: Lithospheric versus asthenospheric mantle sources. Geochimica et Cosmochimica Acta 122, 127–152. https://doi.org/10.1016/j.gca.2013.08.025

McCulloch, M.T., Gamble, J.A., 1991. Geochemical and geodynamical constraints on subduction zone magmatism. Earth and Planetary Science Letters 102, 358–374.

https://doi.org/10.1016/0012-821X(91)90029-H

Nowell, G.M., Kempton, P.D., Noble, S.R., Saunders, A. D., Mahoney, J.J., Taylor, R.N., 1998. High-precision Hf isotopic measurements of MORB and OIB by thermal ionization mass-spectrometry: insights into the depleted mantle. Chemical Geology 149, 211–233.

Panter, K.S., 2006. The Origin of HIMU in the SW Pacific: Evidence from Intraplate Volcanism in Southern New Zealand and Subantarctic Islands. Journal of Petrology 47, 1673–1704. https://doi.org/10.1093/petrology/egl024

Panter, K.S., Castillo, P.R., Krans, S., Deering, C., McIntosh, W., Valley, J.W., Kitajima, K., Kyle, P.R., Hart, S.R., Blusztajn, J., 2018. Melt Origin across a Rifted Continental Margin: a Case for Subduction-related Metasomatic Agents in the Lithospheric Source of Alkaline Basalt, NW Ross Sea, Antarctica. Journal of Petrology 59, 517–558. https://doi.org/10.1093/petrology/egy036

Salters, V.J.M., Mallick, S., Hart, S.R., Langmuir, C.E., Stracke, A., 2011. Domains of depleted mantle: New evidence from hafnium and neodymium isotopes. Geochemistry, Geophysics, Geosystems 12. https://doi.org/10.1029/2011GC003617

Straub, S.M., Layne, G.D., Schmidt, A., Langmuir, C.H., 2004. Volcanic glasses at the Izu arc volcanic front: new perspectives on fluid and sediment melt recycling in subduction zones. Geochemistry, Geophysics, Geosystems 5. https://doi.org/10.1029/2002GC000408

Taylor, R.N., Nesbitt, R.W., 1998. Isotopic characteristics of subduction fluids in an intra-oceanic setting, Izu-Bonin Arc, Japan. Earth and Planetary Science Letters 164, 79–98. https://doi.org/10.1016/S0012-821X(98)00182-4

White, W., Hofmann, A., 1982. Sr and Nd isotope geochemistry of oceanic basalts and mantle evolution. Nature 296, 821–825. https://doi.org/10.1038/296821a0

White, W.M., Hofmann, a. W., Puchelt, H., 1987. Isotope geochemistry of Pacific Mid-Ocean Ridge Basalt. Journal of Geophysical Research 92, 4881. https://doi.org/10.1029/JB092iB06p04881

Zindler, A., Hart, S.R., 1986. Chemical Geodynamics. Annual Review of Earth and Planetary Sciences 14, 493–571. https://doi.org/10.1146/annurev.earth.14.1.493

Chapter 2

An Origin of the along-arc compositional variation in the Izu-Bonin arc system

Abstract

The Izu-Bonin arc system is sediment-poor (~400m thick with no accretionary prism) and, therefore, the influence of the altered oceanic crust (AOC) is most likely the source of the documented along-arc lava compositional variations, especially for Pb isotopes. Izu-Bonin arc lava geochemistry suggests an influx of a subduction component from an Indian-type AOC. However, samples drilled from the western Pacific geochemical reference site at Integrated Ocean Drilling Program Site 1149 implies subduction of a Pacific-type AOC. To solve the apparent discrepancy of slab input versus arc output in this arc system, samples of the AOC were dredged from vertical fault scarps of the subducting Pacific Plate along a transect from 27.5°N to 34.5°N. Samples range from tholeiitic to mildly alkalic mid-ocean ridge basalts as well as trachybasalts, basaltic trachyandesites, tephrites, and phono-tephrites. Samples exhibit a range of isotopic compositions (^{87}Sr/^{86}Sr=0.70282-0.70673, ^{143}Nd/^{144}Nd=0.512552-0.513174, ^{206}Pb/^{204}Pb=18.43-20.00, ^{207}Pb/^{204}Pb=15.40-15.67, ^{208}Pb/^{204}Pb=37.75-39.55). These results suggest that there is a geochemical variation in the AOC that is neither completely due to seawater or hydrothermal alteration, nor to petrogenetic processes. Rather, this isotopic variation is the result of the Pacific-Izanagi Ridge system tapping into a heterogeneous, plume-polluted

mantle source during the Mid-Cretaceous volcanic event. The observed Pacific-type AOC is not responsible for the Indian-type Pb isotopic signature of Izu-Bonin arc lavas. This leads us to propose an alternative scenario where the Izu-Bonin arc lava Indian-type Pb isotopic signature originates from slab-derived fluids interacting and adsorbing Pb from an Indian-type mantle wedge through zone-refining.

2.1. Introduction

A compositional relationship is typically observed between subducting oceanic lithosphere and arc lavas along convergent plate margins (Armstrong, 1968; Tatsumoto, 1969; Gill, 1981; Brown et al., 1982; White and Dupré, 1986; Plank and Langmuir, 1993). While it was initially suggested that such a relationship exists because arc lavas are primarily partial melts of the subducted oceanic crust (Green and Ringwood, 1968; Marsh and Carmichael, 1974), later studies indicate that arc lavas mainly originate from partial melting of the mantle wedge due to the fluxing effect of fluids released from the subducting slab (Gill, 1981; Pearce, 1982; Tatsumi and Nakamura, 1987) and decompression melting due to convection in the mantle wedge (e.g. England and Katz, 2010). These fluids transfer fluid-mobile elements and volatiles, collectively termed the “subduction component”, from the slab and overlying sediments into the mantle wedge which subsequently melts, thus compositionally connecting the subducted slab and the end arc lavas. Although some investigators have reconsidered slab melting in arc settings (e.g., Kay, 1978; Defant and Drummond, 1990; Freymuth et al., 2016), the release of subduction component from the slab is still considered the primary mode of linking subducted material to arc lavas (Pearce et al., 1995; Elliott, 2003; Manning, 2004; Straub et al., 2004; Castillo et al., 2009; Castillo, 2012; Zheng and Hermann, 2014).

Current models suggest that the serpentinized lithospheric mantle – although an important source of water – contributes a major fraction of only a few elements (e.g., B, Cl) to the subduction component (Straub and Layne, 2003) making the subducted sediment and altered oceanic crust (AOC) the principal reservoirs for such a component (Tatsumi and Nakamura, 1987; White and Dupré, 1986; Elliott et al., 1997; Plank & Langmuir, 1998; Taylor and Nesbitt, 1998; Class et al., 2000; Hochstaedter et al., 2000; Hauff et al., 2003). Though sediments comprise ~6% of the total subducting slab volume, their geochemical enrichment and radiogenic signature often overwhelm those of the more voluminous AOC, making the sediment signal easier to identify as the main subduction component in arc lavas (Elliott et al., 1997; Plank and Langmuir, 1998). For example, most along-arc geochemical variations are due to either melting or dehydration of subducting volcaniclastics and other sediments that have variable volume and/or composition (Elliott et al., 1997; Elliott, 2003; Ishizuka et al., 2007; Straub et al., 2010). Several studies, however, indicate that a number of isotopic and trace element (e.g., Pb and Ba, respectively) systematics indicate a strong AOC recycling component regardless of sedimentary input (Brenan et al., 1995; Pearce et al., 1995; Taylor and Nesbitt, 1998; Class et al., 2000; Bryant et al., 2003; Elliott, 2003; Straub et al., 2009). Furthermore, inherent variations of the AOC may become more distinguishable in low-sediment arc systems (e.g., Castillo et al., 2009).

The along-arc compositional variation of Izu Bonin-Marianas arc lavas is one of the most studied among global arc systems (Taylor and Nesbitt, 1998; Hochstaedter et al., 2000; Stern et al., 2003; Ishizuka et al., 2007, Straub et al., 2009). However, the thickness (ca. 400 m) and composition of pelagic sediment subducting into the Izu-Bonin trench are relatively constant (Ewing et al., 1968; Plank et al., 2000; Abrams, 2002; Stern, et al., 2003), making the AOC the logical primary source of geochemical variation within the subduction component (Elliott et al., 1997; Elliott, 2003; Straub et al., 2010). This appears to create a major discrepancy in the Pb isotope signature between arc output and slab input in the Izu-Bonin system. Lead is one of the foremost tracers of recycled AOC, estimated to make up ca. 50% or more of the Pb in global arc magmas (Straub and Zellmer, 2012), and has been estimated to contribute as much as 90% in the Izu-Bonin system (Porter and White, 2009; Straub et al., 2009; Freymuth et al., 2016). It has been suggested that the arc variation in $^{208}Pb/^{204}Pb$ for given $^{206}Pb/^{204}Pb$ (or Δ8/4 values – Hart, 1988) would require an influx of Pb from a subducted Indian-type AOC in the northern section of the Izu-Bonin system (Straub et al., 2009), yet the spot sample of the incoming mid-ocean ridge basalt (MORB) basement drilled seaward of the trench at the Integrated Ocean Drilling Program Site 1149 (hereafter ODP 1149) indicates a contiguous, subducting Pacific-type AOC (Pearce et al., 1999; Hauff et al., 2003; Kelley et al., 2003).

Here we present the major and trace element and Sr-Nd-Pb isotope compositions of AOC samples collected from 27.5°N to 35.5°N along the Pacific Plate subducting into the Izu-Bonin trench. These AOC samples exhibit a variation in their bulk composition. We then investigate the possible origin of such variation and its relationship with the geochemistry of Izu-Bonin arc lavas.

2.1.1 Geologic background of the Izu-Bonin arc-trench system

The N-S trending Izu-Bonin Marianas (IBM) arc system spans an area of approximately 2800km by 1000km in the western Pacific (Fig. 2.1). Subduction initiated ca. 52 Ma as old, dense Pacific oceanic crust spontaneously foundered along a transform fault (Bloomer et al., 1995; Stern et al., 2003; Reagan et al., 2010; Ishizuka et al., 2011). The first lavas to be erupted during the Eocene were low-K tholeiites and high-Mg boninites (Bloomer et al., 1995; Bryant et al., 2003; Stern et al. 2003; Straub, 2003; Ishizuka et al., 2006). Magmatic activity was localized to the present arc when true subduction began although proposals for the timing of this event range from close to initiation to as late as ca. 43 Ma (Stern et al., 2003; Reagan et al., 2010; Ishizuka et al., 2011; Straub et al., 2015).

The Izu-Bonin (northern) and Marianas (southern) arc segments have different subduction structures and characteristics reflecting differences in their tectonic histories. Back arc rifting began in the Mariana arc ca. 31-30 Ma to produce the Parece Vela Basin. Spreading in the Izu-Bonin back arc segment did not initiate until ca. 25 Ma and propagated south to form the Shikoku Basin, which merged with the Parece Vela Basin ca. 23 Ma (Bryant et al., 2003). Ash and turbidite records show volcanic front activity was minimal during back-arc rifting and formation of the Shikoku Basin (Bryant et al., 2003). Back arc spreading ceased in both basins between 17 and 15 Ma, though resumed in the south in the Mariana back arc between 6-2 Ma, forming the Mariana Trough (Bryant et al., 2003). The Izu-Bonin back arc also resumed spreading at this time, coinciding with an increase in eruption rates and a compositional shift towards more evolved, felsic compositions and is currently spreading at a rate between 40 and 60 mm/yr (Taylor, 1992; Bryant et al., 2003; Stern et al., 2003).

Within the trench, the Pacific Plate is steeply faulted as it bends and flexes during subduction. The vertical exposures of these fault scarps grow progressively larger (>410 m) as the plate descends into the trench, which has an average depth of 9 km (Nakamura, 1987). The AOC subducting at Izu-Bonin was accreted along the Izanagi-Pacific Ridge in the Mid-Cretaceous (Müller et al., 2008; Miyazaki et al., 2015; Boschman and Hinsbergen, 2016). A number of Mid-Late Cretaceous secondary volcanic features dot the Pacific plate, though there is a higher density outboard and subducting into the Marianas than Izu-Bonin (Stern et al., 2003).

The largest of these features is the Ogasawara Plateau, which collided with the IBM arc ca. 15 Ma (Miller et al., 2005).

Magnetic anomalies (M19-M5) between 27-34°N are consistent with the Japanese lineation set and range in age from 145 Ma north of Ogasawara Plateau to 131 Ma ~south of Honshu based on the geomagnetic polarity time scale of Gradstein et al. (2012). ODP Site 1149 was initially assumed to be ca. 132 Ma in age as it is purportedly located at the older half of the reversed polarity M-11 magnetic anomaly (Plank et al., 2000). However, detailed radiometric ^{40}Ar/^{39}Ar dating of the basaltic crust drilled at ODP Site 1149 produced an age of 127.1±1.5 Ma (Koppers et al., 2003), which is about 7 million years younger than the assumed age of the site. Thus, the age of the crust immediately outboard of the Izu-Bonin trench is controversial and may be as much as ca. 7 My younger than the documented magnetic anomaly ages.

2.1.2 Along-arc variation of Izu-Bonin arc lavas

A detailed description of the trace element and isotope variation with latitude of IBM arc lavas can be found in Ishizuka et al. (2006). A summary of the overall along-arc isotopic variation of Izu-Bonin arc lavas (from Straub, 2017; data filtered to represent arc front samples with <55wt.% SiO_2, and Ce/Pb values <10) is illustrated in Figure 2.1. Lavas from the southernmost part of the Izu-Bonin arc segment, roughly west of the Ogasawara Plateau, generally have the most radiogenic Pb isotope ratios in the IBM system. Izu-Bonin arc lava ^{87}Sr/^{86}Sr ratios decrease from 25°N to 27°N before increasing northward while there is an overall decrease in ^{206}Pb/^{204}Pb, ^{207}Pb/^{204}Pb and ^{208}Pb/^{204}Pb ratios and roughly constant ^{143}Nd/^{144}Nd ratios with increasing latitude (Fig. 2.1; Taylor and Nesbitt, 1998; Ishizuka et al., 2007). These northern arc lavas have positive Δ8/4 (up to ~50) as well as high ^{207}Pb/^{204}Pb for given ^{206}Pb/^{204}Pb (or positive Δ7/4 values up to ~8) that are typically possessed by Indian MORB (Hart, 1988).

It is important to point out, however, that an Indian MORB-type signature is inherent in many regions of the western Pacific, including the Shikoku and Parece Vela back arc basin crusts west of the IBM system (Hickey-Vargas, 1998; Taylor and Nesbitt, 1998; Flower et al., 2001; Kelley et al., 2003; Hickey-Vargas et al., 2006; Straub et al., 2010; Madrigal et al., 2016). The Indian MORB-type signature in these basins is less radiogenic (i.e., with lower ^{206}Pb/^{204}Pb), appearing more pristine or, at least, less contaminated than the Izu-Bonin arc lava signature (see also, Taylor and Nesbitt, 1998). Several models suggest that this is most probably due to the lesser amounts of subduction component in the back arc basin mantle than in the mantle wedge beneath volcanic arcs (e.g., Martinez and Taylor, 2002). Moreover, as clearly in the case for Tonga-Kermadec (e.g., Hergt and Woodhead, 2007) and New Hebrides (e.g., Crawford et al. 1995), the Indian-type signature of Izu-Bonin arc lavas was introduced later (i.e., starting at ca. 42 Ma) into the Izu-Bonin arc system as the arc transitioned to true subduction (Ishizuka et al 2011).

A variety of possible sources of the along-arc compositional variation of Izu-Bonin arc lavas, particularly the occurrence of Indian MORB-type Pb isotopic ratios in the northern samples, have been proposed, including sediment-wedge mixing (Hochstaedter et al., 2001) and subducted geochemically enriched seamounts (Plank et al., 2000; Sano et al., 2016). In a later model, Straub et al. (2009) proposed that current Izu-Bonin arc frontal volcanoes are influenced by the last vestiges of a subducted AOC generated along an Indian mantle-influenced Pacific-Izanagi Ridge. In this model, which will be described in more detail below, the trailing portion of the subducted ridge comprises the AOC immediately outboard the trench or just subducted into this arc system. It has also been argued that the southern section of the arc system is dominated by andesitic volcanoes because it is underlain by thin crust (10–20 km) that promotes lower pressure partial melting in the underlying mantle whereas the northern section is dominated by basaltic volcanoes because it is underlain by a thicker (~35 km) crust that promotes higher pressure partial melting of the mantle (Tamura et al., 2016).

2.2. Materials and methods

We collected AOC samples by dredging along a N-S latitudinal transect of the Pacific Plate subducting into the Izu-Bonin trench during the RR1412 cruise aboard R/V *Roger Revelle* in October-November 2014 (Fig. 2.1). Dredge locations were determined using bathymetric data collected at sea while avoiding secondary volcanic features and attempting to maintain reasonable spacings between sampling locations. Samples were dredged from the hanging wall of steep, normal faults parallel to the trench-axis with a relief >400m (i.e. greater than sediment thickness).

Almost all the dredged basalts are angular fragments of fine-medium grained lava flows; no plutonic rocks were sampled. Some hand samples have glassy rinds, though the glasses are variably devitrified. Acicular to tabular plagioclase ranging in size from 0.5 to 2.5mm represent the dominant phenocryst phase. Several samples have olivine phenocrysts that are almost always altered. All samples show variable degrees of seawater alteration. Many are coated with Mn crusts of variable thickness and Mn dendrites occur along broken surfaces in many samples. Alteration halos range up to 5mm thick rimming the edges of broken pieces and secondary calcite in-fills amygdules, veins and veinlets in some samples. However, the degree of alteration is highly variable and there is no systematic variation in alteration of the samples from different dredge hauls.

Major element analyses were conducted at the Japan Agency for Marine Earth Science and Technology (JAMSTEC) and Niigata University according to methods described by Tani et al. (2005). Seawater contamination was removed from crushed chips by boiling in deionized water and tested for precipitates with $AgNO_3$ before drying at 100°C overnight. After desalination, samples were cleaned in an ultrasonic bath before picking, crushing and powdering the least visibly altered AOC chips. A mixture of 0.4g of sample and 4g of $Li_2B_4O_7$ was fused and vitrified, before measurement by X-ray fluorescence analyzer (XRF) using a Rigaku Simultix 12. Some trace elements were measured using a pressed powder pellet by XRF using a Rigaku RIX3000, following the method of Goto and Tatsumi (1996).

At the Scripps Institution of Oceanography (SIO), hand samples were examined megascopically and trimmed of vein fillings and alteration rinds prior to crushing in a tungsten-carbide jaw crusher. Chips were then washed in a 2% HNO_3 deionized-water solution and immersed in an ultrasonic bath for approximately two hours to remove any seawater and other contaminants, dried overnight in an oven at 100°C before powdering inside a Spex alumina ceramic grinding container. Trace element concentrations were analyzed from 100mg of homogenized sample powder, following standard analytical procedures on an iCAPq quadrupole ICP-MS at the Scripps Isotope Geochemistry Laboratory according to methods described by Day et al. (2014). Data quality was monitored via repeated measurements of international standards (BHVO-2, BCR-2 and BIR-1) and total procedural blanks. A subset of 22 samples was selected for Pb-Sr-Nd isotope analysis and prepared for isotope analysis according to methods described by Janney and Castillo (1996). Strontium and rare earth elements (REE) were separated using cation-exchange columns, with HCl as eluent. Neodymium isotopes were further separated from the REE using hydroxyisobutyric acid as eluent. Lead separation was performed using standard anion exchange methods in an HBr medium. All isotope ratios were analyzed using a nine-collector, Micromass Sector 54 thermal ionization mass spectrometer (TIMS). Total procedural blanks are 35 pg for Sr, 10 pg for Nd and 60 pg for Pb. Strontium isotopic ratios were fractionation-corrected to ^{86}Sr/^{88}Sr = 0.1194 and are reported relative to ^{87}Sr/^{86}Sr=0.710254 ± 0.000016 (n=7) for NBS 987 during the period of analysis. Neodymium isotopic ratios were measured in oxide form, fractionation corrected to ^{146}NdO/^{144}NdO = 0.72225 (^{146}Nd/^{144}Nd= 0.7219) and are reported relative to ^{143}Nd/^{144}Nd = 0.511856 ± 0.000017 (n = 7) for the La Jolla Nd Standard during the period of analysis. ^{87}Sr/^{86}Sr and ^{143}Nd/^{144}Nd instrumental (2σ) errors are reported in Table 2.1 and refer to the last significant figures. Lead isotopic ratios were analyzed using the double-spike method to correct for mass fractionation during analyses; separate measurements of spiked and unspiked samples were made on different aliquots from the same dissolution. The SBL-74 ^{207}Pb–^{204}Pb double-spike from the University of Southampton (e.g., Taylor and Ishizuka, 2001) was used. During the analysis period, the method produced the following results for NBS 981: ^{206}Pb/^{204}Pb = 16.932 ± 0.005, ^{207}Pb/^{204}Pb = 15.492 ± 0.006 and ^{208}Pb/^{204}Pb = 36.707 ± 0.020 (n = 6).

2.3 Results

2.3.1. Major element abundances

Samples are primarily tholeiitic, depleted normal (N)-MORB and mildly alkalic enriched (E)- MORB, but also include several trachybasalts, basaltic trachyandesites, tephrites, and phonotephrites (Table 2.1; Supplementary Figure 2.1). Loss on ignition (LOI) values are high with an average of 3.05% (±1.48%) but variable, showing no statistically significant trend with latitude (r^2=0.34; Supplementary Figure 2.2). Samples from <30°N (henceforth Group 1, see Fig. 2.1) are almost exclusively tholeiitic N-MORB though our northernmost site also yields N-MORB. Enriched-(E-)MORB-like samples appear to occur from 30-34°N (Group 2). However, these samples clearly reflect some alteration effects such as inflation of alkali content. The presence of alkalic lavas from >34°N (Group 3) is noteworthy given they typically belong to the alkalic ocean island basalt (OIB) lava series or in young, off-axis, submarine volcanoes (Machida et al., 2009; Miyazaki et al., 2015), despite our efforts to dredge normal sections of the AOC. Samples from Group 3 are also typically more differentiated with higher Al_2O_3, K_2O and P_2O_5 but lower CaO. Nevertheless, oxides of Fe_2O_3, Na_2O and TiO_2 remain relatively constant with varying MgO contents across the suite.

2.3.2. Trace element abundances

Our samples display a large range of trace element abundances (Table 2.1; Fig. 2.2), consistent with their tholeiitic to alkalic major element geochemistry and latitudinal subdivisions. Rare earth element diagrams (Fig. 2.2a) generally show smooth, regular patterns indicating the majority of Group 1 samples are slightly enriched or evolved N-MORB. Exceptions are D21-6 and D21-7 samples, which show more typical E-MORB profiles with a small, positive Eu anomaly. Extended trace element diagrams (spidergrams) exhibit irregular patterns as they typically feature variable and anomalous peaks for Cs, Rb, B and Li anomalous peaks (Fig. 2.2d). The trace element contents of Group 1 samples more closely resemble E-MORB profiles in contrast to their N-MORB REE profiles. The D7 sample which, has the most depleted REE pattern is the least enriched of the suite, and a positive Pb peak. The D21 samples have highly variable patterns, spanning an order of magnitude with peaks in U, Sr and Ba. The D8 samples are enriched in Rb and U relative to N-MORB and exhibit two trends; one with higher Ba, Th, Nb, Tb, and La and one depleted in these elements but comparatively enriched in the heavy REE.

Group 2 samples (Figs. 2.2b, 2.2e) have the most variable REE profiles, ranging from depleted N-MORB to E-MORB/OIB-like even within a single sampling site. Enriched-MORB samples from D19 and D16 feature large negative Ce-anomalies. The D15 samples are the outliers in this transitional segment, consistently showing a depleted N-MORB profile. Similarly, Group 2 samples show the most variable spidergram profiles, with high Rb and U, particularly those from D15 and D16. D18 and D19 samples show similar profiles although the latter have higher overall concentrations. The D11 samples have the most variable concentration profiles.

Finally, Group 3 samples have two REE end-member profiles (Fig. 2.2c): flat, N-MORB and OIB-like. D12 and D14 samples are all OIB-like whereas D13 samples are mostly N-MORB type with the exception of D13-4 and D13-7. Group 3 spidergram profiles (Fig. 2.2f) are typically more OIB-like, especially samples from D12 and D14, consistent with their major element geochemistry. The D13 samples show the most variable profiles that are mostly E-MORB like with a peak in U. An important conclusion from this exercise is that caution should be exercised when classifying variably altered submarine lavas based on spidergrams because seawater alteration affects concentrations of fluid-mobile elements such as Cs, Rb, Sr, Pb, U, B, and Li (Seyfried et al., 1998).

2.3.3. Strontium-Nd-Pb isotope ratios

Our measured AOC $^{87}Sr/^{86}Sr$ and $^{143}Nd/^{144}Nd$ values have a wider range than those measured in ODP 1149 samples by Hauff et al. (2003), primarily in Nd-isotope ratios. These ratios do not correlate with latitude. The most $^{87}Sr/^{86}Sr$ radiogenic values are from D16 and altered ODP 1149 samples. The general trend is of the AOC $^{143}Nd/^{144}Nd$ value decreasing towards the north, with the lowest values from samples from D19 and D16. The most unradiogenic $^{143}Nd/^{144}Nd$ values overlap with both Indian and Pacific-type MORB whereas the most evolved mainly trend toward ODP 1149 sediment ($^{87}Sr/^{86}Sr$=0.70956 and $^{143}Nd/^{144}Nd$=0.51231; Plank et al., 2007). In detail, the unradiogenic values are more typical of the Shatsky Rise ($^{143}Nd/^{144}Nd$=0.51336–0.51298; Sano et al., 2012; Heydolph et al., 2014) whereas the radiogenic ones more broadly overlap with the Ontong Java Plateau (Tarduno et al., 1991; Fitton and Godard, 2004; Tejada et al., 2004).

Lead isotope ratios similarly have a wide range of values ($^{206}Pb/^{204}Pb$ = 18.428–19.995) that is greater than that of Hauff et al. (2003). Samples with the most radiogenic Pb isotopes are from D12, D14, D13, D7, D21 and D19; many of these samples tend to correspond to higher $^{87}Sr/^{86}Sr$ and lower $^{143}Nd/^{144}Nd$ values. The highest AOC $^{206}Pb/^{204}Pb$ (19.995) is from D7, the southernmost location, and then decreases northward toward ODP Site 1149 before increasing again. The AOC also has negative $\Delta7/4$ and $\Delta8/4$ values (Table 2.1 or Fig. 2.4). However, AOC $\Delta7/4$ and $\Delta8/4$ values are highly variable and do not show any significant trend with latitude.

Figure 2.3 also shows the age-corrected Sr-Nd-Pb isotope values to 125 Ma. Several AOC $\Delta8/4$ values shift from negative to positive as a result of our age corrections, suggesting that several of our samples may have been derived from an Indian-type upper mantle. The presence and influence of an Indian-type mantle in these samples is supported by their low $^{143}Nd/^{144}Nd$ values for given $^{206}Pb/^{204}Pb$ values. We note, however, that this is not a uniform trend within our dataset as a number of $\Delta8/4$ values actually become more negative after age correction (Table 2.1).

2.4. Discussion

2.4.1. AOC compositional variation and potential origins

As presented in Section 2.3, the AOC subducting into the Izu-Bonin trench exhibits a range of values in major-trace elements and Sr-Nd-Pb isotope ratios despite the dearth of samples and inadequate spacing between sampling locations (Figs. 2.2-2.4). This compositional variation could be due to a number of processes including: seawater alteration, assimilation-fractionational crystallization (AFC) processes, differences in partial melting or inherent heterogeneity of the mantle source. The samples were likely affected by all these processes; in this section we evaluate which is the most likely to have produced the compositional variation.

The most probable explanation for the AOC geochemical variation is that the subducting Pacific Plate was generated from a compositionally heterogeneous upper mantle. Samples dredged from the northern sector of the subducting slab have an OIB-like compositional signature and were accreted ≤125 Ma, or penecontemporaneously with the so-called Mid-Cretaceous volcanic event (ca. 125-100 Ma- Larson, 1991). Magnetic anomaly patterns and the 127 Ma age of the basement at ODP Site 1149 constrain the formation age of the subducting AOC between ca. 145 in the south to possibly as young as c.a. 130 Ma in the north (or c.a. 123 with the observed magnetic anomaly versus ^{40}Ar/^{39}Ar dating offset observed by Koppers et al., 2003), and this range overlaps with the volcanic event (Nakanishi et al., 1992; Nakanishi, 1993; Plank et al.., 2000; Koppers et al., 2003). The event peaked at ca. 125 Ma when the Pacific Basin experienced voluminous volcanism that formed large intraplate bathymetric features such as the Mid-Pacific Mountains and the ancestral Ontong Java-Manihiki-Hikurangi Plateau (Tarduno et al., 1991; Taylor, 2006).

Oceanic crust and secondary volcanic features generated during and immediately after the Mid-Cretaceous volcanic event clearly have an E-MORB and/or OIB-like composition (e.g. Janney and Castillo, 1996, 1997; Tejada et al., 2002; Miyazaki et al., 2015; Madrigal et al., 2016). The geochemically enriched trace element contents and long-lived radiogenic isotopes (ε_{Nd}(T)=8.4-11.6; ^{206}Pb/^{204}Pb=17.9-18.6; ^{87}Sr/^{86}Sr=0.7023-0.7026; (Castillo et al., 1991, 1994; Janney and Castillo, 1996, 1997) of these Mid-Cretaceous rocks indicates that the Pacific upper mantle was contaminated with materials derived from plumes or plume heads responsible for the voluminous volcanism.

We argue that the subducting AOC exhibits geochemical compositional variation, from N-MORB-like in the south to OIB-like in the north, because it was accreted along the Izanagi-Pacific Ridge from the Pacific upper mantle that was contaminated by mantle plume materials during the Mid-Cretaceous volcanic event at ca. 125 Ma (Miyazaki et al., 2015). Our new results, however, clearly indicate that the currently subducting AOC does not have an Indian-type isotopic signature, particularly the high Δ8/4, and is therefore unable to contribute to the Indian Pb-isotope signature of the arc lavas (see Table 2.1 and Fig. 2.3).

The isotopic composition of isolated seamounts near the study area (e.g., Hotta and Bosei Seamounts -Shimoda et al., 2011; Miyazaki et al., 2015; Fig. 2.1) is different from that of our OIB-like Group 3 AOC samples (Fig. 2.3). Thus, the enriched, OIB-like Group 3 samples were most likely not dredged from secondary off-axis seamounts and/or sills intruded into the crust (Hauff et al., 2003). Furthermore, it would be highly unlikely that each of our OIB-like, geochemically enriched samples from multiple dredge sites were systematically dredged from off-axis outcrops in the northern sector of the subducting crust.

We also do not consider high-temperature alteration due to hydrothermal fluids to be the source of the variation of our AOC samples, though it is clearly a process that has affected our samples and complicates the interpretation of initial values. We see classic indicators of alteration such as a decrease in MgO and inflation of K_2O and fluid-mobile trace elements such as U, Sr, Pb, Ba, and Rb concentrations, leading to inflated U/REE and higher than normal MORB $^{87}Sr/^{86}Sr$ ratios (Staudigel et al., 1996; Madrigal et al., 2016). In addition, we see pronounced negative Ce-anomalies in D-16 samples are observed (Fig. 2.2) due to the increased mobility of oxidized Ce^{4+} in seawater. Thus, the high Pb/Ce values (Fig. 2.5) in D16-samples, with their negative Ce-anomalies, likely result from low Ce-concentrations rather than additional

Pb. The radiogenic in-growth of Pb due to U-uptake of Group 3 samples (with the most radiogenic Pb isotope ratios) during alteration (e.g., Krolikowska-Ciaglo et al., 2007), however, is not supported by their observed degree of alteration relative to the different sample groups. Specifically, plots of Pb/Ce and U/Th ratios (Fig. 2.5) indicate that Group 2 (D15 and D16) plus Group 1 (D7-1) are the most altered (i.e., U/Th >> 1 and/or Pb/Ce > 0.05). Accordingly, these samples should have the most radiogenic Pb in-growth. However, our most consistently radiogenic Pb values are from Group 3 samples, rather than from Groups 1 and 2.

Partial melting and fractional crystallization processes can also cause major and trace element variations in lavas (e.g., Bowen, 1928; Shaw, 1970; Wilson, 1989). In the present case, a possible scenario is that a systematic decrease in partial melting of the upper mantle produces the overall northward tholeiitic-transitional-alkalic composition of the AOC (Fig. 2.2). On top of this, the relatively more advanced degree of fractional crystallization (i.e., lower MgO) of the alkalic (D18, D16, D12 and D14) samples enhances their trace element contents relative to the other samples. Thus, partial melting and fractional crystallization processes offer a viable explanation for the observed geochemical variation of the subducting AOC. Besides the absence of a logical causal mechanism that was responsible for the systematic decrease in the degree of partial melting of the upper mantle from ca. 145 to 125 Ma, however, magmatic differentiation is a problematic explanation because the chemical variations are based on the general assumption that the upper mantle is compositionally homogeneous. Since long-lived radiogenic isotopes are not generally affected by magmatic differentiation processes (Faure, 1986; Dickin, 2005), magmatic differentiation is highly inconsistent with our observed isotopic variation (Fig. 2.4). In sum, the enrichment of the AOC subducting at the Izu-Bonin trench is due to upper mantle contamination from the Mid-Cretaceous event rather than alteration or petrogenetic processes (AFC or partial melting).

2.4.2. AOC compositional variation versus Izu-Bonin along-arc arc variation

The Sr-Nd-Pb isotopic variation of the AOC subducting into the Izu-Bonin trench is within the range of Pacific lavas, consistent with previous observations (Miyazaki et al., 2015; Hauff et al., 2003). The major question then is whether or not the compositional variation of subducting AOC produced the observed along-arc variation of Izu-Bonin arc lavas, which requires the presence of Indian-type AOC subducting beneath the northern sector of the arc (Straub et al., 2009). If not, then Izu-Bonin is different from the majority of arc systems that typically exhibit a compositional connection between subducting crustal material and observed arc lava geochemistry.

The relationship between along-arc lava compositional variation and AOC compositional variation is shown in Figure 2.4. Ratios of the fluid-mobile Ba over less fluid-mobile elements such as Zr, Rb and La in the arc lavas increase towards the north (Taylor and Nesbitt, 1998; Ishizuka et al., 2007), and the high northern ratios were previously interpreted to indicate the presence of a strong subduction component from the mafic AOC. Similarly, higher Pb/Ce ratios of the arc lavas are most probably due to the efficient transport of Pb in hydrothermal fluids from the subducting AOC (Porter and White, 2009; Straub and Zellmer, 2012). The along-arc lava variations of trace element ratios such as Th/Ce, Zr/Y and Nb/Zr do not indicate a transfer of fluid-immobile elements from the slab, though may be an indication of either partial melt or mantle heterogeneity instead (e.g. Ishizuka et al., 2003; Freymuth et al., 2016). Furthermore, there is a lack of correlation between AOC and arc lava Pb isotope ratios, despite the predicted efficient transfer of Pb and Sr in this subduction zone (Porter and White, 2009; Straub and

Zellmer, 2012). In sum, there is no correlation between the AOC compositional variation and along-arc lava variation.

2.4.2.1. Contributions from IODP 1149 sediments

Despite the fact that Izu-Bonin represents a sediment-poor arc system, there is a need to consider sediment contributions into the arc system. The sediments at ODP Site 1149 are considered to be representative of sediments that were already subducted beneath the arc (Plank et al., 2000; 2007). The entire sequence of sedimentary units at ODP Site 1149 has been penetrated fully and seismic studies show that these units are laterally extensive throughout the northwestern Pacific immediately adjacent to the trench (Ewing et al., 1968; Abrams, 2002). The sediments primarily consist of carbonate-free clays, variable amounts of volcanic ash and siliceous microfossils (Unit 1), cherts (Unit 2), porcelanites (Unit 3), and calcareous nanofossil chalks or marls (Unit 4; Plank et al., 2000; 2007; Kelley et al., 2003). These are trace element-depleted relative to global subducting sediments (GLOSS) values (Plank et al., 2007), but have high concentrations of REE, Mn, Pb and feature large negative Ce-anomalies. Bulk sediment $^{87}Sr/^{86}Sr$ and $^{143}Nd/^{144}Nd$ (0.7094 and 0.51235, respectively; Hauff et al., 2003) mirror Cretaceous to Holocene seawater values (Elderfield, 1986; Ingram, 1995). However, the clay and volcanic ash isotopes reflect their terrigenous sources particularly those of Pb ($^{206}Pb/^{204}Pb$=18.61, $^{207}Pb/^{204}Pb$=15.60, $^{208}Pb/^{204}Pb$=38.67; Hauff et al., 2003).

Plank et al. (2007) estimated the bulk composition of sediments subducting into the Izu-Bonin trench from the different units described above. In detail, the range of Ce/Pb and Ba/La in the sediments generally vary between Units I and II versus Units III and IV. Down-core Ce/Pb ratios range from ~2 to 4 in Units I and II, respectively, and are highly variable (0.8-8.6) in Units III and IV but decrease down-core. Arc lavas values, on the other hand, range from ~2-15, with lower values towards the north (Porter and White, 2009). Thus, the clay and volcanic ash in Units I and II can be the most likely source of the low Ce/Pb subduction component in the north. That is, the greatest control on the Ce/Pb in the subduction component is the amount of terrigenous sediments, which is dependent on a continental source (e.g. Japan arc and Asia) and, thus, is highest in the northern section of the Izu-Bonin arc system. On the other hand, Ba/La in Units I and II are low (<50) whereas in Units III and IV are variable with high values in Unit IV (up to 150). Arc Ba/La values are highest in the north (up to 150; Taylor and Nesbitt, 1998; Ishizuka et al., 2007). This would imply that the porcelanites and marls in Unit III and, particularly in Unit IV, would be the primary source of the high Ba/La subduction component in the north. This is the opposite of the previous conclusion based on the Ce/Pb of these sediments. Thus, the disagreement between their Ce/Pb and Ba/La values suggests ODP 1149 sediments, while a significant contributor to arc lava geochemistry in global arc systems including Izu-Bonin, are not the primary source of the variation of the arc lava signature in the Izu-Bonin arc system.

2.4.3. Models for the source of Indian-MORB type Pb in northern Izu-Bonin arc lavas

Our results indicate that the AOC at the Izu-Bonin trench does not have the Indian-type Pb isotopes of northern Izu-Bonin arc lavas. Although these results do not directly support the aforementioned proposal that a previously subducted Indian MORB-type AOC (henceforth IOC model) is the main source of the unradiogenic Pb in the northern Izu-Bonin arc lavas (Straub et al., 2009), they also clearly do not rule out the IOC model. This is because the tectonic fabric of the Pacific plate subducting into the Izu-Bonin trench had been modified by major fracture zones with significant offsets parallel to the trench (e.g., the Kashima Fracture Zone – Fig. 2.1). Hence, it is possible that a portion of previously subducted slab may already be under the arc, and seismic tomography indeed indicates the presence of a previously subducted slab in the mantle transition zone in the northern sector of the Izu-Bonin arc system (Gong et al., 2018). We note that Miyazaki et al. (2015) also ascribed the along-arc variation primarily to variation in AOC input except they suggested that the Pacific crust with an Indian-type isotopic signature was not accreted by the Pacific-Izanagi Ridge until later, at ca. 80 Ma.

In the IOC model, the Pb in the fluid from AOC or 'metabasalt fluid' (mbf) is unradiogenic, almost mantle-like, and was determined by extrapolating the ^{208}Pb/^{204}Pb versus ^{206}Pb/^{204}Pb mixing line between sediment and northern Izu-Bonin arc lavas into the field defined by MORB from the Indian Ocean (Straub et al., 2004; 2009). The extrapolation of the metabasalt fluid Pb composition was based on the low Ce/Pb of Izu-Bonin arc lavas, indicating that the Pb is coming from the subducting slab rather than from the highly depleted Izu-Bonin mantle wedge (Hochstaedter et al., 2000; Straub et al., 2004; 2009). As the arc lavas have an Indian-type Pb isotopic signature, it was then inferred that the Pb in metabasalt fluid was derived from MORB with a modern Indian-type Pb isotope signature that is now beneath the arc front. Moreover, the composite fluid is a common component in the arc lavas.

Mixing between metabasalt fluid and sediment fluid of the IOC model is represented by Lines 1 and 1' in Figure 2.6. Many of the arc lavas, including the least radiogenic northern Izu arc lavas from Miyakejima Volcano (Yokoyama et al., 2006) and juvenile particles (glass, volcanic rock) in the Neogene fallout tephras at the Izu arc volcanic front that best represent the composition of slab-derived fluids (Straub et al., 2004; 2009; 2010) indeed plot along or ca. close to these lines. However, there are many lavas that plot on the radiogenic side of the lines (i.e., high ^{206}Pb/^{204}Pb, ^{208}Pb/^{204}Pb and ^{207}Pb/^{204}Pb). Per the IOC model, the radiogenic Pb isotopes of arc lavas diverging from the composite metabasalt-sediment fluid composition have more sediment melt component, which can easily dominate the trace element and isotopic signature of many convergent margin lavas (Straub et al., 2004; 2009). Conversely, the highly depleted mantle wedge contributes limited Pb to Izu-Bonin arc lavas.

A first order implication of our results, however, is that the Pacific-type AOC in the trench may simply be a continuation of or similar to that underneath the arc. But then, where does the Indian-type MORB signature of the arc magmas come from? As sediment variation and crustal contamination are lesser in Izu-Bonin compared to other arcs (e.g., Taylor and Nesbitt, 1998; Ishizuka et al., 2003; 2006; Straub et al., 2009), it is reasonable to reconsider the Indian-type mantle wedge as the major source of the unradiogenic Pb in northern Izu-Bonin arc lavas (Ishizuka et al., 2003). But how does an Indian mantle produce the Indian type Pb isotopic signature of the northern arc lavas given that it is highly depleted in Pb (Straub et al., 2004; 2017)?

Below, we also present an alternative model to demonstrate how an Indian-type mantle wedge (henceforth IMW) can produce the along-arc compositional variation of the Izu-Bonin arc lavas. This model is speculative because of the unconstrained nature of multiple variables in this particular geologic system (e.g. amount and composition of fluids coming off the slab, degree of rock/fluid interaction and degree of partial melting are unknown and, thus, were determined by iteration). In the IMW model, we calculated the isotopic composition of a zone-refined slab fluid that equilibrates, then mixes with the Indian-type mantle wedge in order to approximate an appropriate source composition and isotope ratio that could generate documented Izu-Bonin arc lavas (Ayers, 1998; Straub, 2017). While our model uses the zone-refining method by Ayers (1998), which focused on trace element recycling in arc settings in Tafahi in the Tonga arc system and Guaguan in the Marianas arc system, we focus primarily on Pb isotope recycling in the Izu-Bonin arc system. The main point of our illustration is that through zone refining, the highly depleted nature of the Izu-Bonin mantle wedge is not a necessarily a barrier for the mantle wedge to be a major source of Pb in the Izu-Bonin arc because slab-derived fluids equilibrate with and continuously adsorb Pb from the mantle prior to flux melting the mantle. However, we note that this alternative model is only possible if the AOC fluid can indeed effectively adsorb Pb from a highly depleted mantle wedge prior to flux melting to generate arc magmas.

The basic premise of our qualitative IMW model is that the Pb isotope signature of post 42Ma Izu-Bonin arc lavas comes from three end-sources: (a) Indian-type mantle (IOM), (b) sediment-derived aqueous fluid and (c) AOC-derived aqueous fluid, with the AOC composition represented by the average of Groups 1-3 (Table 2.1) and ODP Hole 1149 (Hauff et al., 2003) lavas. The bulk of post 42Ma Izu-Bonin arc lavas defines a roughly ‘fan-shaped’ distribution that lies above the NHRL and has the Pb isotope characteristics of Indian-type MORB (Figure 2.6; Straub et al., 2004; 2009). They plot within the triangular areas defined by Lines 2 and 2’ (connecting IOM and sediment) and Lines 3 and 3’ (connecting IOM and AOC) in Figure 2.6. There are a few arc lavas that are more radiogenic than both sediment and AOC endmembers but they are still less radiogenic than some of the AOC lavas (not shown). Significantly, the handle of the fan is comprised of unradiogenic arc lavas including the aforementioned lavas and tephra particles from the northern Izu-Bonin arc. Thus, the source of unradiogenic northern Izu-Bonin arc lavas is key to the origin of the along arc compositional variation of post 42Ma Izu-Bonin arc lavas.

Our IMW model calculations start with the Pb concentrations in the slab-derived fluids using the Rayleigh distillation equation (Ayers, 1998):

$$C_{fluid_i} = \frac{C_{slab}}{D_{slab/fluid}}\left(1 - F_{fluid}\right)^{\left(\frac{1}{D_{slab/fluid}} - 1\right)} \qquad (1)$$

where C_{fluid_i} is the Pb concentration in the resultant fluid and C_{slab} is the measured concentration of Pb in the slab. For the average AOC fluid, the Pb content was calculated using an assumed fluid fraction (F_{fluid}) of 6% in the mixture, which is within the range of LOI values (Table 2.1), and Pb eclogite/fluid partition coefficient ($D_{slab/fluid}$) from Ayers (1998). To calculate the Pb in the average sediment fluid, the sediment was assumed to completely dehydrate, creating a fluid/sediment fraction =1. Thus, the distillation equation reduces simply to a division of $[\mathrm{Pb}]_{\mathrm{Sed}}$ by the bulk sediment aqueous fluid partition coefficient from Johnson and Plank (1999). Results show high concentrations of Pb in the fluids ($\mathrm{Pb}_{\mathrm{sed\ fluid}}$ = 24.1 ppm; $\mathrm{Pb}_{\mathrm{AOC\ fluid}}$ = 1.67 ppm) that can readily overwhelm the Pb in the depleted mantle wedge (Pb = 0.036 ppm), making it extremely difficult for the mantle to contribute unradiogenic Pb to Izu-Bonin arc lavas (average $\mathrm{Pb}_{\mathrm{arc\ lavas}}$ = 2.17 ppm - e.g., Straub et al., 2004; 2017). This dilemma is exemplified by adding $\mathrm{Pb}_{\mathrm{sed\ fluid}}$ to IOM to produce the unradiogenic northern arc lavas (Lines 2 and 2’ in Fig. 2.6). Although as much as ca. 99.7% of the IOM is in the binary mixture (or 33.2% of IOM Pb - Straub and Zellmer, 2012), this source with 0.108 ppm Pb would generate arc lavas with only 0.541 ppm upon, e.g., 20% partial melting. This is insufficient to account for the Pb present in the basaltic Izu Bonin magmas and suggests that there must be additional Pb with an Indian MORB-type signature that is contributing Pb to the Izu Bonin arc.

A possible way for the mantle wedge to be a major source of the northern Izu-Bonin arc lavas, then, is for the AOC-derived fluid to adsorb some of the IOM unradiogenic Pb prior to arc magma generation (e.g., Keppler, 1996). Thus, our IMW model assumes that the fluid composition is modified as it moves through the matrix (see inset in Fig. 2.6) through zone refining, which is based on a process to remove impurities from metals and organic compounds by the passage of molten zone through the solid material (Harris, 1957). In the present case, both the Pb content and isotopic composition of the fluids are zone refined as Pb is highly compatible to subduction fluids (e.g., Straub 2004; Straub et al., 2009; Straub and Zellmer, 2012; Porter and White, 2009; Ayers, 1998) even when the solid matrix or mantle is more depleted in Pb than the fluid (e.g., Reiners, 1998).

To determine the degree of interaction between the AOC-derived fluid and mantle, we used the parameter *n*, or rock/fluid mass ratio (Harris, 1974) in the equation derived by Ayers (1998) and used by Kimura et al. (2010):

$$C_{fluid} = \frac{C_{wedge}}{D_{slab/fluid}} - \left[\frac{C_{wedge}}{D_{slab/fluid}} - C_{fluid_i}\right] e^{-nD_{slab/fluid}} \quad (2)$$

where $D_{wedge}/_{fluid}$, C_{wedge} are the mantle/fluid partition coefficient and mantle wedge [Pb], respectively, C_{fluid_i} is the slab-derived fluid component and C_{fluid} represents the resultant refined fluid. To determine the significance of the mantle wedge contribution to this process, zone-refining is treated as a series of small, incremental changes to the fluid over time, where the significance of mantle contribution continually increases. The fraction of IOM Pb in the refined AOC fluid, or $X_{Pb,slab}^{fluid}(n)$ can be calculated using C_{fluid} from Equation 2 and an increment of *n* or $\partial n = 0.1$ in Equation 3 (Ayers, 1998):

$$X_{Pb,slab}^{fluid}(n) = \frac{\left(1-\frac{\partial n}{\partial n+1}\right)C_{fluid}}{\left(1-\frac{\partial n}{\partial n+1}\right)C_{fluid}+\left(\frac{\partial n}{\partial n+1}\right)C_{wedge}} * X_{Pb,slab}^{fluid}(n-\partial n) \quad (3)$$

As the migrating AOC fluid Pb adsorbs IOM Pb, the Pb isotope ratios of the refined fluid also change. The isotopic evolution is dependent on the fraction of Pb in the AOC fluid from Equation 3 and can be calculated using Equation 4 (Ayers, 1998):

$$\frac{^{20x}Pb}{^{204}Pb} = X_{Pb,slab}^{fluid}(n) * \left(\frac{^{20x}Pb}{^{204}Pb}\right)_i^{fluid} + \left(1 - X_{Pb,slab}^{fluid}(n)\right) * \left(\frac{^{20x}Pb}{^{204}Pb}\right)^{wedge} \quad (4)$$

where $\left(\frac{^{20x}Pb}{^{204}Pb}\right)_i^{fluid}$, $\left(\frac{^{20x}Pb}{^{204}Pb}\right)^{wedge}$ are the isotope ratios of the refined AOC fluid and mantle wedge, respectively.

For illustration purposes, we use the Pb content and isotopic composition of a refined AOC fluid after *n* = 40 (i.e. 1:40 – AOC fluid:IOM) to generate the northern Izu-Bonin arc lavas. The refined AOC fluid is simply mixed with IOM, which then partially melts at 20%. All model parameters and results are in presented in Table 2.2 and shown graphically by Lines 3 and 3'in Figure 2.6. Results show that the source of northern arc lavas are a mixture involving ca. 86% of the IOM, translating to direct contributions of 7.0% IOM and 93.0% of the refined fluid Pb in an IAB source with 0.440 ppm Pb that can generate arc lavas with 2.10 ppm Pb. However, the refined AOC fluid also has an IOM component (roughly 51%), thus the total contribution from unmodified mantle wedge is 54.4% of the arc lava Pb. Per the IMW model, the remainder of the lavas is from the mantle wedge metasomatized by zone-refined, AOC-dominated slab fluids with a modified Pb isotope signature. In summary, the origin of the along-arc Pb isotopic variation of Izu-Bonin arc lavas remains an open question. An AOC with an Indian-type Pb isotopic signature is a suitable source for the unradiogenic Pb isotope ratios in the northern Izu-Bonin arc lavas, but our results show that the Mesozoic oceanic crust subducting in the trench does not have an Indian-type Pb isotopic signature. Thus, alternatively, the unradiogenic Pb isotopic signature of the northern arc lavas may possibly be coming from an Indian-type mantle wedge.

2.5. Conclusions

- The AOC atop the Pacific plate subducting into the Izu-Bonin trench is not compositionally homogeneous, as previously assumed, but rather exhibits compositional variation in both major and trace elements as well as in Sr-Nd-Pb isotopes.

- This geochemical variation is likely the result of the Pacific-Izanagi ridge sampling an enriched, heterogeneous upper mantle starting at ca. 125 Ma, or during the Mid-Cretaceous volcanic event.
- The geochemical variation of the AOC currently at the trench is not responsible for the Indian-type isotopic signature of northern Izu-Bonin arc lavas.
- Results of the study do not rule out the possibility that an Indian-type AOC responsible for the unradiogenic Pb isotopic signature of northern arc lavas is directly underneath the northern section of the Izu-Bonin arc. The results, however, also point to an alternative hypothesis that the Indian-type isotopic signature of northern Izu-Bonin arc lavas mainly comes from an Indian-type mantle wedge.

Acknowledgments

We would like to thank Dr. James Day at the SIGL for the invaluable use of his facilities, materials and time. We also thank Ryu Kaneko, at Niigata University for his work in contribution to this manuscript. We sincerely thank all of our editors and anonymous reviewers for their time and conscientious and dedicated efforts to improve this work. This work was funded by the National Science Foundation grants (NSF-1333698) to P. Castillo and (NSF-1333235) to S. Straub. We also sincerely thank Captain T. Desjardin, the R/V Roger Revelle crew, especially our ResTechs, and shipboard scientific party for their time and effort in collecting our samples. All authors certify that there are no financial conflicts of interest related to this work and our results. All data is available in the Supporting Information.

Chapter 2, in full, is a reproduction of material as it appears in Durkin, K., Castillo, P.R., Straub, S.M., Abe, N., Tamura, Y., An origin of the along-arc compositional variation in the Izu-

Bonin arc system, *Geoscience Frontiers*, 2020. The dissertation author was the primary investigator and author of this work.

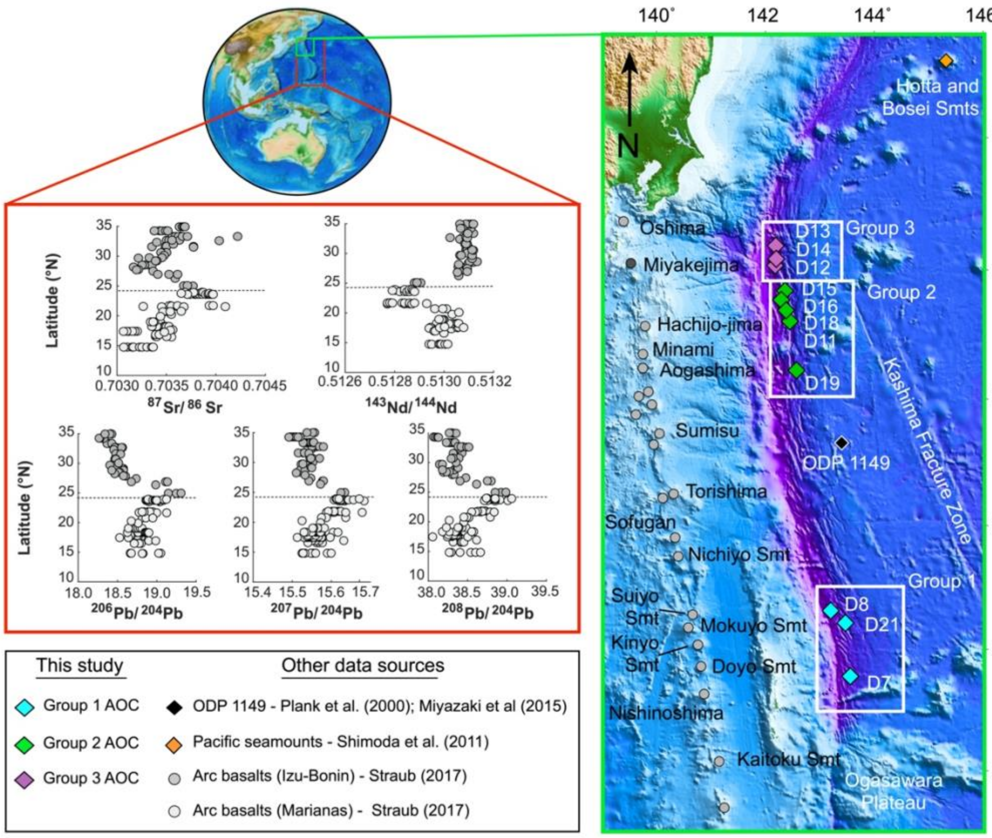

Figure 2.1: Left panel: Global site reference for IBM arc-trench system showing study area and along-arc variations (red insert) of Sr-Nd-Pb isotope ratios in IBM volcanic front lavas (data from Straub, 2017). Right panel: GMT bathymetric map of study area showing Roger Revelle cruise RR1412 dredge sites that retrieved basalt (cyan, green, and purple diamonds), ODP site 1149 (black diamond with white outline) and volcanic seamounts Hotta and Bosei (orange diamond) on the incoming Pacific Plate. Dredge sites are boxed and labeled as Group 1 (<30°N), Group 2 (30-34°N) and Group 3 (>34°N) – see text for group description. Izu-Bonin arc front volcanoes (Straub, 2017) are shown as gray circles.

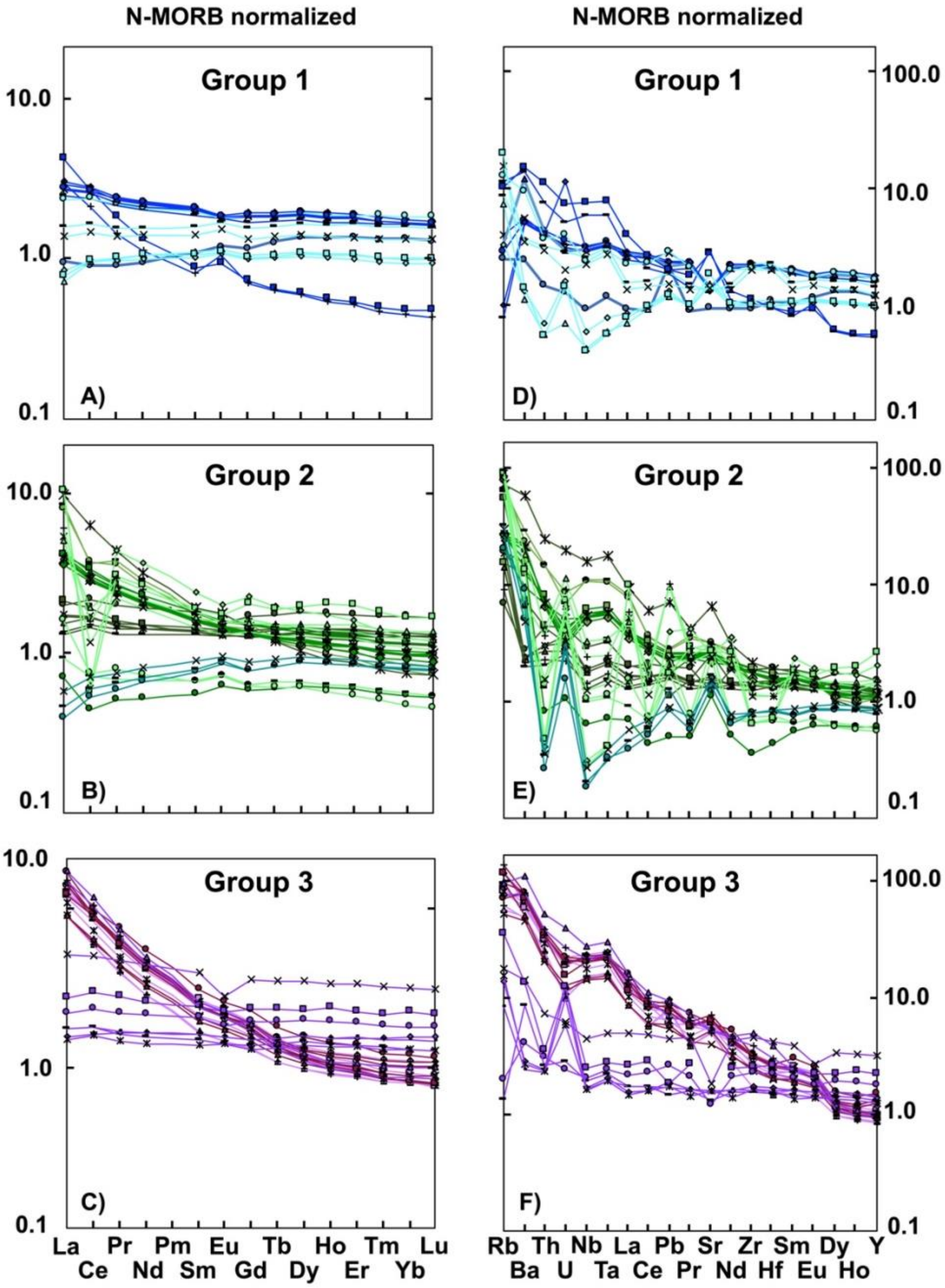

Figure 2.2: N-MORB normalized trace element diagrams for all AOC samples (normalizing values from Sun and McDonough, 1989; data in Supplementary Table 2.S1). Left column consists of REE diagrams (2a-2c) and right column consists of extended trace element diagrams (2d-2f). Figures 2.2a and 2.2d are samples from Group 1; 2.2b and 2.2e - samples from Group 2; 2.2c and 2.2f - samples from Group 3. ODP 1149 AOC data from Hauff et al. (2003).

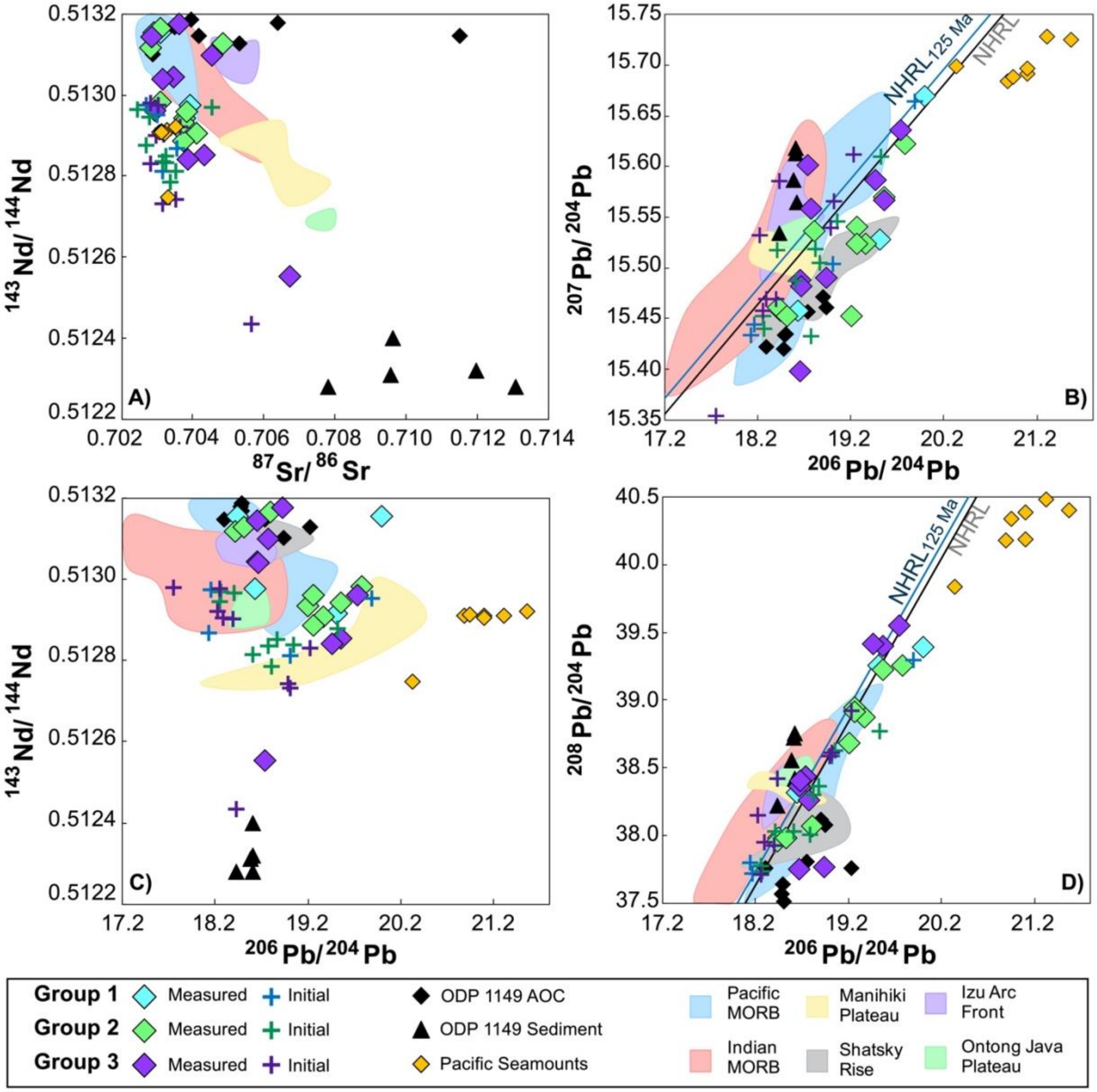

Figure 2.3: Plots of measured and initial A) ^{87}Sr/^{86}Sr versus ^{143}Nd/^{144}Nd, B) ^{206}Pb/^{204}Pb versus ^{207}Pb/^{204}Pb, C) ^{206}Pb/^{204}Pb versus ^{143}Nd/^{144}Nd, and D) ^{206}Pb/^{204}Pb versus ^{208}Pb/^{204}Pb for Izu-Bonin AOC samples. All symbols are larger than analytical errors. Hotta and Bosei seamount data are from Shimoda et al. (2011), ODP 1149 sediment data are from Plank et al. (2007) and AOC ODP 1149 data are from Hauff et al. (2003) and Miyazaki et al. (2015). Reference fields are for Ontong Java (Mahoney et al., 1993; Tejada et al., 2004), Shatsky Rise (Geldmacher et al., 2014), Pacific MORB, Indian MORB and Izu-Bonin arc volcanoes (Straub, 2017 and references therein). NHRL in 2B and 2D are from Hart (1984); NHRL$_{125Ma}$ were calculated using U, Th and Pb concentrations of N-MORB (Sun and McDonough, 1989).

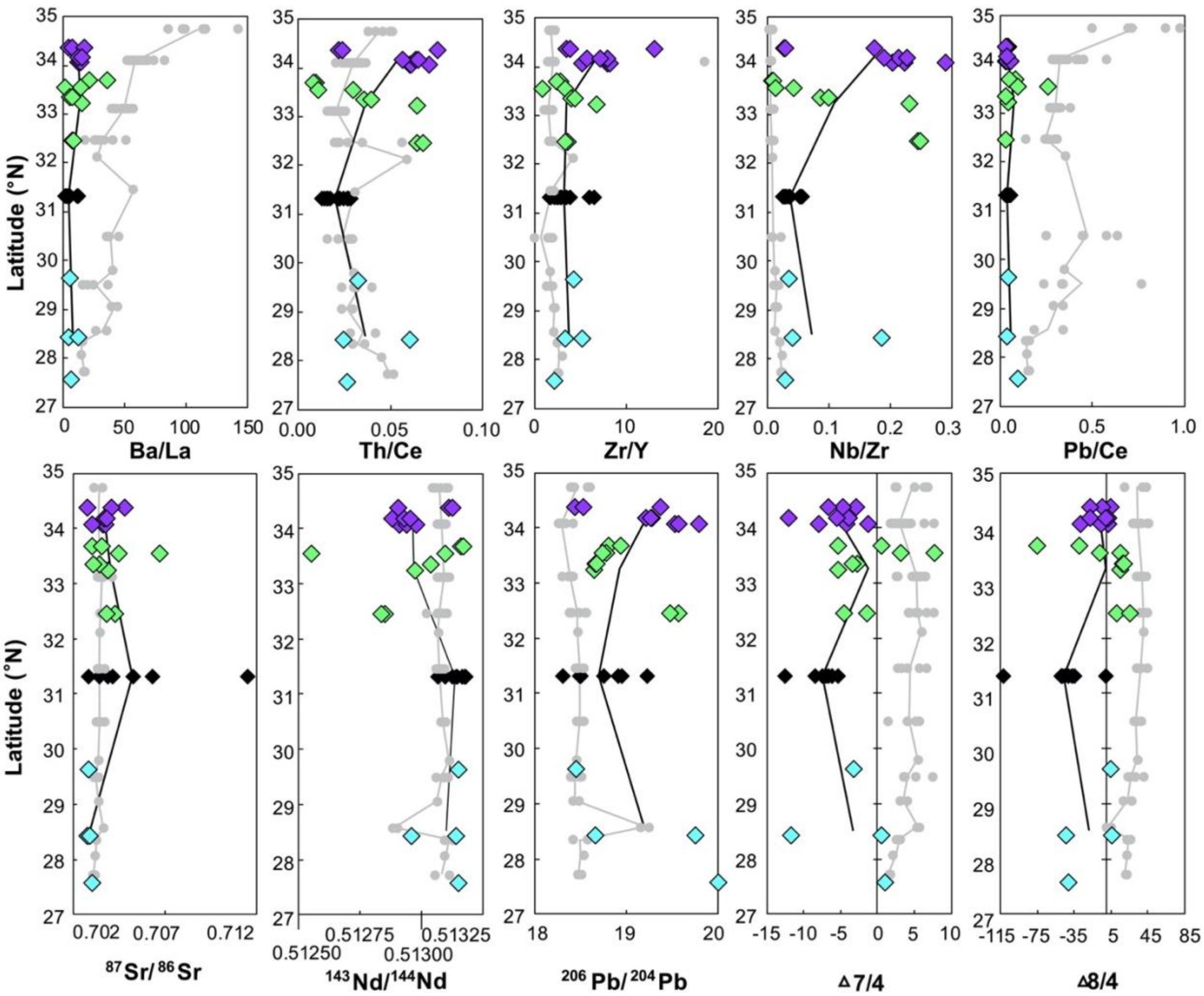

Figure 2.4: Plots from left to right of (top panel) Ba/La, Th/Ce, Zr/Y, Nb/Zr, and Pb/Ce against latitude and (bottom panel) $_{86}$Sr/$_{87}$Sr, $_{143}$Nd/$_{144}$Nd, $_{206}$Pb/$_{204}$Pb, Δ7/4, and Δ8/4 against latitude for Izu-Bonin arc lava (gray circles; Straub et al. 2017 and references therein), AOC and ODP 1149 samples. Running mean of arc lava data as a gray line; running mean of Groups 1-3 and ODP 1149 as a black line in all panels. Symbols and sources of data as in Figure 2.3. See text for discussion.

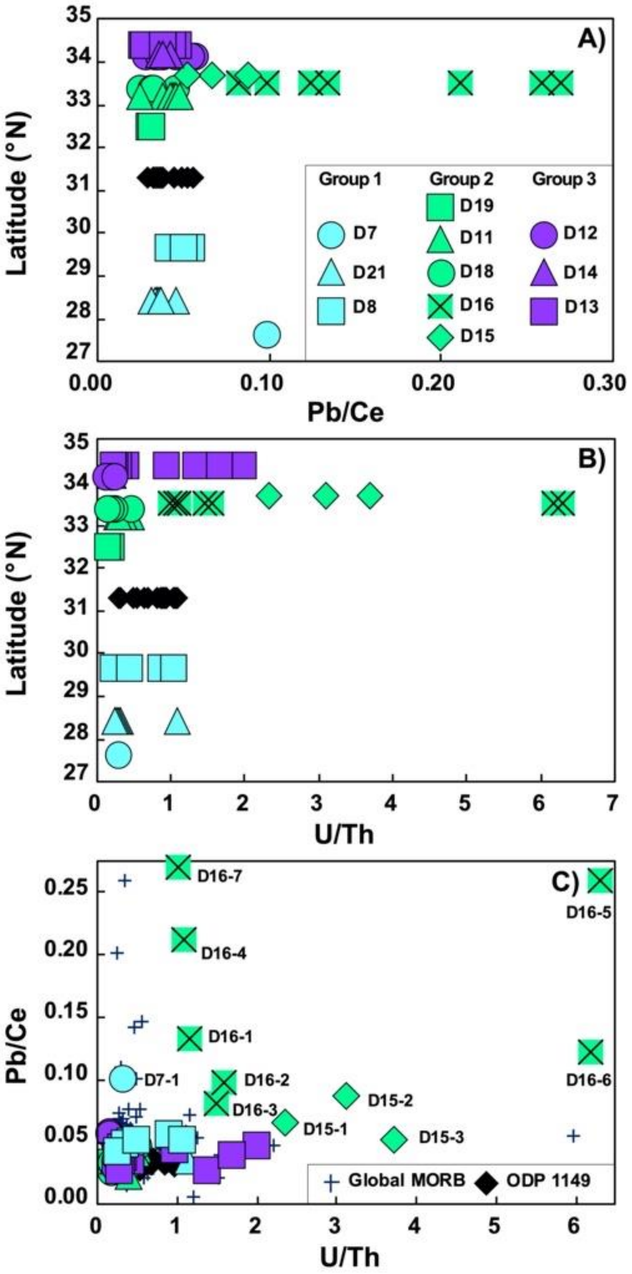

Figure 2.5: Latitude against A) U/Th and B) Pb/Ce, and C) U/Th versus Pb/Ce for Izu-Bonin AOC samples (Supplementary Table 2.S1). Global MORB data are shown for reference in C). Symbols and sources of data as in Figure 2.3.

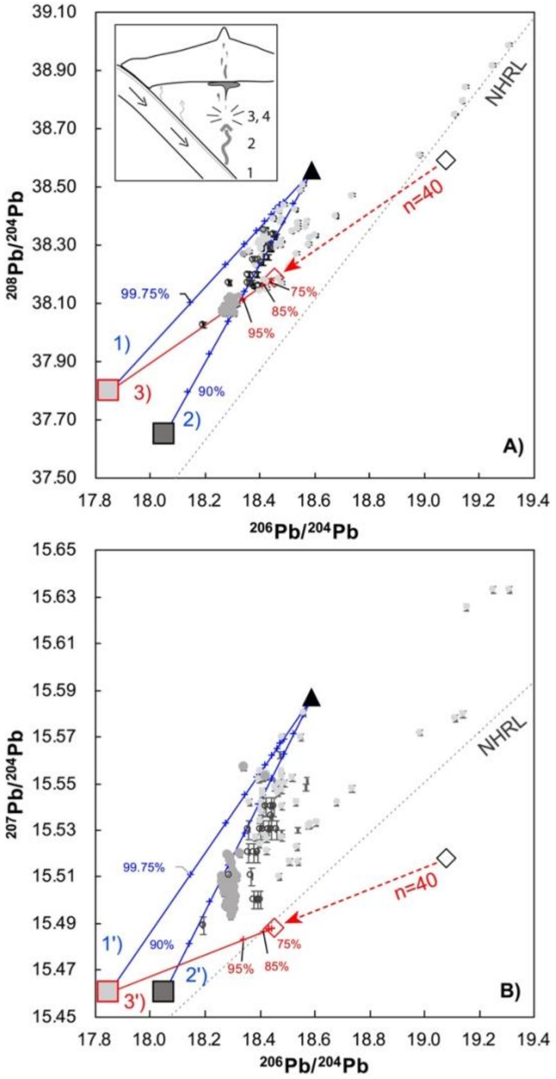

Figure 2.6: A) ^{206}Pb/^{204}Pb versus ^{208}Pb/^{204}Pb and B) ^{206}Pb/^{204}Pb versus ^{207}Pb/^{204}Pb for Izu-Bonin AOC samples. Arc data 2σ error as in Figure 2.4; dark gray-filled circles represent lavas with 2σ error from Miyakejima volcano Straub et al. (2017) and references therein. Tephras as open gray circles with 2σ error (data from: Straub et al., 2004; 2009; 2010; analytical error from Straub et al., 2009). Blue lines illustrate mixing between MBF (dark gray square) and average sediment-derived fluid (black triangle) [lines 1 and 1' with tick marks representing 0.25% increments] and between IOM (gray square with red outline) and sediment-derived fluid [lines 2 and 2'with tick marks representing 10% increments]. Red lines illustrate mixing between IOM and zone-refined AOC fluid at n = 40 (red diamond) [lines 3 and 3' with tick marks representing 10% increments beginning at 95%). Black diamond is average AOC-derived fluid. See text for discussion. Inset schematically illustrates the major steps in the magma generation process at the Izu-Bonin arc system (see Table 2.2 for details of the steps): 1. AOC- and sediment-derived fluids moving upward from the slab; 2. fluids equilibrate with the solid mantle through zone-refining; 3. mixing of fluid and mantle; and 4. flux melting of the mantle wedge.

Table 2.1: Major and trace element data for the AOC samples subducting into the Izu-Bonin Trench with Sr-Nd-Pb isotope data. All major and trace element results are provided in the attached Supporting Information as Supplementary Table S2.1.

Site	**D7-1**	**D8-2**	**D11-8**	**D12-1**	**D12-2**	**D12-7**	**D13-1**	**D13-3**	**D13-4**	**D14-1**	**D14-2**
ISGN	IEKED00-01	IEKED00-0A	IEKED00-0O	IEKED00-17	IEKED00-18	IEKED00-1D	IEKED00-1M	IEKED00-1O	IEKED00-1P	IEKED00-1F	IEKED00-1G
Dredge Depth	7957	7156	7754	7990	7990	7990	8450	8450	8450	8532	8532
Lat (°N)	27.57	29.63	33.23	34.07	34.07	34.07	34.37	34.37	34.37	34.17	34.17
Lon (°E)	143.56	143.20	142.45	142.18	142.18	142.18	142.19	142.19	142.19	142.20	142.20
SiO_2	46.92	48.58	-	46.49	48.79	47.16	48.29	47.70	50.53	49.05	51.90
TiO_2	1.31	2.60	-	2.71	2.64	1.61	2.49	2.56	2.17	2.65	2.50
Al_2O_3	13.68	13.09	-	17.32	16.89	16.17	14.22	12.20	16.54	19.38	19.55
Fe_2O_3	11.27	14.93	-	11.22	11.24	7.88	13.82	15.74	8.92	11.35	10.48
MnO	0.17	0.27	-	0.05	0.13	0.14	0.23	0.24	0.11	0.17	0.08
MgO	7.18	5.51	-	1.78	3.10	5.37	5.57	4.76	3.98	1.43	1.17
CaO	10.74	9.96	-	5.95	4.37	12.29	10.20	8.65	4.90	6.00	5.02
Na_2O	2.66	2.69	-	2.69	2.83	3.07	3.23	2.56	3.87	2.51	3.12
K_2O	0.08	0.26	-	2.55	3.70	2.38	0.21	1.08	4.24	3.29	4.19
P_2O_5	0.07	0.23	-	0.93	0.48	0.36	0.23	0.50	0.50	0.90	0.73
Total	94.09	98.12	-	91.68	94.18	96.45	98.49	95.99	95.76	96.71	98.75
LOI	4.19	0.78	-	5.81	4.34	3.58	1.53	2.98	3.01	3.59	2.38
(ppm)											
Sc	57.4	42.8	23.6	24.9	26.7	33.7	44.8	36.5	21.7	28.1	25.6
Cr	157	60.5	593	134	195	229	13.7	37.0	40.3	105	142
Co	46.3	35.0	39.4	48.2	46.0	37.5	46.2	36.2	23.9	35.9	27.0
Ni	70.0	35.6	221	66.9	186	108	29.4	24.2	18.1	54.5	109
Cu	128	37.3	69.3	123	54.9	61.9	59.7	51.6	36.7	62.3	116
Rb	1.41	5.01	42.7	51.9	72.8	35.6	1.12	10.3	56.5	40.7	56.3
Sr	84.9	117	607	546	619	456	109	167	489	552	580
Y	33.55	41.11	24.42	31.09	26.10	24.21	50.59	90.42	28.99	42.50	30.17
Zr	69.3	171	164	246	212	125	170	346	377	242	238
Nb	2.16	6.16	38.1	50.2	47.6	36.5	4.84	10.5	66.2	52.1	54.4
Cs	0.05	0.22	1.30	2.79	5.45	0.71	0.03	0.34	0.93	1.44	1.08
Ba	15.7	23.6	379	415	416	314	26.6	91.1	721	515	528
La	2.34	3.94	24.02	33.40	28.45	22.16	5.44	12.69	41.34	40.87	33.90
Ce	6.69	12.2	46.7	67.5	60.8	43.5	17.4	37.2	85.8	72.5	67.8
Pr	1.18	2.02	5.65	8.21	7.19	5.14	2.86	6.17	9.51	9.77	8.00
Nd	6.78	11.3	23.0	33.0	29.2	20.6	15.7	32.0	35.4	39.2	31.6
Sm	2.78	4.11	5.01	6.91	6.19	4.36	5.44	10.30	6.72	8.04	6.25
Eu	1.19	1.71	1.79	2.36	2.14	1.48	1.86	2.82	2.25	2.63	2.12
Gd	4.17	5.62	5.28	7.16	6.43	4.75	7.10	12.87	6.78	8.40	6.54
Tb	0.83	1.06	0.78	1.02	0.92	0.72	1.31	2.29	0.94	1.19	0.90
Dy	6.07	7.47	4.67	5.95	5.32	4.48	9.03	15.66	5.51	7.10	5.31
Ho	1.33	1.62	0.92	1.16	1.03	0.92	1.95	3.35	1.10	1.44	1.07
Er	3.95	4.81	2.57	3.20	2.81	2.60	5.65	9.77	3.16	4.05	3.02
Tm	0.59	0.71	0.36	0.44	0.39	0.37	0.83	1.45	0.46	0.56	0.42
Yb	3.96	4.76	2.26	2.80	2.48	2.43	5.44	9.52	3.07	3.62	2.72
Lu	0.57	0.70	0.33	0.40	0.35	0.36	0.81	1.39	0.46	0.53	0.40
Hf	2.23	4.85	3.90	5.76	4.93	3.07	4.65	8.90	8.03	5.67	5.37
Ta	0.16	0.42	2.39	3.09	2.91	2.17	0.33	0.67	4.08	3.13	3.18
Pb	0.66	0.58	2.19	2.33	2.36	2.38	0.79	1.36	2.90	2.73	2.52
Th	0.18	0.40	3.01	4.08	3.73	3.09	0.38	0.90	6.48	4.62	4.44
U	0.06	0.14	0.95	1.01	1.04	0.52	0.12	0.30	1.90	1.06	0.93
U/Pb	0.09	0.24	0.43	0.43	0.44	0.22	0.15	0.22	0.66	0.39	0.37
Th/U	2.96	2.88	3.18	4.02	3.60	5.99	3.27	3.04	3.41	4.35	4.78
Pb/Th	3.73	1.46	0.73	0.57	0.63	0.77	2.08	1.51	0.45	0.59	0.57
$^{206}Pb/^{204}Pb$	19.9950	18.4430	18.6380	19.5180	19.5660	19.7800	18.4280	18.5220	19.3680	19.2670	19.2060
Error	0.0001	0.0010	0.0002	0.0013	0.0002	0.0015	0.0003	0.0009	0.0005	0.0010	0.0004
Initial	19.89	18.15	18.11	18.99	19.03	19.52	18.25	18.26	18.58	18.80	18.76
$^{207}Pb/^{204}Pb$	15.6700	15.4580	15.4580	15.5280	15.5700	15.6220	15.4610	15.4520	15.5240	15.5410	15.4530
Error	0.0001	0.0010	0.0002	0.0013	0.0002	0.0014	0.0003	0.0014	0.0005	0.0010	0.0004
Initial	15.66	15.44	15.43	15.50	15.54	15.61	15.45	15.44	15.49	15.52	15.43
$^{208}Pb/^{204}Pb$	39.3960	37.9830	38.3210	39.2550	39.2300	39.2620	37.9560	37.9840	38.8780	38.9450	38.6810
Error	0.0001	0.0010	0.0002	0.0013	0.0002	0.0015	0.0003	0.0010	0.0005	0.0010	0.0004
Initial	39.29	37.71	37.78	38.56	38.60	38.75	37.77	37.72	37.99	38.28	37.98
Δ7/4	1.14	-3.22	-5.31	-7.86	-4.17	-1.28	-2.79	-4.68	-6.65	-3.87	-11.95
Δ8/4	-40.45	5.87	16.07	3.11	-5.21	-27.85	4.91	-3.68	-16.40	2.36	-16.59
Initial Δ7/4	1.79	-1.49	-2.17	-4.71	-0.99	0.29	-1.72	-3.10	-1.91	-1.06	-9.28
Initial Δ8/4	-37.80	13.59	24.94	-2.56	-3.63	-47.57	7.39	1.91	-9.05	-7.71	-32.48
$^{87}Sr/^{86}Sr$	0.703088	0.702900	0.703930	0.703651	0.703769	0.703092	0.702823	0.704848	0.704124	0.703737	0.703735
Error	0.000012	0.000013	0.000015	0.000014	0.000014	0.000014	0.000014	0.000013	0.000010	0.000013	0.000012
Initial	0.703002	0.702681	0.703568	0.703163	0.703165	0.702691	0.702771	0.704530	0.703530	0.703359	0.703237
$^{143}Nd/^{144}Nd$	0.513154	0.513154	0.512975	0.512915	0.512942	0.512982	0.513116	0.513128	0.512906	0.512886	0.512932
Error	0.000070	0.000070	0.000070	0.000070	0.000070	0.000070	0.000060	0.000014	0.000011	0.000070	0.000010
Initial	0.512951	0.512974	0.512867	0.512811	0.512837	0.512877	0.512945	0.512969	0.512812	0.512785	0.512834

Table 2.1: Continued

D14-4	**D15-2**	**D15-3**	**D16-2**	**D16-5**	**D18-4**	**D18-6**	**D19-1**	**D19-2**	**D21-5**	**D21-7**
IEKED00-1I	IEKED00-15	IEKED00-16	IEKED00-0Y	IEKED00-11	IEKED00-0S	IEKED00-0U	IEKED00-0F	IEKED00-0G	IEKED00-06	IEKED00-08
8532	7453	7453	8053	8053	8100	8100	7420	7420	8106	8106
34.17	33.68	33.68	33.54	33.54	33.35	33.35	32.45	32.45	28.43	28.43
142.20	142.37	142.37	142.30	142.30	142.38	142.38	142.41	142.41	143.47	143.47
49.93	47.39	47.46	49.98	50.73	45.92	44.46	50.11	49.71	48.08	50.39
2.32	1.08	1.12	1.19	1.01	1.94	1.84	1.63	1.68	2.47	1.40
17.77	14.61	15.47	18.24	19.00	15.03	14.80	18.48	18.32	13.90	19.06
10.36	9.29	10.46	11.68	11.23	10.13	11.60	10.35	9.87	13.44	7.61
0.14	0.12	0.13	0.11	0.02	0.20	0.17	0.11	0.07	0.22	0.11
3.12	6.89	4.79	2.36	1.45	6.39	5.78	3.45	4.32	6.44	5.47
6.53	10.23	10.79	6.78	5.12	10.79	9.71	3.70	5.79	11.06	10.11
3.20	2.31	2.27	2.67	2.32	2.55	2.27	2.38	2.42	2.95	3.53
3.06	1.27	1.81	1.67	3.59	0.36	1.36	3.16	2.47	0.14	0.38
0.49	0.07	0.08	0.11	0.11	0.21	0.27	0.29	0.30	0.25	0.19
96.92	93.26	94.38	94.77	94.58	93.52	92.27	93.67	94.96	98.94	98.26
2.45	5.98	4.85	4.17	4.10	7.27	6.14	5.13	4.05	1.19	1.93
33.9	50.6	49.9	44.0	47.7	44.6	47.3	44.5	45.9	54.1	32.3
218	271	298	381	447	394	476	356	539	99.7	302
43.8	44.1	31.5	40.0	37.4	40.4	54.4	39.2	34.4	45.3	43.7
85.4	71.9	61.8	61.3	63.8	108	141	107	104	53.4	66.0
60.2	50.8	67.9	137	213	63.6	76.9	110	103	60.8	56.7
57.0	19.0	15.4	36.4	49.1	12.8	8.80	46.1	39.1	0.57	6.62
487	152	139	210	235	236	243	293	291	121	274
26.41	21.93	25.06	16.57	58.55	36.50	33.76	29.44	32.39	51.51	14.87
186	59.8	60.0	54.4	48.4	143	146	104	106	168	76.0
35.4	0.48	0.63	2.37	0.73	12.5	14.7	25.5	26.5	7.11	14.2
3.62	0.70	0.29	1.48	1.93	0.56	0.41	1.83	1.83	0.02	0.14
335	40.7	30.7	32.4	47.4	61.9	79.4	149	188	33.4	90.8
21.94	1.14	1.42	2.29	25.93	10.56	10.18	19.66	20.95	7.41	7.29
46.7	4.45	5.25	5.33	4.65	24.0	25.0	27.7	27.0	20.6	15.6
5.65	0.84	0.98	0.90	5.70	3.47	3.55	4.68	4.94	3.15	1.86
23.0	5.13	5.81	4.89	26.2	16.5	16.7	19.6	20.8	16.4	8.06
5.06	2.08	2.32	1.77	6.26	4.69	4.67	4.42	4.65	5.47	2.13
1.75	0.90	0.95	0.74	2.01	1.62	1.63	1.51	1.60	1.90	1.07
5.35	2.87	3.20	2.31	8.24	5.62	5.53	5.15	5.53	7.02	2.57
0.81	0.55	0.61	0.44	1.29	0.96	0.94	0.79	0.84	1.29	0.42
4.88	3.95	4.30	3.02	8.24	6.43	6.13	4.89	5.30	8.89	2.73
0.98	0.85	0.93	0.64	1.74	1.34	1.29	0.99	1.08	1.92	0.55
2.76	2.48	2.68	1.83	4.73	3.90	3.69	2.73	3.02	5.59	1.52
0.39	0.37	0.40	0.27	0.63	0.57	0.53	0.37	0.42	0.82	0.21
2.55	2.41	2.58	1.72	3.81	3.71	3.48	2.35	2.57	5.32	1.37
0.37	0.35	0.37	0.24	0.54	0.54	0.51	0.33	0.37	0.78	0.19
4.28	1.73	1.75	1.57	1.48	3.59	3.61	2.65	2.73	4.31	1.94
2.07	0.04	0.05	0.15	0.06	0.76	0.88	1.43	1.51	0.44	0.81
1.82	0.39	0.27	0.52	1.20	0.77	0.80	0.84	0.86	0.72	0.57
2.64	0.04	0.04	0.16	0.05	0.86	1.00	1.79	1.83	0.51	0.94
0.62	0.13	0.16	0.25	0.32	0.25	0.19	0.41	0.33	0.56	0.25
0.34	0.34	0.58	0.47	0.26	0.32	0.24	0.49	0.38	0.78	0.44
4.28	0.32	0.27	0.64	0.16	3.49	5.25	4.33	5.51	0.90	3.76
0.69	9.10	6.37	3.33	24.02	0.90	0.80	0.47	0.47	1.42	0.60
19.2650	18.8070	18.9350	18.7750	18.7380	18.6610	18.6730	19.5600	19.4660	18.6630	19.7400
0.0002	0.0007	0.0004	0.0008	0.0001	0.0004	0.0006	0.0002	0.0005	0.0006	0.0014
18.85	18.39	18.23	18.20	18.42	18.28	18.39	18.97	19.00	17.72	19.21
15.5240	15.5360	15.4900	15.5580	15.6010	15.4880	15.4820	15.5670	15.5870	15.3980	15.6360
0.0002	0.0007	0.0004	0.0008	0.0001	0.0004	0.0006	0.0002	0.0005	0.0006	0.0014
15.50	15.52	15.46	15.53	15.59	15.47	15.47	15.54	15.56	15.35	15.61
38.9170	38.0730	37.7700	38.2650	38.4360	38.3690	38.4050	39.3980	39.4170	37.7540	39.5530
0.0002	0.0007	0.0004	0.0008	0.0001	0.0004	0.0006	0.0002	0.0005	0.0006	0.0014
38.34	38.03	37.71	38.15	38.42	37.93	37.91	38.56	38.58	37.48	38.90
-5.51	0.66	-5.36	3.23	7.84	-2.63	-3.30	-4.44	-1.37	-11.64	0.57
-0.10	-29.17	-74.88	-6.07	15.47	18.06	20.23	12.23	25.66	-43.61	6.01
-3.05	3.13	-1.15	6.64	9.74	-0.33	-1.58	-0.88	1.41	-6.00	3.76
-7.91	16.42	3.80	51.01	52.13	20.69	5.60	-0.12	-1.94	42.40	4.83
0.703842	0.703092	0.703612	0.704552	0.706730	0.703466	0.703163	0.704330	0.703849	0.702842	0.702938
0.000016	0.000006	0.000013	0.000014	0.000012	0.000013	0.000014	0.000013	0.000013	0.000012	0.000014
0.703241	0.702449	0.703044	0.703659	0.705657	0.703188	0.702977	0.703521	0.703159	0.702818	0.702813
0.512959	0.513165	0.513174	0.513099	0.512552	0.513043	0.513039	0.512853	0.512841	0.513144	0.512961
0.000013	0.000090	0.000013	0.000050	0.000070	0.000060	0.000080	0.000070	0.000090	0.000014	0.000060
0.512850	0.512964	0.512976	0.512920	0.512434	0.512903	0.512900	0.512742	0.512731	0.512979	0.512830

Table 2.2: All zone-refining model parameters used in Equations 1-4. Modeling results are illustrated in Figure 2.6.

Input parameters		**Source**
$[Pb]_{Sed}$	15.400	Plank et al. (2007)
$^{206}Pb/^{204}Pb_{Sed}$	18.589	Plank et al. (2007)
$^{207}Pb/^{204}Pb_{Sed}$	15.587	Plank et al. (2007)
$^{208}Pb/^{204}Pb_{Sed}$	38.558	Plank et al. (2007)
$[Pb]_{Avg\ AOC}$	1.015	This study
$^{206}Pb/^{204}Pb_{Avg\ AOC}$	19.079	This study
$^{207}Pb/^{204}Pb_{Avg\ AOC}$	15.518	This study
$^{208}Pb/^{204}Pb_{Avg\ AOC}$	38.595	This study
$[Pb]_{MW}$	0.036	Straub et al. (2004)
$^{206}Pb/^{204}Pb_{MW}$	17.850	Straub et al. (2004)
$^{207}Pb/^{204}Pb_{MW}$	15.460	Straub et al. (2004)
$^{208}Pb/^{204}Pb_{MW}$	37.800	Straub et al. (2004)
$[Pb]_{MBF}$	8.700	Straub et al. (2009)
$^{206}Pb/^{204}Pb_{MBF}$	18.050	Straub et al. (2009)
$^{207}Pb/^{204}Pb_{MBF}$	15.460	Straub et al. (2009)
$^{208}Pb/^{204}Pb_{MBF}$	37.650	Straub et al. (2009)
$D_{Pb,AOC/fluid}$	0.017	Ayers (1998)
$D_{Pb,Sed/fluid}$	0.640	Johnson and Plank (1999)
$D_{Pb,wedge/fluid}$	0.002	Ayers (1998)
D_{melt}	0.012	Brenan et al. (1995)

Step 1- Fluid distillation from slab	**Sediment - Fully dehydrated**		$C_{fluid,i}$	**24.063**
			$^{206}Pb/^{204}Pb_{Sed}$	**18.589**
			$^{207}Pb/^{204}Pb_{Sed}$	**15.587**
			$^{208}Pb/^{204}Pb_{Sed}$	**38.558**
	AOC - Eqn 1		F_{fluid}	**0.06**
			$C_{fluid,i}$	**1.667**
			$^{206}Pb/^{204}Pb_{fluid,i}$	**19.079**
			$^{207}Pb/^{204}Pb_{fluid,i}$	**15.518**
			$^{208}Pb/^{204}Pb_{fluid,i}$	**38.595**
Step 2- Zone refining	**Eqn 2**		n	**40**
			C_{fluid}	**2.923**
	Eqn 3		∂n	**0.1**
			$X_{fluid,MW}$	**0.509**
	Eqn 4		$^{206}Pb/^{204}Pb_{fluid}$	**18.484**
			$^{207}Pb/^{204}Pb_{fluid}$	**15.488**
			$^{208}Pb/^{204}Pb_{fluid}$	**38.190**
Step 3 - Mixing	F_{AOC}	0.14	$C_{IAB\ Source,Pb}$	**0.440**
	F_{MW}	0.86	$^{206}Pb/^{204}Pb_{IAB\ Source}$	**18.411**
			$^{207}Pb/^{204}Pb_{IAB\ Source}$	**15.486**
			$^{208}Pb/^{204}Pb_{IAB\ Source}$	**38.163**
Step 4- Melting	IAB_{avg} [Pb]	2.170	F_{melt}	**0.200**
	Std	1.284	IAB_{melt}	**2.100**

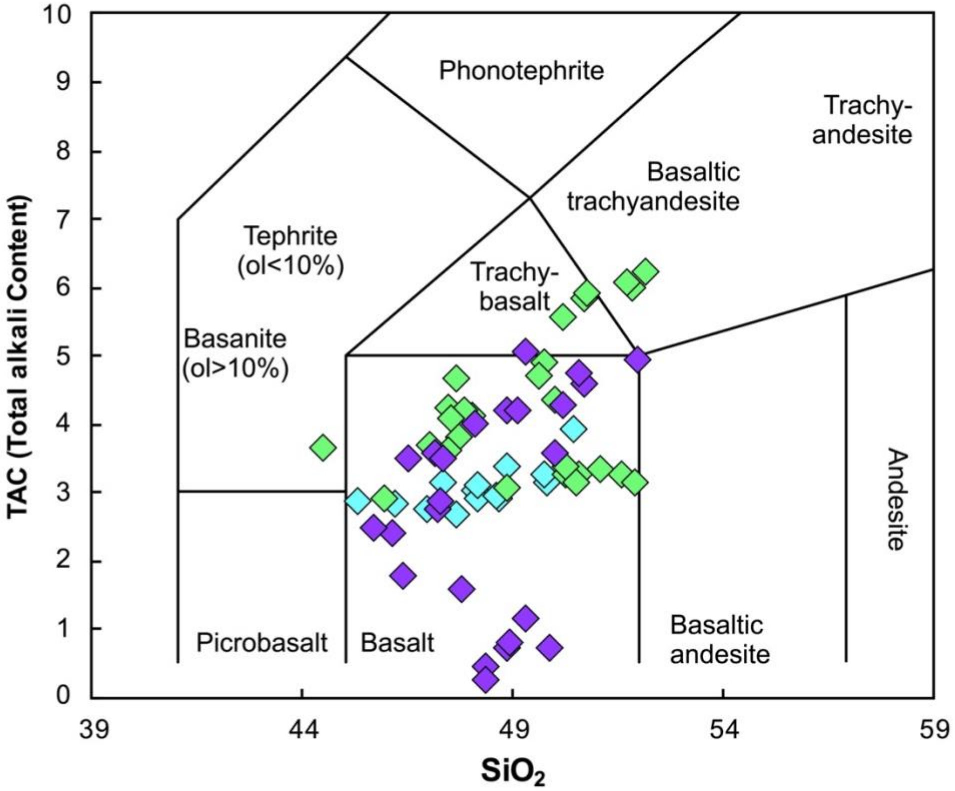

Figure 2.S1: Total alkali versus silica (TAS) diagram for samples. Data from Supplementary Table 2.1. Symbols as is in Figure 2.3.

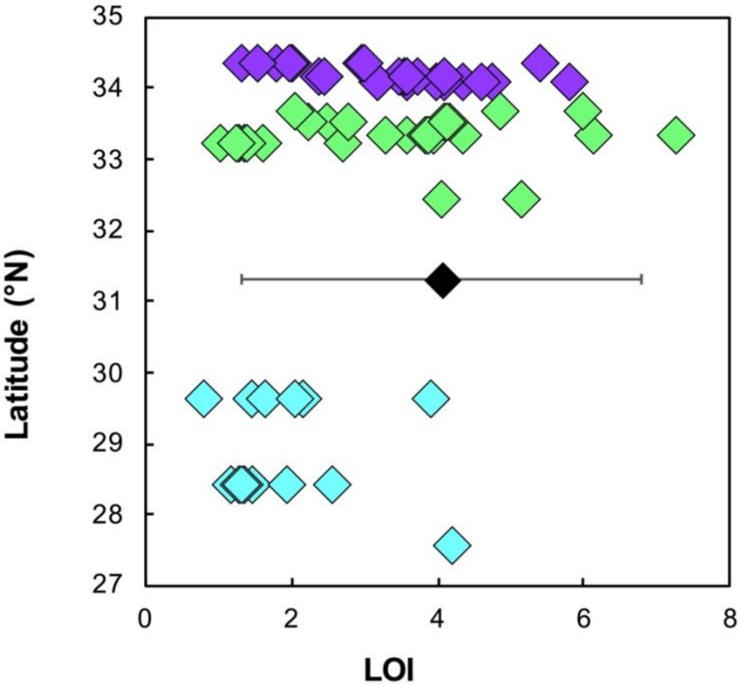

Figure 2.S2: Loss on ignition (LOI) values vs latitude. Data from Supplementary Table 2.1. ODP 1149 data from Kelley et al. (2001), error bars show standard deviation of recovered core basalts and altered basalts. Symbols as is in Figure 2.3.

Table 2.S1: Major and trace element values for all measured samples.

Sample	**D7-1**	**D21-1**	**D21-2**	**D21-3**	**D21-4**	**D21-5**	**D21-6**	**D21-7**	**D8-1**	**D8-2**	**D8-3**	**D8-4**	**D8-5**	**D8-6**
ISGN	IEKED0001	IEKED0002	IEKED0003	IEKED0004	IEKED0005	IEKED0006	IEKED0007	IEKED0008	IEKED0009	IEKED000A	IEKED000B	IEKED000C	IEKED000D	IEKED000E
Lon (°E)	143.56	143.47	143.47	143.47	143.47	143.47	143.47	143.47	143.20	143.20	143.20	143.20	143.20	143.20
Lat (°N)	27.57	28.43	28.43	28.43	28.43	28.43	28.43	28.43	29.63	29.63	29.63	29.63	29.63	29.63
SiO_2	46.92	48.03	47.31	48.10	48.63	48.08	48.79	50.39	49.76	48.58	49.69	47.62	46.12	45.24
TiO_2	1.31	2.45	2.57	2.35	2.38	2.47	1.13	1.40	2.65	2.60	2.54	1.29	1.30	1.21
Al_2O_3	13.68	13.53	14.00	13.24	13.20	13.90	17.29	19.06	14.00	13.09	13.95	15.89	16.22	16.01
Fe_2O_3	11.27	14.74	14.27	14.05	13.91	13.44	9.53	7.61	11.67	14.93	12.38	9.75	11.07	9.04
MnO	0.17	0.21	0.20	0.25	0.26	0.22	0.17	0.11	0.19	0.27	0.18	0.16	0.17	0.15
MgO	7.18	6.00	6.38	6.23	6.41	6.44	6.93	5.47	5.57	5.51	5.35	9.86	6.48	6.65
CaO	10.74	10.84	10.35	11.32	11.17	11.06	10.04	10.11	10.49	9.96	9.90	11.13	11.42	12.81
Na_2O	2.66	2.88	3.02	2.73	2.74	2.95	2.96	3.53	2.80	2.69	2.80	2.62	2.74	2.48
K_2O	0.08	0.14	0.13	0.18	0.17	0.14	0.39	0.38	0.32	0.26	0.44	0.06	0.06	0.37
P_2O_5	0.07	0.25	0.25	0.23	0.24	0.25	0.19	0.19	0.25	0.23	0.22	0.07	0.08	0.07
LOI	4.19	1.32	1.47	1.29	1.37	1.19	2.55	1.93	1.42	0.78	1.63	2.18	2.05	3.89
Total	94.09	99.08	98.48	98.67	99.10	98.94	97.41	98.26	97.71	98.12	97.46	98.44	95.66	94.04
(ppm)														
Sc	57.4	51.1	53.6	52.2	51.5	54.1	27.4	32.3	41.0	42.8	45.1	37.0	36.3	37.5
Cr	157	84	85	94	82	100	280	302	65	61	79	558	460	611
Co	46.3	44.6	42.8	44.3	42.2	45.3	43.7	43.7	46.4	35.0	39.3	47.3	50.1	52.0
Ni	70.0	51.2	48.1	48.9	47.5	53.4	167	66.0	47.5	35.6	41.0	259	191	261
Cu	128	64	58	60	59	61	72	57	52	37	31	61	77	64
Rb	1.41	1.63	0.44	2.30	1.87	0.57	5.95	6.62	7.40	5.01	8.99	4.29	1.90	11.54
Sr	85	128	126	133	131	121	259	274	121	117	126	140	136	169
Y	33.6	48.8	44.2	47.7	48.9	51.5	15.8	14.9	46.3	41.1	34.5	27.9	26.5	27.6
Zr	69.3	170	173	163	166	168	84.6	76.0	157	171	150	81.7	74.3	74.8
Nb	2.16	7.52	7.59	6.91	7.20	7.11	18.14	14.19	5.63	6.16	5.32	0.98	1.39	0.94
Cs	0.05	0.04	0.01	0.08	0.05	0.02	0.11	0.14	0.33	0.22	0.27	0.29	0.09	0.41
Ba	15.67	34.39	32.68	35.73	78.45	33.38	101	90.83	61.08	23.56	22.48	7.08	8.31	8.87
La	2.34	6.80	6.15	6.65	7.23	7.41	10.27	7.29	5.72	3.94	3.39	1.78	2.12	1.95
Ce	6.69	19.47	17.79	18.98	20.08	20.55	20.03	15.56	17.68	12.17	10.92	7.05	7.32	7.30
Pr	1.18	3.09	2.80	2.93	3.06	3.15	2.39	1.86	2.83	2.02	1.82	1.31	1.28	1.32
Nd	6.78	16.04	14.57	15.27	15.84	16.41	9.65	8.06	15.03	11.26	10.05	7.69	7.21	7.63
Sm	2.78	5.38	4.86	5.12	5.25	5.47	2.32	2.13	5.13	4.11	3.64	2.90	2.66	2.78
Eu	1.19	1.85	1.79	1.80	1.84	1.90	0.95	1.07	1.81	1.71	1.53	1.15	1.09	1.12
Gd	4.17	6.84	6.13	6.59	6.72	7.02	2.70	2.57	6.72	5.62	4.86	3.84	3.62	3.68
Tb	0.83	1.24	1.13	1.21	1.23	1.29	0.44	0.42	1.24	1.06	0.91	0.72	0.67	0.69
Dy	6.07	8.59	7.89	8.37	8.47	8.89	2.76	2.73	8.66	7.47	6.34	4.98	4.70	4.88
Ho	1.33	1.84	1.69	1.80	1.82	1.92	0.57	0.55	1.87	1.62	1.37	1.08	1.01	1.06
Er	3.95	5.33	4.93	5.22	5.30	5.59	1.59	1.52	5.52	4.81	4.00	3.18	2.93	3.11
Tm	0.59	0.78	0.74	0.77	0.78	0.82	0.23	0.21	0.83	0.71	0.60	0.46	0.43	0.46
Yb	3.96	5.06	4.95	5.04	5.12	5.32	1.46	1.37	5.47	4.76	3.99	3.07	2.84	3.03
Lu	0.57	0.74	0.72	0.74	0.75	0.78	0.22	0.19	0.81	0.70	0.59	0.45	0.42	0.45
Hf	2.23	4.38	4.43	4.24	4.25	4.31	1.98	1.94	4.49	4.85	4.22	2.27	1.99	2.01
Ta	0.16	0.46	0.47	0.43	0.45	0.44	1.05	0.81	0.39	0.42	0.36	0.08	0.10	0.07
Pb	0.66	0.70	0.61	0.86	0.66	0.72	0.61	0.57	0.88	0.58	0.46	0.36	0.40	0.37
Th	0.18	0.53	0.49	0.50	0.51	0.51	1.40	0.94	0.45	0.40	0.36	0.07	0.08	0.06
U	0.06	0.17	0.16	0.15	0.14	0.56	0.36	0.25	0.19	0.14	0.10	0.03	0.08	0.07

	Sc	Cr	Co	Ni	Cu	Rb	Sr	Y	Zr	Nb	Cs	Ba
BHVO-2 Average	32.15	280.54	45.06	119.09	126.62	9.14	395.43	26.01	172.33	18.10	0.10	130.69
BHVO-2 Standard Deviation	0.77	4.83	0.61	1.57	6.30	0.18	7.51	0.36	2.24	0.22	0.00	1.67
BIR-1 Average	43.44	382.00	53.03	172.43	118.04	0.23	102.05	15.64	15.17	0.54	0.01	14.54
BIR-1 Standard Deviation	0.95	3.81	0.35	1.33	0.95	0.03	1.31	0.20	0.06	0.01	0.00	4.54
BCR-2 Average	33.04	14.79	37.55	12.24	19.73	45.74	451.17	34.70	186.96	12.23	1.13	650.53
BCR-2 Standard Deviation	0.90	0.42	0.64	0.14	0.25	0.81	9.46	0.61	3.20	0.17	0.01	8.45

Table 2.S1: Continued

D19-1	**D19-2**	**D11-1**	**D11-2**	**D11-3**	**D11-4**	**D11-5**	**D11-6**	**D11-7**	**D11-8**	**D18-1**	**D18-2**	**D18-3**	**D18-4**	**D18-5**
IEKED000F	IEKED000G	IEKED000H	IEKED000I	IEKED000J	IEKED000K	IEKED000L	IEKED000M	IEKED000N	IEKED000O	IEKED000P	IEKED000Q	IEKED000R	IEKED000S	IEKED000T
142.41	142.41	142.45	142.45	142.45	142.45	142.45	142.45	142.45	142.45	142.38	142.38	142.38	142.38	142.38
32.45	32.45	33.23	33.23	33.23	33.23	33.23	33.23	33.23	33.23	33.35	33.35	33.35	33.35	33.35
50.11	49.71	51.50	50.54	51.86	50.21	50.19	48.80	51.00	-	46.95	47.60	47.44	45.92	47.95
1.63	1.68	1.78	1.68	1.73	1.89	1.70	1.66	1.78	-	0.72	1.90	1.80	1.94	1.77
18.48	18.32	14.61	14.34	15.24	14.88	14.64	14.31	14.74	-	17.17	16.45	15.97	15.03	15.25
10.35	9.87	9.99	10.17	8.47	9.44	10.42	9.93	10.04	-	9.29	10.98	10.37	10.13	11.48
0.11	0.07	0.17	0.16	0.15	0.17	0.15	0.19	0.17	-	0.14	0.18	0.18	0.20	0.19
3.45	4.32	7.16	6.99	7.86	7.15	6.70	5.85	6.87	-	7.52	6.20	6.23	6.39	7.66
3.70	5.79	10.27	10.70	11.00	10.39	10.55	13.00	10.41	-	9.87	8.94	9.68	10.79	9.26
2.38	2.42	2.93	2.75	2.85	2.90	2.74	2.50	2.94	-	1.81	2.17	2.13	2.55	2.08
3.16	2.47	0.33	0.50	0.28	0.35	0.63	0.56	0.39	-	1.87	2.47	2.12	0.36	2.02
0.29	0.30	0.14	0.12	0.14	0.15	0.14	0.15	0.13	-	0.07	0.30	0.26	0.21	0.20
5.13	4.05	1.05	1.61	1.37	1.40	1.24	2.70	1.29	-	3.86	3.56	3.85	7.27	3.29
93.67	94.96	98.89	97.97	99.57	97.53	97.86	96.96	98.47	-	95.42	97.18	96.18	93.52	97.86
44.5	45.9	44.4	44.7	44.8	45.9	44.4	42.5	47.1	23.6	36.8	43.0	40.7	44.6	36.8
356	539	52	79	88	65	80	161	66	593	416	429	411	394	354
39.2	34.4	49.5	48.2	46.6	46.7	40.7	50.2	54.8	39.4	39.9	42.1	44.0	40.4	47.1
107	104	47.3	45.7	51.1	42.6	54.9	94.0	52.9	221	111	87.5	93.4	108	89.9
110	103	69	94	92	74	54	37	105	69	38	42	53	64	21
46.10	39.07	3.92	8.61	10.67	8.25	13.68	32.32	5.27	42.67	11.02	15.51	16.13	12.77	15.51
293	291	111	122	140	132	151	233	119	607	101	229	225	236	198
29.4	32.4	42.9	35.0	33.8	36.3	34.0	32.3	35.8	24.4	17.0	31.7	31.2	36.5	29.4
104	106	141	93.7	100	109	102	101	103	164	26.4	135	131	143	112
25.45	26.50	4.43	3.05	4.43	4.18	4.49	7.01	3.39	38.14	1.52	13.44	12.98	12.46	11.61
1.83	1.83	0.11	0.26	0.33	0.26	0.44	3.43	0.18	1.30	0.34	0.39	0.51	0.56	0.51
149	188	17.94	12.72	14.93	15.65	15.28	47.27	13.75	379	101	123	136	61.85	105
19.66	20.95	4.99	3.27	4.27	3.85	4.19	5.25	3.39	24.02	1.76	10.11	9.99	10.56	8.88
27.75	26.99	16.14	10.67	12.62	12.38	12.40	14.19	11.18	46.68	3.28	22.38	21.73	23.98	20.85
4.68	4.94	2.59	1.73	1.95	2.01	1.95	2.10	1.85	5.65	0.67	3.31	3.21	3.47	3.15
19.61	20.83	13.84	9.56	10.25	10.90	10.30	10.81	10.22	23.00	3.78	15.59	15.04	16.53	14.97
4.42	4.65	4.74	3.43	3.52	3.78	3.56	3.55	3.66	5.01	1.46	4.21	4.10	4.69	4.11
1.51	1.60	1.55	1.29	1.30	1.40	1.31	1.32	1.39	1.79	0.63	1.51	1.47	1.62	1.42
5.15	5.53	6.17	4.66	4.64	5.05	4.70	4.62	4.89	5.28	2.12	5.02	4.88	5.62	4.79
0.79	0.84	1.15	0.88	0.86	0.94	0.87	0.85	0.92	0.78	0.40	0.84	0.82	0.96	0.80
4.89	5.30	8.10	6.21	6.00	6.57	6.05	5.78	6.51	4.67	2.84	5.53	5.33	6.43	5.16
0.99	1.08	1.76	1.35	1.29	1.42	1.30	1.24	1.40	0.92	0.61	1.16	1.12	1.34	1.06
2.73	3.02	5.14	3.99	3.79	4.16	3.85	3.58	4.08	2.57	1.76	3.32	3.19	3.90	2.99
0.37	0.42	0.77	0.59	0.56	0.61	0.57	0.53	0.61	0.36	0.26	0.48	0.46	0.57	0.42
2.35	2.57	5.18	3.89	3.73	4.05	3.85	3.45	4.00	2.26	1.65	3.13	2.93	3.71	2.74
0.33	0.37	0.75	0.57	0.55	0.59	0.56	0.50	0.59	0.33	0.24	0.45	0.43	0.54	0.40
2.65	2.73	4.06	2.78	2.91	3.14	2.93	2.91	3.02	3.90	0.90	3.29	3.22	3.59	2.91
1.43	1.51	0.30	0.21	0.29	0.28	0.30	0.44	0.23	2.39	0.09	0.80	0.78	0.76	0.71
0.84	0.86	0.60	0.47	0.53	0.54	0.52	0.34	0.51	2.19	0.15	0.74	0.69	0.77	0.52
1.79	1.83	0.53	0.25	0.37	0.33	0.37	0.54	0.28	3.01	0.10	0.91	0.85	0.86	0.81
0.41	0.33	0.15	0.12	0.15	0.13	0.18	0.21	0.11	0.95	0.05	0.17	0.17	0.25	0.14
La	Ce	Pr	Nd	Sm	Eu	Gd	Tb	Dy	Ho	Er	Tm	Yb	Lu	Hf
15.16	37.44	5.33	24.43	6.06	2.06	6.22	0.92	5.29	0.97	2.53	0.33	1.99	0.27	4.34
0.21	0.48	0.08	0.34	0.09	0.03	0.10	0.02	0.10	0.02	0.05	0.01	0.03	0.01	0.09
0.61	2.01	0.37	2.39	1.10	0.52	1.71	0.34	2.56	0.57	1.68	0.25	1.64	0.24	0.58
0.00	0.01	0.00	0.01	0.01	0.00	0.02	0.00	0.01	0.00	0.01	0.00	0.02	0.00	0.00
24.86	52.79	6.84	28.66	6.57	2.06	6.92	1.04	6.42	1.30	3.68	0.52	3.39	0.50	4.87
0.35	0.85	0.10	0.41	0.10	0.03	0.10	0.01	0.09	0.01	0.04	0.01	0.04	0.01	0.06

Table 2.S1: Continued

D18-6 IEKED000U	**D18-7** IEKED000V	**D18-8** IEKED000W	**D16-1** IEKED000X	**D16-2** IEKED000Y	**D16-3** IEKED000Z	**D16-4** IEKED0010	**D16-5** IEKED0011	**D16-6** IEKED0012	**D16-7** IEKED0013	**D15-1** IEKED0014	**D15-2** IEKED0015	**D15-3** IEKED0016	**D12-1** IEKED0017	**D12-2** IEKED0018
142.38	142.38	142.38	142.30	142.30	142.30	142.30	142.30	142.30	142.30	142.37	142.37	142.37	142.18	142.18
33.35	33.35	33.35	33.54	33.54	33.54	33.54	33.54	33.54	33.54	33.68	33.68	33.68	34.07	34.07
44.46	47.67	47.81	49.56	49.98	51.81	50.65	50.73	51.64	52.10	50.45	47.39	47.46	46.49	48.79
1.84	1.83	1.79	1.07	1.19	1.50	1.76	1.01	1.02	1.50	1.10	1.08	1.12	2.71	2.64
14.80	16.16	15.73	19.50	18.24	18.22	17.51	19.00	19.22	17.82	15.15	14.61	15.47	17.32	16.89
11.60	8.96	10.38	11.55	11.68	11.60	13.53	11.23	11.52	12.00	8.88	9.29	10.46	11.22	11.24
0.17	0.22	0.17	0.14	0.11	0.03	0.09	0.02	0.01	0.04	0.15	0.12	0.13	0.05	0.13
5.78	6.39	6.91	3.78	2.36	2.29	1.32	1.45	1.48	1.47	6.78	6.89	4.79	1.78	3.10
9.71	11.66	9.49	5.56	6.78	4.53	5.09	5.12	5.24	4.86	14.38	10.23	10.79	5.95	4.37
2.27	2.07	1.96	2.70	2.67	2.35	3.15	2.32	2.33	2.74	2.32	2.31	2.27	2.69	2.83
1.36	1.71	2.21	1.98	1.67	3.66	2.69	3.59	3.73	3.48	0.80	1.27	1.81	2.55	3.70
0.27	0.22	0.25	0.12	0.11	0.46	0.42	0.11	0.15	0.40	0.08	0.07	0.08	0.93	0.48
6.14	3.96	4.34	2.79	4.17	2.78	4.13	4.10	2.48	2.25	2.04	5.98	4.85	5.81	4.34
92.27	96.91	96.70	95.96	94.77	96.45	96.22	94.58	96.34	96.41	100.08	93.26	94.38	91.68	94.18
47.3	43.2	42.4	39.2	44.0	52.1	55.9	47.7	48.1	51.8	48.1	50.6	49.9	24.9	26.7
476	408	417	411	381	354	153	447	504	278	287	271	298	134	195
54.4	48.4	44.2	43.1	40.0	40.3	83.9	37.4	69.8	19.7	41.6	44.1	31.5	48.2	46.0
141	111	95.0	122	61.3	71.9	66.9	63.8	67.3	52.9	64.2	71.9	61.8	66.9	186
77	67	32	170	137	160	136	213	200	151	80	51	68	123	55
8.80	15.72	17.21	48.90	36.44	47.70	51.41	49.06	52.91	56.18	11.74	19.02	15.39	51.86	72.79
243	236	223	266	210	243	276	235	249	283	124	152	139	546	619
33.8	30.3	32.1	15.7	16.6	40.6	43.6	58.5	75.6	42.0	23.6	21.9	25.1	31.1	26.1
146	135	129	49.4	54.4	82.8	106	48.4	48.2	84.9	60.1	59.8	60.0	246	212
14.66	13.38	12.74	2.47	2.37	2.94	7.82	0.73	0.65	5.72	0.43	0.48	0.63	50.21	47.63
0.41	0.49	0.68	4.68	1.48	1.92	2.16	1.93	2.01	2.54	0.37	0.70	0.29	2.79	5.45
79.44	88.53	137	33.06	32.37	46.05	117	47.40	87.05	44.87	58.06	40.69	30.71	415	416
10.18	9.42	9.55	3.97	2.29	13.27	12.38	25.93	25.36	14.93	0.98	1.14	1.42	33.40	28.45
25.04	22.39	21.12	5.53	5.33	8.67	14.18	4.65	4.31	11.55	3.92	4.45	5.25	67.51	60.81
3.55	3.28	3.15	1.04	0.90	2.90	3.32	5.70	3.98	3.85	0.77	0.84	0.98	8.21	7.19
16.65	15.29	14.79	5.31	4.89	13.91	15.77	26.25	19.30	17.85	4.77	5.13	5.81	32.95	29.15
4.67	4.24	4.09	1.73	1.77	3.75	4.32	6.26	4.87	4.75	1.98	2.08	2.32	6.91	6.19
1.63	1.49	1.46	0.73	0.74	1.32	1.58	2.01	1.75	1.58	0.87	0.90	0.95	2.36	2.14
5.53	4.94	4.84	2.27	2.31	4.99	5.65	8.24	7.38	5.95	2.83	2.87	3.20	7.16	6.43
0.94	0.83	0.81	0.40	0.44	0.85	1.00	1.29	1.25	1.00	0.55	0.55	0.61	1.02	0.92
6.13	5.46	5.37	2.77	3.02	5.76	6.86	8.24	8.84	6.55	3.93	3.95	4.30	5.95	5.32
1.29	1.14	1.13	0.58	0.64	1.26	1.50	1.74	2.02	1.40	0.85	0.85	0.93	1.16	1.03
3.69	3.26	3.28	1.60	1.83	3.61	4.41	4.73	5.84	3.99	2.50	2.48	2.68	3.20	2.81
0.53	0.46	0.47	0.23	0.27	0.51	0.64	0.63	0.81	0.57	0.37	0.37	0.40	0.44	0.39
3.48	2.99	3.02	1.44	1.72	3.28	4.15	3.81	5.02	3.73	2.45	2.41	2.58	2.80	2.48
0.51	0.44	0.45	0.20	0.24	0.48	0.61	0.54	0.74	0.55	0.36	0.35	0.37	0.40	0.35
3.61	3.33	3.16	1.41	1.57	2.33	2.80	1.48	1.49	2.31	1.69	1.73	1.75	5.76	4.93
0.88	0.81	0.77	0.15	0.15	0.19	0.47	0.06	0.05	0.33	0.04	0.04	0.05	3.09	2.91
0.80	0.74	0.68	0.73	0.52	0.71	3.00	1.20	0.53	3.12	0.26	0.39	0.27	2.33	2.36
1.00	0.90	0.84	0.17	0.16	0.19	0.51	0.05	0.06	0.44	0.03	0.04	0.04	4.08	3.73
0.19	0.21	0.15	0.19	0.25	0.28	0.55	0.32	0.35	0.44	0.07	0.13	0.16	1.01	1.04

Ta	Pb	Th	U
1.13	1.58	1.21	0.40
0.02	0.15	0.03	0.01
0.04	3.07	0.03	0.01
0.00	0.19	0.00	0.00
0.76	10.09	5.93	1.61
0.01	0.15	0.11	0.03

Table 2.S1: Continued

D12-3 IEKED0019 142.18 34.07	**D12-4** IEKED001A 142.18 34.07	**D12-5** IEKED001B 142.18 34.07	**D12-6** IEKED001C 142.18 34.07	**D12-7** IEKED001D 142.18 34.07	**D12-8** IEKED001E 142.18 34.07	**D14-1** IEKED001F 142.20 34.17	**D14-2** IEKED001G 142.20 34.17	**D14-3** IEKED001H 142.20 34.17	**D14-4** IEKED001I 142.20 34.17	**D14-5** IEKED001J 142.20 34.17	**D14-6** IEKED001K 142.20 34.17	**D14-7** IEKED001L 142.20 34.17	**D13-1** IEKED001M 142.19 34.37
46.07	45.62	48.01	47.09	47.16	47.27	49.05	51.90	46.32	49.93	50.13	49.26	50.63	48.29
2.80	1.51	2.39	3.13	1.61	2.28	2.65	2.50	2.11	2.32	2.54	2.61	2.53	2.49
16.52	15.64	15.64	17.54	16.17	17.02	19.38	19.55	16.10	17.77	18.91	19.05	19.08	14.22
9.32	7.67	11.68	12.70	7.88	9.62	11.35	10.48	9.78	10.36	10.61	11.02	11.21	13.82
0.10	0.14	0.16	0.13	0.14	0.12	0.17	0.08	0.14	0.14	0.09	0.11	0.08	0.23
6.38	5.53	4.55	3.21	5.37	4.19	1.43	1.17	7.02	3.12	2.07	1.13	1.34	5.57
7.55	14.37	4.38	4.57	12.29	7.68	6.00	5.02	8.64	6.53	5.00	4.39	4.86	10.20
2.76	2.56	3.16	2.51	3.07	2.68	2.51	3.12	2.90	3.20	2.96	3.05	2.56	3.23
1.86	2.11	3.50	2.96	2.38	3.02	3.29	4.19	1.41	3.06	3.72	4.46	3.94	0.21
0.50	0.34	0.50	0.62	0.36	0.45	0.90	0.73	0.36	0.49	0.56	0.60	0.65	0.23
4.74	4.08	4.00	4.60	3.58	3.20	3.59	2.38	3.74	2.45	4.08	3.54	3.47	1.53
93.87	95.49	93.98	94.46	96.45	94.32	96.71	98.75	94.78	96.92	96.59	95.69	96.88	98.49
26.9	33.4	25.9	28.3	33.7	26.7	28.1	25.6	33.2	33.9	26.4	26.9	27.5	44.8
123	232	89	179	229	220	105	142	221	218	105	115	113	14
38.3	32.8	21.2	61.5	37.5	42.0	35.9	27.0	38.2	43.8	18.0	53.4	14.9	46.2
140	75.0	48.9	332	108	162	54.5	109	135	85.4	73.4	140	67.4	29.4
49	48	43	53	62	49	62	116	53	60	44	74	54	60
47.48	33.08	67.17	47.08	35.56	46.77	40.65	56.31	30.10	56.97	67.99	67.28	79.62	1.12
529	474	483	553	456	527	552	580	360	487	600	592	650	109
27.3	24.6	33.7	28.6	24.2	26.5	42.5	30.2	28.2	26.4	35.4	27.3	37.8	50.6
232	125	198	235	125	180	242	238	179	186	233	232	242	170
52.73	36.38	55.60	53.51	36.51	43.10	52.07	54.38	34.05	35.41	49.48	49.42	51.18	4.84
1.55	0.47	2.22	3.06	0.71	0.92	1.44	1.08	1.14	3.62	1.84	4.35	4.32	0.03
387	323	504	380	314	458	515	528	293	335	471	469	515	26.61
30.76	22.33	32.78	30.36	22.16	26.45	40.87	33.90	21.83	21.94	34.67	29.56	36.06	5.44
66.33	43.77	65.28	66.39	43.48	53.21	72.48	67.83	45.65	46.69	63.51	65.87	67.58	17.43
7.81	5.20	7.76	8.01	5.14	6.39	9.77	8.00	5.73	5.65	7.97	7.62	8.29	2.86
31.68	20.69	30.81	32.46	20.56	25.78	39.17	31.59	23.97	23.01	31.92	30.27	33.17	15.69
6.77	4.44	6.33	6.93	4.36	5.49	8.04	6.25	5.36	5.06	6.46	6.29	6.66	5.44
2.30	1.49	2.11	2.33	1.48	1.92	2.63	2.12	1.82	1.75	2.14	2.11	2.26	1.86
6.89	4.84	6.81	6.98	4.75	5.82	8.40	6.54	5.72	5.35	6.78	6.33	7.01	7.10
0.97	0.73	1.00	0.99	0.72	0.85	1.19	0.90	0.86	0.81	0.95	0.90	1.01	1.31
5.57	4.50	6.15	5.67	4.48	5.10	7.10	5.31	5.27	4.88	5.76	5.28	5.95	9.03
1.06	0.93	1.25	1.09	0.92	1.00	1.44	1.07	1.07	0.98	1.18	1.03	1.23	1.95
2.91	2.64	3.57	2.96	2.60	2.80	4.05	3.02	2.98	2.76	3.37	2.84	3.50	5.65
0.39	0.38	0.51	0.40	0.37	0.39	0.56	0.42	0.42	0.39	0.47	0.40	0.50	0.83
2.51	2.47	3.37	2.48	2.43	2.54	3.62	2.72	2.72	2.55	3.10	2.51	3.28	5.44
0.35	0.37	0.50	0.35	0.36	0.37	0.53	0.40	0.40	0.37	0.47	0.36	0.50	0.81
5.37	3.08	4.69	5.13	3.07	4.24	5.67	5.37	4.15	4.28	5.30	5.27	5.48	4.65
3.24	2.19	3.35	3.12	2.17	2.61	3.13	3.18	1.99	2.07	2.97	2.92	3.05	0.33
2.26	2.49	2.98	1.87	2.38	1.93	2.73	2.52	1.67	1.82	2.68	2.32	2.54	0.79
4.05	3.11	4.52	3.99	3.09	3.61	4.62	4.44	2.51	2.64	4.24	4.15	4.32	0.38
0.95	0.48	1.08	0.90	0.52	1.03	1.06	0.93	0.55	0.62	1.01	0.75	1.00	0.12

Table 2.S1: Continued

D13-2	**D13-3**	**D13-4**	**D13-5**	**D13-6**	**D13-7**	**D13-8**	**D13-9**
IEKED001N	IEKED001O	IEKED001P	IEKED001Q	IEKED001R	IEKED001S	IEKED001T	IEKED001U
142.19	142.19	142.19	142.19	142.19	142.19	142.19	142.19
34.37	34.37	34.37	34.37	34.37	34.37	34.37	34.37
48.29	47.70	50.53	48.81	49.28	47.20	49.80	48.87
1.84	2.56	2.17	2.11	2.16	1.82	1.99	2.11
13.78	12.20	16.54	14.74	14.40	16.83	14.48	15.07
12.10	15.74	8.92	12.29	11.90	8.03	11.45	11.20
0.20	0.24	0.11	0.17	0.20	0.13	0.18	0.17
6.88	4.76	3.98	5.70	6.03	5.86	5.98	5.63
11.57	8.65	4.90	10.61	10.15	7.21	11.16	10.95
2.59	2.56	3.87	2.83	2.76	3.97	2.78	2.91
0.08	1.08	4.24	0.54	0.93	2.34	0.53	0.53
0.17	0.50	0.50	0.18	0.20	0.52	0.18	0.23
2.02	2.98	3.01	1.53	1.78	5.41	1.31	1.98
97.50	95.99	95.76	97.98	98.02	93.92	98.52	97.67
45.9	36.5	21.7	56.2	70.2	20.6	54.7	55.5
268	37	40	58	96	91	64	69
42.1	36.2	23.9	55.4	60.5	31.6	42.2	52.6
71.2	24.2	18.1	78.2	91.7	56.1	58.6	70.1
65	52	37	52	85	37	51	66
0.76	10.30	56.51	7.87	20.72	43.03	8.99	4.88
121	167	489	148		483	145	137
37.1	90.4	29.0	39.2	62.5	27.2	35.3	40.8
117	346	377	129	193	294	123	121
4.54	10.51	66.17	3.97	5.94	51.13	3.91	3.81
0.03	0.34	0.93	0.22	0.59	0.84	0.26	0.13
55.39	91.06	721	18.45	86.92	521	17.11	15.63
4.40	12.69	41.34	3.91	6.75	36.21	3.76	4.37
13.26	37.24	85.77	12.15	21.87	76.27	11.98	13.38
2.13	6.17	9.51	2.18	3.62	8.62	1.91	2.22
11.41	31.99	35.44	11.91	18.60	32.68	10.30	12.12
3.93	10.30	6.72	4.23	6.34	6.23	3.64	4.27
1.43	2.82	2.25	1.60	2.28	2.09	1.44	1.59
5.09	12.87	6.78	5.50	8.57	6.24	4.79	5.48
0.94	2.29	0.94	1.03	1.56	0.86	0.89	1.02
6.60	15.66	5.51	7.14	10.40	4.99	6.26	7.18
1.42	3.35	1.10	1.53	2.40	0.98	1.36	1.55
4.10	9.77	3.16	4.55	6.66	2.80	3.99	4.59
0.61	1.45	0.46	0.70	0.98	0.40	0.59	0.68
3.99	9.52	3.07	4.77	6.82	2.63	3.95	4.51
0.58	1.39	0.46	0.71	0.97	0.39	0.58	0.67
3.18	8.90	8.03	3.55	5.53	6.37	3.33	3.37
0.30	0.67	4.08	0.27	0.38	3.17	0.26	0.26
0.45	1.36	2.90	0.57	0.56	2.07	0.53	0.51
0.32	0.90	6.48	0.29	0.44	4.82	0.29	0.28
0.14	0.30	1.90	0.59	0.60	1.29	0.28	0.48

References

Abrams, L.J., 2002. Correlation between core, logging, and seismic data at Site 1149 in the Nadezhda Basin. Proceedings of the Ocean Drilling Program, 185 Scientific Results 185, 1–14. https://doi.org/10.2973/odp.proc.sr.185.001.2002

Armstrong, R.L., 1968. A model for the evolution of strontium and lead isotopes in a dynamic Earth. Reviews of Geophysics 6, 175–199. https://doi.org/10.1029/RG006i002p00175

Ayers, J., 1998. Trace element modeling of aqueous fluid - peridotite interaction in the mantle wedge of subduction zones. Contributions to Mineralogy and Petrology 132, 390–404. https://doi.org/10.1007/s004100050431

Bloomer, S.H., Taylor, Brian, MacLeod, C.J., Stern, R.J., Fryer, P., Hawkins, J.W., Johnson, L., 1995. Early arc volcanism and the ophiolite problem: A perspective from drilling in the western Pacific. In: Taylor, B., Natland, J.H. (Eds.), Active Margins and Marginal Basins of the Western Pacific 88, 1–30. https://doi.org/10.1029/GM088p0001

Boschman, L.M., Hinsbergen, D.J.J. Van, 2016. On the enigmatic birth of the Pacific Plate within the Panthalassa Ocean. Science Advances. https://doi.org/10.1126/sciadv.1600022

Bowen, N.L., 1928. The evolution of the igneous rocks. Princeton University Press, Princeton, New Jersey.

Brenan, J.M., Shaw, H.F., Ryerson, F.J., 1995. Experimental evidence for the origin of lead enrichment in convergent-margin magmas. Letters to Nature 378, 54–56.

Brown, L., Klein, J., Middleton, R., Sacks, I.S., Tera, F., 1982. 10Be in island-arc volcanoes and implications for subduction. Nature 299, 718–720.

Bryant, C.J., Arculus, R.J., Eggins, S.M., 2003. The geochemical evolution of the Izu-Bonin arc system: a perspective from tephras recovered by deep-sea drilling. Geochemistry, Geophysics, Geosystems 4. https://doi.org/10.1029/2002GC000427

Castillo, P.R., 2012. Adakite petrogenesis. Lithos 134–135, 304–316. https://doi.org/10.1016/j.lithos.2011.09.013

Castillo, P.R., Carlson, R.W., Batiza, R., 1991. Origin of Nauru Basin igneous complex: Sr, Nd and Pb isotope and REE constraints. Earth and Planetary Science Letters 103, 200–213. https://doi.org/10.1016/0012-821X(91)90161-A

Castillo, P.R., Lonsdale, P.F., Moran, C.L., Hawkins, J.W., 2009. Geochemistry of mid-Cretaceous Pacific crust being subducted along the Tonga-Kermadec Trench: Implications for the generation of arc lavas. Lithos 112, 87–102. https://doi.org/10.1016/j.lithos.2009.03.041

Castillo, P.R., Pringle, M.S., Carlson, R.W., 1994. East Mariana Basin tholeiites: Cretaceous intraplate basalts or rift basalts related to the Ontong Java plume? Earth and Planetary Science Letters 123, 139–154. https://doi.org/10.1016/0012-821X(94)90263-1

Class, C., Miller, D.M., Goldstein, S.L., Langmuir, C.H., 2000. Distinguishing melt and fluid subduction components in Umnak Volcanics, Aleutian Arc. Geochemistry Geophysics Geosystems 1. https://doi.org/10.1029/1999GC000010

Crawford, A.J., Briqueu, L., Laporte, C., Hasenaka, T., 1995. Coexistence of Indian and Pacific oceanic upper mantle reservoirs beneath the central New Hebrides Island Arc. Active Margins and Marginal Basins of West Pacific 88, 199–218. https://doi.org/10.1029/GM088p0199

Day, J.M.D., Peters, B.J., Janney, P.E., 2014. Oxygen isotope systematics of South African olivine melilitites and implications for HIMU mantle reservoirs. Lithos 202–203, 76–84. https://doi.org/10.1016/j.lithos.2014.05.009

Defant, M.J., Drummond, M.S., 1990. Derivation of some modern arc magmas by melting of young subducted lithosphere. Letters to Nature 347, 662–665. https://doi.org/10.1038/347662a0

Dickin, A.P., 2005. Radiogenic Isotope Geology, 2nd Editio. ed, CEUR Workshop Proceedings. Cambridge University Press, New York. https://doi.org/10.1017/CBO9781107415324.004

Elderfield, H., 1986. Strontium isotope stratigraphy. Palaeogeography, Palaeoclimatology, Palaeoecology 57, 71–90. https://doi.org/10.1016/0031-0182(86)90007-6

Elliott, T., 2003. Tracers of the slab. Inside the Subduction Factory. 23–45. https://doi.org/10.1029/138gm03

Elliott, T., Plank, T., Zindler, A., White, W., Bourdon, B., 1997. Element transport from slab to volcanic front at the Mariana arc. Journal of Geophysical Research 102, 14991–15019.

Ewing, J., Ewing, M., Aitken, T., Ludwig, W.J., 1968. North Pacific sediment layers measured by seismic profiling. The Crust and Upper Mantle of the Pacific Area: Geophysical Monograph Series 12 12, 147–173. https://doi.org/10.1029/GM012p0147

Faure, G., 1986. Principles of Isotope Geology, 2nd Editio. ed. John Wiley & Sons, New York.

Fitton, J.G., Godard, M., 2004. Origin and evolution of magmas on the Ontong Java Plateau. Geological Society, London, Special Publications 229, 151–178. https://doi.org/10.1144/GSL.SP.2004.229.01.10

Flower, M.F.J., Russo, R.M., Tamaki, K., Hoang, N., 2001. Mantle contamination and the Izu-Bonin-Mariana (IBM) “high-tide mark”: evidence for mantle extrusion caused by Tethyan closure. Tectonophysics 333, 9–34. https://doi.org/10.1016/S0040-1951(00)00264-X

Freymuth, H., Ivko, B., Gill, J.B., Tamura, Y., Elliott, T., 2016. Thorium isotope evidence for melting of the mafic oceanic crust beneath the Izu arc. Geochimica et Cosmochimica Acta 186, 49–70. https://doi.org/10.1016/j.gca.2016.04.034

Geldmacher, J., van den Bogaard, P., Heydolph, K., Hoernle, K., 2014. The age of Earth's largest volcano: Tamu Massif on Shatsky Rise (northwest Pacific Ocean). International Journal of Earth Sciences 103, 2351–2357. https://doi.org/10.1007/s00531-014-1078-6

Gill, J.B., 1981. Orogenic Andesites and Plate Tectonics, Orogenic Andesites and Plate Tectonics. https://doi.org/10.1007/978-3-642-68012-0

Gong, W., Xing, J., Jiang, X., 2018. Heterogeneous subduction structure within the Pacific plate beneath the Izu-Bonin arc. Journal of Geodynamics 116, 1–12. https://doi.org/10.1016/j.jog.2018.01.006

Goto, A., Tatsumi, Y., 1996. Quantitative analysis of rock samples by an X-ray fluorescence spectrometer (II). The Rigaku Journal 13, 20–39.

Gradstein, F.M., Ogg, J.G., Schmitz, M.D., Ogg, G.M., 2012. The Geologic Time Scale 2012, The Geologic Time Scale 2012. https://doi.org/10.1016/C2011-1-08249-8

Green, T.H., Ringwood, A.E., 1968. The genesis of the calc-alkaline rock suite. Contributions to Mineralogy and Petrology 18, 105–162. https://doi.org/10.1016/0012-821X(72)90171-9

Gust, D.A., Arculus, R.J., Kersting, A.B., 1997. Aspects of magma sources and processes in the Honshu arc. The Canadian Mineralogist 35, 347–365. https://doi.org/scopus/2-s2.0-0030715656

Hart, S.R., 1988. Heterogeneous mantle domains: signatures, genesis and mixing chronologies. Earth and Planetary Science Letters 90, 273–296. https://doi.org/10.1016/0012-821X(88)90131-8

Hauff, F., Hoernle, K., Schmidt, A., 2003. Sr-Nd-Pb composition of Mesozoic Pacific oceanic crust (Site 1149 and 801, ODP Leg 185): Implications for alteration of ocean crust and the input into the Izu-Bonin-Mariana subduction system. Geochemistry, Geophysics, Geosystems 4. https://doi.org/10.1029/2002GC000421

Hergt, J.M., Woodhead, J.D., 2007. A critical evaluation of recent models for Lau-Tonga arc-backarc basin magmatic evolution. Chemical Geology 245, 9–44. https://doi.org/10.1016/j.chemgeo.2007.07.022

Heydolph, K., Murphy, D.T., Geldmacher, J., Romanova, I. V., Greene, A., Hoernle, K., Weis, D., Mahoney, J., 2014. Plume versus plate origin for the Shatsky Rise oceanic plateau (NW Pacific): insights from Nd, Pb and Hf isotopes. Lithos 200–201, 49–63. https://doi.org/10.1016/j.lithos.2014.03.031

Hickey-Vargas, R., 1998. Origin of the Indian Ocean-type isotopic signature in basalts from Philippine sea plate spreading centers: An assessment of local versus large-scale processes. Journal of Geophysical Research 108, 20,963-20,979.

Hickey-Vargas, R., Hergt, J.M., Spadea, P., 1995. The indian ocean-type isotopic signature in western pacific marginal basins: Origin and significance. Geophysical Monograph Series 88, 175–197. https://doi.org/10.1029/GM088p0175

Hickey-Vargas, R., Savov, I.P., Bizimis, M., Ishii, T., Fujioka, K., 2006. Origin of Diverse Geochemical Signatures in Igneous Rocks from the West Philippine Basin: Implications for Tectonic Models. Back-Arc Spreading Systems: Geological, Biological, Chemical, and Physical Interactions 287–303. https://doi.org/10.1029/166GM15

Hochstaedter, A., Gill, J., Peters, R., Broughton, P., Holden, P., Taylor, B., 2001. Across-arc geochemical trends in the Izu-Bonin arc: Contributions from the subducting slab. Geochemistry, Geophysics, Geosystems 2. https://doi.org/10.1029/2009GC002847

Hochstaedter, A.G., Gill, J.B., Taylor, B., Ishizuka, O., Yuasa, M., Morita, S., 2000. Across-arc geochemical trends in the Izu-Bonin arc: constraints on source composition and mantle melting. Journal of Geophysical Research 105, 495–512. https://doi.org/10.1029/1999jb900125

Ingram, B.L., 1995. Ichthyolith strontium isotopic stratigraphy of deep-sea clays: sites 885 and 886 (North Pacific Transect). Proceedings of the Ocean Drilling Program, Scientific Results 145, 399–412.

Ishizuka, O., Tani, K., Reagan, M.K., Kanayama, K., Umino, S., Harigane, Y., Sakamoto, I., Miyajima, Y., Yuasa, M., Dunkley, D.J., 2011. The timescales of subduction initiation and subsequent evolution of an oceanic island arc. Earth and Planetary Science Letters 306, 229–240. https://doi.org/10.1016/j.epsl.2011.04.006

Ishizuka, O., Taylor, R.N., Milton, J.A., Nesbitt, R.W., 2003. Fluid–mantle interaction in an intra-oceanic arc: constraints from high-precision Pb isotopes. Earth and Planetary Science Letters 211, 221–236. https://doi.org/10.1016/S0012-821X(03)00201-2

Ishizuka, O., Taylor, R.N., Milton, J.A., Nesbitt, R.W., Yuasa, M., Sakamoto, I., 2006. Variation in the mantle sources of the northern Izu arc with time and space - Constraints from high-precision Pb isotopes. Journal of Volcanology and Geothermal Research 156, 266–290. https://doi.org/10.1016/j.jvolgeores.2006.03.005

Ishizuka, O., Taylor, R.N., Yuasa, M., Milton, J.A., Nesbitt, R.W., Uto, K., Sakamoto, I., 2007. Processes controlling along-arc isotopic variation of the southern Izu-Bonin arc. Geochemistry, Geophysics, Geosystems 8. https://doi.org/10.1029/2006GC001475

Janney, P.E., Castillo, P.R., 1997. Geochemistry of Mesozoic Pacific mid-ocean ridge basalt: constraints on mantle generation and the evolution of the Pacific upper mantle. Journal of

Geophysical Research 102, 5207–5229.

Janney, P.E., Castillo, P.R., 1996. Basalts from the Central Pacific Basin: evidence for the origin of Cretaceous igneous complexes in the Jurassic western Pacific. Journal of Geophysical Research 101, 2875–2893. https://doi.org/10.1029/95JB03119

Kay, R.W., 1978. Aleutian magnesian andesites: melts from subducted Pacific ocean crust. Journal of Volcanology and Geothermal Research 4, 117–132. https://doi.org/10.1016/0377-0273(78)90032-X

Kelley, K.A., Plank, T., Ludden, J., Staudigel, H., 2003. Composition of altered oceanic crust at ODP Sites 801 and 1149. Geochemistry, Geophysics, Geosystems 4. https://doi.org/10.1029/2002GC000435

Keppler, H., 1996. Constraints from partitioning experiments on the composition of subduction-zone fluids. Nature 380.

Koppers, A.A.P.P., Staudigel, H., Duncan, R. a., 2003. High-resolution 40Ar/39Ar dating of the oldest oceanic basement basalts in the western Pacific basin. Geochemistry, Geophysics, Geosystems 4. https://doi.org/10.1029/2003GC000574

Krolikowska-Ciaglo, S., Deyhle, A., Hauff, F., Hoernle, K., 2007. Boron isotope geochemistry and U-Pb systematics of altered MORB from the Australian Antarctic Discordance (ODP Leg 187). Chemical Geology 242, 455–469. https://doi.org/10.1016/j.chemgeo.2007.05.004

Larson, R.L., 1991. Latest pulse of the Earth; evidence for a mid- Cretaceous superplume. Geology 19, 547–550. https://doi.org/10.1130/0091-7613(1991)019<0547

Machida, S., Hirano, N., Kimura, J.I., 2009. Evidence for recycled plate material in Pacific upper mantle unrelated to plumes. Geochimica et Cosmochimica Acta 73, 3028–3037. https://doi.org/10.1016/j.gca.2009.01.026

Madrigal, P., Gazel, E., Flores, K.E., Bizimis, M., Jicha, B., 2016. Record of massive upwellings from the Pacific large low shear velocity province. 7, 13309.

Mahoney, J.J., Storey, M., Duncan, R. a., Spencer, K.J., Pringle, M., 1993. Geochemistry and age of the Ontong Java Plateau. The Mesozoic Pacific: Geology, Tectonics, and Volcanism. 233–261. https://doi.org/10.1029/GM077p0233

Manning, C.E., 2004. The chemistry of subduction-zone fluids. Earth and Planetary Science Letters 223, 1–16. https://doi.org/10.1016/j.epsl.2004.04.030

Marsh, B.D., Carmichael, I.S.E., 1974. Benioff zone magmatism. Journal of Geophysical Research 79, 1196–1206.

Martinez, F., Taylor, B., 2002. Mantle wedge control on back-arc crustal accretion. Nature 416, 417–420. https://doi.org/10.1038/416417a

Miller, M.S., Gorbatov, A., Kennett, B.L.N., 2005. Heterogeneity within the subducting Pacific slab beneath the Izu-Bonin-Mariana arc: Evidence from tomography using 3D ray tracing inversion techniques. Earth and Planetary Science Letters 235, 331–342. https://doi.org/10.1016/j.epsl.2005.04.007

Miyazaki, T., Kimura, J.I., Senda, R., Vaglarov, B.S., Chang, Q., Takahashi, T., Hirahara, Y., Hauff, F., Hayasaka, Y., Sano, S., Shimoda, G., Ishizuka, O., Kawabata, H., Hirano, N., Machida, S., Ishii, T., Tani, K., Yoshida, T., 2015. Missing western half of the Pacific Plate: Geochemical nature of the Izanagi-Pacific Ridge interaction with a stationary boundary between the Indian and Pacificmantles. Geochemistry, Geophysics, Geosystems 16, 3309–3332. https://doi.org/10.1002/2014GC005684.Key

Müller, R.D., Sdrolias, M., Gaina, C., Steinberger, B., Heine, C., 2008. Long-Term Sea-Level Fluctuations. 319, 1357–1362.

Nakamura, K., 1987. Trench depth and relative motion between overriding plates. Recent Plate Movements and Deformation. American Geophysical Union, 21–26. https://doi.org/10.1029/GD020p0021

Nakanishi, M., 1993. Topographic expression of five fracture zones in the northwestern Pacific Ocean. Geophysical Monograph Series 77, 121–136. https://doi.org/10.1029/GM077p0121

Nakanishi, M., Tamaki, K., Kobayashi, K., 1992. A new Mesozoic isochron chart of the northwestern Pacific Ocean: paleomagnetic and tectonic implications. Geophysical Research Letters 19, 693–696.

Pearce, J. A., Baker, P.E., Harvey, P.K., Luff, I.W., 1995. Geochemical evidence for subduction fluxes, mantle melting and fractional crystallization beneath the south Sandwich island arc. Journal of Petrology 36, 1073–1109. https://doi.org/10.1093/petrology/36.4.1073

Pearce, J. A., Kempton, P.D., Nowell, G.M., Noble, S.R., 1999. Hf-Nd element and isotope perspective on the nature and provenance of mantle and subduction components in western Pacific arc-basin systems. Journal of Petrology 40, 1579–1611. https://doi.org/10.1093/petroj/40.11.1579

Pearce, J.A., 1982. Trace element characteristics of lavas from destructive plate boundaries. Orogenic Andesites and Related Rocks. Wiley & Sons, 525–548.

Plank, T., Kelley, K. a., Murray, R.W., Stern, L.Q., 2007. Chemical composition of sediments subducting at the Izu-Bonin trench. Geochemistry, Geophysics, Geosystems 8, 1–16. https://doi.org/10.1029/2006GC001444

Plank, T., Langmuir, C.H., 1998. The chemical composition of subducting sediment and its consequences for the crust and mantle. Chemical Geology 145, 325–394.

https://doi.org/10.1016/S0009-2541(97)00150-2

Plank, T., Langmuir, C.H., 1993. Tracing trace elements from sediment input to volcanic output at subduction zones. Letters to Nature 362, 739–743. https://doi.org/10.1038/362739a0

Porter, K. a., White, W.M., 2009. Deep mantle subduction flux. Geochemistry, Geophysics, Geosystems 10. https://doi.org/10.1029/2009GC002656

Reagan, M.K., Ishizuka, O., Stern, R.J., Kelley, K.A., Ohara, Y., Blichert-Toft, J., Bloomer, S.H., Cash, J., Fryer, P., Hanan, B.B., Hickey-Vargas, R., Ishii, T., Kimura, J.I., Peate, D.W., Rowe, M.C., Woods, M., 2010. Fore-arc basalts and subduction initiation in the Izu-Bonin-Mariana system. Geochemistry, Geophysics, Geosystems 11, 1–17. https://doi.org/10.1029/2009GC002871

Reiners, P.W., 1998. Reactive Melt Transport in the Mantle and Geochemical Signatures of Mantle-derived Magmas. Journal of Petrology 39, 1039–1061.

Sano, T., Shimizu, K., Ishikawa, A., Senda, R., Chang, Q., Kimura, J.I., Widdowson, M., Sager, W.W., 2012. Variety and origin of magmas on Shatsky Rise, northwest Pacific Ocean. Geochemistry, Geophysics, Geosystems 13, 1–25. https://doi.org/10.1029/2012GC004235

Sano, T., Shirao, M., Tani, K., Tsutsumi, Y., Kiyokawa, S., Fujii, T., 2016. Progressive enrichment of arc magmas caused by the subduction of seamounts under Nishinoshima volcano, Izu–Bonin Arc, Japan. Journal of Volcanology and Geothermal Research 319, 52–65. https://doi.org/10.1016/j.jvolgeores.2016.03.004

Seyfried, W.E., Chen, X., Chan, L.H., 1998. Trace element mobility and lithium isotope exchange during hydrothermal alteration of seafloor weathered basalt: an experimental study at 350°C, 500 bars. Geochimica et Cosmochimica Acta 62, 949–960. https://doi.org/10.1016/S0016-7037(98)00045-3

Shaw, D.M., 1970. Trace element fractionation during anatexis. Geochimica et Cosmochimica Acta 34, 237–243. https://doi.org/10.1016/0016-7037(70)90009-8

Shimoda, G., Ishizuka, O., Yamashita, K., Yoshitake, M., Ogasawara, M., Yuasa, M., 2011. Tectonic influence on chemical composition of ocean island basalts in the West and South Pacific: Implication for a deep mantle origin. Geochemistry, Geophysics, Geosystems 12, 1–23. https://doi.org/10.1029/2011GC003531

Shipboard Scientific Party, 2000. Site 1149. Proceedings of the Ocean Drilling Program, Initial Reports 185, 1–190. https://doi.org/10.2973/odp.proc.ir.185.104.2000

Staudigel, H., Plank, T., White, B., Schmincke, U., 1996. Geochemical fluxes during seafloor alteration of the basaltic crust: DSDP Sites 417 and 418. Geophysical Monograph 96. 19–38.

Stern, Robert J., Fouch, Matthew J., Klemperer, S.L., 2003. An overview of the Izu-Bonin Mariana Subduction Factory. Inside the Subduction Factory. 175–222.

Straub, S.M., 2003. The evolution of the Izu Bonin-Mariana volcanic arcs (NW Pacific) in terms of major element chemistry. Geochemistry, Geophysics, Geosystems 4, 1–33. https://doi.org/10.1029/2002GC000357

Straub, S.M., Goldstein, S.L., Class, C., Schmidt, A., 2009. Mid-ocean-ridge basalt of Indian type in the northwest Pacific Ocean basin. Nature Geoscience 2, 286–289. https://doi.org/10.1038/ngeo471

Straub, S.M., Goldstein, S.L., Class, C., Schmidt, A., Gomez-Tuena, A., 2010. Slab and mantle controls on the Sr-Nd-Pb-Hf isotope evolution of the Post 42 Ma Izu-Bonin volcanic arc. Journal of Petrology 51, 993–1026. https://doi.org/10.1093/petrology/egq009

Straub, S.M., Layne, G.D., 2003. The systematics of chlorine, fluorine, and water in Izu arc front volcanic rocks: Implications for volatile recycling in subduction zones. Geochimica et Cosmochimica Acta 67, 4179–4203. https://doi.org/10.1016/S0016-7037(03)00307-7

Straub, S.M., Layne, G.D., Schmidt, A., Langmuir, C.H., 2004. Volcanic glasses at the Izu arc volcanic front: new perspectives on fluid and sediment melt recycling in subduction zones. Geochemistry, Geophysics, Geosystems 5. https://doi.org/10.1029/2002GC000408

Straub, S.M., Woodhead, J.D., Arculus, R.J., 2015. Temporal evolution of the Mariana Arc: Mantle wedge and subducted slab controls revealed with a tephra perspective. Journal of Petrology 56, 409–439. https://doi.org/10.1093/petrology/egv005

Straub, S.M., Zellmer, G.F., 2012. Volcanic arcs as archives of plate tectonic change. Gondwana Research 21, 495–516. https://doi.org/10.1016/j.gr.2011.10.006

Sun, S. -s., McDonough, W.F., 1989. Chemical and isotopic systematics of oceanic basalts: implications for mantle composition and processes. Geological Society, London, Special Publications 42, 313–345. https://doi.org/10.1144/GSL.SP.1989.042.01.19

Tamura, Y., Sato, T., Fujiwara, T., Kodaira, S., Nichols, A., 2016. Advent of continents: a new hypothesis. Scientific Reports 6, 33517. https://doi.org/10.1038/srep33517

Tani, K., Kawabata, H., Chang, Q., Sato, K., Tatsumi, Y., 2005. Quantitative analyses of silicate rock major and trace elements by X-ray fluorescence spectrometer: evaluation of analytical precision and sample preparation. Frontier Research on Earth Evolution 2, 1–8.

Tarduno, A.J.A., Sliter, W. V, Kroenke, L., Leckie, M., Mayer, H., Mahoney, J.J., Storey, M., Winterer, E.L., 1991. Rapid formation of Ontong Java Plateau by Aptian mantle plume volcanism. Science 254, 399–403.

Tatsumi, Y., Nakamura, N., 1986. Composition of aqueous fluid from serpentinite in the subducted lithosphere. Geochemical Journal 20, 191–196. https://doi.org/10.2343/geochemj.20.191

Tatsumoto, M., 1969. Lead isotopes in volcanic rocks and possible ocean-floor thrusting beneath island arcs. Earth and Planetary Science Letters 6, 369–376. https://doi.org/10.1016/0012-821X(69)90187-3

Taylor, B., 2006. The single largest oceanic plateau: Ontong Java–Manihiki–Hikurangi. Earth and Planetary Science Letters 241, 372–380. https://doi.org/10.1016/j.epsl.2005.11.049

Taylor, B., 1992. Rifting and the volcanic-tectonic evolution of the Izu-Bonin-Mariana arc. Proceedings of the Ocean Drilling Program, Scientific Results 126, 627–651.

Taylor, R., Ishizuka, O., 2001. Lead Isotope Measurement by Lead Double Spike and Thallium Spike Using MC-ICP-MS and TIMS - a Comparison Using Basaltic Samples. AGU Fall Meeting Abstracts 82.

Taylor, R.N., Nesbitt, R.W., 1998. Isotopic characteristics of subduction fluids in an intra-oceanic setting, Izu-Bonin Arc, Japan. Earth and Planetary Science Letters 164, 79–98. https://doi.org/10.1016/S0012-821X(98)00182-4

Tejada, M.L.G., Mahoney, J.J., Castillo, P.R., Ingle, S.P., Sheth, H.C., Weis, D., 2004. Pin-pricking the elephant: evidence on the origin of the Ontong Java Plateau from Pb-Sr-Hf-Nd isotopic characteristics of ODP Leg 192 basalts. Geological Society, London, Special Publications 229, 133–150. https://doi.org/10.1144/GSL.SP.2004.229.01.09

Tejada, M.L.G., Mahoney, J.J., Neal, C.R., Duncan, R.A., Petterson, M.G., 2002. Basement geochemistry and geochronology of Central Malaita , Solomon Islands , with Iimplications for the origin and evolution of the Ontong Java Plateau. Journal of Petrology 43, 449–484.

White, W.M., Dupré, B., 1986. Sediment subduction and magma genesis in the Lesser Antilles: isotopic and trace element constraints. Journal of Geophysical Research: Solid Earth 91, 5927–5941. https://doi.org/10.1029/JB091iB06p05927

Wilson, M., 1989. Igneous Petrogenesis: A Global Tectonic Approach. Unwin Hyman, London.

Yokoyama, T., Kuritani, T., Kobayashi, K., Nakamura, E., 2006. Geochemical evolution of a shallow magma plumbing system during the last 500 years, Miyakejima volcano, Japan: Constraints from $_{238}$U–$_{230}$Th–$_{226}$Ra systematics. Geochimica et Cosmochimica Acta 70, 2885–2901. https://doi.org/10.1016/j.gca.2006.02.027

Zheng, Y.-F., Hermann, J., 2014. Geochemistry of continental subduction-zone fluids. Earth, Planets and Space 66, 93. https://doi.org/10.1186/1880-5981-66-93

Chapter 3

Widespread contamination of the Pacific upper mantle during the Mid-Cretaceous

Abstract

We contribute to the expanding Hf isotope data set of altered oceanic crust in the Pacific basin with ^{177}Hf/^{176}Hf measurements from a targeted, along flow-line transect of oceanic crust in order to constrain the evolution of the upper mantle during the mid-Cretaceous. The samples, accreted along the Pacific-Izanagi ridge system, can be separated into a normal (N) mid-ocean ridge basalt (MORB) and an enriched (E) MORB group by their La/Sm$_N$ ratios (E-MORB La/Sm$_N$ >1). Normal MORB Nd-Hf-Pb isotope and trace element values are similar to those for >125 Ma lavas from DSDP sites 166, 197, 303, 304, 307 and (I)ODP sites 801, 1149 and 1179. Their isotopic signatures are also similar to the bulk of Shatsky Rise lavas. Enriched MORBs are compositionally similar to <125 Ma lavas from DSDP sites 196 and 462 and ODP site 802. Their isotopic signatures are akin to Ontong Java, Manihiki and Hikurangi plateau lavas. The Pacific-Izanagi N-MORBs are primarily sourced from a depleted MORB mantle (DMM) containing variable amounts of the focus zone (FOZO) component whereas E-MORBs indicate a DMM source containing a larger amount of FOZO plus enriched mantle I (EMI) components. Our results suggest a widespread contamination of the Pacific upper mantle by enriched heterogeneities from the source of Ontong Java, Manihiki and Hikurangi plateaus during the ca. 125-120 Ma large igneous province (LIP) building event. Subsequently, the contaminated upper

mantle was then tapped by the migrating oceanic spreading centers such as the Pacific-Izanagi ridge.

3.1. Introduction

The Pacific Plate (ca. 150 x 10^6 km^2) is the Earth's largest lithospheric plate, covering a large portion of the Earth's mantle. Pacific Jurassic ocean floor basalts (Hauff et al., 2003; Kelley et al., 2003) and the bulk of modern normal mid-ocean ridge basalts (N-MORBs: Ito et al., 1987; Gale et al., 2013) indicate that the sub-Pacific upper mantle is geochemically depleted in highly to moderately incompatible trace elements and in terms of its Sr-Nd-Hf-Pb isotopic composition. However, spatially and temporally discrete suites of ≤125 Ma oceanic basalts sampled from the Nauru and East Mariana basins (Castillo et al., 1994; Janney and Castillo, 1996) and of Mesozoic glasses from accreted pillow basalts from the Nicoya Peninsula along the Pacific coast of Costa Rica (Madrigal et al., 2016) show variable enrichment in both trace element concentrations and their Sr-Nd-Pb isotope ratios. The compositions of these slightly enriched oceanic basalts either trend toward or overlap with the composition of Pacific large igneous provinces (LIPs; Castillo et al., 1994; Janney and Castillo, 1996; Madrigal et al., 2016). Although these basalts have generally been considered typical enriched (E-) MORBs accreted along oceanic spreading centers (Castillo et al., 1991; 1994; Janney and Castillo, 1996; Madrigal et al., 2016), they may in fact be 'anomalous' as they were purportedly emplaced as sills and dikes emanating from the LIPs that intruded into pre-existing Jurassic crust (e.g., Larson and Schlanger, 1981; Saunders, 1986) and/or emplaced as accreted terranes of Pacific LIPs (Madrigal et al., 2016).

Large igneous provinces are massive magmatic features formed by short-lived, voluminous eruptions of mafic magmas generated from presumably deeper but definitely larger volumes of the underlying mantle (Larson, 1991; Coffin and Eldholm, 1992; Doubrovine et al., 2016; Svensen et al., 2017). The Pacific Plate contains a number of such massive and complex tectonic features including the Shatsky and Hess rises and the Ontong Java, Manihiki and Hikurangi plateaus. These plateaus have isotopic characteristics that are intermediate between the proposed enriched mantle (EMI), high-μ ($\mu = {}^{238}U/{}^{204}Pb$; HIMU) and focus zone (FOZO) mantle components (Zindler and Hart, 1986; Sager et al., 2016). The EMI component has high ${}^{87}Sr/{}^{86}Sr$ (ca. 0.70530), low ${}^{143}Nd/{}^{144}Nd$ (ca. 0.51236) and relatively unradiogenic ${}^{206}Pb/{}^{204}Pb$ (ca. 17.40), but high ${}^{207}Pb/{}^{204}Pb$ (≥ 15.47) for a given ${}^{206}Pb/{}^{204}Pb$ whereas HIMU has very low ${}^{87}Sr/{}^{86}Sr$ (0.7029) and high ${}^{206}Pb/{}^{204}Pb$ (>21.0) - Zindler and Hart, 1986; Hart et al., 1992; Eisele et al., 2002; Hanyu et al., 2011; Hofmann, 2013). On the other hand, FOZO, also referred to as "C" component, is common to all oceanic basalts and has radiogenic Pb (e.g., ${}^{206}Pb/{}^{204}Pb$ ca. 19.4) and unradiogenic ${}^{87}Sr/{}^{86}Sr$ (0.7030-0.7032 - Hart et al., 1992; Hanan et al., 2004; Stracke et al., 2005; Hofmann, 2013).

Although the exact provenance of the Pacific oceanic LIPs is still unresolved, paleo-plate reconstructions, temporal connections among these features and available geophysical data have indicated that they may be petrologically and tectonically related. Explanations include formation during a "superplume" (Larson, 1991; Janney and Castillo, 1996; Xue and King, 2016) or "mantle overturning" (Stein and Hofmann, 1994) event during the mid-Cretaceous at 125 - 120 Ma (Stein and Hofmann, 1994; Janney and Castillo, 1996) and by discrete pulses of mantle upwellings at 140, 120 and 90 Ma (Madrigal et al., 2016). A significant potential consequence tied to Pacific LIP formation is that the upper mantle may have been contaminated by the mantle source or sources of the LIPs, which then generated anomalous E-MORB until the ridges had moved past the contamination zone (Castillo et al., 1991; Janney and Castillo, 1996; Madrigal et al., 2016; Durkin et al., 2020).

To provide additional constraints on the effects of LIP formation on the nature of the Pacific upper mantle during the mid-Cretaceous, we focus on a suite of samples from a physically and temporally contiguous and, hence 'typical' section of the oceanic crust generated along the Pacific-Izanagi spreading center (Durkin et al., 2020). Significantly, this crustal section had been drilled at Integrated Ocean Drilling Project (IODP) Site 1149, which together with Ocean Drilling Program (ODP) Site 801, provides a geochemical reference for old Pacific MORB (e.g., Hauff et al., 2003; Kelley et al., 2003). We analyze the Hf isotopes of these samples as the Lu-Hf isotope systematics, paired with the Sm-Nd systematics, are generally less susceptible to seawater alteration than Rb-Sr and U-Th-Pb isotope systems (Cohen and O'nions, 1982; Chauvel and Blichert-Toft, 2001; Krolikowska-Ciaglo et al., 2005). Moreover, this Pacific-Izanagi transect was accreted away from the massive oceanic LIPs and, thus, is likely to provide a broader insight to the evolution of the ambient Pacific upper mantle during Pacific oceanic LIP formation.

3.1.1 Tectonic evolution of the Pacific plate

Initiation of Pacific Plate formation occurred at the Izanagi-Farallon-Phoenix triple junction roughly 190-175 Ma during a large-scale plate reorganization due to the breakup of Pangea and the cessation of subduction on the fringes of the Panthalassa Sea (Bartolini and Larson, 2001; Seton et al., 2012; Boschman and Hinsbergen, 2016). The plate grew inside a relatively stable, diverging three-ridge system that generated the Japanese (at the Pacific-Izanagi ridge striking NE-SW), Phoenix (at the Pacific-Phoenix ridge striking E-W) and Hawaiian (at the

Pacific-Farallon ridge striking NW-SE) magnetic lineation sets. At present, remnants of the Phoenix, Izanagi and Farallon plates are almost to completely subducted (Seton et al., 2012).

At ca. 147 Ma, the Shatsky Rise formed at the Pacific-Izanagi-Farallon triple junction, coinciding with the clockwise rotation of the triple junction by 24° and a resulting change in the spreading direction at the Pacific-Izanagi Ridge (Seton et al., 2012). Spreading rate, direction and accretion along the Pacific-Izanagi ridge was constant after M0 (ca. 120 Ma). The cessation of spreading occurred later (ca. 55-50 Ma) due to the complete subduction of the Izanagi Plate into the Izu-Bonin-Marianas arc system (Seton et al., 2012). The Phoenix-Pacific ridge spread in a N-S direction until a major plate reorganization at ~120 Ma, roughly coincident, but somewhat preceded by the formation of the Ontong Java, Manihiki and Hikurangi plateaus (Timm et al., 2011; Seton et al., 2012) or, perhaps, an ancestral Ontong Java-Manihiki-Nui plateau (Taylor, 2006; see also Castillo, 2004). Notably, such a massive plateau ($\sim 5 \times 10^6$ km^2; Chandler et al., 2012) represents one of the known largest volcanic constructs in the solar system, even exceeding the Olympus Mons on Mars ($\sim 3 \times 10^5$ km^2; Wu et al., 1984). The next re-organization of the plate occurred at ca. 100 Ma, as spreading slowed at the Pacific-Phoenix ridge presumably due to the break-up of the ancestral plateau (Taylor, 2006). Spreading along the Phoenix-Pacific ridge fully stopped at ca. 88 Ma, when spreading was accommodated by the Pacific-Farallon and Pacific-Antarctic ridges. This final reorganization marks the Pacific Plate’s rise to prominence and the consequent shift in terminology from the Panthalassa Sea to the modern Pacific Ocean (Seton et al., 2012).

The area of study in this work is a section of the Pacific-Izanagi crust (Fig. 3.1) with magnetic anomalies M19 to M5 (ca. 145-130 Ma Gradstein et al., 2012) from south to north. The M11 magnetic anomaly identified at IODP Site 1149 located roughly in the middle of the section

(Fig. 3.1) was initially assumed to have an age of 132 Ma (Shipboard Scientific Party, 2000), but this age is inconsistent with the results of subsequent $^{40}Ar/^{39}Ar$ investigation that gave an absolute age of 127.1±1.5 Ma (Koppers et al., 2003). The discrepancy between assumed and radiometric ages for IODP Site 1149 indicates that the crust immediately outboard of the Izu-Bonin trench can be as much as ca. 7 m.y. younger than the magnetic anomaly-based ages. That is, the samples collected from the contiguous, normal segment of Pacific-Izanagi crust likely range from ca. 138-123 Ma from south to north. Ultimately, crust to the south of the site is >127 Ma and that to the north is <127 Ma.

3.1.2 Geochemistry of the Pacific LIPs and Pacific-Izanagi transect

Pacific LIPs typically consist of several lava types, with at least one exhibiting geochemical signatures indicative of a source or sources more geochemically enriched than the upper, depleted mantle MORB (DMM) source. The major plateau-building lavas of Shatsky Rise (~148-138.5 Ma - Tominaga and Sager, 2010; Sager et al., 2016) consist of three primary types; normal, low-Ti and high-Nb basalts. Normal Shatsky Rise basalts are the most voluminous lava type and are distinguished by a slight enrichment in incompatible elements relative to N-MORB, though are isotopically similar to Pacific Mesozoic MORB (Sano et al., 2012; Heydolph et al., 2014). Lesser volume, low-Ti basalts have lower TiO_2, FeO* and MnO contents for a given MgO but are isotopically indistinct from normal Shatsky Rise basalts (Sano et al., 2012; Heydolph et al., 2014). High-Nb basalts are notable for their enrichment in incompatible elements and lower $^{143}Nd/^{144}Nd$ and $^{176}Hf/^{177}Hf$ (Sano et al., 2012). Similarly, Ontong-Java (120-125 Ma – Mahoney et al., 1993; Tejada et al., 2002) has two primary lava-types, Singgalo and Kwaimbaita lavas. Singgalo lavas have an EMI-like signature ($\varepsilon Nd = 3.7-5.3$, $^{206}Pb/^{204}Pb = 17.71-17.99$, $^{87}Sr/^{86}Sr = 0.7039-0.7044$; Tejada et al., 2002). Kwaimbaita lavas, on the other hand, show more HIMU-like geochemical characteristics (εNd = 5.4-6.4, $^{206}Pb/^{204}Pb$ = 18.21-18.42, $^{87}Sr/^{86}Sr$ = 0.7034-0.7039; Tejada et al., 2002). Manihiki Plateau (124.6 ± 1.6 Ma – Timm et al., 2011) high-Ti lavas are similar to Singgalo lavas while Hikurangi Plateau (118 ± 4.2 Ma – Hoernle et al., 2010) lavas are similar to Kwaimbaita lavas (Hoernle et al., 2010).

The Pacific-Izanagi samples considered in this study (Fig. 3.1 inset) were filtered from the Durkin et al. (2020) dataset (see discussion below) and consist primarily of basalts (n=30) and one trachybasalt based on their SiO_2 versus total alkali contents (Fig. 3.2a, large diamonds). Their rare earth element (REE) contents divide them into two groups: N-MORB with $La/Sm_N < 1.4$ and E-MORB basalts with $La/Sm_N \geq 1.4$ (normalized relative to chondrite; Sun and McDonough, 1989). The REE-determined groupings are generally consistent with major element data (Fig. 3.2). The bulk of N-MORB are tholeiitic whereas the bulk of E-MORB are alkalic and a trachybasalt. Moreover, E-MORB systematically have lower FeO* but higher K_2O/TiO_2 values for given MgO than N-MORB.

In general, the bulk of E-MORB are from north of IODP Site 1149 whereas the bulk of N-MORB are from the south. The younger (<127 Ma), northern E-MORB generally have higher $^{87}Sr/^{86}Sr$ and lower $^{208}Pb/^{204}Pb$ for a given $^{206}Pb/^{204}Pb$ (i.e. Δ8/4 - Hart, 1984) than the older (≥127 Ma), southern N-MORB (Durkin et al., 2020). Consequently, E-MORB samples generally overlap with the radiogenic Sr-Nd-Pb end of MORB values, overlapping with FOZO (Hart et al., 1992; Stracke et al., 2005). By contrast, N-MORB samples plot in the geochemically depleted end of the Sr-Nd-Pb isotopic signature of global MORB.

3.2. Methods

Masses of sample powders with the aim of obtaining at least 250 ng Hf were initially dissolved at the Scripps Institution of Oceanography according to the procedure of Münker et al.

(2001). Samples were then suspended in distilled MilliQ water and transported to Brown University for the final stage of digestion. Hafnium separation was performed at Brown University's Department of Earth, Environmental and Planetary Sciences' Mass Spectrometer Analytical Facility following a one-column procedure using EICHROM Ln-Spec resin (100-150µm, H^+ form) as in Münker et al. (2001). Hafnium isotopes were measured on a THERMO NEPTUNE PLUS MC-ICPMS also at Brown University's Department of Earth, Environmental and Planetary Sciences' Mass Spectrometer Analytical Facility following DeFelice et al. (2019). Briefly, samples were introduced using an APEX-IR and a ~77 µl/min PFA nebulizer. The instrument was equipped with an H-sampler and an H-skimmer cone. $^{176}Hf/^{177}Hf$ was corrected for instrumental mass fractionation using an exponential law and an $^{179}Hf/^{177}Hf = 0.7325$. Reproducibility is monitored measuring Hf standard JMC 475 and an in-house standard solution purchased from High Purity Solution (HPS). JMC 475 (n=6) was measured with a $^{176}Hf/^{177}Hf = 0.282159\pm6$ (2σ), in agreement with Salters et al. (2011), and HPS was measured with $^{176}Hf/^{177}Hf = 0.282212 \pm6$ (2σ). Geochemical reference material BHVO-2 and BCR-2 were also processed along with the samples and yielded values that are in agreement with values from Bizzarro et al. (2003) and Khanna et al. (2014) (Table 3.1). Total procedural blank for Hf is < 30 pg.

The Pacific-Izanagi samples were first analyzed with an intent to study geochemical cycling in the Izu-Bonin arc (Durkin et al., 2020). As such, they were not subjected to a harsh leaching procedure to attempt to account for alteration (cf., Weis and Frey, 1991; Finlayson et al., 2018). As our new Hf isotope analyses will be combined with other geochemical and isotopic data to constrain the mantle source of the mid-Cretaceous oceanic crust accreted along the Pacific-Izanagi Ridge, it is necessary to first eliminate, or at least mitigate, the effects of alteration on the existing geochemical data. Noting that E-MORB have higher volatile contents than N-MORB (Sisson and Layne, 1993; Cervantes and Wallace, 2003), we excluded samples with LOI >5 wt.% to eliminate strongly altered samples. Additionally, we retained only those samples with MgO >5 wt.% to exclude fractionated samples. We also tried to limit the effects of fractionation by modeling illustrative liquid lines of descent (LLDs) for the samples using Petrolog3 (Fig. 3.2c and 2d; Danyushevsky and Plechov, 2011) and, then, recalculating their major element compositions to 8 wt% MgO. However, we deciphered that the fractionation-correction procedure is inappropriate particularly for E-MORBs as no reasonable LLDs suitably capture the full diversity of their major element compositions. As such, we report major oxides corrected to 8 wt% MgO in the Supplementary Material for the interested reader. However, our data interpretation below primarily uses raw major element data for only those samples with MgO >5 wt.%.

We also apply the above major element data filtering procedure to samples from IODP, ODP and Deep-Sea Drilling Project (DSDP) drill sites throughout the Pacific (i.e. DSDP 166, 196, 197, 303, 304, 307, 462; IODP 1149; ODP 801C, 802) and Pacific LIPs. Moreover, all Hf, Sr, Nd, and Pb isotope ratios used in the discussion are age-corrected for radiogenic in-growth since eruption at ca.125 Ma using sample parent/daughter element data.

3.3. Results

Measured Hf isotope ratios show a range of values (^{176}Hf/^{177}Hf = 0.283026-0.282816; εHf=5.6–13.3; Table 3.1). The range of ^{176}Hf/^{177}Hf values within individual dredge sites varies. Some sites have homogeneous values (e.g., D19) whereas several sites show a large range in values (e.g., D21, D16 and D13). The highest measured ^{176}Hf/^{177}Hf ratio is from D8-2 whereas D7-1 has the lowest ratio.

In general, age-corrected Hf isotopes correlate well with age-corrected Nd isotopes (εNd_I = 2.2–6.8; Durkin et al., 2020), and their values fall on or slightly below the terrestrial Hf-Nd array (Vervoort et al., 1999; Fig. 3.3a). Global MORB values on average have slightly higher εHf for given εNd in comparison to our samples, which are similar to Pacific MORB values (Mallick et al., 2019). Two E-MORB samples (i.e. D19-1 and D19-2) have relatively higher εHf for given εNd relative to other E-MORB samples. Another sample, D16-5, has low εNd_I for a given εHf_I. The good correlation (R_2= 0.833) between the Hf and Nd isotopes in our samples (excluding D16-5, D19-1 and 19-2) and their close association with the canonical terrestrial Hf-Nd array (Vervoort et al., 1999) indicate that both isotope systematics were not significantly affected by seawater alteration and may indeed act as a powerful tracer of the source and history of the Pacific-Izanagi oceanic crust.

The parameter ΔεHf in Figure 3.3b is a measure of the vertical offset of a given sample from the Hf-Nd terrestrial array that can be used to quantitatively differentiate HIMU from the other proposed mantle end-member sources (Carpentier et al., 2009; Nebel et al., 2013). By pairing ΔεHf with $_{207}$Pb/$_{206}$Pb, HIMU's low ΔεHf and low $_{207}$Pb/$_{206}$Pb can be isolated *sensu stricto* from other oceanic basalt (Nebel et al., 2013). Significantly, aside from the aforementioned samples D19-1 and D19-2, all Pacific-Izanagi samples plus the majority of Pacific oceanic lavas do not have a HIMU signature. Moreover, although D19-1 and D19-2 plot in the HIMU field, as mentioned earlier they have higher εHf for given εNd or higher ΔεHf than the other E-MORBs and, thus, their HIMU signature is suspect. Figure 3.3c shows age-corrected $_{176}$Hf/$_{177}$Hf$_I$ vs Nd/Hf for Pacific-Izanagi basalts, Pacific LIPs and Pacific and global MORB. The bulk of Pacific-Izanagi samples fall within global MORB Nd/Hf values with the exception of a number of N-MORB with low (≤ 3) Nd/Hf and sample D16-5 with high Nd/Hf (18). In general, N-MORB samples have Nd/Hf <4, similar to global MORB and the plateau-building Shatsky Rise lavas.

Sample D16-5 shows inconsistent behavior in its chemical and Sr-Nd-Pb isotope compositions (Durkin et al., 2020). In particular, D16-5 has <5% MgO content and exhibits a significant fractionation of its Nd/Hf value. Furthermore, D16-5 has elevated $^{87}Sr/^{86}S_I$ relative to $^{143}Nd/^{144}Nd_I$ and $^{206}Pb/^{204}Pb_I$ values (Table 3.1; Durkin et al., 2020) which is a sign of seawater alteration. Thus, D16-5 will no longer be included in the discussion.

3.4. Discussion

3.4.1. Pacific-Izanagi crust in relation to Mesozoic Pacific oceanic lavas

In general, Pacific-Izanagi N-MORB samples have trace element compositions akin to >125 Ma geochemical reference samples from IODP Site 1149 and ODP Site 801 and samples from DSDP sites 166, 197, 303, 304 and 307 and ODP Site 1179 whereas E-MORB samples are more similar to measurements from <125 Ma samples from DSDP 169 and 462 and IODP 802. For example, Figure 3.4a shows the relative enrichment of the Pacific-Izanagi samples relative to global MORB and crustal lavas from DSDP and (I)ODP drill sites. Global MORB Th/La versus Sm/La forms a coherent negative linear trend ($R^2 = 0.620$). The Pacific-Izanagi N- and E-MORB generally plot within this trend but are clearly distinct from each other: N-MORB characteristically have higher Sm/La and lower Th/La ratios than E-MORB, which in turn overlap with a typical OIB value (Sun and McDonough, 1989). A somewhat similar relationship is shown by other Pacific oceanic lavas, with ≤125 Ma crustal lavas having intermediate Th/La and Sm/La values that are systematically higher and lower (average Th/La of Ontong Java = 0.09; Manihiki = 0.11; Hikurangi = 0.16), respectively, than those values in ≥125 Ma crustal lavas (average Shatsky Rise Th/La = 0.06). A similar distinction between the different sample groups can also be seen in Figure 3.4b. Both the Pacific-Izanagi basalts and global MORB form a tight linear array, due to the similarly incompatible behavior of Th and Nb relative to Yb and the resistance to submarine alteration of these elements (Pearce, 2008). Normal-MORB samples, however, have low Nb/Yb and Th/Yb ratios in comparison to E-MORB. Again, the Pacific drill site samples also show a systematic difference, with the Nb/Yb and Th/Yb values of ≤125 Ma lavas higher than those of ≥125 Ma lavas. Similarly, Shatsky Rise basalts form an array that encompasses the low Nb/Yb and Th/Yb up to intermediate values, while Ontong Java and Manhihiki Plateau data range from the intermediate to higher Nb/Yb and Th/Yb. While melting in the presence of garnet in deeper/high pressure conditions can increase Nb/Yb and Th/Yb due to the higher affinity of Yb in garnet (Shimizu and Kushiro, 1975), garnet would not cause similar fractionation of Th/La or Sm/La as shown in Figure 3.4a and the differences in their isotopic compositions (Figs. 3.3 and 3.5).

Pacific-Izanagi N-MORB and E-MORB samples also generally separate into depleted and enriched clusters not only in terms of Hf and Nd isotopes (Fig. 3.3), but in Pb isotopes as well (Fig. 3.5). Specifically, the $^{143}Nd/^{144}Nd_I$ of E-MORB samples are on average respectively lower and higher than those of N-MORB, which plot closer to the proposed DMM source (Fig. 3.5a). The same is true for <125 Ma crustal lavas as well as for Ontong Java, Manihiki and Hikurangi plateau lavas relative to >125 Ma crustal lavas. The ca. 140 Ma Shatsky Rise lavas also plot with the Pacific-Izanagi N-MORB and ≥125 Ma oceanic lavas. The Pacific-Izanagi E-MORB samples and <125 Ma crustal and plateau lavas, on average, also have lower $^{176}Hf/^{177}Hf_I$ and higher $^{208}Pb/^{204}Pb_I$ values than the N-MORB samples and >125 Ma lavas, which again plot closer to DMM (Fig. 3.5b). The Shatsky Rise lavas again plot with the Pacific MORB and Pacific-Izanagi N-MORB samples.

In summary, the trace element and Hf-Nd-Pb isotope geochemistry of the temporally and physically contiguous section of the Pacific-Izanagi oceanic crust (see also, Durkin et al., 2020) provide further evidence of the aforementioned compositional shift in Pacific oceanic lavas ca. 125 Ma (Castillo et al., 1994; Janney and Castillo, 1996, 1997; Madrigal et al., 2016). That is, the Pacific-Izanagi N-MORB samples have geochemically depleted incompatible trace element and Hf-Nd-Pb isotope signatures similar to that of the ≥125 Ma Late Jurassic to Early Cretaceous Pacific crust and ca. 140 Ma plateau-building Shatsky Rise lavas. In comparison, the E-MORB samples have the trace element and Hf-Nd-Pb isotope signature that is akin to that of ≤125 Ma Late-Early Cretaceous lavas and Ontong Java-Manihiki-Hikurangi plateau lavas.

3.4.2. An enriched and depleted source in the Mesozoic Pacific upper mantle

When considering the geochemistry and mantle source of the Mesozoic lavas from the Pacific-Izanagi transect, DSDP/(I)ODP drill sites and Pacific LIPs, it is critical to consider whether their compositional variations are a result of primary magmatic or secondary processes on melts coming from a common source instead of due to different sources. Secondary processes (i.e. seawater alteration) would cause enhancement and/or unusually large variations in their aqueous fluid-mobile major and trace element values such as K_2O, Rb, Ba, and Pb (e.g., Staudigel et al., 1996; Staudigel, 2003). While the Pacific-Izanagi samples are variably altered, we primarily focus our prior discussion (Section 4.1) on aqueous fluid immobile elements such as Th, Yb, Nb, and REE as these elements are less susceptible to seawater alteration (Fig. 3.4). The comparably consistent behavior of our Pacific-Izanagi trace element data with global MORB and other old Pacific oceanic lavas suggests that our interpretations regarding the similarities and differences of the different sample suites are generally independent of the effects of seawater alteration. Moreover, the overall colinearity of the Nd and Hf isotopes with terrestrial samples

(Fig. 3.3a) also indicate that their signals are coming from their mantle source. Although Pb is mobile during seawater alteration, the clear coherence of their isotopes with alteration-resistant Nd and Hf (Fig. 3.5) also indicates that the bulk of Pb isotopes were also not affected by seawater alteration. Ultimately, the Nd-Hf-Pb isotope systematics clearly indicate two separate enriched and depleted sources.

Although our LOI- and MgO-filtered AOC samples are not primitive enough to be considered primary melts that are in equilibrium with the mantle (i.e. with >7 wt.% MgO; Wilkinson, 1982), the E-MORB samples are slightly more primitive than the N-MORB samples. If higher alkaline content of the E-MORB basalts is an artifact of fractional crystallization, we expect to see them with systematically higher SiO_2 values in Figure 3.2a. However, the E-MORB samples have similar or lower SiO_2 content than N-MORB (Fig. 3.2a). Thus, fractional crystallization is not likely a primary process that caused the compositional difference between the E-MORB and N-MORB Pacific-Izanagi samples.

Assuming a common source, variations in the fraction and/or depth of melting are another possibility that could generate the compositional differences between the Pacific-Izanagi N-MORB and E-MORB. For example, it is possible to interpret E-MORB elemental enrichment globally as a result of a smaller degree of partial melting of the same source of global N-MORB basalts. A smaller fraction of melting predicts elevated concentrations of Na_2O, TiO_2, and Al_2O_3, and correspondingly lower SiO_2 if melting is isobaric, or higher SiO_2 and lower FeO if the extent of melting relates to the length of the melting column (Langmuir et al., 1992). Our E-MORB samples conformingly exhibit lower FeO* (Fig. 3.2c) and higher Al_2O_3 for a given MgO, relative to our N-MORB samples. However, our E-MORB also demonstrate both comparable or lower SiO_2 (Fig. 3.2a) and lower Na_2O for a given MgO, contrary to the predictions of variable melting fractions. Hydrous melting of the mantle can also affect the extent of melting, and thus the composition of primary melts: water has the effect of promoting low-*F* melting in the deep “wings” of the sub-ridge melting regime. This will lead to greater total melting, but lower the mean extent of melting, thus leading to higher FeO, Na_2O, and Al_2O_3. However, our E-MORB samples have lower FeO* for a given MgO relative to N-MORB (Fig. 3.2c). These major element systematics argue against variable degrees of melting of a homogeneous source as the origin of the geochemical differences observed in our <127 Ma E-MORB samples.

Different source compositions for the N-MORB and E-MORB samples, on the other hand, are consistent with both major and trace element data. Enriched-MORB do not fall along the calculated N-MORB LLD, clearly indicating that the two groups do not have a common magmatic evolutionary history (Fig. 3.2c and 3.2d). While acknowledging the substantial difficulties in attaining reliable K_2O values in highly altered samples, E-MORB samples show a consistently higher K_2O/TiO_2 ratio than N-MORB, suggesting a distinctly more enriched parental melt given the insensitivity of K_2O/TiO_2 to fractional crystallization (Fig. 3.2d). Moreover, Figure 3.4a clearly indicates that, similar to global MORB, the Pacific-Izanagi basalts show a negative linear trend in Th/La versus Sm/La, which is consistent with mixing between depleted and enriched components in the upper mantle instead of following a partial melting trend (Gale et al., 2011). That is, although a number of E-MORBs with high Th/La and low Sm/La ratios could be generated through a low degree (0.1-0.2%) of partial melting of a fertilized or enriched mantle, and some N-MORB basalts with low Th/La and high Sm/La ratios could be generated by higher degree (>1%) of partial melting of the same source, the remaining samples do not lie along the partial melting curves. Clearly, a second later mantle-melt mixing process would be required to explain their linear array. As a hypothetical scenario, Figure 3.4a shows that a 0.5% melt from the depleted mantle could self-fertilize the mantle which, in a second stage melting event, can produce the enriched Th/La. However, again, the required degrees of melting are smaller than the typical range of melting (5-20%) in a mid-ocean ridge setting (Langmuir et al., 1992).

A more convincing argument for the different mantle sources for Pacific-Izanagi N- and E-MORB is their generally different Hf-Nd (Fig. 3.3) and Hf-Pb-Nd isotopic signatures (Fig. 3.5; see also, Durkin et al., 2020). The isotopic signature of E-MORB generally overlaps with global N-MORB and FOZO (Hart et al., 1992; Stracke et al., 2005). Mixing between FOZO and DMM is unsurprising since FOZO represents a well-mixed or common source component for both OIB and MORB (Hanan and Graham, 1996; Castillo, 2017). Moreover, the significant correlation between the Hf and Nd isotopes in the Pacific-Izanagi samples suggests that their isotopic variability is strongly controlled by mixing between two components. The N-MORB samples generally have a lesser amount of a FOZO contaminant (up to ~30% FOZO) and are within both Shatsky Rise and global MORB values. In comparison, E-MORB samples represent a ternary mixture between DMM:FOZO:EMI. Samples have a higher FOZO content (up to ~70%) in a DMM:FOZO mix or up to 70% mixing with a 20:80 EMI:FOZO mix (Fig. 3.5). The difference in Hf-Nd-Pb isotope ratios of the two basalt groups is significant because it helps to identify more than one mantle source for Pacific-Izanagi crust. That is, rather than successively generating discreet high and low degree partial melts from a common mantle source and, later mixing the melts to generate the entire sample suite (Fig. 3.4a), the isotopic difference indicates that the upper mantle source of the samples became relatively more geochemically enriched with decreasing age.

Consequently, a source of this enrichment would be contamination by a deeper, plume-like source, similar to proposed formation models of Pacific LIPs. Our data show that contamination by Pacific LIP sources is possible given the similar isotope ratios between Pacific-Izanagi N-MORB basalts and the Late Jurassic to Early Cretaceous (>125 Ma) basalts at DSDP Sites 166, 197, 303, 304 and 307 and (I)ODP 801, 1149 and 1179 and plateau-building Shatsky Rise lavas. Furthermore, E-MORB samples are compositionally similar, and therefore potentially related, to <125 Ma mid-Cretaceous Pacific oceanic crust at DSDP 196, 462 and ODP 802 as well as Ontong Java, Manihiki and Hikurangi plateau lavas.

3.4.3. The mantle sources of Pacific LIPs

A majority of formation models for Pacific LIPs gravitate toward a deeper or mantle plume origin indicating a source or sources more geochemically enriched and isotopically more radiogenic than DMM. As is typical in petrologic studies of oceanic basalts, the compositions of Pacific LIP mantle sources are described in terms of mantle plume end-members (e.g., Zindler and Hart, 1986; Wilson, 1989; Hofmann, 2013). The similarity of the E-MORB and Pacific LIP isotopic ratios potentially indicate a direct, contaminative LIP influence on the upper mantle that ultimately produced the Pacific-Izangi E-MORB. The question now becomes, was the generation of E-MORB related to mantle plume activities and, if so, which mantle end-members contributed to the enriched mantle source of the Pacific LIPs, and thus the Pacific-Izanagi E-MORB samples and Pacific ≤125 Ma oceanic crust in general?

Janney and Castillo (1997) proposed that the change in trace element geochemistry of oceanic crust produced <125 Ma was influenced by an enriched mantle whereas Madrigal et al. (2016) suggested that Pacific LIPs exhibit a mixed DMM+HIMU mantle signature. Some Mesozoic Pacific oceanic basalts have been attributed to a HIMU mantle source because they have highly radiogenic $^{206}Pb/^{204}Pb$ isotopic ratios. For example, the radiogenic (e.g., $^{206}Pb/^{204}Pb$ = 19.4 – 20.5) nature of the Pacific Mesozoic oceanic lavas are consistently indicated in leached (e.g., Janney and Castillo, 1996; Hauff et al., 2003) and unleached (e.g., Tejada et al., 2004) samples. However, this feature cannot be unequivocally qualified as the Mesozoic oceanic lavas are variably altered. For the same reason, the characteristically low $^{87}Sr/^{86}Sr$ of HIMU cannot be constrained with certainty in these Mesozoic lavas. On the other hand, the radiogenic Pb isotopic signatures of many oceanic lavas are within the range of the FOZO component, which is also described as "young HIMU" (Vidal, 1992; Stracke et al., 2005; Castillo, 2015, 2017). Significantly, a FOZO contribution to our Pacific-Izanagi crust – particularly the E-MORB samples and Pacific oceanic LIPs – is indeed indicated in both Hf-Pb and Nd-Pb isotope spaces (Fig. 3.5).

Furthermore, Figure 3.3 shows that HIMU as a primary mantle end-member source for Pacific Mesozoic LIPS is suspect. Oceanic basalts from Saint Helena and a few Cook-Austral islands with an archetypal HIMU signature trend tangentially below the Hf-Nd mantle array (Fig. 3.3a; Nebel et al., 2013; Castillo, 2017). Nearly all Pacific LIP samples do not possess a HIMU Hf-Pb isotopic signature (Fig. 3.3b). Thus, the Pacific plateaus are more FOZO-like. As a result, since HIMU is not primarily responsible in the generation of the bulk of mid-Cretaceous Pacific LIPs, it should not be a major contaminating mantle end-member for Pacific crustal samples. This is consistent with our data as our Pacific-Izanagi basalts and available Mesozoic western Pacific data trend towards FOZO rather than HIMU.

We propose that the bulk of Mesozoic Pacific LIPs, specifically the Ontong Java, Manihiki and Hikurangi plateaus, mainly come from a FOZO or a mixed FOZO-EMI mantle source (see also, Sager et al., 2016). Shatsky Rise lavas are compositionally more akin to typical or depleted N-MORB derived from DMM variably influenced by FOZO (Hanan and Graham, 1996; Castillo, 2015; 2017) whereas Ontong-Java, Manihiki and Hikurangi Plateaus represent a DMM:EMI:FOZO ternary mixture. Significantly, Pacific oceanic crust of a similar age to Shatsky Rise or Ontong Java bear similar geochemical signatures, respectively.

3.4.4. Implications to the evolution of the Pacific upper mantle during the Mesozoic

While the observed association between enriched Mesozoic Pacific crust with Pacific LIPs is not new, the methods invoked to illustrate such an association vary (Janney and Castillo, 1996, 1997; Madrigal et al., 2016). Using drill core data, Janney and Castillo (1997) suggested a single large phase of enrichment occurred at ca. 125 Ma, based on the then published ages of the massive eruptions that formed separate Ontong Java, Manihiki and Hikurangi plateaus. On the other hand, Madrigal et al. (2016) created a kinematic model that traces the occurrence of Pacific LIPs to several pulses of mantle upwelling activity when the edge of the Pacific LLSVP coincides with a MOR. The pulses occurred at 140 Ma, 120 Ma and 90 Ma coinciding with the formation of Shatsky Rise, Ontong Java and the Caribbean LIP, respectively (Fig 3.6).

The 140 Ma volcanic pulse is roughly consistent with the radiometric ages for Shatsky Rise (144.6 ±0.8 Ma; Mahoney et al., 2005). However, the 120 Ma pulse is slightly young for the established age data associated with the earliest formation of Ontong Java and Manihiki and Hikurangi Plateaus and/or their ancestral plateau. Ontong Java, in particular radiometric ages ranging from 125 to 120 (Mahoney et al., 1993; Tejada et al., 2002) but also as early as 129 Ma (Tejada et al., 2002). As a result, if we consider the eruption of Ontong Java, Manihiki and Hikurangi plateaus as a singular event, the timing of the enrichment or contamination event described by Janney and Castillo (1997) is more consistent with the age range data. Furthermore, as the Pacific-Izanagi transect offers insight into the timing of this enrichment as it likely ranges from 138-123 Ma (Durkin et al., 2020) based on the offset magnetic anomaly and radiometric ages at IODP 1149 (Section 2.2). Consequently, the transect overlaps with the transition between the 140 Ma and the early stages of the 125-120 Ma pulse, thus illuminating the contamination effects of LIP formation on the Pacific upper mantle between these two pulses of massive volcanism. However, since the only radiometric age in this transect is IODP 1149, we can only argue that a contamination event of the Pacific upper mantle occurred after 127 Ma, most likely between 125 Ma and 120 Ma.

Plume-ridge interactions have been well-documented from both geochemical and geophysical perspectives (Asimow et al., 2004; Whittaker et al., 2015; Mittal and Richards, 2017; Yang et al., 2017). Geochemical effects of plume-ridge interaction range from trace-element to isotopic enrichment (i.e. E-MORB along spreading ridges adjacent to e.g., Iceland, Galapagos and Crozet plumes; e.g., Wilson, 1989). For instance, the Iceland hotspot and the Reykjanes ridge show degrees of plume influence ranging from 5-15° latitude (~1500km) in a smooth geochemical gradient away from the Iceland hotspot. While global E-MORB are commonly found in ridges adjacent to active mantle plumes, they have also been found independent from hotspot influences (e.g. Langmuir et al., 1986; Donnelly et al., 2004). Such E-MORB may have come from enriched heterogeneities in the otherwise depleted upper mantle (e.g., Zindler et al., 1984; Graham et al., 1992).

The similarity of Pacific-Izanagi N-MORB and Shatsky Rise trace element and isotopic data may suggest that the 140 Ma magmatic pulse proposed by Madrigal et al. (2016) may have indeed contaminated the Pacific upper mantle at and/or shortly after this time. However, the degree of contamination is difficult to assess given the lack of Pacific Jurassic oceanic crust data to establish a pre-140 Ma geochemical baseline. More important, the composition of the bulk Shatsky Rise lavas and Pacific-Izanagi N-MORB fall within the range of global MORB and >125 Ma Pacific MORB. Thus, although the formation of Shatsky Rise is clearly associated with a massive outpouring of mafic magmas from the upper mantle with some geochemical evidence of an enriched mantle source, such magmas do not indicate a major contribution from a deep mantle source. The geochemical similarity between the <127 Ma Pacific-Izanagi E-MORB and the Ontong Java, Manihiki and Hikurangi Plateaus is much more indicative of a contamination from a deeper mantle source. These enriched mantle heterogeneities coming from FOZO and EM1 mantle components must have been in the upper mantle at the time of E-MORB sample formation.

In summary, although mantle plume influence may be typically manifested in the geochemistry of the oceanic crust smoothly and systematically away from discreet plume locations, alternatively it could be manifested by the presence of relatively more enriched heterogeneities in the upper mantle especially if the sphere of plume influence is very large. The latter scenario is what we propose to explain the preponderance of E-MORB in the younger section of the Pacific-Izanagi crust. That is, the massive mantle event that formed the Ontong Java, Manihiki and Hikurangi plateaus contaminated a wider region of the Pacific upper mantle than previously thought through a widespread distribution of enriched heterogeneities that, in turn, resulted in the accretion of more abundant E-MORB in a relatively wide region in the mid-Cretaceous Pacific.

3.5. Conclusions

Despite the variably altered state of the Pacific-Izanagi crust, our new ^{176}Hf/^{177}Hf measurements, together with published major, trace element and Sr-Nd-Pb data (Durkin et al.,

2020) and in conjunction with available similar data for Pacific LIPs and other Mesozoic crusts, provide unambiguous evidence for a shift from a geochemically depleted to enriched signature of the Pacific upper mantle after 127 Ma. Our results show a compositional relationship among Pacific-Izanagi N-MORBs, Pacific oceanic crust older than 125 Ma and the plateau-building Shatsky Rise lavas and among Pacific-Izanagi E-MORBs, oceanic crust younger than 125 Ma and Ontong Java, Manihiki and Hikurangi Plateaus. This suggests that the Pacific upper mantle experienced contamination by a FOZO and/or a mixed FOZO:EMI source, thus providing unequivocal evidence for a widespread plume influence or contamination of the Pacific upper mantle at 125 – 120 Ma. This conclusion is based on several key findings:

- Pacific-Izanagi basalts ≥127Ma and similarly aged Pacific oceanic crust are dominated by upper mantle compositions, exhibiting typical N-MORB geochemical pattern in their alteration resistant trace element concentrations and Hf-Nd-Pb isotope signatures. In contrast, portions of <127 Ma crust is dominated by more enriched in incompatible trace elements and have more radiogenic isotope ratios.
- The older N-MORB samples are typical Pacific N-MORB and geochemically akin to the 140 Ma Shatsky Rise whereas the younger E-MORB samples indicate a stronger compositional relationship with Ontong-Java, Manihiki and Hikurangi Plateaus and <125 Ma oceanic lavas.
- Pacific oceanic lavas produced before 125 Ma lie primarily between DMM and FOZO whereas enriched <127 Ma lavas fall on a mixing line between DMM and FOZO or a 0-20% FOZO-EMI mixture.
- Available data also affirm that the HIMU end member was not a major source component for mid-Cretaceous LIPs.

3.S1. Supplemental Information

This appendix provides our calculations and description of our shallow-level fractionation corrections to 8 wt% MgO. We provide a full description of input parameters used to calculate the comparative and illustrative liquid lines of descent for both the Pacific-Izanagi transect basalts and Global MORB (Figure 3.2c and 3.2d in the text) using Petrolog3 (Danyushevsky and Plechov, 2011). We compose a table of the polynomial regression slopes for that were used in our correction following the methods of Niu and Batiza (1991). The attached data set includes the fractionation-corrected values for Pacific-Izanagi samples, LLD outputs and an filtered global MORB dataset from Gale et al. (2013) filtered as in the main text.

Text S1.

We calculate for shallow-level fractionation using the polynomial regression calculation by (Niu, 1992):

$$Oxide_8 = oxide_{meas} + m_1(64 - MgO_{meas}^2) + m_2(8 - MgO_{meas})$$

Liquid lines of descent (LLDs) were calculated using Petrolog3 (Danyushevsky and Plechov, 2011) using the FMQ redox buffer and mineral partition coefficients for olivine, plagioclase and clinopyroxene (Langmuir et al., 1992).

In the case of Pacific-Izanagi basalts, we used the our highest MgO-content sample (D8-4) as our input. Based on the mineral modes of the assumed starting mantle, the oxide values were slightly shifted, but remain mostly constant from this starting point. Output from our Petrolog3 run is provided in Table 3.S2. We then used polynomial regressions of the LLD various oxides against MgO to isolate the slopes to make our shallow-level fractionation corrections.

In the case of Global MORB, we used the Petrolog3 default settings with the parameters described above to calculate purely illustrative and qualitative LLD for reference in Figures 3.2c and 2d. Output from our Petrolog3 run is provided in Table 3.S2.

Acknowledgements

This work was funded by National Science Foundation grants (NSF-1333698) to P. Castillo and (NSF-1333235) to S. Straub. We also thank Emily Chin for her advice and time in the preparation of this manuscript and its data. All authors certify that there are no financial conflicts of interest related to this work and our results. All data are available in the text and Supporting Information.

Chapter 3, in full, is a reproduction of material that is in preparation for submission to Geochemistry, Geophysics, Geosystems as Durkin, K., Castillo, P.R., Straub, S.M., Mallick, S., Saal, A., Muller, J. K., Widespread contamination of the Pacific upper mantle during the Mid-Cretaceous. The dissertation author was the primary investigator and author of this work.

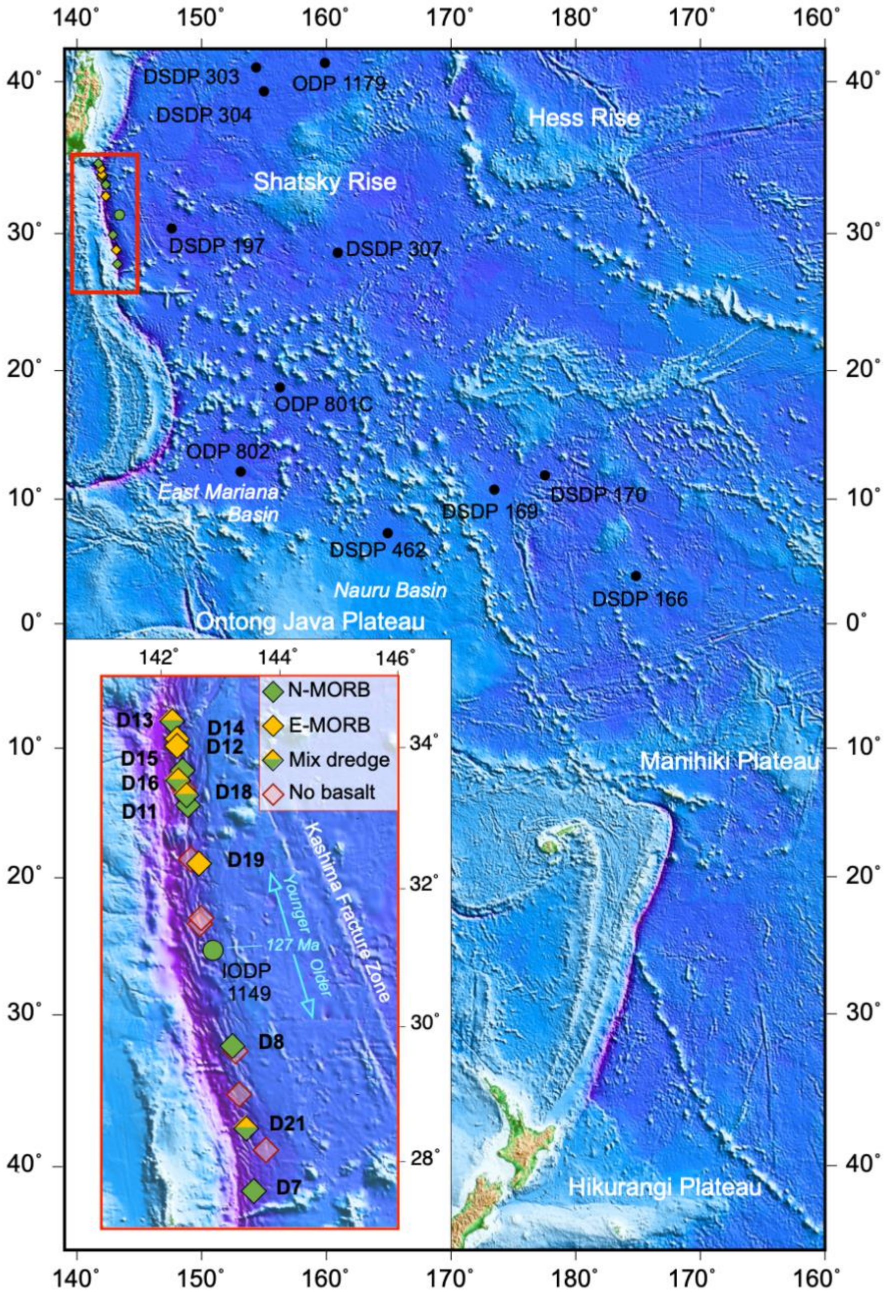

Figure 3.1: Map of the northwestern Pacific showing the dredging locations during the RR1412 cruise aboard R/V *Roger Revelle* in 2014. Dredging sites are represented by colored diamonds. IODP 1149 as a green circle with black outline in inset. Other cited (I)ODP and DSDP sites cited in the text are represented by black circles and labeled accordingly.

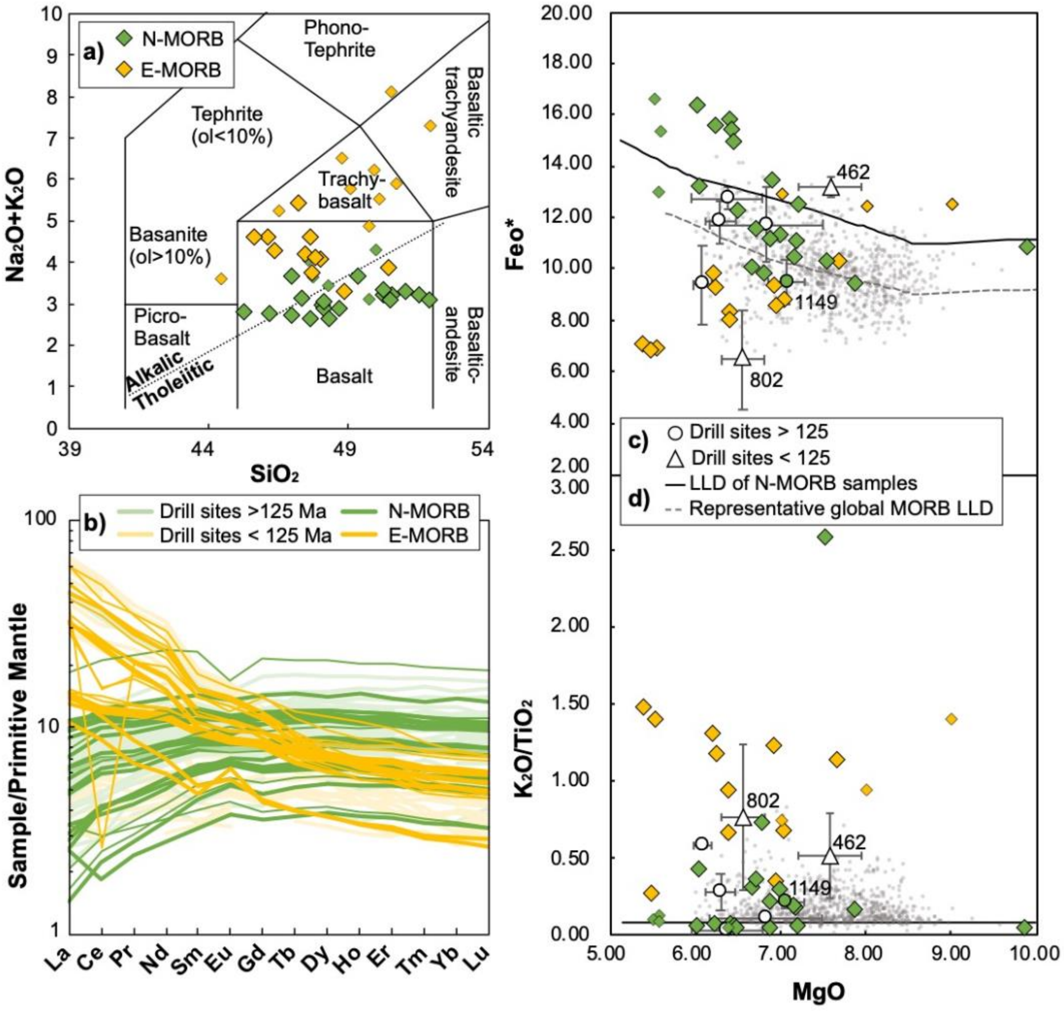

Figure 3.2: a) $Na_2O + K_2O$ versus SiO_2 of samples (after Le Bas et al., 1986). Alkaline-tholeiite line as in Macdonald and Katsura (1964). Small green and yellow diamonds show samples with isotope ratios that did not meet our filtering criteria described in the Methods section. b) Normal-MORB normalized REE concentration diagrams for dredged Pacific-Izanagi samples illustrating the classification of samples as N-MORB and E-MORB (data from Durkin et al., 2020; normalizing values from Sun and McDonough, 1989). Thin lines show samples with isotope ratios that did not meet our filtering criteria as in 2A. c) FeO* versus MgO diagram. Global MORB as gray circles (data from Gale et al., 2013). Calculated LLD for shallow level fractionation for AOC samples and drill sites as solid black line. Calculated LLD for global MORB as dashed gray line. Average DSDP sites 166, 197, 303, 304 and 307 and IODP 1179 data are represented by open circles with 1SD error bars (Janney and Castillo, 1997; Hauff et al., 2003; Mahoney et al., 2005; Heydolph et al., 2014). IODP 1149 as green-filled circle with 1SD error bar. IODP Site 802 and DSDP sites 169 and 462 data are open triangles with 1SD error bars (Batiza et al., 1980; Floyd et al., 1992; Castillo, 2004). d) K_2O/TiO_2 versus MgO diagram.

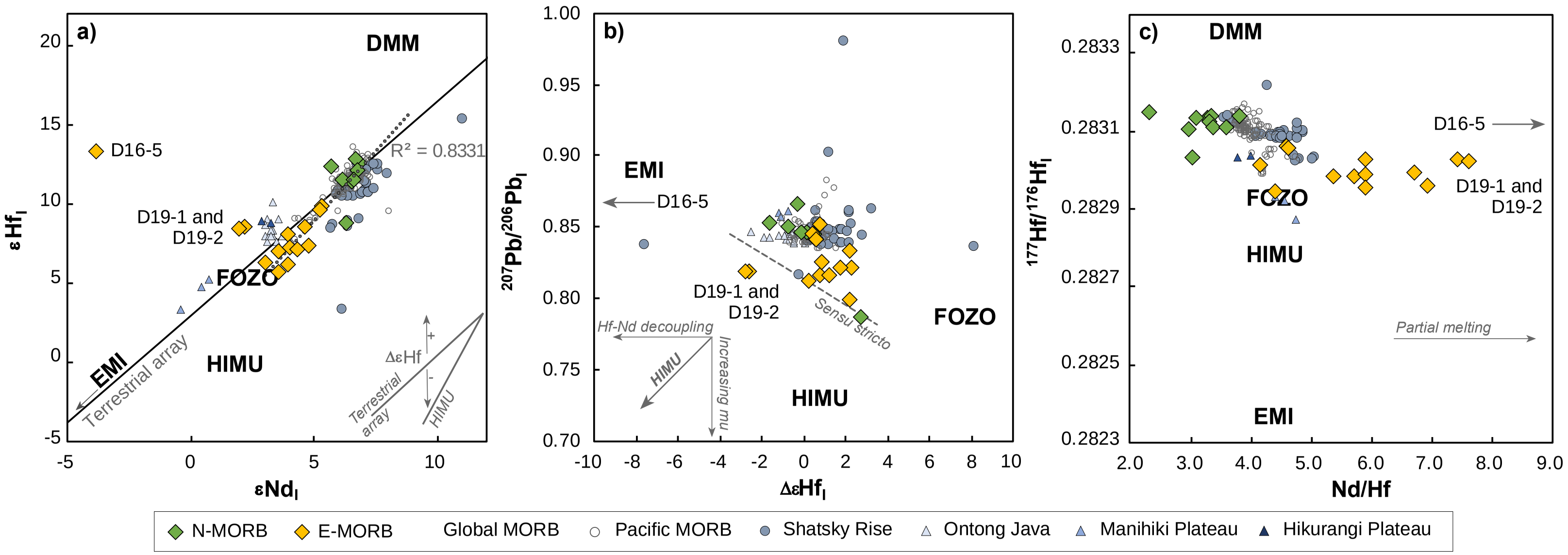

Figure 3.3: ε Hf_I versus ε Nd_I for Pacific-Izanagi samples, Pacific MORB, global MORB, Shatsky Rise, Ontong Java, Manihiki Plateau and Hikurangi Plateau. Terrestrial array is from Vervoort et al. (1999). Inset shows HIMU deviation from mantle-terrestrial array ($\Delta\varepsilon_{Hf} = (1.36*\varepsilon_{Nd}+2.95)-\varepsilon_{Hf}$). b) $\Delta\varepsilon$ Hf_I versus $^{207}Pb/^{206}Pb_I$. The *sensu stricto* line marks the distinction between HIMU and other mantle end-members as a result of the deviation from the terrestrial-mantle Nd-Hf isotope array. Inset illustrates fractionation on the x-axis is due to $\varepsilon_{Hf}-\varepsilon_{Nd}$ decoupling, whereas $^{207}Pb/^{206}Pb_I$ decoupling is a result of increasing μ (after Nebel et al., 2013). c) $^{176}Hf/^{177}Hf_I$ versus Nd/Hf. Mantle end-members represent sources rather than melts and are included for reference. Normal MORB and E-MORB as in Figure 2. Pacific MORB as open dark gray circles (data from Mallick et al., 2019), global MORB as in Figure 2. Shatsky Rise, Manihiki Plateau and Ontong Java plateau data from GEOROC and references therein. Also shown are DMM, FOZO, HIMU and EMI for reference (Stracke et al., 2005; Workman and Hart, 2005; Gale et al., 2013)

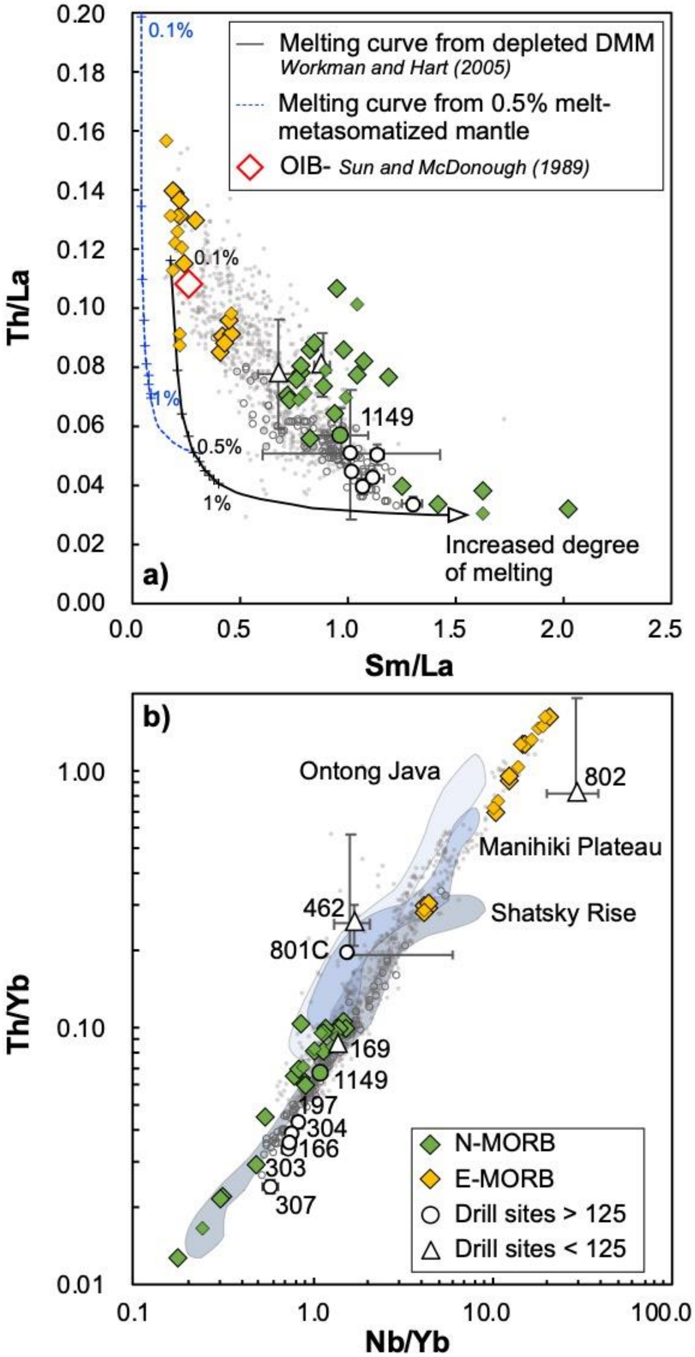

Figure 3.4: a) Th/La versus Sm/La diagram for Pacific-Izanagi samples. Typical OIB as open red diamond (Sun and McDonough, 1989). Batch melting model as black line. Blue dashed line illustrates a batch melt of a hypothetical metasomatized mantle made of a 80:20 ratioed mix between DMM and a 0.5% DMM melt. Model parameters are given in Table 3.2. b) Th/Yb versus Nb/Yb diagram. Data as in Figures 3.2 and 3.3.

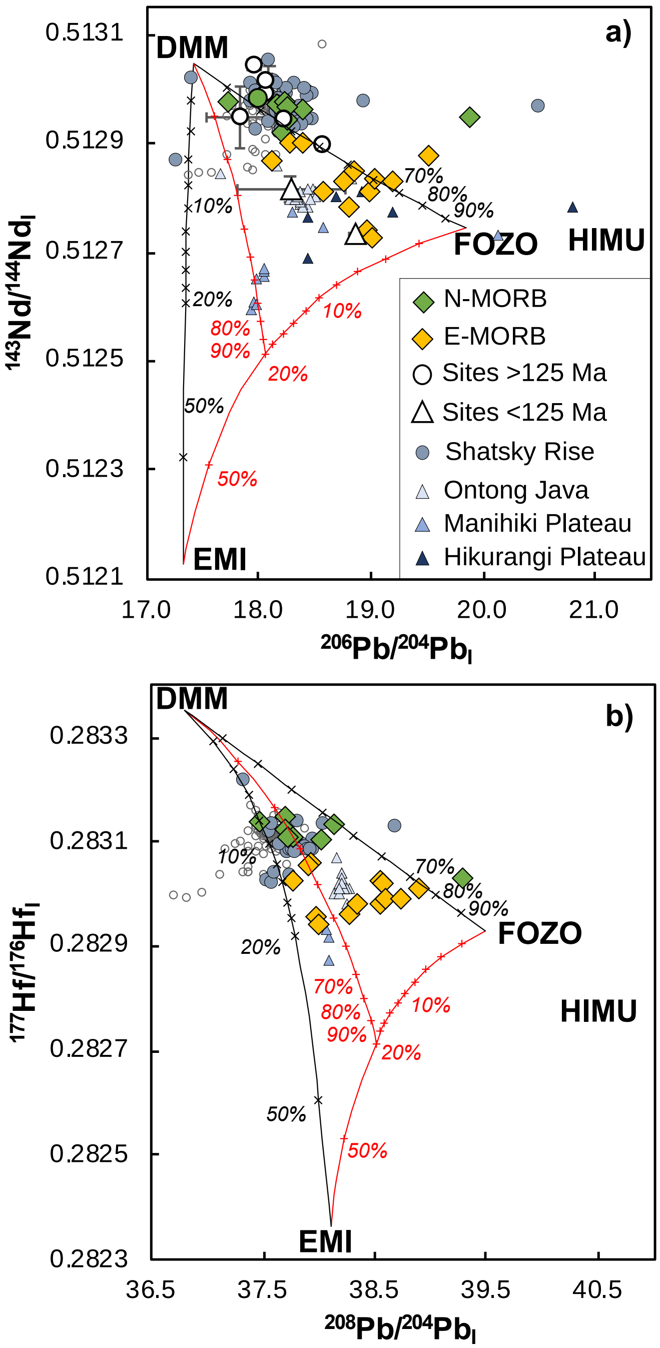

Figure 3.5: a) ^{143}Nd/^{144}Nd$_I$ versus ^{206}Pb/^{204}Pb$_I$ diagram for Pacific-Izanagi samples. b) ^{176}Hf/^{177}Hf$_I$ versus ^{208}Pb/^{204}Pb$_I$ diagram. Mantle source components used as mixing end-members are DMM (Workman and Hart, 2005), EMI (Salters and Sachi-Kocher, 2010), HIMU (Stracke et al., 2003) and FOZO (Stracke et al., 2005). Mixing increments indicate percent contamination of DMM by respective end-members. Data and sources as in Figures 3.2, 3.3, and 3.4. All modeling parameters are provided in Table 3.2.

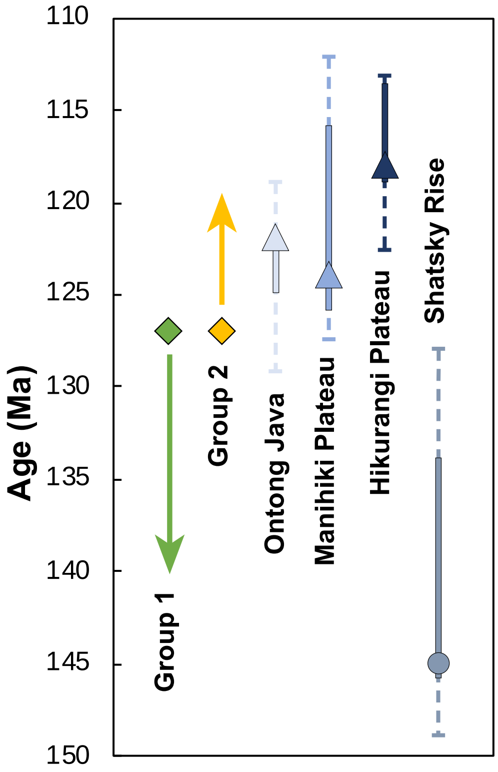

Figure 3.6: Ages of Pacific LIPs relative to Groups 1 and 2.

Table 3.1: Sr-Nd-Pb-Hf isotope ratios and initial values from Pacific-Izanagi transect. New Hf isotope ratios are bolded. Major and trace element concentrations and Sr-Nd-Pb isotopic ratios values from Durkin et al. (2020). Bold sample names indicate samples that passed filtering.

Site	**D7-1**	**D21-5**	D8-2	**D8-4**	**D8-5**	**D8-6**	**D11-1**	**D11-2**	**D11-3**	**D11-4**	**D11-5**	**D11-7**	**D18-1**
IGSN	IEKED0001	IEKED0006	IEKED000A	IEKED000C	IEKED000D	IEKED000E	IEKED000H	IEKED000I	IEKED000J	IEKED000K	IEKED000L	IEKED000N	IEKED000P
Lat (°N)	27.57	143.47	29.63	143.20	143.20	143.20	142.45	142.45	142.45	142.45	142.45	142.45	142.38
Lon (°E)	143.56	28.43	143.20	29.63	29.63	29.63	33.23	33.23	33.23	33.23	33.23	33.23	33.35
SiO_2	46.92	48.08	48.58	47.62	46.12	45.24	51.50	50.54	51.86	50.21	50.19	51.00	46.95
TiO_2	1.31	2.47	2.60	1.29	1.30	1.21	1.78	1.68	1.73	1.89	1.70	1.78	0.72
Al_2O_3	13.68	13.90	13.09	15.89	16.22	16.01	14.61	14.34	15.24	14.88	14.64	14.74	17.17
FeO*	12.52	14.94	16.59	10.84	12.31	10.04	11.10	11.30	9.41	10.48	11.58	11.16	10.32
MgO	7.18	6.44	5.51	9.86	6.48	6.65	7.16	6.99	7.86	7.15	6.70	6.87	7.52
Na_2O	2.66	2.95	2.69	2.62	2.74	2.48	2.93	2.75	2.85	2.90	2.74	2.94	1.81
Na_2O+K_2O	2.74	3.08	2.95	2.67	2.80	2.85	3.26	3.25	3.13	3.25	3.37	3.33	3.68
K_2O/TiO_2	0.06	0.05	0.10	0.05	0.05	0.31	0.18	0.30	0.16	0.19	0.37	0.22	2.58
La	2.34	7.41	3.94	1.78	2.12	1.95	4.99	3.27	4.27	3.85	4.19	3.39	1.76
Ce	6.69	20.55	12.17	7.05	7.32	7.30	16.14	10.67	12.62	12.38	12.40	11.18	3.28
Pr	1.18	3.15	2.02	1.31	1.28	1.32	2.59	1.73	1.95	2.01	1.95	1.85	0.67
Nd	6.78	16.41	11.26	7.69	7.21	7.63	13.84	9.56	10.25	10.90	10.30	10.22	3.78
Sm	2.78	5.47	4.11	2.90	2.66	2.78	4.74	3.43	3.52	3.78	3.56	3.66	1.46
Eu	1.19	1.90	1.71	1.15	1.09	1.12	1.55	1.29	1.30	1.40	1.31	1.39	0.63
Gd	4.17	7.02	5.62	3.84	3.62	3.68	6.17	4.66	4.64	5.05	4.70	4.89	2.12
Tb	0.83	1.29	1.06	0.72	0.67	0.69	1.15	0.88	0.86	0.94	0.87	0.92	0.40
Dy	6.07	8.89	7.47	4.98	4.70	4.88	8.10	6.21	6.00	6.57	6.05	6.51	2.84
Ho	1.33	1.92	1.62	1.08	1.01	1.06	1.76	1.35	1.29	1.42	1.30	1.40	0.61
Er	3.95	5.59	4.81	3.18	2.93	3.11	5.14	3.99	3.79	4.16	3.85	4.08	1.76
Tm	0.59	0.82	0.71	0.46	0.43	0.46	0.77	0.59	0.56	0.61	0.57	0.61	0.26
Yb	3.96	5.32	4.76	3.07	2.84	3.03	5.18	3.89	3.73	4.05	3.85	4.00	1.65
Lu	0.57	0.78	0.70	0.45	0.42	0.45	0.75	0.57	0.55	0.59	0.56	0.59	0.24
La/Sm_N	0.54	0.88	0.62	0.40	0.52	0.45	0.68	0.62	0.78	0.66	0.76	0.60	0.78
Nd/Hf	3.04	3.80	2.32	3.39	3.62	3.81	3.41	3.43	3.52	3.48	3.52	3.38	4.18
Th/La	0.08	0.07	0.10	0.04	0.04	0.03	0.11	0.08	0.09	0.09	0.09	0.08	0.06
Sm/La	1.19	0.74	1.04	1.63	1.25	1.42	0.95	1.05	0.83	0.98	0.85	1.08	0.83
Th/Yb	0.04	0.10	0.08	0.02	0.03	0.02	0.10	0.06	0.10	0.08	0.10	0.07	0.06
Nb/Yb	0.54	1.33	1.29	0.32	0.49	0.31	0.85	0.78	1.19	1.03	1.17	0.85	0.92
$^{176}Hf/^{177}Hf$	**0.283117**	**0.283200**	**0.283194**	-	-	-	-	-	-	-	-	-	-
$^{176}Lu/^{177}Hf$	**0.036653**	**0.025731**	**0.020516**	-	-	-	-	-	-	-	-	-	-
$^{176}Hf/^{177}Hf_{125}$	**0.283031**	**0.283140**	**0.283146**	-	-	-	-	-	-	-	-	-	-
εHf	**11.7**	**14.7**	**14.5**	-	-	-	-	-	-	-	-	-	-
εHf_{125}	**8.7**	**12.6**	**12.8**	-	-	-	-	-	-	-	-	-	-
$^{143}Nd/^{144}Nd_{125}$	0.512951	0.512979	0.512974	-	-	-	-	-	-	-	-	-	-
εNd_{125}	6.3	6.8	6.7	-	-	-	-	-	-	-	-	-	-
$^{208}Pb/^{204}Pb_{125}$	39.290	37.476	37.711	-	-	-	-	-	-	-	-	-	-
$^{207}Pb/^{204}Pb_{125}$	15.665	15.352	15.444	-	-	-	-	-	-	-	-	-	-
$^{206}Pb/^{204}Pb_{125}$	19.885	17.722	18.155	-	-	-	-	-	-	-	-	-	-
$^{207}Pb/^{206}Pb_{125}$	0.788	0.866	0.851	-	-	-	-	-	-	-	-	-	-
$\Delta\varepsilon Hf_{125}$	2.76	-0.33	-0.70	-	-	-	-	-	-	-	-	-	-

Table 3.1: Continued

D16-2 IEKED000Y	**D15-1** IEKED0014	**D15-2** IEKED0015	D15-3 IEKED0016	D13-1 IEKED001M	**D13-2** IEKED001N	D13-3 IEKED001O	**D13-6** IEKED001R	**D21-6** IEKED0007	**D21-7** IEKED0008	D19-1 IEKED000F	D19-2 IEKED000G	D11-8 IEKED000O	**D18-2** IEKED000Q	**D18-3** IEKED000R
33.54	142.37	33.68	33.68	142.19	142.19	34.37	142.19	143.47	28.43	32.45	32.45	33.23	142.38	142.38
142.30	33.68	142.37	142.37	34.37	34.37	142.19	34.37	28.43	143.47	142.41	142.41	142.45	33.35	33.35
49.98	50.45	47.39	47.46	48.29	48.29	47.70	49.28	48.79	50.39	50.11	49.71	-	47.60	47.44
1.19	1.10	1.08	1.12	2.49	1.84	2.56	2.16	1.13	1.40	1.63	1.68	-	1.90	1.80
18.24	15.15	14.61	15.47	14.22	13.78	12.20	14.40	17.29	19.06	18.48	18.32	-	16.45	15.97
12.98	9.87	10.32	11.62	15.35	13.45	15.35	13.23	10.59	8.46	11.51	10.97	-	12.20	11.52
2.36	6.78	6.89	4.79	5.57	6.88	5.57	6.03	6.93	5.47	3.45	4.32	-	6.20	6.23
2.67	2.32	2.31	2.27	3.23	2.59	2.56	2.76	2.96	3.53	2.38	2.42	-	2.17	2.13
4.34	3.12	3.58	4.09	3.44	2.67	3.44	3.69	3.35	3.91	5.55	4.89	-	4.64	4.25
1.40	0.73	1.18	1.62	0.08	0.05	0.08	0.43	0.34	0.27	1.94	1.47	-	1.30	1.17
2.29	0.98	1.14	1.42	5.44	4.40	12.69	6.75	10.27	7.29	19.66	20.95	24.02	10.11	9.99
5.33	3.92	4.45	5.25	17.43	13.26	37.24	21.87	20.03	15.56	27.75	26.99	46.68	22.38	21.73
0.90	0.77	0.84	0.98	2.86	2.13	6.17	3.62	2.39	1.86	4.68	4.94	5.65	3.31	3.21
4.89	4.77	5.13	5.81	15.69	11.41	31.99	18.60	9.65	8.06	19.61	20.83	23.00	15.59	15.04
1.77	1.98	2.08	2.32	5.44	3.93	10.30	6.34	2.32	2.13	4.42	4.65	5.01	4.21	4.10
0.74	0.87	0.90	0.95	1.86	1.43	2.82	2.28	0.95	1.07	1.51	1.60	1.79	1.51	1.47
2.31	2.83	2.87	3.20	7.10	5.09	12.87	8.57	2.70	2.57	5.15	5.53	5.28	5.02	4.88
0.44	0.55	0.55	0.61	1.31	0.94	2.29	1.56	0.44	0.42	0.79	0.84	0.78	0.84	0.82
3.02	3.93	3.95	4.30	9.03	6.60	15.66	10.40	2.76	2.73	4.89	5.30	4.67	5.53	5.33
0.64	0.85	0.85	0.93	1.95	1.42	3.35	2.40	0.57	0.55	0.99	1.08	0.92	1.16	1.12
1.83	2.50	2.48	2.68	5.65	4.10	9.77	6.66	1.59	1.52	2.73	3.02	2.57	3.32	3.19
0.27	0.37	0.37	0.40	0.83	0.61	1.45	0.98	0.23	0.21	0.37	0.42	0.36	0.48	0.46
1.72	2.45	2.41	2.58	5.44	3.99	9.52	6.82	1.46	1.37	2.35	2.57	2.26	3.13	2.93
0.24	0.36	0.35	0.37	0.81	0.58	1.39	0.97	0.22	0.19	0.33	0.37	0.33	0.45	0.43
0.84	0.32	0.35	0.40	0.65	0.72	0.80	0.69	2.87	2.21	2.88	2.91	3.10	1.55	1.57
3.10	2.82	2.97	3.32	3.37	3.58	3.60	3.36	4.88	4.16	7.41	7.62	5.89	4.74	4.66
0.07	0.03	0.04	0.03	0.07	0.07	0.07	0.06	0.14	0.13	0.09	0.09	0.13	0.09	0.09
0.77	2.03	1.83	1.63	1.00	0.89	0.81	0.94	0.23	0.29	0.22	0.22	0.21	0.42	0.41
0.09	0.01	0.02	0.02	0.07	0.08	0.09	0.06	0.96	0.69	0.76	0.71	1.33	0.29	0.29
1.38	0.18	0.20	0.24	0.89	1.14	1.10	0.87	12.41	10.36	10.85	10.31	16.85	4.29	4.42
0.283183	-	**0.283174**	**0.283196**	**0.283166**	-	**0.283160**	-	-	**0.283044**	**0.283068**	**0.283067**	**0.283054**	-	-
0.022092	-	**0.029031**	**0.030451**	**0.024915**	-	**0.022271**	-	-	**0.014314**	**0.017963**	**0.019375**	**0.012174**	-	-
0.283132	-	**0.283106**	**0.283125**	**0.283108**	-	**0.283108**	-	-	**0.283011**	**0.283026**	**0.283021**	**0.283025**	-	-
14.1	-	**13.8**	**14.5**	**13.5**	-	**13.3**	-	-	**9.2**	**10.0**	**10.0**	**9.5**	-	-
12.3	-	**11.4**	**12.0**	**11.4**	-	**11.4**	-	-	**8.0**	**8.5**	**8.4**	**8.5**	-	-
0.512920	-	0.512964	0.512976	0.512945	-	0.512969	-	-	0.512830	0.512742	0.512731	0.512867	-	-
5.7	-	6.5	6.8	6.1	-	6.6	-	-	3.9	2.2	2.0	4.6	-	-
38.146	-	38.030	37.708	37.766	-	37.723	-	-	38.896	38.557	38.580	37.775	-	-
15.530	-	15.516	15.456	15.452	-	15.439	-	-	15.610	15.538	15.564	15.433	-	-
18.20	-	18.394	18.233	18.251	-	18.259	-	-	19.207	18.966	19.002	18.113	-	-
0.853	-	0.844	0.848	0.847	-	0.846	-	-	0.813	0.819	0.819	0.852	-	-
-1.61	-	0.47	0.11	-0.12	-	0.51	-	-	0.28	-2.61	-2.74	0.76	-	-

Table 3.1: Continued

D18-4	**D18-5**	D18-6	**D18-7**	**D18-8**	D16-5	D12-1	D12-2	**D12-3**	**D12-4**	**D12-7**	D14-1	D14-2	**D14-3**	D14-4	D13-4
IEKED000S	IEKED000D	IEKED000U	IEKED000V	IEKED000W	IEKED0011	IEKED0017	IEKED0018	IEKED0019	IEKED001A	IEKED001D	IEKED001F	IEKED001G	IEKED001H	IEKED001I	IEKED001P
142.38	143.20	33.35	142.38	142.38	33.54	34.07	34.07	142.18	142.18	34.07	34.17	34.17	142.20	34.17	34.37
33.35	29.63	142.38	33.35	33.35	142.30	142.18	142.18	34.07	34.07	142.18	142.20	142.20	34.17	142.20	142.19
45.92	47.95	44.46	47.67	47.81	50.73	46.49	48.79	46.07	45.62	47.16	49.05	51.90	46.32	49.93	50.53
1.94	1.77	1.84	1.83	1.79	1.01	2.71	2.64	2.80	1.51	1.61	2.65	2.50	2.11	2.32	2.17
15.03	15.25	14.80	16.16	15.73	19.00	17.32	16.89	16.52	15.64	16.17	19.38	19.55	16.10	17.77	16.54
11.26	12.31	12.89	9.96	11.54	12.47	12.46	12.49	10.36	8.52	8.75	12.61	11.64	10.86	11.51	17.49
6.39	6.48	5.78	6.39	6.91	1.45	1.78	3.10	6.38	5.53	5.37	1.43	1.17	7.02	3.12	4.76
2.55	2.08	2.27	2.07	1.96	2.32	2.69	2.83	2.76	2.56	3.07	2.51	3.12	2.90	3.20	3.87
2.91	2.80	3.63	3.78	4.17	5.91	5.24	6.53	4.63	4.67	5.45	5.80	7.31	4.31	6.25	3.64
0.19	0.05	0.74	0.93	1.23	3.55	0.94	1.40	0.67	1.40	1.48	1.24	1.68	0.67	1.32	0.42
10.56	8.88	10.18	9.42	9.55	25.93	33.40	28.45	30.76	22.33	22.16	40.87	33.90	21.83	21.94	41.34
23.98	20.85	25.04	22.39	21.12	4.65	67.51	60.81	66.33	43.77	43.48	72.48	67.83	45.65	46.69	85.77
3.47	3.15	3.55	3.28	3.15	5.70	8.21	7.19	7.81	5.20	5.14	9.77	8.00	5.73	5.65	9.51
16.53	14.97	16.65	15.29	14.79	26.25	32.95	29.15	31.68	20.69	20.56	39.17	31.59	23.97	23.01	35.44
4.69	4.11	4.67	4.24	4.09	6.26	6.91	6.19	6.77	4.44	4.36	8.04	6.25	5.36	5.06	6.72
1.62	1.42	1.63	1.49	1.46	2.01	2.36	2.14	2.30	1.49	1.48	2.63	2.12	1.82	1.75	2.25
5.62	4.79	5.53	4.94	4.84	8.24	7.16	6.43	6.89	4.84	4.75	8.40	6.54	5.72	5.35	6.78
0.96	0.80	0.94	0.83	0.81	1.29	1.02	0.92	0.97	0.73	0.72	1.19	0.90	0.86	0.81	0.94
6.43	5.16	6.13	5.46	5.37	8.24	5.95	5.32	5.57	4.50	4.48	7.10	5.31	5.27	4.88	5.51
1.34	1.06	1.29	1.14	1.13	1.74	1.16	1.03	1.06	0.93	0.92	1.44	1.07	1.07	0.98	1.10
3.90	2.99	3.69	3.26	3.28	4.73	3.20	2.81	2.91	2.64	2.60	4.05	3.02	2.98	2.76	3.16
0.57	0.42	0.53	0.46	0.47	0.63	0.44	0.39	0.39	0.38	0.37	0.56	0.42	0.42	0.39	0.46
3.71	2.74	3.48	2.99	3.02	3.81	2.80	2.48	2.51	2.47	2.43	3.62	2.72	2.72	2.55	3.07
0.54	0.40	0.51	0.44	0.45	0.54	0.40	0.35	0.35	0.37	0.36	0.53	0.40	0.40	0.37	0.46
1.46	1.40	1.41	1.44	1.51	2.68	3.12	2.97	2.93	3.25	3.28	3.29	3.50	2.63	2.80	3.98
4.60	5.14	4.61	4.59	4.69	17.71	5.72	5.91	5.90	6.72	6.69	6.91	5.88	5.77	5.38	4.41
0.08	0.09	0.10	0.10	0.09	0.00	0.12	0.13	0.13	0.14	0.14	0.11	0.13	0.11	0.12	0.16
0.44	0.46	0.46	0.45	0.43	0.24	0.21	0.22	0.22	0.20	0.20	0.20	0.18	0.25	0.23	0.16
0.23	0.30	0.29	0.30	0.28	0.01	1.46	1.51	1.61	1.26	1.27	1.27	1.63	0.92	1.03	2.11
3.36	4.24	4.21	4.48	4.22	0.19	17.95	19.21	21.04	14.73	15.04	14.38	19.97	12.53	13.86	21.55
0.283113	-	**0.283103**	-	-	**0.283280**	**0.283006**	**0.283012**	-	-	**0.283032**	**0.282991**	**0.282981**	-	**0.283012**	**0.282963**
0.021571	-	**0.020175**	-	-	**0.051470**	**0.009908**	**0.009983**	-	-	**0.016583**	**0.013252**	**0.010649**	-	**0.012232**	**0.008145**
0.283062	-	**0.283055**	-	-	**0.283160**	**0.282983**	**0.282989**	-	-	**0.282993**	**0.282960**	**0.282956**	-	**0.282983**	**0.282944**
11.6	-	**11.2**	-	-	**17.5**	**7.8**	**8.0**	-	-	**8.7**	**7.3**	**6.9**	-	**8.0**	**6.3**
9.8	-	**9.6**	-	-	**13.3**	**7.0**	**7.2**	-	-	**7.4**	**6.2**	**6.1**	-	**7.0**	**5.6**
0.512903	-	0.512900	-	-	0.512434	0.512811	0.512837	-	-	0.512877	0.512785	0.512834	-	0.512850	0.512812
5.3	-	5.3	-	-	-3.8	3.5	4.0	-	-	4.8	3.0	4.0	-	4.3	3.6
37.931	-	37.911	-	-	38.420	38.563	38.603	-	-	38.748	38.277	37.983	-	38.343	37.994
15.469	-	15.468	-	-	15.586	15.502	15.544	-	-	15.609	15.518	15.431	-	15.504	15.486
18.277	-	18.385	-	-	18.421	18.992	19.035	-	-	19.518	18.798	18.760	-	18.854	18.576
0.846	-	0.841	-	-	0.846	0.816	0.817	-	-	0.800	0.826	0.823	-	0.822	0.834
0.39	-	0.56	-	-	-15.52	0.77	1.23	-	-	2.15	0.85	2.31	-	1.78	2.17

Table 3.2: Batch melting and mantle mixing model parameters used in Figures 4 and 5. Metasomatized mantle is DMM fertilized by a 0.5% DMM melt in an 80:20 mantle:melt ratio All mantle end-members have been age-corrected to 125 Ma. a) Partition coefficients from Gale et al. (2011). b) DMM Th, La, Sm, Hf, Nd, and Pb concentrations, ^{176}Hf/^{177}Hf, ^{143}Nd/^{144}Nd and ^{206}Pb/^{204}Pb from Workman and Hart (2005). c) DMM ^{208}Pb/^{204}Pb from Kimura et al. (2017). d) EMI isotope data from Salters and Sachi-Kocher (2010). e) Hf, Nd and Pb concentrations for FOZO taken as the ambient mantle of OIB source (Stracke et al., 2003), concentrations for HIMU as a basaltic crust with 0% sediment addition after 3Ga and EMI as a basaltic crust with 5% sediment addition aged after 3Ga. f) FOZO ^{143}Nd/^{144}Nd, ^{206}Pb/^{204}Pb and ^{208}Pb/^{204}Pb from Stracke et al. (2005). g) FOZO ^{176}Hf/^{177}Hf from Nebel et al. (2018).

Modal batch melting	**K_d ol/melt[a]**	**K_d opx/melt[a]**	**K_d cpx/melt[a]**	**bulk K_d**	*Mantle mixing*	**DMM[b,c]**	**EMI[d,e]**	**FOZO[e,f,g]**	**EMI-FOZO mixture**
Th	0.00005	0.00005	0.003	0.000345	**^{176}Hf/^{177}Hf**	0.283353	0.282365	0.282929	0.282719
La	0.00005	0.00005	0.042	0.004245	**^{143}Nd/^{144}Nd**	0.513045	0.512129	0.512744	0.512515
Sm	0.0006	0.01	0.28	0.046112	**^{206}Pb/^{204}Pb**	17.418	17.315	19.852	18.063
Mineral mode	52%	38%	10%		**^{208}Pb/^{204}Pb**	36.800	38.100	39.500	38.513
[Th]	**DMM[b]**	0.00	**Metasomatized mantle**	0.15	**[Hf]**	0.127	0.395	0.167	0.213
[La]		0.13		3.01	**[Nd]**	0.483	1.755	0.738	0.941
[Sm]		0.21		0.99	**[Pb]**	0.014	0.172	0.018	0.049

Table 3.S1: Table of slopes used in polynomial shallow-fractionation corrections as described by Niu and Batiza (1991).

	AOC polynomial regression slopes		Global MORB polynomial regression slopes	
Oxide	**m_1**	**m_2**	**m_1**	**m_2**
SiO_2	0.0218	-0.8846	0.0456	-1.2441
TiO_2	0.0453	-0.9447	0.0483	-1.0314
Al_2O_3	-0.1712	3.5120	-0.2153	4.1316
FeO	0.1524	-3.1521	0.3542	-6.1044
CaO	-0.0648	0.8947	-0.0875	1.4284
Na_2O	0.0082	-0.2534	0.0178	-0.4309
K_2O	0.0039	-0.0802	0.0042	-0.0887

Table 3.S2: Full dataset of 8 wt% MgO shallow-fractionation corrected values for Pacific-Izanagi samples. Also provided are calculated LLD compositions and regressions used to correct for shallow-level fractionation of Pacific-Izanagi samples. Slopes used in these corrections are summarized in Table S1.

Site	**D7-1**	**D21-5**	D8-2	**D8-4**	**D8-5**	**D8-6**	**D11-1**	**D11-2**	**D11-3**	**D11-4**	**D11-5**	**D11-7**	**D18-1**	D16-2	**D15-1**	**D15-2**
IGSN	IEKED0 001	IEKED0 006	IEKED0 00A	IEKED0 00C	IEKED0 00D	IEKED0 00E	IEKED0 00H	IEKED0 00I	IEKED0 00J	IEKED0 00K	IEKED0 00L	IEKED0 00N	IEKED0 00P	IEKED0 00Y	IEKED0 014	IEKED0 015
Lat (°N)	27.57	143.47	29.63	143.20	143.20	143.20	142.45	142.45	142.45	142.45	142.45	142.45	142.38	33.54	142.37	33.68
Lon (°E)	143.56	28.43	143.20	29.63	29.63	29.63	33.23	33.23	33.23	33.23	33.23	33.23	33.35	142.30	33.68	142.37
SiO_2	46.92	48.08	48.58	47.62	46.12	45.24	51.50	50.54	51.86	50.21	50.19	51.00	46.95	49.98	50.45	47.39
Si_8	46.47	47.20	47.11	48.54	45.26	44.48	51.04	49.98	51.78	49.74	49.45	50.36	46.69	46.26	49.76	46.77
TiO_2	1.31	2.47	2.60	1.29	1.30	1.21	1.78	1.68	1.73	1.89	1.70	1.78	0.72	1.19	1.10	1.08
Ti_8	1.10	2.01	1.78	1.54	0.86	0.84	1.56	1.42	1.70	1.67	1.34	1.48	0.61	-1.49	0.76	0.78
Al_2O_3	13.68	13.90	13.09	15.89	16.22	16.01	14.61	14.34	15.24	14.88	14.64	14.74	17.17	18.24	15.15	14.61
Al_8	14.43	15.51	16.08	15.05	17.80	17.36	15.38	15.30	15.35	15.66	15.94	15.83	17.58	28.05	16.34	15.68
Fe_2O_3	11.27	13.44	14.93	9.75	11.07	9.04	9.99	10.17	8.47	9.44	10.42	10.04	9.29	11.68	8.88	9.29
FeO*	12.52	14.94	16.59	10.84	12.31	10.04	11.10	11.30	9.41	10.48	11.58	11.16	10.32	12.98	9.87	10.32
Fe_8	11.84	13.46	13.86	11.64	10.86	8.81	10.39	10.43	9.31	9.77	10.39	10.16	9.94	4.10	8.78	9.34
MgO	7.18	6.44	5.51	9.86	6.48	6.65	7.16	6.99	7.86	7.15	6.70	6.87	7.52	2.36	6.78	6.89
CaO	10.74	11.06	9.96	11.13	11.42	12.81	10.27	10.70	11.00	10.39	10.55	10.41	9.87	6.78	14.38	10.23
Ca_8	10.67	11.00	10.01	11.61	11.36	12.74	10.20	10.62	10.98	10.32	10.48	10.34	9.82	8.04	14.30	10.15
Na_2O	2.66	2.95	2.69	2.62	2.74	2.48	2.93	2.75	2.85	2.90	2.74	2.94	1.81	2.67	2.32	2.31
Na_8	2.55	2.74	2.33	2.81	2.54	2.30	2.82	2.62	2.84	2.79	2.57	2.79	1.75	1.72	2.16	2.17
K_2O	0.08	0.14	0.26	0.06	0.06	0.37	0.33	0.50	0.28	0.35	0.63	0.39	1.87	1.67	0.80	1.27
K_8	0.06	0.10	0.19	0.08	0.02	0.34	0.31	0.48	0.28	0.34	0.60	0.37	1.86	1.44	0.77	1.25

Table 3.S2: Continued

D15-2	D15-3	D13-1	**D13-2**	D13-3	**D13-6**	**D21-6**	**D21-7**	D19-1	D19-2	D11-8	**D18-2**	**D18-3**	**D18-4**	**D18-5**	D18-6	**D18-7**	**D18-8**	D16-5	D12-1	D12-2
IEKED0015	IEKED0016	IEKED001M	IEKED001N	IEKED001O	IEKED001R	IEKED0007	IEKED0008	IEKED000F	IEKED000G	IEKED000O	IEKED000Q	IEKED000R	IEKED000S	IEKED000D	IEKED000U	IEKED000V	IEKED000W	IEKED0011	IEKED0017	IEKED0018
33.68	33.68	142.19	142.19	34.37	142.19	143.47	28.43	32.45	32.45	33.23	142.38	142.38	142.38	143.20	33.35	142.38	142.38	33.54	34.07	34.07
142.37	142.37	34.37	34.37	142.19	34.37	28.43	143.47	142.41	142.41	142.45	33.35	33.35	33.35	29.63	142.38	33.35	33.35	142.30	142.18	142.18
47.39	47.46	48.29	48.29	47.70	49.28	48.79	50.39	50.11	49.71	-	47.60	47.44	45.92	47.95	44.46	47.67	47.81	50.73	46.49	48.79
46.77	45.52	46.86	47.66	45.74	48.14	48.19	48.90	47.22	47.45	-	46.56	46.42	45.00	47.77	43.16	46.76	47.20	46.28	42.32	45.64
1.08	1.12	2.49	1.84	2.56	2.16	1.13	1.40	1.63	1.68	-	1.90	1.80	1.94	1.77	1.84	1.83	1.79	1.01	2.71	2.64
0.78	-0.05	1.69	1.54	1.37	1.56	0.84	0.55	-0.31	0.26	-	1.36	1.27	1.47	1.69	1.13	1.36	1.50	-2.37	-0.41	0.48
14.61	15.47	14.22	13.78	12.20	14.40	17.29	19.06	18.48	18.32	-	16.45	15.97	15.03	15.25	14.80	16.16	15.73	19.00	17.32	16.89
15.68	19.71	17.10	14.87	16.50	16.58	18.31	22.12	25.53	23.48	-	18.40	17.88	16.73	15.53	17.36	17.84	16.77	31.42	28.74	24.78
9.29	10.46	13.82	12.10	15.74	11.90	9.53	7.61	10.35	9.87	-	10.98	10.37	10.13	11.48	11.60	8.96	10.38	11.23	11.22	11.24
10.32	11.62	15.35	13.45	17.49	13.23	10.59	8.46	11.51	10.97	-	12.20	11.52	11.26	12.76	12.89	9.96	11.54	12.47	12.46	12.49
9.34	7.76	12.72	12.45	13.58	11.23	9.65	5.67	5.11	6.28	-	10.41	9.78	9.71	12.50	10.56	8.42	10.58	1.25	2.13	5.34
6.89	4.79	5.57	6.88	4.76	6.03	6.93	5.47	3.45	4.32	-	6.20	6.23	6.39	7.66	5.78	6.39	6.91	1.45	1.78	3.10
10.23	10.79	10.20	11.57	8.65	10.15	10.04	10.11	3.70	5.79	-	8.94	9.68	10.79	9.26	9.71	11.66	9.49	5.12	5.95	4.37
10.15	11.00	10.23	11.49	8.87	10.12	9.96	10.16	4.40	6.15	-	8.90	9.63	10.73	9.22	9.72	11.60	9.41	6.97	7.57	5.23
2.31	2.27	3.23	2.59	2.56	2.76	2.96	3.53	2.38	2.42	-	2.17	2.13	2.55	2.08	2.27	2.07	1.96	2.32	2.69	2.83
2.17	1.80	2.89	2.44	2.08	2.49	2.82	3.17	1.66	1.86	-	1.92	1.89	2.33	2.03	1.96	1.85	1.82	1.17	1.61	2.03
1.27	1.81	0.21	0.08	1.08	0.93	0.39	0.38	3.16	2.47	-	2.47	2.12	0.36	2.02	1.36	1.71	2.21	3.59	2.55	3.70
1.25	1.72	0.14	0.06	0.98	0.88	0.36	0.31	3.00	2.35	-	2.43	2.07	0.33	2.01	1.30	1.67	2.19	3.31	2.29	3.52

Table 3.S2: Continued

D12-3 IEKED0019	**D12-4** IEKED001A	**D12-7** IEKED001D	D14-1 IEKED001F	D14-2 IEKED001G	**D14-3** IEKED001H	D14-4 IEKED00 1I	D13-4 IEKED00 1P
142.18	142.18	34.07	34.17	34.17	142.20	34.17	34.37
34.07	34.07	142.18	142.20	142.20	34.17	142.20	142.19
46.07	45.62	47.16	49.05	51.90	46.32	49.93	50.53
45.15	44.16	45.61	44.58	47.23	45.78	46.80	48.03
2.80	1.51	1.61	2.65	2.50	2.11	2.32	2.17
2.33	0.69	0.72	-0.76	-1.11	1.85	0.17	0.55
16.52	15.64	16.17	19.38	19.55	16.10	17.77	16.54
18.22	18.60	19.38	31.86	32.80	17.03	25.63	22.41
9.32	7.67	7.88	11.35	10.48	9.78	10.36	8.92
10.36	8.52	8.75	12.61	11.64	10.86	11.51	9.91
8.80	5.82	5.83	1.33	-0.33	10.02	4.40	4.58
6.38	5.53	5.37	1.43	1.17	7.02	3.12	3.98
7.55	14.37	12.29	6.00	5.02	8.64	6.53	4.90
7.49	14.42	12.37	7.87	7.07	8.57	7.38	5.38
2.76	2.56	3.07	2.51	3.12	2.90	3.20	3.87
2.54	2.21	2.70	1.35	1.91	2.77	2.41	3.25
1.86	2.11	2.38	3.29	4.19	1.41	3.06	4.24
1.83	2.04	2.31	3.00	3.89	1.39	2.88	4.11

References

Asimow, P.D., Dixon, J.E., Langmuir, C.H., 2004. A hydrous melting and fractionation model for mid-ocean ridge basalts: Application to the Mid-Atlantic Ridge near the Azores. Geochemistry, Geophysics, Geosystems 5, 1–24. https://doi.org/10.1029/2003GC000568

Bartolini, A., Larson, R.L., 2001. Pacific microplate and the Pangea supercontinent in the Early to Middle Jurassic. Geology 29, 735–738. https://doi.org/10.1130/0091-7613(2001)029<0735:PMATPS>2.0.CO;2

Batiza, R., Larson, R.L., Schlanger, S.O., Shcheka, S.A., Tokuyama, H., 1980. Trace element abundance of Nauru Basin . Nature 286, 476–478.

Bizzarro, M., Baker, J.A., Ulfbeck, D., 2003. A new digestion and chemical separation technique for rapid and highly reproducible determination of Lu/Hf and Hf isotope ratios in geological materials by mc-ICP-MS. Geostandards Newsletter 27, 133–145. https://doi.org/10.1111/j.1751-908X.2003.tb00641.x

Boschman, L.M., Hinsbergen, D.J.J. Van, 2016. On the enigmatic birth of the Pacific Plate within the Panthalassa Ocean. Science Advances. https://doi.org/10.1126/sciadv.1600022

Carpentier, M., Chauvel, C., Maury, R.C., Mattielli, N., 2009. The “zircon effect” as recorded by the chemical and Hf isotopic compositions of Lesser Antilles forearc sediments. Earth and Planetary Science Letters 287, 86–99. https://doi.org/10.1016/j.epsl.2009.07.043

Castillo, P.R., 2017. An alternative explanation for the Hf-Nd mantle array. Science Bulletin 62, 974–975. https://doi.org/10.1016/j.scib.2017.05.002

Castillo, P.R., 2016. A proposed new approach and unified solution to old Pb paradoxes. Lithos 252–253, 32–40. https://doi.org/10.1016/j.lithos.2016.02.015

Castillo, P.R., 2015. The recycling of marine carbonates and sources of HIMU and FOZO ocean island basalts. Lithos 216–217, 254–263. https://doi.org/10.1016/j.lithos.2014.12.005

Castillo, P.R., 2004. Geochemistry of Cretaceous volcaniclastic sediments in the Nauru and East Mariana basins provides insights into the mantle sources of giant oceanic plateaus. Geological Society, London, Special Publications 229, 353–368. https://doi.org/10.1144/gsl.sp.2004.229.01.20

Castillo, P.R., Carlson, R.W., Batiza, R., 1991. Origin of Nauru Basin igneous complex: Sr, Nd and Pb isotope and REE constraints. Earth and Planetary Science Letters 103, 200–213. https://doi.org/10.1016/0012-821X(91)90161-A

Castillo, P.R., Pringle, M.S., Carlson, R.W., 1994. East Mariana Basin tholeiites: Cretaceous intraplate basalts or rift basalts related to the Ontong Java plume? Earth and Planetary

Science Letters 123, 139–154. https://doi.org/10.1016/0012-821X(94)90263-1

Cervantes, P., Wallace, P.J., 2003. Role of H2O in subduction-zone magmatism: New insights from melt inclusions in high-Mg basalts from central Mexico. Geology 31, 235–238. https://doi.org/10.1130/0091-7613(2003)031<0235:ROHOIS>2.0.CO;2

Chandler, M.T., Wessel, P., Taylor, B., Seton, M., Kim, S.S., Hyeong, K., 2012. Reconstructing Ontong Java Nui: Implications for Pacific absolute plate motion, hotspot drift and true polar wander. Earth and Planetary Science Letters 331–332, 140–151. https://doi.org/10.1016/j.epsl.2012.03.017

Chauvel, C., Blichert-Toft, J., 2001. A hafnium isotope and trace element perspective on melting of the depleted mantle. Earth and Planetary Science Letters 190, 137–151. https://doi.org/10.1016/S0012-821X(01)00379-X

Coffin, M.F., Eldholm, O., 1992. Volcanism and continental break-up: a global compilation of large igneous provinces. Geological Society, London, Special Publications 68, 17–30. https://doi.org/10.1144/gsl.sp.1992.068.01.02

Cohen, R.S., O’Nions, R.K., 1982. The lead, neodymium and strontium isotopic structure of ocean ridge basalts. Journal of Petrology 23, 299–324. https://doi.org/10.1093/petrology/23.3.299

Danyushevsky, L. V., Plechov, P., 2011. Petrolog3: Integrated software for modeling crystallization processes. Geochemistry, Geophysics, Geosystems 12. https://doi.org/10.1029/2011GC003516

DeFelice, C., Mallick, S., Saal, A.E., Huang, S., 2019. An isotopically depleted lower mantle component is intrinsic to the Hawaiian mantle plume. Nature Geoscience 12, 487–492. https://doi.org/10.1038/s41561-019-0348-0

Donnelly, K.E., Goldstein, S.L., Langmuir, C.H., Spiegelman, M., 2004. Origin of enriched ocean ridge basalts and implications for mantle dynamics. Earth and Planetary Science Letters 226, 347–366. https://doi.org/10.1016/j.epsl.2004.07.019

Doubrovine, P. V., Steinberger, B., Torsvik, T.H., 2016. A failure to reject: Testing the correlation between large igneous provinces and deep mantle structures with EDF statistics. Geochemistry Geophysics Geosystems 17, 1130–1163. https://doi.org/10.1002/2015GC006044

Durkin, K., Castillo, P.R., Straub, S.M., Abe, N., Tamura, Y., 2020. An origin of the along-arc compositional variation in the Izu-Bonin arc system. Geoscience Frontiers. https://doi.org/10.1016/j.gsf.2019.12.004

Eisele, J., Sharma, M., Galer, S.J.G., Blichert-Toft, J., Devey, C.W., Hofmann, A.W., 2002. The role of sediment recycling in EM-1 inferred from Os, Pb, Hf, Nd, Sr isotope and trace element systematics of the Pitcairn hotspot. Earth and Planetary Science Letters 196, 197–212. https://doi.org/10.1016/S0012-821X(01)00601-X

Finlayson, V.A., Konter, J.G., Konrad, K., Koppers, A.A.P., Jackson, M.G., Rooney, T.O., 2018. Sr–Pb–Nd–Hf isotopes and ^{40}Ar/^{39}Ar ages reveal a Hawaii–Emperor-style bend in the Rurutu hotspot. Earth and Planetary Science Letters 500, 168–179. https://doi.org/10.1016/j.epsl.2018.08.020

Floyd, P.A., Winchester, J.A., Castillo, P.R., 1992. Geochemistry and petrography of Cretaceous sills and lava flows, Sites 800 and 802. Proc., Scientific Results, ODP, Leg 129, Old Pacific Crust 345–359. https://doi.org/10.2973/odp.proc.sr.129.128.1992

Gale, A., Dalton, C.A., Langmuir, C.H., Su, Y., Schilling, J.G., 2013. The mean composition of ocean ridge basalts. Geochemistry, Geophysics, Geosystems 14, 489–518. https://doi.org/10.1029/2012GC004334

Gale, A., Escrig, S., Gier, E.J., Langmuir, C.H., Goldstein, S.L., 2011. Enriched basalts at segment centers: The Lucky Strike (37°17'N) and Menez Gwen (37°50'N) segments of the Mid-Atlantic Ridge. Geochemistry, Geophysics, Geosystems 12, 1–26. https://doi.org/10.1029/2010GC003446

Gradstein, F.M., Ogg, J.G., Schmitz, M.D., Ogg, G.M., 2012. The Geologic Time Scale 2012, The Geologic Time Scale 2012. https://doi.org/10.1016/C2011-1-08249-8

Graham, D.W., Humphris, S.E., Jenkins, W.J., Kurz, M.D., 1992. Helium isotope geochemistry of some volcanic rocks from Saint Helena. Earth and Planetary Science Letters 110, 121–131. https://doi.org/10.1016/0012-821X(92)90043-U

Hanan, B.B., Blichert-Toft, J., Pyle, D.G., Christie, D.M., 2004. Constrasting origins of the upper mantle revealed by hafnium and lead isotopes from the Southeast Indian Ridge. Nature 432, 91–94.

Hanan, B.B., Graham, D.W., 1996. Lead and Helium Isotope Evidence from Oceanic Basalts for a Common Deep Source of Mantle Plumes Author (s): B . B . Hanan and D . W . Graham Published by : American Association for the Advancement of Science Stable URL : http://www.jstor.org/stable/2889. Science 272, 991–995.

Hanyu, T., Tatsumi, Y., Kimura, J.I., 2011. Constraints on the origin of the HIMU reservoir from He-Ne-Ar isotope systematics. Earth and Planetary Science Letters 307, 377–386. https://doi.org/10.1016/j.epsl.2011.05.012

Hart, S.R., 1984. A large-scale isotope anomaly in the Southern Hemisphere mantle. Nature 309, 753–757.

Hart, S.R., Hauri, E.H., Oschman, L.A., Whitehead, J.A., 1992. Mantle plumes and entrainment: the isotopic evidence. Science 256, 517–520.

Hauff, F., Hoernle, K., Schmidt, A., 2003. Sr-Nd-Pb composition of Mesozoic Pacific oceanic crust (Site 1149 and 801, ODP Leg 185): Implications for alteration of ocean crust and the input into the Izu-Bonin-Mariana subduction system. Geochemistry, Geophysics, Geosystems 4. https://doi.org/10.1029/2002GC000421

Heydolph, K., Murphy, D.T., Geldmacher, J., Romanova, I. V., Greene, A., Hoernle, K., Weis, D., Mahoney, J., 2014. Plume versus plate origin for the Shatsky Rise oceanic plateau (NW Pacific): insights from Nd, Pb and Hf isotopes. Lithos 200–201, 49–63. https://doi.org/10.1016/j.lithos.2014.03.031

Hoernle, K., Hauff, F., van den Bogaard, P., Werner, R., Mortimer, N., Geldmacher, J., Garbe-Schönberg, D., Davy, B., 2010. Age and geochemistry of volcanic rocks from the Hikurangi and Manihiki oceanic Plateaus. Geochimica et Cosmochimica Acta 74, 7196–7219. https://doi.org/10.1016/j.gca.2010.09.030

Hofmann, A.W., 2013. Sampling Mantle Heterogeneity through Oceanic Basalts: Isotopes and Trace Elements, 2nd ed, Treatise on Geochemistry: Second Edition. Elsevier Ltd. https://doi.org/10.1016/B978-0-08-095975-7.00203-5

Ito, E., White, W.M., Göpel, C., 1987. The O, Sr, Nd and Pb isotope geochemistry of MORB. Chemical Geology 62, 157–176. https://doi.org/10.1016/0009-2541(87)90083-0

Janney, P.E., Castillo, P.R., 1997. Geochemistry of Mesozoic Pacific mid-ocean ridge basalt: constraints on mantle generation and the evolution of the Pacific upper mantle. Journal of Geophysical Research 102, 5207–5229.

Janney, P.E., Castillo, P.R., 1996. Basalts from the Central Pacific Basin: evidence for the origin of Cretaceous igneous complexes in the Jurassic western Pacific. Journal of Geophysical Research 101, 2875–2893. https://doi.org/10.1029/95JB03119

Johnson, M.C., Plank, T., 2000. Dehydration and melting experiments constrain the fate of subducted sediments. Geochemistry, Geophysics, Geosystems 1. https://doi.org/10.1029/1999GC000014

Kelley, K.A., Plank, T., Ludden, J., Staudigel, H., 2003. Composition of altered oceanic crust at ODP Sites 801 and 1149. Geochemistry, Geophysics, Geosystems 4. https://doi.org/10.1029/2002GC000435

Khanna, T.C., Bizimis, M., Yogodzinski, G.M., Mallick, S., 2014. Hafnium-neodymium isotope systematics of the 2.7Ga Gadwal greenstone terrane, Eastern Dharwar craton, India: Implications for the evolution of the Archean depleted mantle. Geochimica et Cosmochimica Acta 127, 10–24. https://doi.org/10.1016/j.gca.2013.11.024

Kimura, J.I., Gill, J.B., Van Keken, P.E., Kawabata, H., Skora, S., 2017. Origin of geochemical mantle components: Role of spreading ridges and thermal evolution of mantle. Geochemistry Geophysics Geosystems 1–26.

https://doi.org/10.1002/2016GC006679.Received

Koppers, A.A.P., Staudigel, H., Duncan, R.A., 2003. High-resolution 40Ar/39Ar dating of the oldest oceanic basement basalts in the western Pacific basin. Geochemistry, Geophysics, Geosystems 4. https://doi.org/10.1029/2003GC000574

Krolikowska-Ciaglo, S., Hauff, F., Hoernle, K., 2005. Sr-Nd isotope systematics in 14-28 Ma low-temperature altered mid-ocean ridge basalt from the Australian Antarctic Discordance, Ocean Drilling Program Leg 187. Geochemistry, Geophysics, Geosystems 6, 1–18. https://doi.org/10.1029/2004GC000802

Langmuir, C.H., Bender, J.F., Batiza, R., 1986. Petrological and tectonic segmentation of the East Pacific Rise, 5°30’-14°30’ N., Nature.

Langmuir, C.H., Klein, E.M., Plank, T., 1992. Petrological systematics of mid-ocean ridge basalts: Constraints on melt generation beneath ocean ridges. Mantle Flow and Melt Generation at Mid-Ocean Ridges. 183–280. https://doi.org/10.1029/GM071p0183

Larson, R.L., 1991. Latest pulse of the Earth; evidence for a mid- Cretaceous superplume. Geology 19, 547–550. https://doi.org/10.1130/0091-7613(1991)019<0547

Larson, R.L., Schlanger, S.O., 1981. Geological evolution of the Nauru Basin, and regional implications. Initial Reports DSDP, Leg 61, Guam to Majuro Atoll, (U.S. Govt Printing Office; U.K. Distributors, IPOD Committee, NERC, Swindon) 841–862. https://doi.org/10.2973/dsdp.proc.61.138.1981

Le Bas, M.J., Le Maitre, R.W., Streckeisen, A., Zanettin, B., 1986. A chemical classification of volcanic rocks based on the total alkali silica diagram. Journal of Petrology 27, 745–750. https://doi.org/10.1093/petrology/27.3.745

Macdonald, G.A., Katsura, T., 1964. Chemical composition of Hawaiian lavas. Journal of Petrology 5, 82–133. https://doi.org/10.1093/petrology/5.1.82

Madrigal, P., Gazel, E., Flores, K.E., Bizimis, M., Jicha, B., 2016. Record of massive upwellings from the Pacific large low shear velocity province. 7, 13309.

Mahoney, J.J., Duncan, R.A., Tejada, M.L.G., Sager, W.W., Bralower, T.J., 2005. Jurassic-Cretaceous boundary age and mid-ocean-ridge-type mantle source for Shatsky Rise. Geology 33, 185–188. https://doi.org/10.1130/G21378.1

Mahoney, J.J., Storey, M., Duncan, R. a., Spencer, K.J., Pringle, M., 1993. Geochemistry and age of the Ontong Java Plateau. The Mesozoic Pacific: Geology, Tectonics, and Volcanism. 233–261. https://doi.org/10.1029/GM077p0233

Mallick, S., Salters, V.J.M., Langmuir, C.H., 2019. Geochemical Variability Along the Northern East Pacific Rise: Coincident Source Composition and Ridge Segmentation. Geochemistry, Geophysics, Geosystems 20, 1889–1911. https://doi.org/10.1029/2019GC008287

Mittal, T., Richards, M.A., 2017. Plume-ridge interaction via melt chanelization at Galapagos and other near-ridge hotspot provinces. Geochemistry, Geophysics, Geosystems 18, 1711–1738. https://doi.org/10.1002/2016GC006454

Münker, C., Weyer, S., Scherer, E., Mezger, K., 2001. Separation of high field strength elements (Nb, Ta, Zr, Hf) and Lu from rock samples for MC-ICPMS measurements. Geochemistry, Geophysics, Geosystems 2. https://doi.org/10.1029/2001GC000183

Nebel, O., Arculus, R.J., van Westrenen, W., Woodhead, J.D., Jenner, F.E., Nebel-Jacobsen, Y.J., Wille, M., Eggins, S.M., 2013. Coupled Hf-Nd-Pb isotope co-variations of HIMU oceanic island basalts from Mangaia, Cook-Austral islands, suggest an Archean source component in the mantle transition zone. Geochimica et Cosmochimica Acta 112, 87–101. https://doi.org/10.1016/j.gca.2013.03.005

Nebel, O., Sossi, P.A., Foden, J., Bénard, A., Brandl, P.A., Stammeier, J.A., Arculus, R.J., Lupton, J., Richter, M., Arculus, R.J., 2018. Iron isotope variability in ocean floor lavas and mantle sources in the Lau back-arc basin. Geochimica et Cosmochimica Acta 241, 150–163. https://doi.org/10.1016/j.gca.2018.08.046

Pearce, J.A., 2008. Geochemical fingerprinting of oceanic basalts with applications to ophiolite classification and the search for Archean oceanic crust. Lithos 100, 14–48. https://doi.org/10.1016/j.lithos.2007.06.016

Sager, W.W., Sano, T., Geldmacher, J., 2016. Formation and evolution of Shatsky Rise oceanic plateau: Insights from IODP Expedition 324 and recent geophysical cruises. Earth-Science Reviews 159, 306–336. https://doi.org/10.1016/j.earscirev.2016.05.011

Salters, V.J.M., Mallick, S., Hart, S.R., Langmuir, C.E., Stracke, A., 2011. Domains of depleted mantle: New evidence from hafnium and neodymium isotopes. Geochemistry, Geophysics, Geosystems 12. https://doi.org/10.1029/2011GC003617

Salters, V.J.M., Sachi-Kocher, A., 2010. An ancient metasomatic source for the Walvis Ridge basalts. Chemical Geology 273, 151–167. https://doi.org/10.1016/j.chemgeo.2010.02.010

Sano, T., Shimizu, K., Ishikawa, A., Senda, R., Chang, Q., Kimura, J.I., Widdowson, M., Sager, W.W., 2012. Variety and origin of magmas on Shatsky Rise, northwest Pacific Ocean. Geochemistry, Geophysics, Geosystems 13, 1–25. https://doi.org/10.1029/2012GC004235

Saunders, A.D., 1986. Geochemistry of Basalts from the Nauru Basin, Deep Sea Drilling Project legs 61 and 89: Implications for the origin of oceanic flood basalts. Initial Reports of the Deep Sea Drilling Project, 89 89, 499–511.

Seton, M., Müller, R.D., Zahirovic, S., Gaina, C., Torsvik, T., Shephard, G., Talsma, A., Gurnis, M., Turner, M., Maus, S., Chandler, M., 2012. Global continental and ocean basin reconstructions since 200Ma. Earth-Science Reviews 113, 212–270. https://doi.org/10.1016/j.earscirev.2012.03.002

Sisson, T.W., Layne, G.D., 1993. H2O in basalt and basaltic andesite glass inclusions from four subduction-related volcanoes. Earth and Planetary Science Letters 117, 619–635. https://doi.org/10.1016/0012-821X(93)90107-K

Staudigel, H., 2003. Hydrothermal alteration processes in the oceanic crust. Treatise on Geochemistry 3–9, 511–535. https://doi.org/10.1016/B0-08-043751-6/03032-2

Staudigel, H., Plank, T., White, B., Schmincke, U., 1996. Geochemical fluxes during seafloor alteration of the basaltic crust: DSDP Sites 417 and 418. Geophysical Monograph 96. 19–38.

Stein, M., Hofmann, A.W., 1994. Episodic Crustal Growth and Mantle Evolution. Nature 372, 420–421. https://doi.org/10.1180/minmag.1994.58a.1.219

Stracke, A., Bizimis, M., Salters, V.J.M., 2003. Recycling oceanic crust: Quantitative constraints. Geochemistry, Geophysics, Geosystems 4. https://doi.org/10.1029/2001GC000223

Stracke, A., Hofmann, A.W., Hart, S.R., 2005. FOZO, HIMU, and the rest of the mantle zoo. Geochemistry, Geophysics, Geosystems 6. https://doi.org/10.1029/2004GC000824

Sun, S. -s., McDonough, W.F., 1989. Chemical and isotopic systematics of oceanic basalts: implications for mantle composition and processes. Geological Society, London, Special Publications 42, 313–345. https://doi.org/10.1144/GSL.SP.1989.042.01.19

Svensen, H.H., Jerram, D.A., Polozov, A.G., Planke, S., Neal, C.R., Augland, L.E., Emeleus, H.C., 2017. Thinking about LIPs: A brief history of ideas in Large igneous province research. Tectonophysics 1–23. https://doi.org/10.1016/j.tecto.2018.12.008

Taylor, B., 2006. The single largest oceanic plateau: Ontong Java–Manihiki–Hikurangi. Earth and Planetary Science Letters 241, 372–380. https://doi.org/10.1016/j.epsl.2005.11.049

Tejada, M.L.G., Mahoney, J.J., Castillo, P.R., Ingle, S.P., Sheth, H.C., Weis, D., 2004. Pin-pricking the elephant: evidence on the origin of the Ontong Java Plateau from Pb-Sr-Hf-Nd isotopic characteristics of ODP Leg 192 basalts. Geological Society, London, Special Publications 229, 133–150. https://doi.org/10.1144/GSL.SP.2004.229.01.09

Tejada, M.L.G., Mahoney, J.J., Neal, C.R., Duncan, R.A., Petterson, M.G., 2002. Basement geochemistry and geochronology of Central Malaita , Solomon Islands , with Iimplications for the origin and evolution of the Ontong Java Plateau. Journal of Petrology 43, 449–484.

Timm, C., Hoernle, K., Werner, R., Hauff, F., den Bogaard, P. van, Michael, P., Coffin, M.F., Koppers, A., 2011. Age and geochemistry of the oceanic Manihiki Plateau, SW Pacific:

New evidence for a plume origin. Earth and Planetary Science Letters 304, 135–146. https://doi.org/10.1016/j.epsl.2011.01.025

Vervoort, J.D., Patchett, P.J., Blichert-Toft, J., Albarède, F., 1999. Relationships between Lu-Hf and Sm-Nd isotopic systems in the global sedimentary system. Earth and Planetary Science Letters 168, 79–99. https://doi.org/10.1016/S0012-821X(99)00047-3

Vidal, P., 1992. Mantle: More HIMU in the future? Geochimica et Cosmochimica Acta 56, 4295–4299. https://doi.org/10.1016/0016-7037(92)90269-O

Weis, D., Frey, F.A., 1991. Isotope Geochemistry of Ninetyeast Ridge Basement Basalts: Sr, Nd, and Pb Evidence for Involvement of the Kerguelen Hot Spot. Proceedings of the Ocean Drilling Program, 121 Scientific Results 121. https://doi.org/10.2973/odp.proc.sr.121.170.1991

Whittaker, J.M., Afonso, J.C., Masterton, S., Müller, R.D., Wessel, P., Williams, S.E., Seton, M., 2015. Long-term interaction between mid-ocean ridges and mantle plumes. Nature Geoscience 8, 479–484. https://doi.org/10.1038/NGEO2437

Wilkinson, J.F.G., 1982. The genesis of mid-ocean ridge basalt. Earth Science Reviews 18, 1–57. https://doi.org/10.1016/0012-8252(82)90002-2

Wilson, M., 1989. Igneous Petrogenesis: A Global Tectonic Approach. Unwin Hyman, London.

Workman, R.K., Hart, S.R., 2005. Major and trace element composition of the depleted MORB mantle (DMM). Earth and Planetary Science Letters 231, 53–72. https://doi.org/10.1016/j.epsl.2004.12.005

Wu, S.S.C., Garcia, P.A., Jordan, R., Schafer, F.J., Skiff, B.A., 1984. Topography of the shield volcano, Olympus Mons on Mars. Nature 309, 432–435. https://doi.org/10.1038/309432a0

Xue, J., King, S.D., 2016. Geodynamic investigation of a Cretaceous superplume in the Pacific ocean. Physics of the Earth and Planetary Interiors 257, 137–148. https://doi.org/10.1016/j.pepi.2016.05.018

Yang, A.Y., Zhao, T.P., Zhou, M.F., Deng, X.G., 2017. Isotopically enriched N-MORB: A new geochemical signature of off-axis plume-ridge interaction—A case study at 50°28′E, Southwest Indian Ridge. Journal of Geophysical Research: Solid Earth 122, 191–213. https://doi.org/10.1002/2016JB013284

Zindler, A., Hart, S.R., 1986. Chemical Geodynamics. Annual Review of Earth and Planetary Sciences 14, 493–571. https://doi.org/10.1146/annurev.earth.14.1.493

Zindler, A., Staudigel, H., Batiza, R., 1984. Isotope and trace element geochemistry of young Pacific seamounts: implications for the scale of upper mantle heterogeneity. Earth and Planetary Science Letters 70, 175–195. https://doi.org/10.1016/0012-821X(84)90004-9

Chapter 4

Causes of isotopic variations across an oceanic-continental transition, Ross Sea Embayment, Antarctica

Abstract

The West Antarctic Rift System (WARS) is one of the largest active rift systems and alkalic provinces in the world. Volcanism in this system crosscuts between oceanic and continental crust while maintaining similar Sr-Nd-Pb isotopic signatures. In this chapter, I present new Re-Os and HSE data from an ocean-continent transect previously studied by Panter et al. (2018). This new data suggests that lower crustal contamination has occurred to varying degrees in the WARS and is the controlling geochemical process in this system. Several samples from the Adare Basin have experienced minimal crustal contamination and are used to assess the mantle source of the WARS lavas and assess previously proposed hypotheses regarding the origin of the alkalic volcanism. Previous explanations of WARS alkalic lava origins range from plume-derived to continental lithospheric mantle metasomatized by subduction fluids prior to the cessation of subduction by the Phoenix Plate underneath the Gondwana Margin. However, samples from the ocean-continent transect do not exhibit classic arc-lava geochemical signatures. Rather, they indicate fertile mantle with a FOZO isotopic composition was upwelled and melted due to lithospheric thinning during the Cenozoic.

4.1. Introduction

The West Antarctic Rift System (WARS; Fig. 4.1) is one of the world's largest continental rift systems and has experienced significant alkalic volcanism since the Cenozoic. The WARS underwent two primary periods of extension; an amagmatic period during the Cretaceous followed by a second phase during the Cenozoic. This second phase has been the subject of much discussion as it is accompanied by widespread alkalic volcanism of the McMurdo Volcanic Group that has been divided into the Hallet, Melbourne, Balleny, and Erebus volcanic provinces (Kyle et al., 1990). Alkalic volcanism in the WARS is remarkable as it occurs in a transect from the West Antarctic continent in Northern Victoria Land (NVL) to the oceanic crust in the northwest Ross Sea (NWRS) region (Panter and Castillo, 2007; Panter et al., 2018; Aviado et al., 2015). Only two other locations in the world are known to host a continent-ocean transect of petrologically and geochemically related volcanoes. The first, and perhaps best studied, is the Cameroon Volcanic line (CVL; Fitton and Dunlop, 1985; Ngwa et al., 2017), although its source still remains enigmatic. Recently, the magmatic extension of East African Rift System (EARS), the largest continental rift system and alkalic volcanic province in the world, has also been demonstrated to extend from continental crust to the Indian Ocean offshore southern Mozambique via the Mozambique Ridge. Studies have identified Miocene to recent dome-like volcanic structures at the Mozambique Ridge, but their exact origins are also unknown (O'Connor et al., 2019).

Alkalic volcanic rocks from the continental to oceanic transition in the WARS have been sampled through field-based investigation and oceanic dredging (Panter and Castillo, 2007; Panter et al., 2018; Aviado et al., 2015). Their analyses have indicated that the volcanic rocks collected from NVL and nearby Adare Basin in NWRS share similar geochemical signatures despite differences in the composition of lithosphere and overlying crust that they pass through (Panter and Castillo, 2007; Panter et al., 2018). The Adare Basin likely represents a contiguous manifestation of Cenozoic extension since it is blanketed by a sequence of sedimentary strata that can be traced to the adjacent Ross Sea sedimentary basins, and overlies a set of magnetic anomalies striking NNW-SSE, generally orthogonal to the rift extensional direction (Cande and Stock, 2006; Davey et al., 2006). Samples from the crustal basement and a number of seamounts in the Adare Basin (collectively called ABS hereafter) and from NVL, Daniel Peninsula, Coulman Islands, and Possession Islands in the neighboring Hallet Volcanic Province and from the Melbourne Volcanic Province show a slight geochemical enrichment trend and weak northward age progression from continental to oceanic crust (Panter et al., 2018). Overall, however, they are characterized by elevated high field strength element/large ion lithophile element (HFSE/LILE) ratios, low $_{87}$Sr/$_{86}$Sr (~0.7028) and high $_{206}$Pb/$_{204}$Pb (~22.0) Their Sr-Nd-Pb isotope ratios are similar to ocean island basalt (OIB) with HIMU signatures (Hart et al., 1992; Panter et al., 2018). The occurrence of contiguous alkalic volcanism from continental to oceanic lithosphere in WARS presents two major questions: (1) is this volcanism a manifestation of a common magmatic source and mechanism and (2) can some of the geochemical differences between continental and oceanic regimes be accounted for through the interaction of cogenetic magmas with oceanic or continental crust and lithosphere?

Previous work in the WARS has suggested several mechanisms to explain both the timing as well as the geochemically enriched isotopic signatures of its alkalic volcanism. The first proposed mechanism is the presence of a mantle plume under Mt. Erebus (Kyle et al. 1990). This hypothesis posits that the plume controlled the second phase of extension also provided the so-called high μ (HIMU)-like isotopic signature of the volcanics (Lanyon et al., 1993; Weaver et al., 1994; Storey et al., 1999). A variant of the plume hypothesis argues that fossil plumes underplated and accreted to the base of Gondwana lithosphere prior to its break-up (Rocholl et al., 1995; Hart et al., 1997; Panter et al., 2000; Kipf et al., 2014). The other proposed mechanisms can be collectively grouped as a non-plume hypothesis, which claims that the controlling factor on the similar geochemical signatures of NWRS alkalic basalts is the nature of continental lithospheric mantle (CLM). The CLM could have been formed or metasomatized by subduction-related fluids ± mantle plume (e.g., Finn et al., 2005; Aviado et al., 2015; Day et al., 2019) or carbonate-rich melts from previously subducted slabs that also feed mantle plumes (Castillo, 2015; 2016) beneath the Gondwana margin (Panter et al., 2018). In these models, WARS magmas are generated from the metasomatized CLM during rifting or due to the influx of the warm Pacific mantle (e.g., Finn et al., 2005; Panter et al., 2007; Nardini et al., 2009).

In this chapter, I use a combined approach to investigate the source and mechanism of alkaline volcanism in WARS through the analysis of ABS samples from the ocean and continental samples from NVL. The samples were analyzed for their major and trace elements and Sr-Nd-Pb isotopes to give a better resolution on the petrology and geochemistry of the alkaline volcanics from the continent-ocean transect previously studied by Panter and co-workers (Panter and Castillo, 2007; Panter et al., 2018). In addition to these geochemical tracers, I have employed ^{187}Re-^{187}Os isotope and abundance of highly siderophile element (HSE; Os, Ir, Ru, Pt, Pd, Re) systematics to the lavas. Since HSE are both siderophile and chalcophile, and are generally strongly compatible, they provide a complementary tracer to lithophile element isotopes and abundances. In particular, Os isotopes are sensitive tracers of continental crust, which has highly radiogenic ^{187}Os/^{188}Os (~1), and both the upper mantle (~0.129) and CLM (typically <0.125; Day, 2013). The combined use of Sr-Nd-Os-Pb isotopes, in conjunction with

O isotope data reported previously (Panter et al., 2018) can therefore help better constrain the origin of alkalic magmatism in the WARS.

4.2. Geologic Background

4.2.1 Tectonics

Northern Victoria Land is the westernmost continental crust of the East Antarctic Craton in NWRS (Fig. 4.1). It consists of three lithotectonic blocks fused during the Ross Orogeny in the Proterozoic as part of the larger Terra Australis orogen (Borg and Stump, 1987; Boger and Miller, 2004; Di Vincenzo et al., 2016). The Terra Australis orogen concluded with the formation of Pangea and was followed by the Gondwanide orogeny in the Triassic as the Phoenix plate subducted beneath the Gondwana margin (Cawood, 2005). Subduction ceased abruptly in the Cretaceous (Bradshaw, 1989), but the mechanism of subduction cessation along this margin is still unresolved. An oblique subduction of the Phoenix-Pacific spreading center (Bradshaw, 1989) and slab capture (Luyendyk, 1995) have both been suggested as methods by which this abrupt termination may have occurred. Subduction cessation in the Cretaceous marks a shift from a compressional to an extensional tectonic regime that led to the formation of the WARS (Panter et al., 2018).

The WARS crustal thinning occurred in two stages. The first stage of crustal extension occurred during the early Late Cretaceous (Davey and Brancolini, 1995; Salvini et al., 1997; Cande et al., 2000). In this phase, amagmatic lithospheric thinning led to 500-1000 km widening of the Ross Sea and was likely associated with the contemporaneous separation of New Zealand, Antarctica and Australia (Davey and Brancolini, 1995). The second phase formed the Transantarctic mountains and further opened the Ross Sea by ~300 km and was paired with alkalic magmatism as well as high measured heat flow values (Risk and Hochstein, 1974) and low shear velocities in the underlying mantle (Lawrence et al., 2006). This phase of extension was focused primarily in the western Ross Sea, near NVL and the Transantarctic Mountains (Huerta and Harry, 2007; Ji et al., 2018). The resultant WARS is a region of thinned lithosphere that stretches from the Antarctic Peninsula to the Ross Sea Embayment-NVL and separates West Antarctica from the East Antarctic Craton. The broadest part of the WARS, the Ross Sea, is comprised of a series of N-S oriented sedimentary basins (e.g., Northern Victoria Land Basin, Northern Basin, Adare Basin).

The Adare Basin is a marine basin immediately east of the Adare Peninsula, at the northern end of the Ross Sea. It was formed as an arm of a ridge-ridge-ridge triple junction (Cande et al., 2000). The ridge accommodated 140-170 km of ENE-WSW extension (Cande et al., 2000; Cande and Stock, 2006; Granot et al., 2013). Subsequent separation was accommodated by normal faulting, creating a rifting graben, the Adare Trough (Granot et al., 2010, 2013). The Adare Basin is underlain by a set of magnetic anomalies that strike NNW-SSE which constrain its formation to 43-26 Ma (Cande et al., 2000). These magnetic anomalies have been shown to extend into the Northern Basin, the closest Ross Sea continental crustal basin, indicating a link between Adare seafloor spreading and the extensional tectonics of the western Ross Sea (Cande and Stock, 2006; Davey et al., 2006). Further evidence of the tectonic connection includes a continuous Bouguer anomaly and contiguous sedimentary sequences in these two basins (Cande and Stock, 2006; Davey et al., 2006).

4.2.2. A brief magmatic history

The McMurdo Volcanic Group is considered one of the most extensive alkali volcanic provinces in the world, stretching along the entire western boundary of the Ross Sea and greater WARS (Kyle et al., 1990; Fig. 4.1). It is made up of Cenozoic basaltic shield volcanoes, trachytic or phonolitic stratovolcanoes and scattered basaltic cinder cones, lava flows, and evolved lava domes (Kyle et al., 1990). The McMurdo Group is regionally subdivided into the Balleny, Erebus, Melbourne, and Hallett volcanic provinces. While unique tectonic settings contribute to different rock types within each volcanic province, the McMurdo Group can be described as silica-undersaturated and alkaline (Kyle et al., 1990).

The Melbourne volcanic province extends northward from Mount Melbourne to the south/southwestern boundary of the Hallett volcanic province and can be subdivided into four major volcanic fields (Malta Plateau, The Apeiades, Mount Overlord, and Mount Melbourne) with a series of small basaltic vents and lava flows that are located mainly in the Transantarctic Mountains (Kyle et al., 1990). Lava compositions range from basaltic to felsic and peralkaline compositions with stratovolcanoes located in the Mount Overlord, the Pleiades and Mount Melbourne sub-provinces (Kyle et al., 1990). Malta Plateau lavas are the oldest of this province (6-11Ma) whereas Mount Overlord is the oldest stratovolcano (7.2Ma; Kyle et al., 1990).

Similar to the Melbourne province, the Hallett volcanic province consists of N-S elongated shield volcanoes that occur at the Adare Peninsula, Hallett Peninsula, Daniell Peninsula, and Coulman Island. Associated volcanic rocks also occur on the Possession Islands. The southernmost volcano, Coulman Island, is the oldest (~10 Ma) dated volcanic edifice, whereas the Adare Peninsula is the youngest (0-13 Ma; Kyle et al., 1990). The Hallett volcanic group shows little variation and is predominantly basanites, alkali basalts and hawaiites. However, both the Hallett and Adare peninsulas trend to more evolved lava compositions (Kyle et al., 1990).

Additional volcanism covering an area of ~35,000 km^2 was relatively recently discovered in the adjacent Adare Basin based on ocean bottom bathymetry (Panter and Castillo, 2007). These small volcanic centers exhibit a N-S orientation, similar to regional faulting, and are aligned with the Hallett province volcanism (Panter and Castillo, 2007; Panter et al., 2018). The relative young (~2.88 Ma; Panter et al., 2018) ages of these volcanoes were first determined by seismic stratigraphic relationships (Granot et al., 2010), which additionally showed these volcanic centers are a continuation of continental WARS volcanism. Follow-up Ar-Ar dating has further demonstrated this relationship (Panter et al., 2018).

4.3. Methods

Samples analyzed in this study consist of submarine lavas collected by dredging from the Adare Basin seamounts and local crust during the US National Science Foundation (NSF) funded NBP0710 expedition in the Northwestern Ross Sea aboard the icebreaker RV/IB Nathaniel B. Palmer in the Austral summer of 2006-2007 (Panter and Castillo, 2007; Panter et al., 2018). Subaerial samples from the volcanic provinces were obtained from the Polar Rock Repository (PRR), Byrd Polar and Climate Research Center (http://research.bpcrc.osu.edu/rr/), and were collected in various prior field expeditions. The first set of samples, including those used by Panter and co-workers (Panter and Castillo, 2007; Panter et al., 2018), were crushed in a tungsten carbide-lined jaw crusher into cm-sized fragments, examined megascopically to remove visibly altered chips, and powdered using a Spex alumina ceramic grinding container. Major element oxide and some trace element analyses were performed by X-ray fluorescence (XRF) spectrometry at the GeoAnalytical Laboratory of Washington State University (WSU) using the procedure described by Johnson et al. (1999). Additional trace elements were analyzed at the Scripps Isotope Geochemistry Laboratory (SIGL). For the analysis, 50 mg of sample powder was dissolved and analyzed using an iCAP Qc ICP-MS following standard analytical procedures outlined in Day et al (2014). Data quality was monitored via repeated measurements of international standards (BHVO-2, BCR-2 and BIR-1) and total procedural blanks.

These powders were also used for all Sr, Nd, and Pb isotope analyses, which were performed at Scripps Institution of Oceanography (SIO) according to methods described by Janney and Castillo (1996). Strontium and rare earth elements (REE) were initially separated using cation-exchange columns and HCl as eluent. The REE cut underwent a second separation using hydroxyisobutyric acid as eluent to isolate Nd for isotope analyses. Lead separation was conducted using standard anion exchange methods in an HBr medium. All Pb-Sr-Nd isotope ratios were analyzed using a 9-collector, Micromass Sector 54 thermal ionization mass spectrometer (TIMS). A subset of these powders was investigated for Re-Os isotope systematics at State Key Laboratory of Isotope Geochemistry at Guangzhou Institute of Geochemistry. These measurements used a Carius tube digestion procedure similar to that described by Li et al. (2010). Approximately 0.5-2 g of powdered sample was spiked with ^{185}Re and ^{190}Os and digested in reverse aqua regia in sealed Carius tubes at 240°C for twenty-four hours. Osmium was separated using a single solvent extraction into CCl_4 prior to a back extraction into concentrated HBr. Finally, samples were microdistilled. Rhenium was then separated from the residual aqua regia using anion column chromatography.

In a later part of the study, rock powders free from any metal preparation were crushed and powdered in alumina ceramic containers prior to HSE abundance and ^{187}Os/^{188}Os analyses, also at SIGL. Samples with >6 wt.% MgO were selected for the analyses (n=19). Approximately 800 mg of homogenized powder was combined with multi-element spikes (^{185}Re, ^{106}Pd, ^{194}Pt, ^{191}Ir, ^{99}Ru, ^{190}Os) prior to digestion in a sealed borosilicate Carius tube. The exceptions are

$A210B_1$ = 0.20440 g, AW82214 = 0.38124 g, $A233D_1$ = 0.35294 and $A232B_1$ = 0.71194 which used the entirety of the sample. Digestion used a 1:2 mixture of multiply Teflon-distilled HCl and Os-purged HNO_3 heated to a maximum temperature of 270°C for 72 hours. Osmium was separated using a triple-extraction of CCl_4 and back-extracted into HBr (Cohen and Waters, 1996) prior to double micro-distillation (Birck et al., 1997; Day et al., 2016). The other HSE were recovered and extracted using column anion exchange separation techniques (Day et al., 2016).

4.3.1 Rhenium-osmium inter-laboratory comparison

Twelve samples were analyzed at both SIGL and State Key Laboratory of Isotope Geochemistry to monitor the consistency between measurements made in the two laboratories. The $^{187}Os/^{188}Os$ measurements have very good agreement (R^2 = 0.9855) and fall on a 1:1 ratio line, with the exception of A232B and P74833 (Fig. 4.2a). However, systematic inconsistencies are observed in $^{187}Re/^{188}Os$ values (Fig. 4.2b; R^2 = 0.9509) as SIGL measurements have systematically higher $^{187}Re/^{188}Os$ values. Again, samples P74833 and A232B show the highest degree of deviation from the correlation line.

Rhenium and Os concentration measurements in the two laboratories also do not have good agreement. This may be due to a “nuggeting effect,” as a result of inefficient mixing or settling of olivines from matrix material in the powders. Since Os partitions strongly into olivine a small degree of settling and mixing of sample powder could account for the lower Os concentrations observed from State Key Laboratory measurements. Another possible reason for the differences in Re and Os measurements could be interference from W. As the powders used for State Key Laboratory measurements were prepared using a tungsten carbide-lined jaw crusher, these may have been contaminated with W. This is most likely the scenario and, thus, we do not use the State Key Laboratory HSE concentration measurements in the following discussion. In any case, the agreement between ^{187}Re/^{188}Os and ^{187}Os/^{188}Os makes the isotope measurements from both laboratories valid and, thus, are used in this investigation.

4.4. Results

4.4.1 Major elements

Major element analyses are presented in Table 4.1. The samples analyzed consist of lava suites from Hallet-Melbourne provinces (hereafter HMp), Possession Island (hereafter PI), Adare Peninsula (hereafter AP), and ABS that were selected to constrain the composition of magmas that penetrate the lithosphere and overlying crust transitioning from continental to oceanic (Fig. 4.1b). The majority of samples from the continental-oceanic transect are basanites and the remainder are alkalic basalts, trachybasalts, basaltic trachyandesites, trachydacites, a trachyandesite, and a rhyolite (Fig. 4.3a). In detail, the bulk of ABS and PI lavas erupted on oceanic crust are highly alkalic, similar to the basanites from seamounts and Franklin and Beaufort islands in the adjacent Terror Rift region in the southern Ross Sea (Aviado et al., 2015). Both basanite suites, in turn, mainly plot in the field for the Erebus volcanic province (LeMasurier and Thomson, 1990; Kyle et al., 1992). Samples from AP and HMp erupted on continental crust are mainly alkalic basalts and plot within the field for the Melbourne-Hallett volcanic province (LeMasurier and Thomson, 1990; Armienti et al., 1991). A few lavas are highly evolved, with an ABS rhyolite having 72 wt.% SiO_2. This rhyolite also exhibits an unusual depletion in $Na_2O + K_2O$ values, a feature that is also observed in some of the highly evolved lavas from all WARS volcanic provinces (LeMasurier and Thomson, 1990; Armienti et al., 1991; Kyle et al., 1992).

Sample suites from the different volcanoes define generally overlapping negative SiO_2, K_2O and Na_2O, and positive TiO_2, FeO* and CaO trends with increasing MgO (Figs. 4.3b-h). In general, these trends are similar to the basaltic to rhyolite fractional crystallization trends of some, though not all, samples from the WARS volcanic provinces (e.g., Kyle et al., 1990; Armienti and Perinelli, 2010). Some of the basaltic samples (< 52 wt.% SiO_2) from each lava suite are quite primitive (> 8 wt.% MgO) and could be representative of parental liquids to more differentiated lavas. For the differentiated lavas, Al_2O_3 contents show an obvious inflection with MgO at ~4 wt.%, consistent with the removal of feldspar or feldspathoids and/or mica (Fig. 4.3c). A subtle difference among the continent-oceanic lava suites is discernable in the fractionation trend of the incompatible element K (Fig. 4.3g) that is consistent with the relative alkalinity of the suites (Fig. 4.3a). At > 5 wt.% MgO, ABS samples have the highest K_2O whereas AP samples have the lowest, and PI and HMp samples have intermediate contents (Fig. 4.3g). A similar, though poorer relationship is shown by the moderately incompatible element Na in the Na_2O versus MgO trend (Fig. 4.3h). At > 5 wt.% MgO, the ABS and PI Na_2O values on average are higher than those of the AP and HMp lava suites. Such differences, however, are not displayed by the fractionation trend of the incompatible element Ti (Fig. 4.3d) and P_2O_5 concentration (Table 4.1).

4.4.2 Trace elements

All samples are enriched in incompatible trace elements relative to primitive mantle, similar to ocean island basalts (OIB; Fig. 4.4a). They display overlapping concentration patterns that partially overlap with, although in lower absolute concentration, than southern Ross Sea and NVL data (Aviado et al., 2015). The same is true for REE, which also show that the ABS sample suite has higher REE concentrations than the AP suite (Fig. 4.4b), consistent with the subtle differences shown by some of the major oxides (Fig. 4.3). Both PI and HMp sample suites again have intermediate values. The same relationship is shown in Figure 4.4c, where the ABS suite on average has higher La/Sm_N ratio than the AP suite whereas the PI and HMp suite La/Sm ratios are highly variable for given MgO values.

Figure 4.5 shows plots of incompatible trace element contents and ratios against MgO for the different sample suites from the continent-ocean transect. A distinction between ABS and AP plus HMp sample suites can clearly be seen in their Nb and Zr contents as the former on average have higher Nb and Zr contents than the latter, with PI samples having intermediate average values. The Th/La ratio also shows a sort of distinction, with the ABS samples suite on average having lower values than the other three suites. Although no clear differences among the sample suites are shown by the Nb/U and Ce/Pb against MgO, it is important to note that almost all the samples plot around or above the mantle values (Nb/U = 45 ± 10, Ce/Pb = 25 ± 5; Hofmann et al., 1986).

4.4.3 Strontium, neodymium and lead isotopes

The samples have a relatively large range of $^{87}Sr/^{86}Sr$ (0.702874-0.703307), $^{143}Nd/^{144}Nd$ (0.512803-0.513001) and $^{206}Pb/^{204}Pb$ (19.237-20.237) ratios (Table 4.1; Fig. 4.6). These values are completely within the range of isotopic analyses for WARS lavas including those reported in previous continent-oceanic transect investigations (Panter and Castillo, 2007; Aviado et al., 2015; Panter et al., 2018). On average, the oceanic ABS and PI lava suites have slightly higher $^{143}Nd/^{144}Nd$ and lower $^{87}Sr/^{86}Sr$ than the continental AP lava suite; this is consistent with some of the major and trace element differences described earlier. However, their $^{206}Pb/^{204}Pb$ completely overlap although most of the ABS samples have low values. The latter samples together with many PI samples also form $^{207}Pb/^{204}Pb$ and $^{208}Pb/^{204}Pb$ for given $^{206}Pb/^{204}Pb$ arrays that are slightly lower than the AP lava suite. Interestingly, the two HMp samples are split between the two groups, with the Hallet Province sample (PRR-3839) similar to AP samples whereas the Melbourne Province sample (MA-117) similar to ABS samples.

In general, the samples show coherent negative ^{87}Sr/^{86}Sr versus ^{143}Nd/^{144}Nd array and positive ^{207}Pb/^{204}Pb and ^{208}Pb/^{204}Pb versus ^{206}Pb/^{204}Pb arrays that are typically shown by many oceanic lavas. They plot in the so-called focus zone (FOZO; see also, Aviado et al., 2015; Panter et al., 2018) where oceanic lavas converge in any ternary permutations of the Sr-Nd-Pb-Hf isotopic diagrams (Hart et al., 1992; Hauri et al., 1994; Castillo, 2017), although as mentioned earlier a number of previous studies had interpreted the WARS isotopic signature as HIMU-like (Panter, 2006; Nardini et al., 2009; Martin et al., 2013; Aviado et al., 2015; Panter et al., 2018). Although overlapping, the new analyses have generally higher ^{143}Nd/^{144}Nd and lower ^{87}Sr/^{86}Sr, ^{206}Pb/^{204}Pb, ^{207}Pb/^{204}Pb, and ^{208}Pb/^{204}Pb than CVL lavas (www.earthchem.org/petdb). Significantly, the Sr, Nd and especially Pb isotopic characteristics of the CVL lavas, which are similarly erupted in both continental and oceanic settings, are generally characterized as HIMU-like (Fitton and Dunlop, 1985; Hart et al., 1992; Ngwa et al., 2017). Moreover, some continental EARS lavas are HIMU-like (e.g., Furman et al., 2006; Rooney and Deering, 2014).

4.4.4 Rhenium-osmium isotopes and HSE abundances

The HSE abundance patterns for the Antarctic samples are similar to those of basaltic melts that have experienced different extents of fractional crystallization (Day, 2013). The most comparable HSE (Os, Ir, Ru) show decreasing abundance with decreasing MgO, with the highest abundances occurring in an ABS and AP sample (Table 4.2; Fig 4.7; D4-1, D4-1rpt, A210B). These samples have some of the highest MgO contents in the continental-oceanic transect. The lowest Os, Ir and Ru concentrations are observed in the AP sample suite (P74833 and A232B), which have some of the lowest MgO contents (Table 4.2). Compared to Os, Ir and Ru, Pd and Re abundances in samples are significantly less variable and in higher abundances relative to the primitive mantle normalization, with Pt being at lower relative abundances.

The samples show an extreme range of values for both ^{187}Os/^{188}Os (0.12548-1.166) and ^{187}Re/^{188}Os (4.1-2577; Table 4.2, Fig. 4.8), and do not define a single isochron, but instead show significant scatter on a ^{187}Re/^{188}Os-^{187}Os/^{188}Os diagram. Although ^{187}Os/^{188}Os values do not correlate well with MgO content, the most radiogenic values are observed in the lowest MgO samples. The highest MgO lavas from the suite which both have 13.3 wt.% MgO include the AB sample D-1 with ^{187}Os/^{188}Os of 0.1255, and the AP A210B sample with ^{187}Os/^{188}Os of 0.1465. Although the transect samples do not form linearly coherent trends between ^{187}Os/^{188}Os and ^{187}Re/^{188}Os (Fig. 8a), ^{187}Os/^{188}Os has a positive curved relationship with ^{87}Sr/^{86}Sr (Fig. 4.8b) but a negative curved relationship with both εNd and ^{206}Pb/^{204}Pb (Figs. 4.8c and 4.8d). Adare Peninsula samples have the widest range in ^{187}Os/^{188}Os values, having both oceanic and continental values (P74833=1.166). Adare Basin seamount samples with MgO > 6 wt.% have the second largest range in ^{187}Os/^{188}Os (0.12548-0.79790). Possession Island and HMp samples are mostly similar to ABS samples with the exception of MA117, which was sampled from the Melbourne Province further inland at the Malta Plateau.

4.5. Discussion

Panter et al. (2018; see also Panter and Castillo, 2007) showed systematic compositional variations in different lava types from the WARS continent-oceanic transect. The new results compliment and extend existing data for these previous investigations. The new data also show regular compositional variations between lavas erupted in oceanic and continental crust settings (Fig. 4.9). The observed variations hold crucial information on the source(s) and formation mechanism of alkaline magmatism in WARS and, thus, need to be fully understood. To assess if there are indeed compositional similarities and differences in the mantle source of continent-ocean transect samples, it is first necessary to consider whether the effects of magmatic differentiation processes and crustal contamination could have produced the observed geochemical signatures.

4.5.1 Assimilation and fractional crystallization processes

Evidence of fractional crystallization in the samples can be seen in the systematic behavior of the major oxides and trace elements with decreasing MgO, including the aforementioned inflection of the Al_2O_3 trend that probably represents the onset of feldspar and/or feldspathoid precipitation (Fig. 4.4). These trends generally form liquid lines of descent with little variation, despite the continental and oceanic locations of the samples. Thus, there is plenty of evidence that fractional crystallization is responsible for some of the geochemical and lithologic variations that are observed in WARS lavas (see also, e.g., Panter, 2006; Nardini et al., 2009; Martin et al., 2013; Aviado et al., 2015; Panter et al., 2018). This begs the question; what other secondary processes are either partially or primarily responsible for the systematic continent-ocean compositional variation of WARS lavas?

4.5.1.1. Evidence for crustal contamination from Re-Os and O isotopes

As highly siderophile elements are compatible elements, HSE concentrations in the ocean-continent transect are controlled by fractional crystallization (Figs 4.8 and 4.10). Consequently, HSE-content decreases with increasing fractional crystallization. The fractionation model in Figure 4.8 shows the differences between the most primitive samples (i.e. MgO > 10%) and the most evolved (i.e. MgO = 7-8%). The model affirms that fractional crystallization has occurred in the WARS system. This relationship can also be seen in Figure

4.10a, with a sharp decrease in Os-content with decreasing MgO. However, fractional crystallization (i.e. decreasing MgO) does not have the same control on $^{187}Os/^{188}Os$, as shown in Figure 4.10b. While HSE abundance is usually controlled by fractional crystallization processes, crustal contamination also has a dilutional effect on HSE abundance, but will disproportionately increase radiogenic $^{187}Os/^{188}Os$ (e.g. Fig. 4.8; Day, 2013). Continental crust $^{187}Os/^{188}Os$ is typically in the range of 1.1 ± 0.2 in comparison to primitive mantle values ($^{187}Os/^{188}Os$ = 0.1296; Meisel et al., 2001; Day, 2013). Assimilation of continental crust (i.e. radiogenic, low-Os concentrations) by a primitive melt (i.e. unradiogenic, high Os) will lower Os concentrations, but increase $^{187}Os/^{188}Os$. This makes the Re-Os isotope system a sensitive indicator of crustal contamination.

Adare Peninsula samples have some of the lowest HSE abundances (especially Os, Ir, Ru) and the largest range in $^{187}Os/^{188}Os$ (Figs. 4.8 and 4.9). For instance, olivine grains in AP samples have low Fo contents (Fig. 4.13a) while samples with high MgO still have more radiogenic $^{187}Os/^{188}Os$ ratios (i.e. A210B = 0.14654) than typical mantle values. Similarly, the HMp continental samples have elevated $^{187}Os/^{188}Os$, low MgO and their olivines have low Fo contents (Figs. 4.9, 4.10, and 4.13a). On the other hand, the most primitive ABS lavas (> 7 wt% MgO; except D4-3) have the highest Os abundances, mantle-like $^{187}Os/^{188}Os$ values and olivines with the highest Fo content (Figs. 4.9, 4.10 and 4.13a) among the transect samples. The most primitive ABS sample, D4-1 (MgO = 13.3 wt. %) has a mantle signature with $^{187}Os/^{188}Os$ value of 0.125-0.129 whereas the most primitive sample from the crustally-contaminated Adare Peninsula (A210B; MgO = 13.3 wt, %) has a higher $^{187}Os/^{188}Os$= 0.146.

The observed ranges in $^{187}Os/^{188}Os$ suggest the presence of an old, radiogenic component within the ocean-continent transect. The decay of the Re-Os system can be modeled on isochrons that reflect the time of a melt's crystallization. Figure 4.9 models two isochrons that show the evolution of mantle samples that crystallized at 100 Ma and 1 Ga, respectively. Samples from the ocean-continent transect plot between these two isochrons, indicating either an intermediate age or mixing between young and old mantle components (i.e. crustal contamination) has taken place. However, the ocean-continent samples cannot be modeled by a single isochron, which would be consistent with an intermediate crystallization age. The fact that the transect samples do not fall along a single isochron suggests that mixing occurred between old and young mantle, to varying degrees.

Oxygen isotopes are also sensitive tracers of contamination, and contamination type as they are major components of silicate rocks (>40% of total). Various igneous reservoirs have increasing $\delta^{18}O$ with increasing SiO_2. However, alteration via hydrothermal or meteoric waters can lead to decreasing $\delta^{18}O$ as meteoric water is progressively fractionated by precipitation at higher latitudes (Craig, 1961). Consequently, Antarctic precipitation has been well-established as strongly negative ($\delta^{18}O$ as low as -32‰; Gonfiantini and Picciotto, 1959) but typical continental crust $\delta^{18}O$ is much more positive (e.g. Transantarctic Mountains $\delta^{18}O$ = ~10‰; Molzahn et al., 1996). Such a wide range of $\delta^{18}O$ values could generate a wider range of local contamination effects, some of which may be different from that exhibited by the AP samples. This range of $^{187}Os/^{188}Os$ and $\delta^{18}O$ can be used to assess the type of crustal contamination in this old, high-latitude continental crust system.

The types of contaminants in the WARS can best be distinguished by contamination models in Figure 13b. Continental samples (i.e. AP and HMp samples) and PI samples indicate varying degrees of contamination from two types of contaminants. Both models use mantle $^{187}Os/^{188}Os$ and $\delta^{18}O$ and lower crustal $^{187}Os/^{188}Os$ and Os concentrations from Molzahn et al.

(1996). Model 1 shows contamination of a picritic melt by a lower crustal component whereas the contaminant of Model 2 has been fitted to PI samples. Notably, AP samples still have mantle-like $\delta^{18}O$ (typically 5.3 ± 0.3; King et al., 1998) for given $^{187}Os/^{188}Os$ values (Fig. 4.13b). Adare Peninsula samples fit Model 1 and show a range of contamination (>40%). By comparison, oceanic PI samples do not have the wide range of Os isotopes observed in AP samples. However, PI samples also have lower $\delta^{18}O$ but a smaller range of $^{187}Os/^{188}Os$ (Fig. 4.13b). The difference in the range in $^{187}Os/^{188}Os$ and $\delta^{18}O$ may indeed reflect modification of their O isotopes by isotopically light $\delta^{18}O$ material. That is, PI lavas most likely assimilate a hydrated oceanic crust with low $\delta^{18}O$ values but a less radiogenic Os isotope signature. That is, rather than having an upper crustal or sediment-like values (e.g. $\delta^{18}O$ = 8‰; Molzahn et al., 1996), low PI $\delta^{18}O$ values are indicative of contamination by crustal material that may have been altered by weathering with an isotopically light $\delta^{18}O$ signal.

4.5.1.2. Crustal contamination in incompatible trace elements and Sr-Nd-Pb isotopes?

Samples from this ocean-continent transect were previously analyzed by Panter et al. (2018), though crustal contamination was rejected as a mechanism to explain the geochemical trends of these samples. However, as previously discussed, new HSE and Re-Os isotope data indicate crustal contamination plays a significant role in WARS geochemistry. This new data in conjunction with Sr-Nd-Pb isotopes can reveal some subtle geochemical modifications to WARS lavas from crustal contamination.

The ocean-continent transect samples separate themselves into two groups in Sr-Nd-Pb isotope space (Fig. 4.7). Specifically, the Sr, Nd and Pb isotope ratios of AP samples are clearly offset from the majority of transect samples and previously published WARS data (Fig. 4.7;

Panter, 2006; Nardini et al., 2009; Martin et al., 2013; Aviado et al., 2015; Panter et al., 2018). These results could be interpreted as indicative of either two separate sources or an effect of crustal contamination. However, when Sr-Nd-Pb isotopes are considered relative to geographic location (i.e. transitioning from oceanic to crustal samples), $^{87}Sr/^{86}Sr$ increases while εNd and $^{206}Pb/^{204}Pb$ decrease (Fig. 4.12). These changes suggest an enriched component (i.e. EMI) and are consistent with the HSE, Re-Os and O isotope data, further indicating that crustal contamination plays a significant role in the WARS.

While the degree of contamination in our sample suite is variable, the effects are most clearly seen in AP continental samples (Fig. 4.11). On average, AP samples have the highest $^{87}Sr/^{86}Sr$ but the lowest εNd and $^{206}Pb/^{204}Pb$, trending towards EMI or enriched continental crust values. The aforementioned curved relationships are consistent with illustrative crustal contamination or mixing models between a primitive, picritic melt and a lower-crustal signature with a $^{187}Os/^{188}Os = 3.5$ (Fig. 4.11; after Molzahn et al., 1996). Average picrite Nd, Sr and Pb concentrations are from Norman and Garcia (1999) and lower crust $^{206}Pb/^{204}Pb$ values are from Rudnick (1995). The ranges of $^{87}Sr/^{86}Sr$, εNd and $^{206}Pb/^{204}Pb$ versus $^{187}Os/^{177}Os$ values of the few HMp samples analyzed also generally overlap with that of AP samples (Figs 4.11). However, HMp samples are less contaminated than AP samples (20-80% contamination; 4.11). Similarly, PI samples also indicate contamination of Sr-Nd-Pb isotopes has occurred in these samples, though not to the same extent as AP or HMp samples. The primitive, alkaline and geochemically most enriched ABS oceanic sample suite are the least contaminated among the WARS samples though the less primitive ABS lavas (<7 wt% MgO) have relatively higher $^{87}Sr/^{86}Sr$ and generally lower εNd than the rest of ABS samples. These ABS samples generally approach the Sr and Nd isotopic values of the crustally contaminated AP samples and, thus, are also slightly contaminated.

Using the most primitive ABS samples as a model source, the crustal contamination models in Figure 4.11 indicate that the variations of WARS lavas are controlled by both the extent and type of crustal contamination. Contamination is pervasive in the WARS, though it is possible to assess the mantle source of the WARS lavas through the geochemical effects of contamination. The high $^{143}Nd/^{144}Nd$, generally high $^{206}Pb/^{204}Pb$ and low $^{87}Sr/^{86}Sr$ values of primitive ABS samples best represent the isotopic composition of mantle source of WARS magmas (see also, Panter et al., 2018). In other words, all the continental-oceanic transect samples come from a common mantle source, but the some of the samples are variably contaminated by crustal (AP and HMp continental samples) or hydrous (PI oceanic samples) materials.

4.5.2 The mantle source of WARS alkaline lavas

Models for the origin of WARS alkaline magmatism generally converge to the question of whether the magmas come from either a mantle plume or a subduction fluid-metasomatized CLM source. The radiogenic signature and incompatible trace element enrichment exhibited by the WARS samples have been interpreted as indicative of a HIMU-type mantle plume source (Kyle et al., 1992; Rocholl et al., 1995; Sims et al., 2008). However, both geochemical and geophysical indicators of a plume or fossilized plume are lacking in the WARS (Nardini et al., 2009; Aviado et al., 2015; Panter et al., 2018; Day et al., 2019). For example, Cenozoic lavas from the NVL have $^{3}He/^{4}He$ values from 5.7-7.2R_A (Nardini et al., 2009). These $^{3}He/^{4}He$ values are too low to be indicative of a deep, non-degassed plume source. Furthermore, despite the presence of a low-velocity thermal anomaly beneath Ross Island (Hansen et al., 2014), its shallow depth and broad extent is inconsistent with the dimensions and extent of the plume proposed by Kyle et al. (1992) and other proponents of the plume model (Aviado et al., 2015).

An alternative hypothesis of WARS alkalic volcanism posits that the CLM source in the WARS was metasomatized by fluids originating from Mesozoic Phoenix plate subduction at the Gondwana margin. Metasomatic models argue for a fertilization of the CLM in the form of metasomes created by the interaction of the mantle wedge and slab-derived fluids (i.e. aqueous fluids, silicate melts and/or supercritical silicate-aqueous fluids; Aviado et al., 2015). Fertilization of CLM by such LILE-enriched fluids and subsequent radiogenic decay of ^{87}Rb, ^{235}U, ^{238}U, and ^{232}Th could explain the geochemically enriched signature high μ, FOZO-like Sr and Pb isotopic ratios of WARS lavas (Finn et al., 2005; Panter et al., 2018). These heterogeneities would be more susceptible to small-degree partial melting as a result of rifting in the Cenozoic, either resulting in eruption or further interaction with a refractory mantle (Panter et al., 2018; Day et al., 2019).

However, a metasomatized CLM source for WARS lavas is most likely not a mantle fertilized by typical subduction-related fluids. Arc magmas generated from such a subduction fluid-metasomatized mantle are distinctively depleted in high field-strength elements (HFSE), particularly Nb, and enriched in Pb (e.g., Wilson, 1989). However, alkaline lavas in the WARS are generally enriched in HFSE or display the so-called positive TITAN concentration anomaly (Jackson et al., 2007; Peters and Day, 2014) and negative Pb concentration anomaly that are typically possessed by OIB (Fig. 4.5). WARS lavas also exhibit mantle-like or higher Ce/Pb and Nb/U ratios in contrast to the characteristically low Ce/Pb and Nb/U ratios of arc lavas generated from a subduction fluid-metasomatized mantle (Fig. 4.6; Hofmann et al., 1986). Furthermore, many arc lavas have higher ^{87}Sr/^{86}Sr for given ^{143}Nd/^{144}Nd due to the greater aqueous fluid mobility of Sr relative to Nd (Zindler and Hart, 1986), though WARS samples do not exhibit this behavior. Similarly, oxygen isotopes do not indicate a subduction component in the WARS mantle source. The different reservoirs of δ^{18}O within the subducting slab (e.g. sediments, carbonates, hydrated upper oceanic crust) have recognizable signatures that are typically isotopically heavier than the δ^{18}O values measured in the WARS samples (Bindeman et al., 2005 and references therein). Rather, δ^{18}O, ^{87}Sr/^{86}Sr and ^{143}Nd/^{144}Nd indicate the presence of a fertilized mantle with a FOZO signature rather than metasomatized CLM source.

As discussed in the previous section, primitive ABS samples reveal the characteristic features of the mantle source of WARS alkaline magmatism. Figure 4.14 isolates the contaminated WARS samples using ^{187}Os/^{188}Os versus ^{206}Pb/^{204}Pb (inset), revealing the mantle source of the WARS lavas. Adare Basin ^{187}Os/^{188}Os = 0.129 are primitive mantle values and fairly radiogenic Pb isotopic values (^{206}Pb/^{204}Pb = 19.30 to 20.24). Their ^{87}Sr/^{86}Sr and ^{143}Nd/^{144}Nd data also indicate their mantle source has a long-time integrated history of geochemical depletion as they plot roughly between the values of primitive mantle or bulk silicate Earth (BSE) and the depleted mantle source of MORB (DMM; Fig. 4.7). These also mean that the mantle source does not originate from, or is not heavily contaminated by, a geochemically enriched continental material represented by EM1. As a whole, WARS lavas have the compositional features of FOZO (Hart et al., 1992; Hauri et al., 1994). The origin of the FOZO-like signature of the ABS lava suite can then be used to evaluate the origin of Cenozoic alkalic volcanism in the WARS.

The similarity of WARS alkaline lavas to global OIB is especially relevant to the origin of FOZO in the WARS. Ocean island basalts most likely come from recycled crustal materials, or crustal materials that had already gone through subduction dehydration, where FOZO is a ubiquitous component of all OIB (Hart et al., 1992; Hauri et al., 1994; Hanan and Graham, 1996; Stracke et al., 2005; Jackson et al., 2007; Castillo, 2015). Critically, FOZO could not have been directly fertilized by subduction-related fluid as the bulk of OIB are erupted away from active or prior subduction environments. Instead, FOZO most likely comes from recycled slab material and represents a fertilized mantle (Day et al., 2010; Castillo, 2015). In the case of WARS alkaline magmatism, the FOZO-like signature likely resulted from melting upwelling fertile mantle as a result of extension. While fertilization of a depleted mantle wedge by subduction fluids and small degree partial melts and melting facilitated by extensional tectonics likely occurred (Panter et al., 2018; see also, Day et al.,2019), the majority of WARS samples do not have the expected arc lava geochemical signatures from metasomatized CLM.

4.5.3 Constraints from the other ocean-continent volcanic transects

As noted earlier, continent-oceanic alkaline volcanism also occurs along the Cameroon volcanic line (CVL) and East African Rift System (EARS), making these tectonic settings interesting analogs or comparison points for the origin of WARS alkalic lavas. The CVL consists of a series of plutonic and volcanic centers from the island of Pagalu through Cameroon and into the central part of Africa (Ngwa et al., 2017), passing between the West African and Congo cratons. The CVL originates from the boundary between these cratons and, consequently, has a thicker and older lithosphere than the WARS. The most widely accepted hypothesis for its origin posits mantle upwelling (hotlining) in a SW-NE linear orientation due to reactivation of Pan-African lineaments between the cratonic blocks which creates enriched heterogeneities as a result of repeated mixing between compositionally diverse melts (Ngwa et al., 2017). The EARS, an intra-continental ridge system, is frequently interpreted as a representative model of early rifting systems where magmatism is intricately tied to both mantle plume and lithospheric thinning

(Chorowicz, 2005). The EARS is comprised of two main rift valleys, the Eastern and Western branches which diverge around the Tanzanian craton. However, the eastern-bounding Southeastern branch, or Mozambique channel, crosscuts continental and oceanic crust, similar to the WARS.

The EARS represents one of the best studied rift systems in the world, where alkalic magma generation results from either melting of hydrated metasomes within the lithospheric mantle due to thermal perturbations of the lithosphere or due to lithospheric thinning (Rooney, 2020). However, as a consequence of its massive size, EARS volcanism represents one of the largest ranges in lava geochemistry in the world (Rooney, 2020). Accordingly, we only consider samples from the Mozambique ridge and other samples from the Mobile Belt, in contrast to the Cratonic belt of the EARS (Chorowicz, 2005 and references therein). Mobile belt samples have "C", or FOZO-like Sr-Nd-Pb isotopic signatures, similar to that observed in WARS samples. On the other hand, CVL lavas have more radiogenic $^{206}Pb/^{204}Pb$ or are more HIMU-like than WARS samples. Recent studies have also indicated that more radiogenic $^{206}Pb/^{204}Pb$ or the HIMU-like signature is stronger in older lavas and diminishes with time (Wembenyui et al., 2020 and references therein). This means the earliest CVL magmas from the thick continental cratons may have been more contaminated than the younger, more pristine CVL mantle source. In other words, the higher $^{206}Pb/^{204}Pb$ signature or HIMU-like signature of CVL may have come from crustal contamination. Similarly, EARS magmatic alkalinity has declined over time, especially in the Kenya Rift (within the Eastern rift), which transitions from alkaline lavas to transitional lavas ca. 7 Ma. This transition from has not yet been observed in the WARS.

Similar to the WARS, a metasomatized CLM hypothesis has been proposed to account for the alkalic lavas of the CVL. However, the metasomatizing fluid of the CVL is most likely not subduction-related, but probably low-degree partial melts from the sub-lithospheric mantle generated during the extension between the Congo and West African cratons that stalled within the mantle and later mixed with other melts (Ngwa et al., 2017). By contrast, the origin of WARS alkaline lavas is superficially more akin to the origin of alkaline lavas in the EARS (e.g., Rooney, 2019). Both the WARS and EARS were sites of prior plate subduction and, thus, the generation of the bulk of EARS magmas has also been generally tied to a CLM metasomatized by subduction-related fluids (Rooney, 2019 and references therein). However, it is also possible that the CLM in the EARS is metasomatized by partial melts from crustal thinning, similar to that suggested for the CVL.

Contrary to my findings in the WARS, the role of crustal contamination in the EARS and CVL has proven elusive, or is not considered to be a major contributor to alkalic lavas in these systems (Chorowicz, 2005; Ngwa et al., 2017; O’Connor et al., 2019; Rooney, 2020). However, a detailed comparison shows that the slightly more radiogenic Sr and depleted Nd isotopic compositions of CVL lavas are more akin to those of continental WARS samples with Sr and Nd isotopic compositions that have been modified by crustal contamination (Fig. 4.7). Thus, similar to the WARS samples, crustally-contaminated lavas in the CVL modify the true mantle source signature, although the contaminant in WARS is more EMI-like whereas in CVL is more HIMU-like.

4.6. Conclusions

The results of this study indicate that the continental-oceanic samples in the WARS come from a common, FOZO-like mantle source. The new Re-Os and PGE data suggest that crustal contamination is an ancillary process that can strongly affect continental samples and is largely responsible for creating some geochemical trends among the transect samples. Although further work is necessary, the new results indicate that lithospheric-thinning caused FOZO-like mantle upwelling in the WARS. The upwelling FOZO mantle and, to a lesser extent, metasomatized CLM hypothesis can better explain the origin of WARS alkaline magmatism than the plume hypothesis. Furthermore, the compositional similarities between the WARS, EARS and CVL continent-oceanic transect lavas indicate that the HIMU-like isotopic signature most likely come from crustal contamination, and that these systems have a FOZO-like mantle source.

Acknowledgments

This work was funded by National Science Foundation grants (NSF-1333698; EAR 1918322) to P. Castillo and J. Day. All authors certify that there are no financial conflicts of interest related to this work and our results. All data are available in the text.

Chapter 4, in full, is material that is in preparation for submission to Earth Planetary Science Letters as Durkin, K., Day, J. M. D., Panter, K., Xu, J., Juda, N., Castillo, P. R., Causes of isotopic variations across an ocean-continental transition, Ross Sea Embayment, Antarctica. The dissertation author was the primary investigator and author of this work.

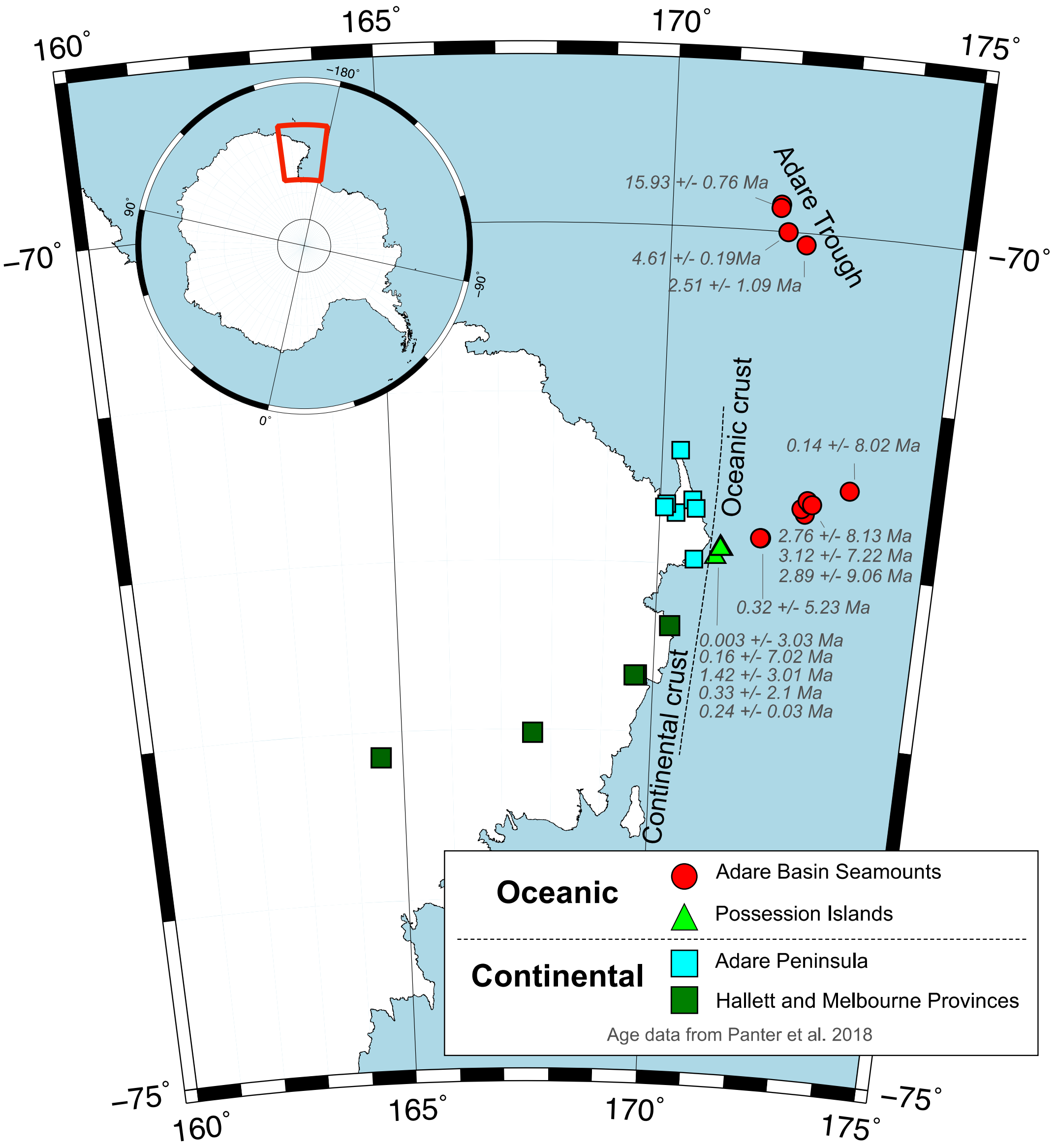

Figure 4.1. Location map of samples from; Adare Basin and Adare Trough (red circles), Adare Peninsula (cyan squares), Possession Islands (green triangles) and continental samples (dark green squares). Inset shows location of study area relative to Antarctic continent. Data from this study and Panter et al. (2018). Ages from Panter et al. (2018).

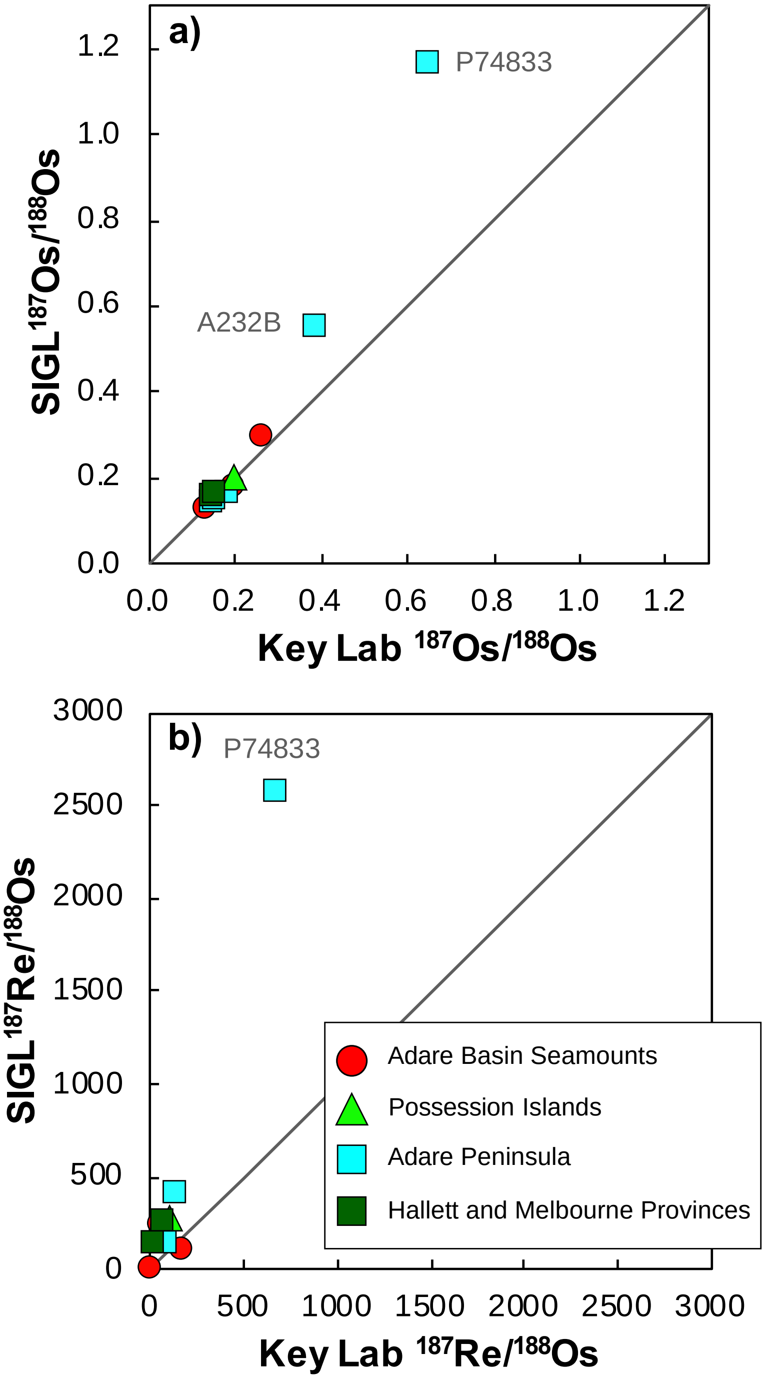

Figure 4.2. Inter-laboratory comparison of a) ^{187}Os/^{188}Os and b) ^{187}Re/^{188}Os of 12 samples with measurements made at both State Key Laboratory and SIGL.

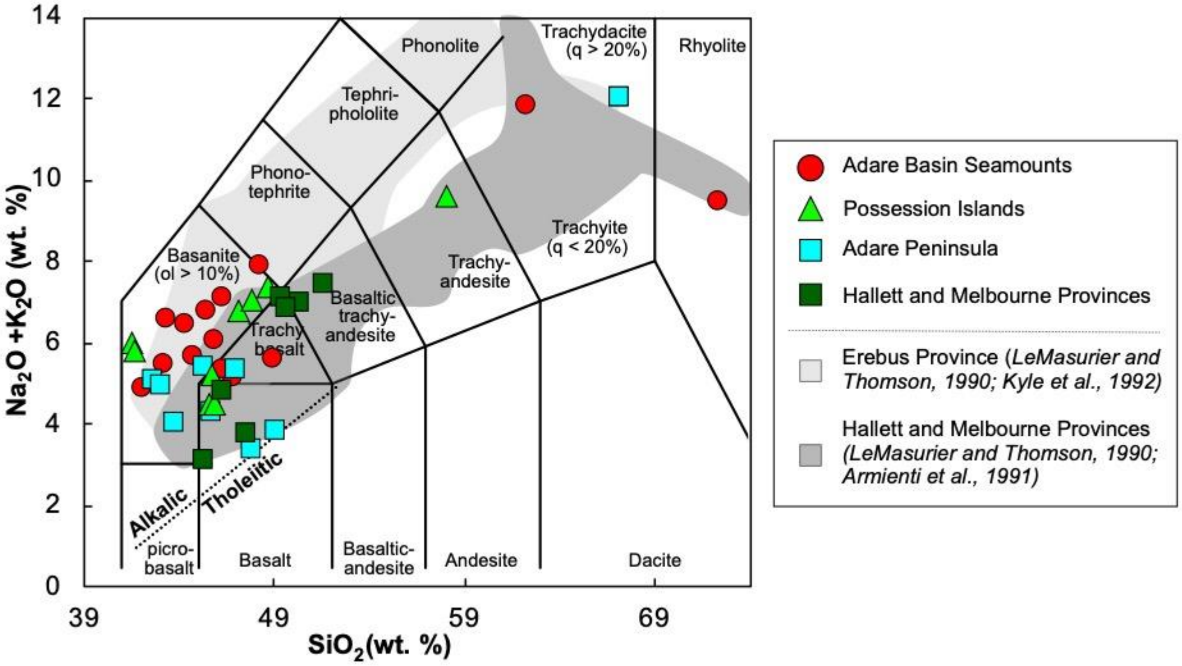

Figure 4.3. Total akali versus silica (after Le Bas et al., 1986). Alkaline-tholeiite line as in Macdonald and Katsura (1964). Light gray shaded region represents data from the Erebus Province (data from LeMasurier and Thompson, 1990 and Kyle et al., 1992). Dark gray shaded region shows data range from the Hallett and Melbourne provinces (data from LeMasurier and Thompson, 1990 and Armienti et al., 1991).

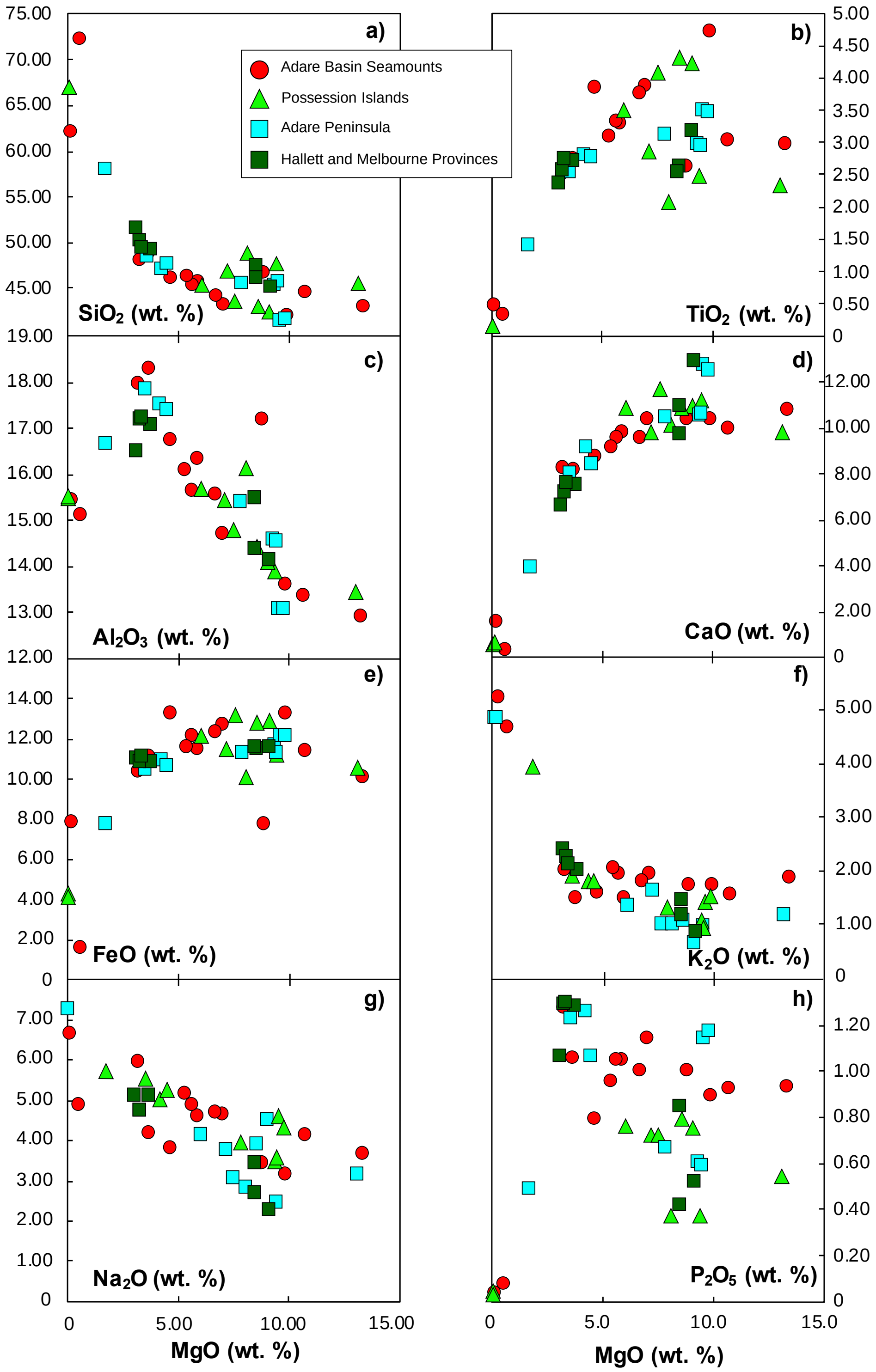

Figure 4.4. Various major oxide concentrations versus MgO. All symbols for continental -ocean transect as in Figure 1.

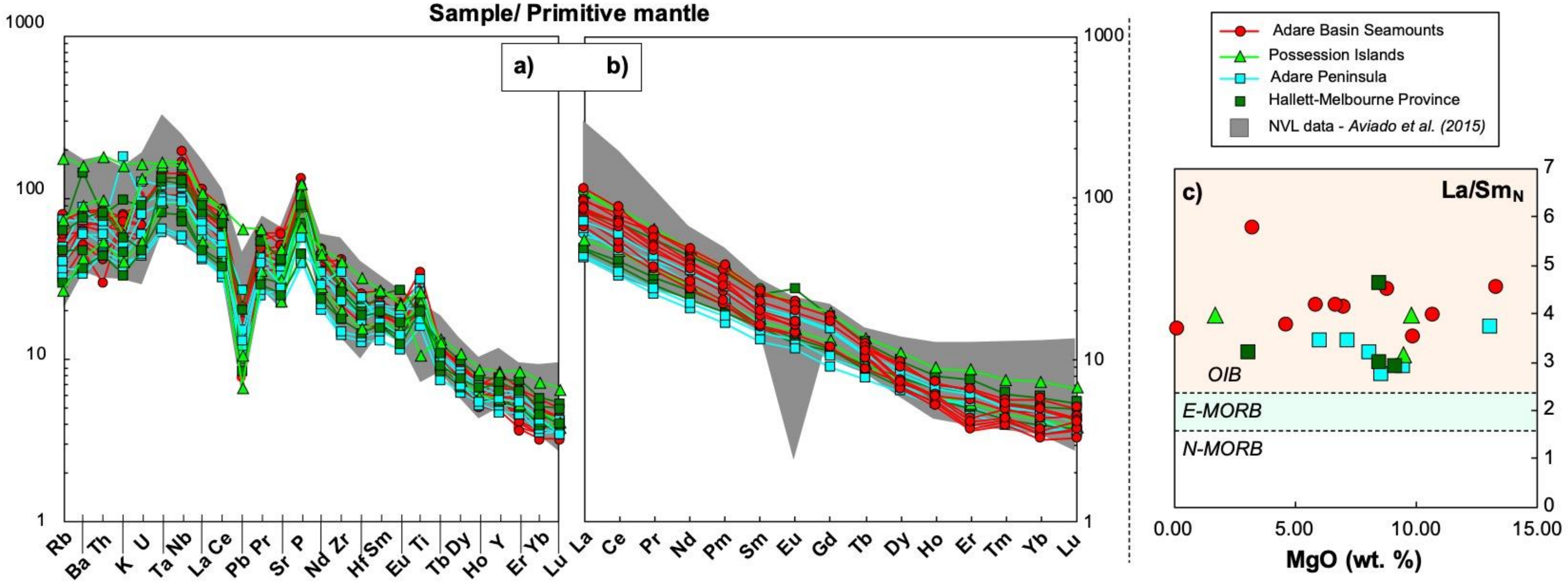

Figure 4.5 a and b) Primitive mantle-normalized incompatible element concentration diagrams and REE for WARS continental-oceanic transect samples (normalizing values from Sun and McDonough, 1989). Shaded region represents WARS data from Aviado et al. (2015). c) Chondrite-normalized La/Sm$_N$ versus MgO. Demarcation between E-MORB and N-MORB as in Gale et al. (2013), OIB La/Sm$_N$ value from Sun and McDonough (1989).

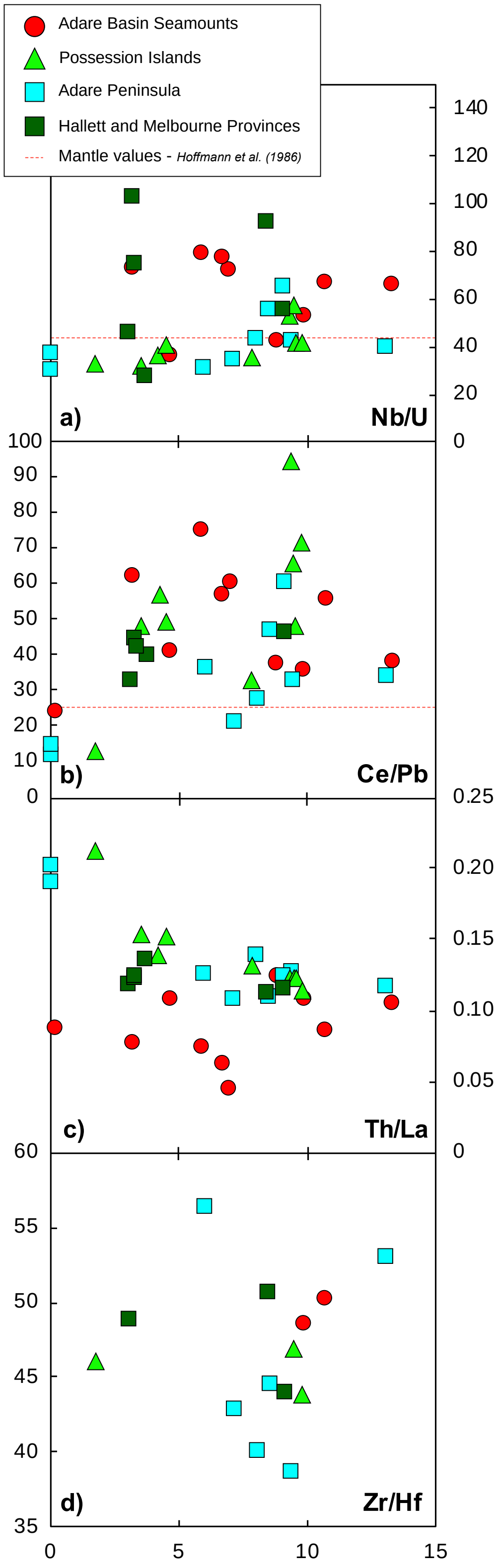

Figure 4.6. Nb/Y, U/Th, Th/La, Zr/Y versus MgO. All symbols as in Figures 1 and 3. Mantle values from Hoffman et al. (1986).

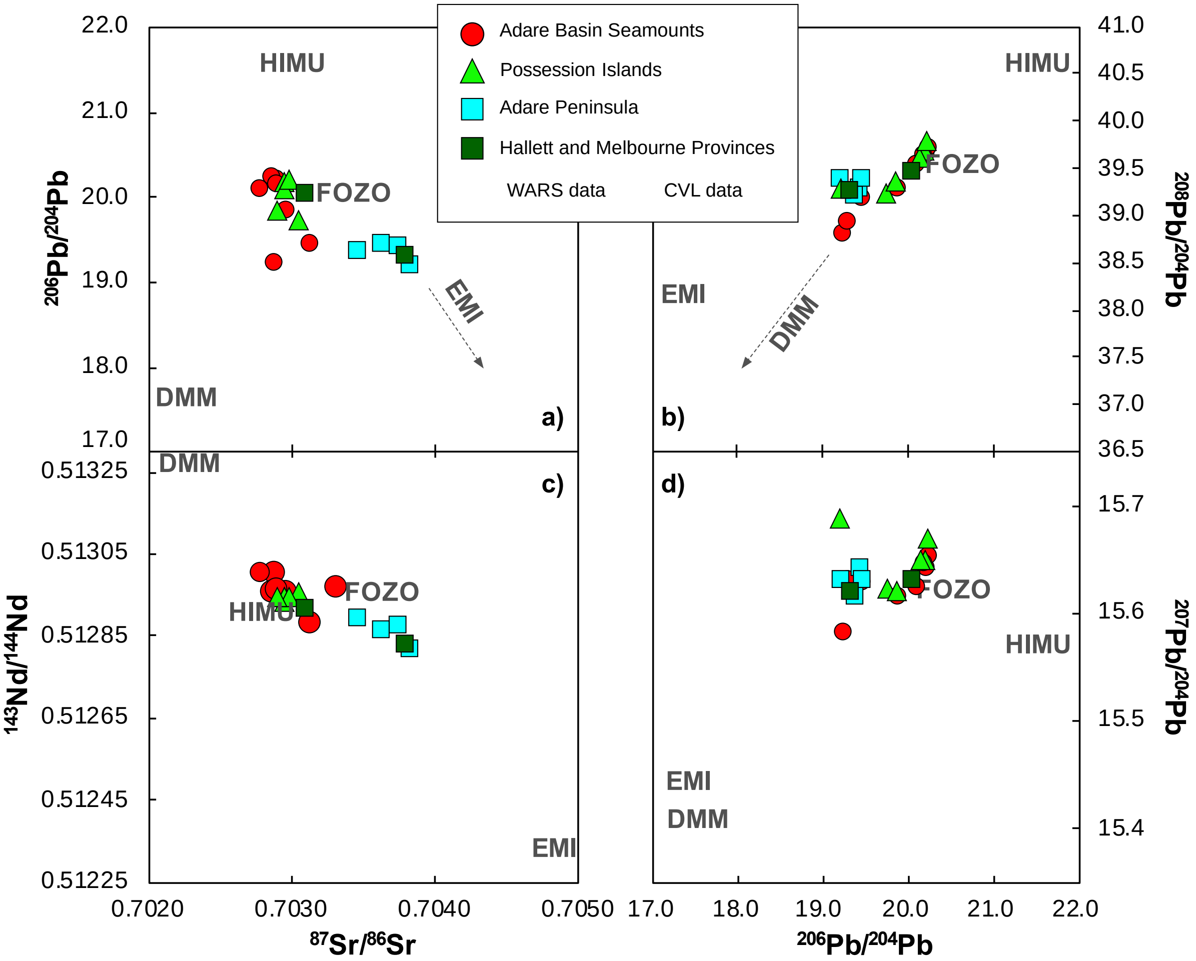

Figure 4.7: a) ^{206}Pb/^{204}Pb versus ^{87}Sr/^{86}Sr diagram. b) ^{143}Nd/^{144}Nd versus ^{87}Sr/^{86}Sr diagram. c) ^{208}Pb/^{204}Pb versus ^{206}Pb/^{204}Pb diagram. d) ^{207}Pb/^{204}Pb versus ^{206}Pb/^{204}Pb diagram. Mantle source components are DMM (Workman and Hart, 2005), EMI (Salters and Sachi-Kocher, 2010), HIMU (Stracke et al., 2003) and FOZO (Stracke et al., 2005). Data and symbols as in Figures 1, 3, and 5.

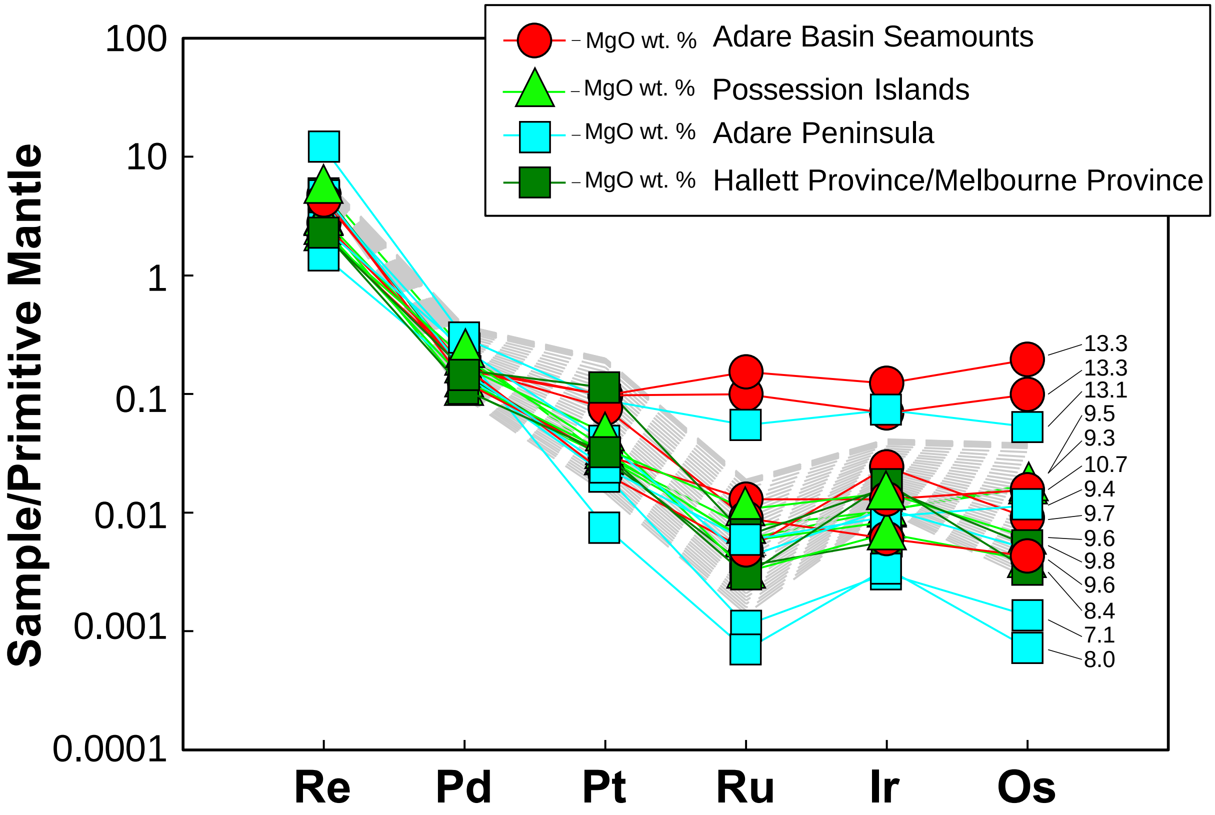

Figure 4.8: Primitive mantle normalized HSE abundance patterns of ocean-continent samples (normalizing values from Day et al., 2017).

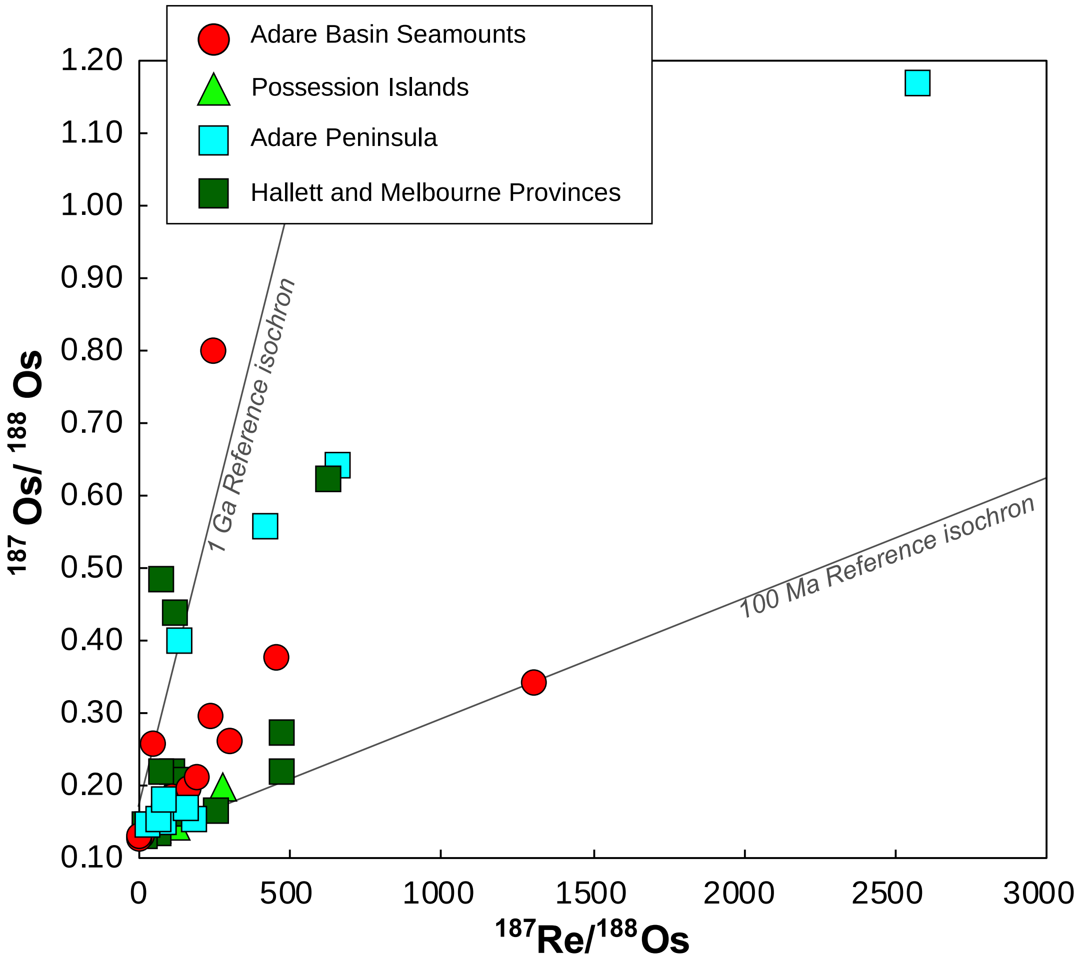

Figure 4.9: ^{187}Os/^{188}Os versus ^{187}Re/^{188}Os diagram with modeled 100Ma and 1Ga isochron reference lines.

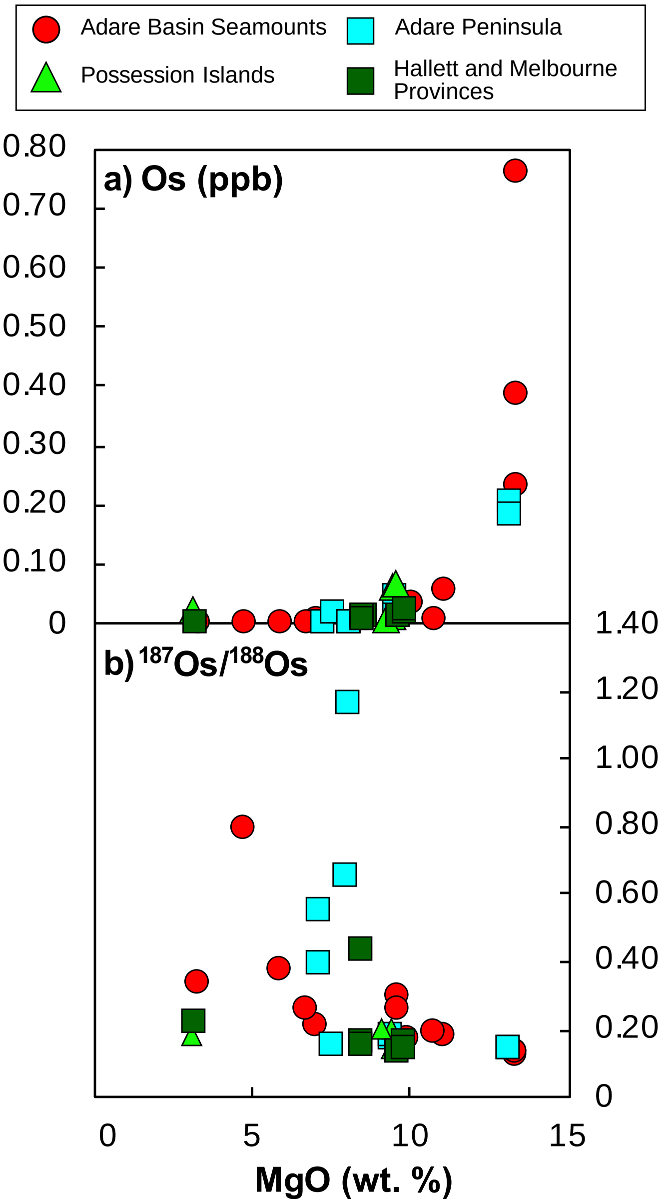

Figure 4.10: a) Os concentrations (ppb) versus MgO. b) ^{187}Os/^{188}Os versus MgO.

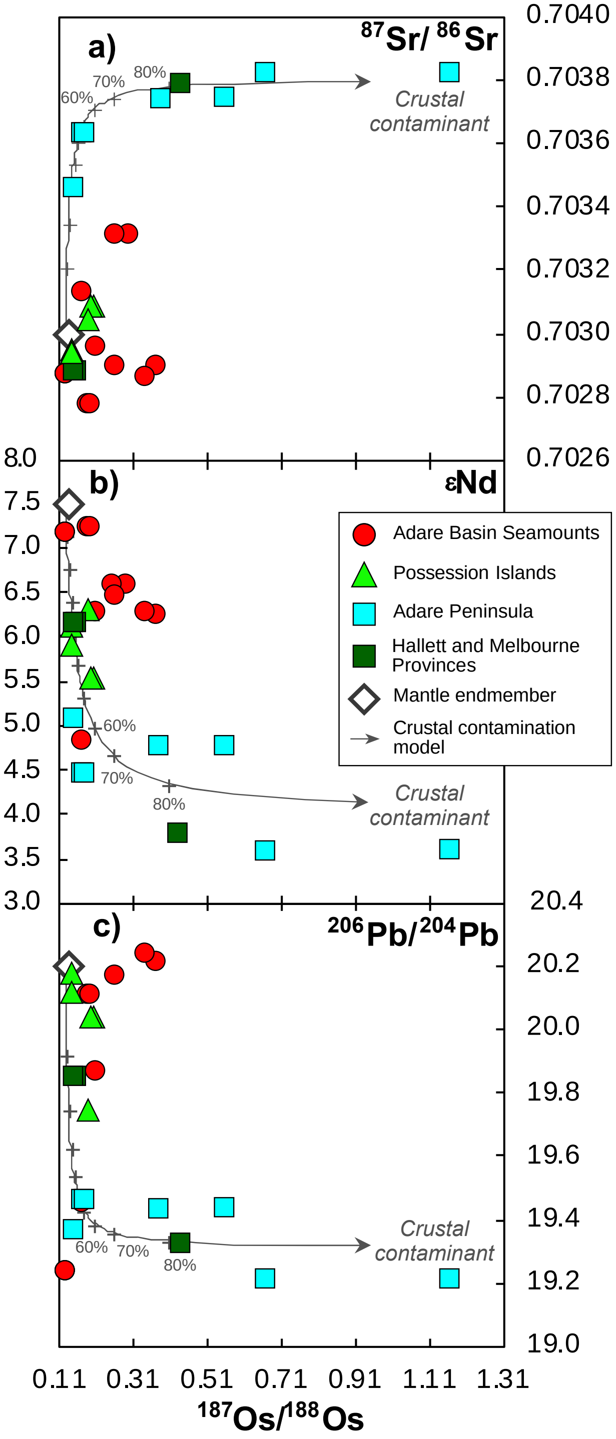

Figure 4.11: a) ^{87}Sr/^{86}Sr versus ^{187}Os/^{188}Os diagram. b) εNd versus ^{187}Os/^{188}Os diagram. c) ^{206}Pb/^{204}Pb versus ^{187}Os/^{188}Os diagram. Crustal contamination model melt and crustal ^{87}Sr/^{86}Sr and ^{187}Os/^{188}Os values from Molzahn et al. (1996). Lower crustal concentrations of Nd and Pb from Rudnick (1995). average picritic Nd and Pb values from Norman and Garcia (1999). εNd, ^{206}Pb/^{204}Pb and ^{87}Sr/^{86}Sr of contaminant are fit to data. All symbols as in Figures 1, 3, 5, and 6.

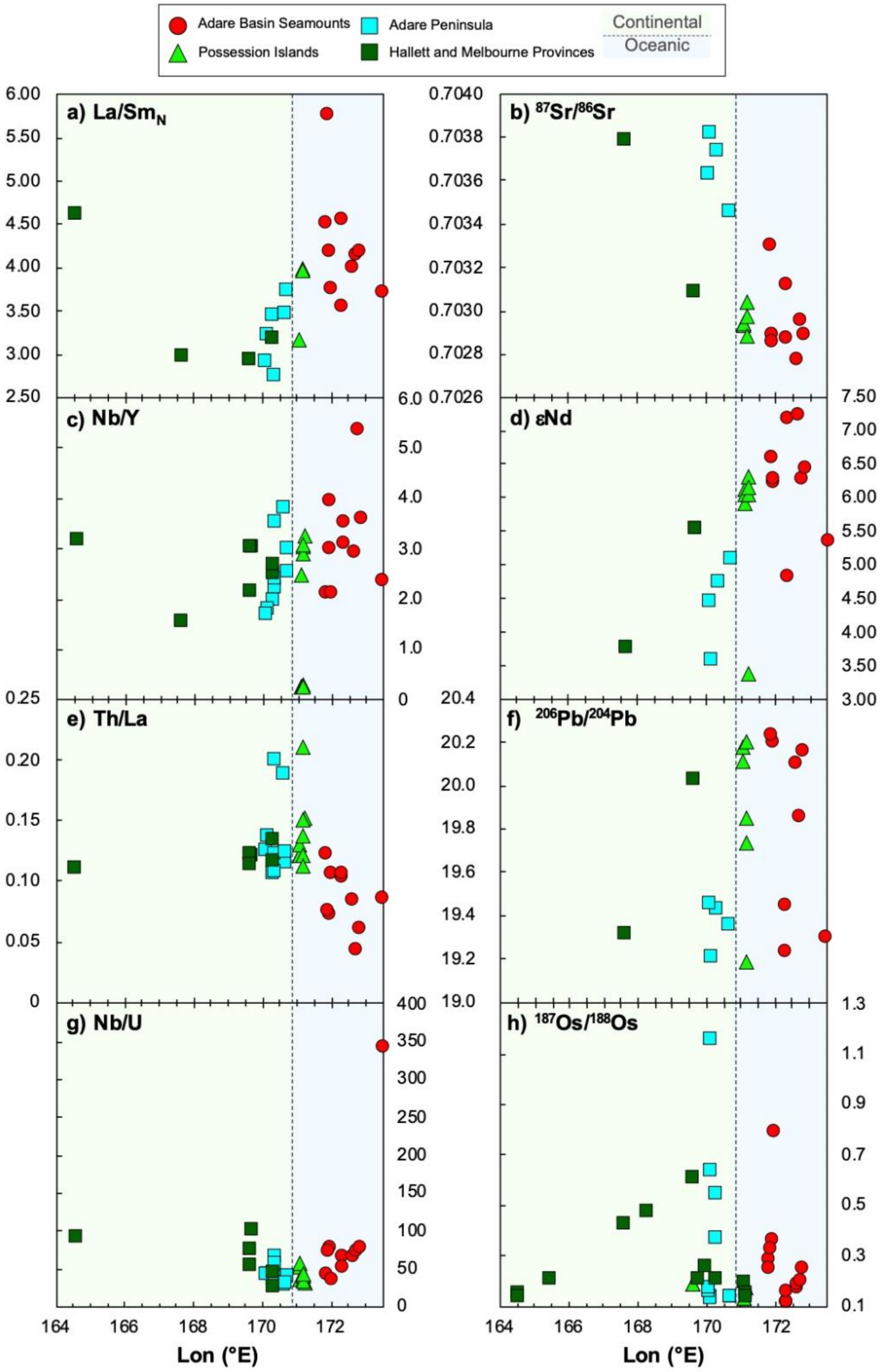

Figure 4.12: Various trace element ratios and isotopes against longitude. Data and symbols as in Figures 1, 3, 5, 6 and 8.

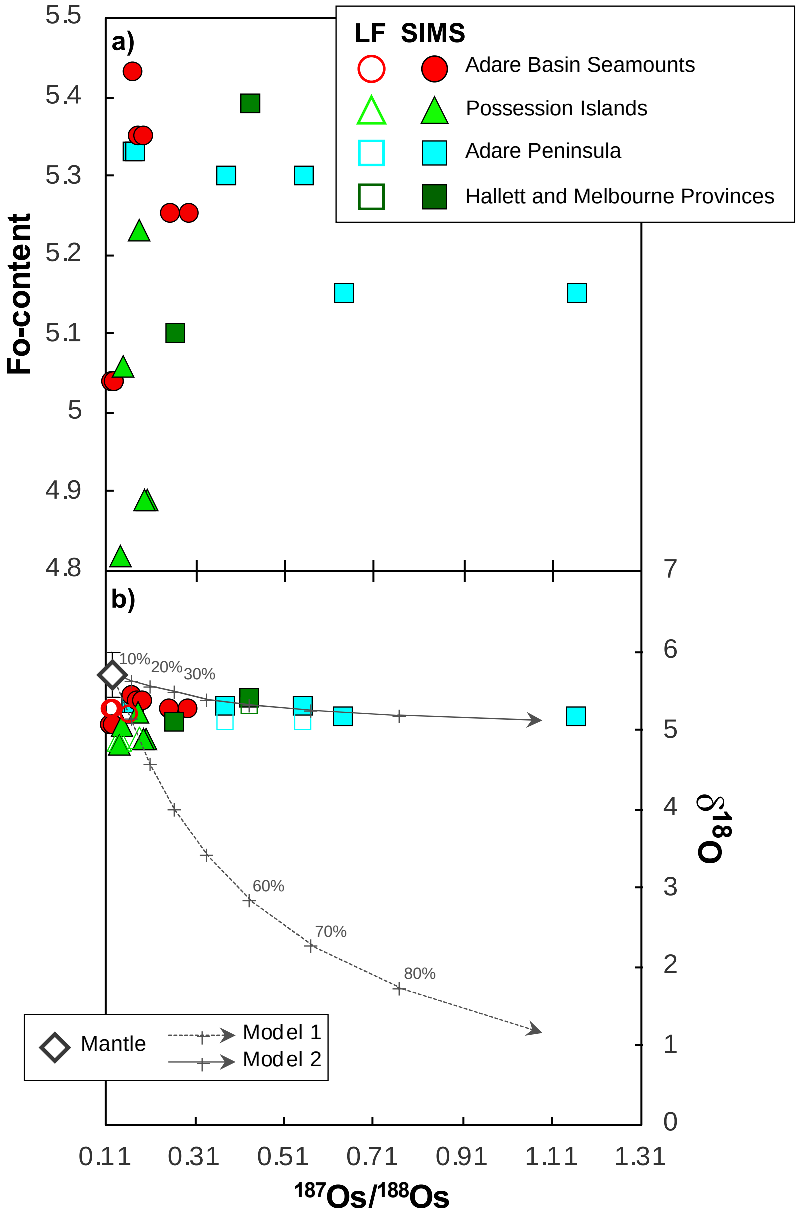

Figure 4.13: a) Forsterite content versus $^{187}Os/^{188}Os$ diagram. b) $\delta^{18}O$ versus $^{187}Os/^{188}Os$ diagram. $\delta^{18}O$ data from Panter et al. (2018); data measured by SIMS as filled symbols, data measured by LF as open symbols. Modeled contamination $\delta^{18}O$ and $^{187}Os/^{188}Os$ values for picritic melt and lower crustal contaminant from Molzahn et al. (1996).

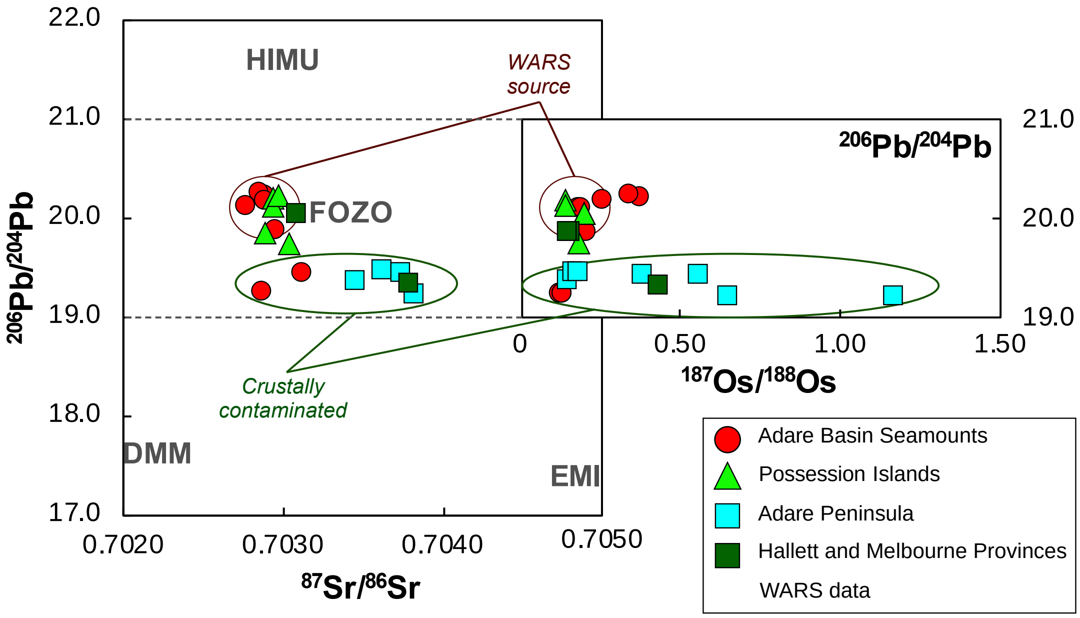

Figure 4.14: The mantle source of the WARS alkalic lavas. $^{206}Pb/^{204}Pb$ versus $^{87}Sr/^{86}Sr$. Inset as $^{206}Pb/^{204}Pb$ versus $^{187}Os/^{188}Os$. Symbols and data as in Figure 7.

Table 4.1. Major, trace elements and Sr-Nd-Pb isotope data. Labs labeled as: a) major elements via XRF at Washington State University b) Trace elements via XRF at Washington State University c) trace elements via ICP-MS at SIGL d) Sr-Nd-Pb isotopes via TIMS at SIO e) Data from Panter et al. (2018) and references therein (italicized).

ID	D1-1	D2-1	D3-1	D4-3	D5-1	D6-1	D7-1	D9-1	D11-1	D12-1	D14-1	D15-1
Lab	a, b	c, d, e	a, b	c, d, e	c	a, b, d	a, b, d	a, c	a, b	c, e	a, b	a, b, d
Alternate ID												
Location	AB	AB	AB	AB	AB	AB	AB	AB	AB	AB	AB	AB
Lat	69.84	69.86	70.00	70.07	71.91	71.82	71.82	71.63	71.66	71.63	71.60	71.58
Lon	171.85	171.84	171.99	172.32	171.90	171.92	171.90	172.52	172.70	172.65	172.79	172.73
SiO_2	48.92	*46.75*	46.24	*41.98*	-	45.77	48.17	45.26	45.40	*44.60*	46.26	43.19
TiO_2	2.77	*2.63*	3.88	*4.75*	-	3.31	2.53	3.18	3.33	*3.06*	3.12	3.89
Al_2O_3	18.32	*17.18*	16.76	*13.59*	-	16.34	17.95	15.18	15.66	*13.34*	16.08	14.70
FeO	11.19	*7.85*	13.31	*13.35*	-	11.53	10.39	11.48	12.17	*11.47*	11.65	12.82
MnO	0.21	*0.15*	0.20	*0.27*	-	0.20	0.26	0.26	0.34	*0.21*	0.25	0.24
MgO	3.68	*8.83*	4.67	*9.86*	-	5.86	3.21	6.39	5.63	*10.70*	5.34	6.99
CaO	8.23	*10.43*	8.81	*10.41*	-	9.88	8.28	9.42	9.62	*10.02*	9.17	10.44
Na_2O	4.15	*3.43*	3.77	*3.15*	-	4.56	5.93	5.58	4.87	*4.12*	5.13	4.65
K_2O	1.48	*1.73*	1.57	*1.74*	-	1.49	2.00	2.16	1.94	*1.54*	2.03	1.94
P_2O_5	1.06	*1.01*	0.80	*0.90*	-	1.05	1.28	1.09	1.05	*0.93*	0.96	1.15
Total	100.00	*100.00*	100.00	*100.00*	-	100.00	100.00	100.00	100.00	*100.00*	100.00	100.00
LOI	3.58	*3.68*	0.55	*1.22*	-	0.80	0.29	1.73	2.57	*1.17*	2.06	1.50
Sc	15.4	25.6	17.5	29.7	7.4	16.8	7.9	19.2	15.8	24.2	14.2	20.9
V	197	192	254	328	122	222	125	186	229	209	210	249
Cr	13.9	304	9.2	227	0.4	100	1.7	131	47.8	337	48.9	105
Ni	20.0	200	14.9	148	3.1	49.3	1.8	76.5	68.6	216	42.1	58.7
Cu	28.5	44.7	22.9	49.3	16.7	38.0	11.9	39.5	75.2	62.3	32.7	41.1
Zn	151	77.0	91.8	142	136	102	121	143	143	110	133	124
Ga	17.9	18.3	17.5	25.7	25.1	18.5	21.4	26.8	21.2	21.5	20.3	20.9
Rb	-	24.7	46.0	35.7	43.3	25.4	50.7	55.7	-	38.1	-	20.9
Sr	-	776	1297	1081	1228	1055	1278	1226	-	919	-	832
Y	-	27	37	32	37	30	35	41	-	31	-	22
Zr	295	243	278	390	430	309	469	544	450	338	461	431
Nb	118	74.3	79.5	100	134	90.4	140	168	134	96.2	131	118
Ba	-	492	576	558	541	380	475	655	-	441	-	342
La	-	45.52	66.69	65.15	84.41	53.57	78.08	98.47	-	59.17	-	56.77
Ce	-	84.43	130	142	177	109	153	203	-	124	-	116
Pr	-	9.89	16.93	17.09	19.95	11.84	15.36	22.85	-	14.07	-	12.79
Nd	-	37.17	62.73	65.81	73.03	46.11	55.04	85.18	-	53.46	-	51.10
Sm	-	7.00	11.44	11.85	12.41	8.23	8.74	14.51	-	10.10	-	8.81
Eu	-	2.41	3.82	3.63	3.94	2.77	2.71	4.58	-	3.34	-	2.69
Gd	-	7.10	-	11.09	12.10	15.07	19.72	14.42	-	10.06	-	16.53
Tb	-	0.95	1.28	1.34	1.44	1.15	1.26	1.69	-	1.27	-	1.11
Dy	-	5.26	7.11	6.62	7.32	5.05	5.52	8.67	-	6.67	-	4.86
Ho	-	0.98	1.16	1.18	1.37	0.88	0.99	1.55	-	1.18	-	0.84
Er	-	2.70	3.16	3.14	3.77	1.81	2.10	4.18	-	3.13	-	1.77
Tm	-	0.36	0.42	0.39	0.48	0.31	0.37	0.55	-	0.40	-	0.29
Yb	-	2.35	2.81	2.49	3.06	1.73	2.15	3.46	-	2.40	-	1.60
Lu	-	0.33	0.37	0.33	0.43	0.27	0.33	0.48	-	0.31	-	0.24
Hf	-	5.24	-	8.01	8.09	-	-	10.54	-	6.90	-	-
Ta	-	4.33	-	5.86	7.63	-	-	9.77	-	5.33	-	-
Pb	-	2.18	3.17	3.99	3.71	1.45	2.46	5.14	-	3.27	-	1.93
Th	-	5.75	7.18	7.03	9.61	3.93	6.03	12.84	-	7.23	-	2.55
U	-	1.22	2.19	1.89	3.09	1.14	1.92	3.64	-	1.96	-	1.63
$^{87}Sr/^{86}Sr$	-	0.70331	-	0.70313	-	0.702895	0.70286	-	-	*0.70278*	-	0.702956
error	-	0.000042	-	0.000018	-	-	-	-	-	-	-	-
$^{143}Nd/^{144}Nd$	-	0.51297	-	0.51288	-	0.51295	0.512952	-	-	*0.513*	-	0.512952
error	-	8E-06	-	9E-06	-	-	-	-	-	-	-	-
$^{206}Pb/^{204}Pb$	-	-	-	19.449	-	20.207	20.237	-	-	*20.111*	-	19.863
$^{207}Pb/^{204}Pb$	-	-	-	15.63	-	15.643	15.653	-	-	*15.625*	-	15.616
$^{208}Pb/^{204}Pb$	-	-	-	39.179	-	39.636	39.72	-	-	*39.551*	-	39.292

Table 4.1: Continued

D16-1	D17-1	D17-5	P74833	P74794	PRR-3831	PRR-5173	PRR-5178	PRR-5179	PRR-5200	PRR-3842	PRR-5169	PRR-5171	PRR-3870
a, b, d	a, b, d	a, b	d, e	d, e	a, b	a, b	a, b	a, d	a, d	d, e	c, d, e	d, e	a, b
					HC-AP-NR-1	NV-6	NV-6D	NV-6E	VC-21	HC-FI-2A	NV-4	NV-4c	HC-PI-1E
AB	AB	AB	AP	AP	AP	AP	AP	AP	AP	PI	PI	PI	PI
71.60	71.50	71.50	71.65	71.67	71.62	71.33	71.33	71.33	71.67	71.95	71.95	71.95	71.89
172.82	173.49	173.49	170.12	170.08	170.60	170.33	170.33	170.33	170.67	171.08	171.08	171.08	171.17
44.21	62.20	72.30	*48.95*	*47.71*	67.09	42.49	67.10	43.03	45.28	*45.46*	*45.73*	*45.64*	47.05
3.78	0.50	0.35	*2.10*	*2.49*	0.18	4.25	0.18	4.32	3.52	*3.01*	*2.97*	*3.13*	2.81
15.56	15.44	15.13	*16.15*	*13.88*	15.49	14.08	15.54	14.42	15.67	*14.58*	*14.55*	*15.39*	17.50
12.43	7.91	1.62	*10.17*	*11.32*	4.34	13.00	4.22	12.86	12.18	*11.71*	*11.39*	*11.32*	10.95
0.24	0.30	0.08	*0.16*	*0.17*	0.13	0.20	0.13	0.19	0.18	*0.19*	*0.19*	*0.19*	0.22
6.68	0.17	0.56	*8.04*	*9.41*	0.04	9.08	0.06	8.54	6.01	*9.33*	*9.45*	*7.84*	4.21
9.63	1.58	0.36	*10.23*	*11.26*	0.63	11.04	0.68	10.92	10.96	*10.62*	*10.65*	*10.55*	9.18
4.66	6.62	4.84	*2.83*	*2.45*	7.21	4.48	7.23	3.86	4.10	*3.45*	*3.55*	*3.95*	5.01
1.79	5.24	4.68	*1.00*	*0.94*	4.84	0.62	4.84	1.07	1.33	*1.05*	*0.93*	*1.31*	1.81
1.01	0.04	0.08	*0.37*	*0.38*	0.05	0.75	0.04	0.79	0.76	*0.61*	*0.60*	*0.67*	1.26
100.00	100.00	100.00	*100.00*	*100.00*	100.00	100.00	100.00	100.00	100.00	*100.00*	*100.00*	*100.00*	100.00
1.79	0.88	1.22	*-0.48*	*0.54*	0.90	6.39	0.97	4.58	4.05	*0.38*	*2.70*	*0.49*	2.31
17.2	2.1	4.9	*21.0*	*31.0*	-	29.3	0.5	30.9	27.5	*25.3*	25.7	*24.2*	10.2
234	3.2	19.5	*180*	*259*	2.0	286	1.9	303	291	*251*	257	*253*	149
51.1	1.2	1.3	*304*	*477*	3.3	219	2.3	229	175	*174*	338	*119*	19.3
60.0	0.9	-	*99.0*	*150*	-	131	1.9	140	86	*367*	172	*269*	17.5
41.7	3.6	1.3	*28.0*	*69.0*	6.1	69.4	7.8	76.7	55.5	*55.0*	61.3	*53.7*	26.0
122	175	56.8	*74.0*	*88.0*	296	92.7	293	109	101	*96.6*	101	*96.1*	111
20.9	33.5	15.7	*21.0*	*20.0*	41.2	17.9	42.4	20.8	21.1	*19.3*	19.9	*21.2*	22.6
29.2	97.9	-	*22.9*	*20.5*	287	19.4	303	25.8	46.5	*24.0*	17.4	*33.3*	35.9
1076	25	-	*585*	*477*	15	477	15	704	802	*672*	663	*761*	1038
31	52	-	*22*	*24*	131	29	135	30	28	*224*	26	*269*	33
389	702	236	*160*	*167*	1566	252	1511	259	308	*27*	229	*29*	366
111	125	13.7	*40.1*	*41.3*	505	65.2	478	71.6	84.4	*64.1*	65.7	*77.8*	103
364	74.81	-	*252*	*236*	10.76	313	17.63	431	512	*311*	299	*379*	488
57.64	65.01	-	*29.00*	*29.80*	245	42.93	238	40.54	48.66	*43.23*	37.68	*50.30*	73.31
123	137	-	*58.30*	*61.10*	457	89.84	446	92.09	104	*84.56*	82.33	*101*	141
13.50	16.10	-	*7.01*	*7.54*	-	-	-	11.31	12.03		9.88		
49.21	60.68	-	*27.80*	*30.30*	159	44.62	156	47.44	47.58	*40.14*	39.04	*45.42*	60.06
8.87	11.30	-	*5.81*	*6.60*	-	-	-	9.47	9.06	-	7.69	-	-
2.88	2.07	-	*1.95*	*2.23*	-	-	-	3.18	3.05	-	2.57	-	-
16.38	18.73	-	*5.36*	*6.16*	-	-	-	9.21	9.06	-	7.82	-	-
1.23	1.75	-	*0.82*	*0.94*	-	-	-	1.18	1.14	-	1.02	-	-
5.38	8.38	-	*4.67*	*5.22*	-	-	-	6.28	5.96	-	5.54	-	-
0.97	1.50	-	*0.87*	*0.98*	-	-	-	1.16	1.10	-	0.99	-	-
1.98	3.68	-	*2.22*	*2.43*	-	-	-	3.00	2.95	-	2.59	-	-
0.32	0.57	-	*0.29*	*0.32*	-	-	-	0.37	0.38	-	0.34	-	-
1.81	3.53	-	*1.74*	*1.85*	-	-	-	2.32	2.33	-	2.09	-	-
0.31	0.56	-	*0.27*	*0.27*	-	-	-	0.31	0.32	-	0.28	-	-
-	-	-	*3.99*	*4.32*	-	-	-	5.82	5.46	-	4.87	-	-
-	-	-	*2.56*	*2.67*	-	-	-	4.14	4.88	-	3.87	-	-
2.16	5.65	-	*2.13*	*1.87*	38.35	1.49	30.48	1.98	2.85	*0.90*	1.26	*3.09*	2.49
3.53	5.68	-	*4.02*	*3.78*	46.41	5.28	48.01	4.41	6.09	*5.28*	4.59	*6.57*	10.16
1.42	0.36	-	*0.92*	*0.96*	16.73	1.00	12.75	1.27	2.66	*1.20*	1.14	*2.19*	2.79
0.702893	-	-	0.70382	0.70363	-	-	-	-	-	0.702946	0.702938	0.702945	-
-	-	-	0.000021	0.000014	-	-	-	-	-	0.000013	0.000057	0.000035	-
0.512961	0.512905	-	0.512814	0.512859	-	-	-	-	-	0.512944	0.512933	0.51294	-
-	-	-	0.000014	0.000008	-	-	-	-	-	0.000009	0.00001	0.000009	-
20.169	19.302	-	19.211	19.459	-	-	-	-	-	20.18	20.115	-	-
15.646	15.632	-	15.632	15.631	-	-	-	-	-	15.65	15.65	-	-
39.644	38.924	-	39.383	39.386	-	-	-	-	-	39.688	39.62	-	-

Table 4.1: Continued

PRR-4910	PRR-3872	PRR-3873	PRR-5166	PRR-5194	PRR-5189	PRR-3837	PRR-6787	PRR-3839
a, b	d, e	d, e	c, d, e	a, d	a, b	a, b	a, b	c, d, e
HC-SPI-7	HC-SPI-2	HC-SPI-4	NV-3C	VC-9	VC-3	HC-DP-3	NV-8F	HC-DP-3
PI	PI	PI	PI	HP	HP	DP	DP	DP
71.90	71.89	71.89	71.89	72.37	72.37	72.67	72.67	72.67
171.20	171.17	171.17	171.17	170.28	170.28	169.67	169.63	169.63
48.54	41.48	47.75	58.05	51.56	49.31	50.25	49.53	45.16
2.57	3.53	2.78	1.42	2.38	2.74	2.58	2.76	3.18
17.86	13.08	17.41	16.66	16.48	17.06	17.21	17.22	14.12
10.51	12.20	10.73	7.85	11.07	10.94	10.91	11.14	11.68
0.23	0.22	0.22	0.18	0.25	0.23	0.24	0.24	0.19
3.54	9.56	4.51	1.73	3.07	3.73	3.25	3.32	9.11
8.09	12.79	8.46	4.00	6.66	7.59	7.28	7.65	12.94
5.53	4.59	5.26	5.69	5.08	5.09	4.74	4.72	2.25
1.89	1.41	1.81	3.95	2.38	2.02	2.24	2.12	0.85
1.24	1.15	1.07	0.49	1.07	1.28	1.29	1.30	0.52
100.00	100.00	100.00	100.00	100.00	100.00	100.00	100.00	100.00
0.31	0.70	0.00	0.63	1.34	1.42	2.44	2.33	2.44
8.4	26.8	10.8	7.7	15.6	7.9	7.8	8.2	35.5
130	255	167	36.7	85.5	121	103	149	317
7.5	156	32.8	0.2	12.6	-	-	-	401
10.2	332	44.2	0.7	9.4	3.7	2.8	4.4	123
16.7	64.9	24.5	9.9	18.3	11.1	11.2	11.5	81.8
114	109	109	108	115	112	108	106	100
21.5	19.6	22.3	27.5	24.1	20.6	19.1	20.1	19.1
49.3	44.0	47.5	113	42.8	48.0	54.5	52.7	18.9
1034	1034	923	489	853	883	1043	1051	633
35	331	396	39	35	39	37	37	25
411	34	33	461	305	349	295	309	201
115	108	105	113	88.0	105	113	112	55.7
542	564	473	1101	1007	601	630	611	258
76.89	73.90	73.31	73.62	56.59	74.10	81.47	77.39	33.05
163	139	142	154	125	148	159	155	72.35
			17.83	15.10	-	-	-	8.95
67.53	61.25	58.96	65.66	60.01	69.02	71.61	69.02	36.59
-	-	-	11.90	11.43	-	-	-	7.26
-	-	-	3.84	4.60	-	-	-	2.31
-	-	-	11.59	11.05	-	-	-	7.04
-	-	-	1.48	1.38	-	-	-	0.93
-	-	-	8.12	7.31	-	-	-	5.04
-	-	-	1.45	1.29	-	-	-	0.92
-	-	-	4.15	3.59	-	-	-	2.43
-	-	-	0.56	0.46	-	-	-	0.31
-	-	-	3.62	2.89	-	-	-	1.96
-	-	-	0.49	0.40	-	-	-	0.28
-	-	-	10.00	6.23	-	-	-	4.57
-	-	-	6.62	5.23	-	-	-	3.34
3.39	2.89	2.89	12.17	3.80	3.69	3.59	3.69	1.57
11.75	9.06	11.06	15.51	6.66	10.06	9.96	9.56	3.77
3.59	2.59	2.59	3.44	1.90	3.78	1.10	1.49	1.00
-	0.703044	0.702973	-	-	-	-	-	0.70309
-	0.000061	0.00001	-	-	-	-	-	0.000005
-	0.512954	0.51294	0.512803	-	-	-	-	0.512914
-	0.00001	0.000008	0.0000075	-	-	-	-	0.000008
-	19.743	20.21	19.193	-	-	-	-	20.038
-	15.623	15.67	15.685	-	-	-	-	15.631
-	39.24	39.785	39.276	-	-	-	-	39.455

Table 4.2. Highly siderophile element abundances and 187Re-187Os for Antarctic lavas.

Sample ID	Lab	Location	Lon (°E)	Age (Ma)	MgO	Ni (ppm)	Re (ppb)	Pd (ppb)	Pt (ppb)	Ru (ppb)	Ir (ppb)	Os (ppb)
BHVO-2	SIGL				7.4	121	2.892	3.191	8.008	0.125	0.124	0.124
D2-1	SIGL	AB	171.8	15.93	9.6	200	0.836	0.895	0.569	0.071	0.022	0.017
D2-1	China	AB	171.8	15.93	9.6	200	0.142	-	-	-	-	0.015
D3-1	China	AB	172.0	4.61	4.7	15	0.106	-	-	-	-	0.002
D4-1	SIGL	AB	172.3	3.35	13.3	338	1.298	0.876	0.730	0.787	0.250	0.387
Rpt	SIGL	AB	172.3	3.35	13.3	338	1.377	0.842	0.730	1.212	0.442	0.762
D4-1	China	AB	172.3	3.35	13.3	338	0.199	-	-	-	-	0.233
D4-3	SIGL	AB	172.3	2.51	9.9	148	0.661	0.902	0.160	0.038	0.088	0.035
D6-1	China	AB	171.9	3	5.9	49	0.408	-	-	-	-	0.004
D7-1	China	AB	171.9	0.32	3.2	2	0.251	-	-	-	-	0.001
D9-1	China	AB	171.9	2.89	6.4	71	0.284	-	-	-	-	0.008
D12-1	SIGL	AB	172.6	2.89	11.0	216	1.440	0.673	0.229	0.102	0.047	0.061
D12-1	China	AB	172.6	2.89	10.7	205	0.282	-	-	-	-	0.008
D15-1	China	AB	172.7	3.12	7.0	59	0.329	-	-	-	-	0.008
D16-1	China	AB	172.8	2.76	6.7	60	0.366	-	-	-	-	0.006
A232B	SIGL	AP	170.3	-	7.1	99	0.437	0.782	0.157	0.009	0.011	0.005
A232B	China	AP	170.3	-	7.1	99.0	0.139	-	-	-	-	0.005
A210B	SIGL	AP	170.2	-	13.1	-	3.574	1.582	0.668	0.433	0.265	0.206
Rpt	SIGL	AP	170.2	-	13.1	-	-	-	-	-	-	-
A210B	China	AP	170.2	-	13.1	-	1.130	-	-	-	-	0.183
A223D	SIGL	AP	170.7	-	7.5	-	0.754	1.271	0.298	0.033	0.039	0.019
A233D	China	AP	170.7	-	7.5	-	0.297	-	-	-	-	0.020
P74833	SIGL	AP	170.1	-	8.0	99	1.328	1.152	0.057	0.006	0.012	0.003
P74833	China	AP	170.1	-	8.0	99	0.226	-	-	-	-	0.002
P74794	SIGL	AP	170.1	-	9.4	150	1.451	0.823	0.181	0.046	0.033	0.045
P74794	China	AP	170.1	-	9.4	150	0.251	-	-	-	-	0.014
PRR 3839	SIGL	PI	169.6	-	9.4	123	0.902	0.900	0.351	0.025	0.024	0.016
PRR-3839	China	PI	169.6	-	9.1	123	0.195	-	-	-	-	0.009
PRR 3842	SIGL	PI	171.1	-	9.3	367	1.604	1.215	0.218	0.048	0.038	0.063
Rpt	SIGL	PI	171.1	-	9.3	367	-	-	-	-	-	-
PRR 5169	SIGL	PI	171.1	-	9.5	0.67	0.896	0.581	0.223	0.060	0.037	0.068
PRR 5171	SIGL	PI	171.1	0.33	9.5	172	0.743	0.691	0.244	0.045	0.030	-
Rpt	SIGL	PI	171.1	0.33	7.8	269	-	-	-	-	-	-
PRR 3872	SIGL	PI	171.2	-	3.1	9	0.667	1.071	0.262	0.085	0.053	0.024
24583	China	HP	163.4	-	9.6	332	0.187	-	-	-	-	0.013
24591	China	HP	163.4	-	10.9	258	0.307	-	-	-	-	0.057
PRR-5194	China	HP	170.3	-	3.1	9	0.087	-	-	-	-	0.004
A225C-2	China	HP	171.1	-	6.1	-	0.354	-	-	-	-	0.013
AW82214	SIGL	HP	171.2	-	9.8	167	0.673	0.843	0.850	0.050	0.058	0.021
AW82214	China	HP	171.2	-	9.8	167	0.132	-	-	-	-	0.025
A277	China	HP	169.6	-	5.1	-	0.147	-	-	-	-	0.001
82107	China	HP	168.3	-	9.5	83	0.136	-	-	-	-	0.009
A214B	China	HP	170.0	-	4.1	-	0.160	-	-	-	-	0.002
A216	China	HP	169.8	-	5.4	-	0.246	-	-	-	-	0.003
25679	China	MP	165.5	-	7.2	-	0.261	-	-	-	-	0.017
MA-117	SIGL	MP	167.6	-	8.5	93	1.497	0.778	0.214	0.028	0.021	-
Rpt	SIGL	MP	167.6	-	8.5	93	-	-	-	-	-	-
MA-117	China	MP	167.6	-	8.5	93	0.299	-	-	-	-	0.012
81510	SIGL	MP	164.6	-	8.4	-	0.699	0.577	0.238	0.024	0.064	0.013
81510	China	MP	164.6	-	8.4	-	0.136	-	-	-	-	0.009

Table 4.2: Continued

^{187}Re/^{188}Os	2SE	^{187}Os/^{188}Os	2SE	γ Os	Fo	∂18O ol	∂18O ol	^{87}Sr/^{86}Sr	εNd	^{206}Pb/^{204}Pb
113	2	0.15467	0.00015	21		SIMS	LF			
246	4	0.29368	0.00079	79	87	5.25	-	0.703	6.6	-
48	1	0.25730	0.00070	92	87	5.25	-	0.703	6.6	-
253	4	0.79790	0.00410	510	-	-	-	-	-	-
16.2	0.2	0.12900	0.00009	0	90	5.04	5.25	0.703	7.2	19.237
8.7	0.1	0.12548	0.00025	-2	90	5.04	5.25	0.703	7.2	19.237
4.1	0.1	0.12960	0.00040	1	90	5.04	5.25	0.703	7.2	19.237
91	1	0.17001	0.00019	30	79	5.43	5.17	0.703	4.8	19.449
462	7	0.37420	-	175	-	-	-	0.703	6.2	20.207
1305	20	0.34050	-	161	-	-	-	0.703	6.3	20.237
161	2	-	-	-	79	5.05	-	-	-	-
115	2	0.1830	0.0012	39	84	5.35	-	0.703	7.2	20.111
165	2	0.1946	0.0007	46	84	5.35	-	0.703	7.2	20.111
200	3	0.2081	0.0016	55	-	-	-	0.703	6.3	19.863
305	5	0.2594		92	-	-	-	0.703	6.5	20.169
419	6	0.5550	0.0029	335	81	5.3	5.06	0.704	4.8	19.432
134	2	0.3831	0.0020	200	81	5.3	5.06	0.704	4.8	19.432
84	1	0.14654	0.00024	15	-	-	-	0.703	5.1	19.363
-	-	-	-	-	-	-	-	0.703	5.1	19.363
29.9	0.4	0.1433	0.0029	12	-	-	-	-	-	-
188	3	0.1506	0.0014	18	-	-	-	-	-	-
70	1	0.1501	-	18	-	-	-	-	-	-
2577	39	1.166	0.018	814	70	5.15	-	0.704	3.6	19.211
683	10	0.64700	0.00400	407	70	5.15	-	0.704	3.6	19.211
157	2	0.16857	0.00060	32	80	5.33	-	0.704	4.5	19.459
88	1	0.17960	-	41	80	5.33	-	0.704	4.5	19.459
282	4	0.1990	0.0014	56	84	4.89	-	0.703	5.5	20.038
107	2	0.1966	0.0011	54	84	4.89	-	0.703	5.5	20.038
123	2	0.14395	0.00026	13	81	5.06	4.88	0.703	6.1	20.18
-	-	-	-	-	81	5.06	4.88	0.703	6.1	20.18
64	1	0.14041	0.00025	10	83	4.82	4.86	0.703	5.9	20.115
-	-	-	-	-	82	4.71	-	0.703	6.0	-
-	-	-	-	-	82	4.71	-	0.703	6.0	-
133	2	0.18444	0.00068	45	75	5.23	4.9	0.703	6.3	19.743
71	1	0.13131	0.00043	3	-	-	-	-	-	-
26.0	0.4	0.12775	0.00025	0	-	-	-	-	-	-
113	2	0.218	-	71	-	-	-	-	-	-
131	2	0.20580	-	61	-	-	-	-	-	-
158	2	0.15861	0.00055	24	-	-	-	0.703	6.1	19.851
25.3	0.4	0.14590	0.00040	14	-	-	-	0.703	6.1	19.851
634.1	9.5	0.61890	0.00890	385	-	-	-	-	-	-
80	1	0.48230	0.00120	278	-	-	-	-	-	-
480	7	0.26920	0.00130	111	76	5.1	-	-	-	-
472	7	0.21630	-	70	-	-	-	-	-	-
74	1	0.21650	-	70	-	-	-	-	-	-
-	-	-	-	-	79	5.39	5.26	0.704	3.8	19.32
-	-	-	-	-	79	5.39	5.26	0.704	3.8	19.32
126	2	0.4357	0.0019	242	79	5.39	5.26	0.704	3.8	19.32
261	4	0.1650	0.0015	29	-	-	-	-	-	-
76	1	0.1480	0.0012	16	-	-	-	-	-	-

References

Armienti, P., Perinelli, C., 2010. Cenozoic thermal evolution of lithospheric mantle in northern Victoria Land (Antarctica): Evidences from mantle xenoliths. Tectonophysics 486, 28–35. https://doi.org/10.1016/j.tecto.2010.02.006

Aviado, K.B., Rilling-Hall, S., Bryce, J.G., Mukasa, S.B., 2015. Submarine and subaerial lavas in the west Antarctic Rift System: Temporal record of shifting magma source components from the lithosphere and asthenosphere. Geochemistry Geophysics Geosystems 16, 4344–4361. https://doi.org/10.1002/2015GC006076

Birck, J.L., Barman, M.R., Capmas, F., 1997. Re-Os Isotopic Measurements at the Femtomole Level in Natural Samples. Geostandards and Geoanalytical Research 20, 19–27.

Boger, S.D., Miller, J.M.L., 2004. Terminal suturing of Gondwana and the onset of the Ross-Delamerian Orogeny: The cause and effect of an Early Cambrian reconfiguration of plate motions. Earth and Planetary Science Letters 219, 35–48. https://doi.org/10.1016/S0012-821X(03)00692-7

Borg, S.G., Stump, E., 1987. Paleozoic Magmatism and Associated Tectonic Problems of Northern Victoria Land, Antarctica. Gondwana Six: Structure, Tectonics, and Geophysics. Geophysical Monograph, 40, 67–75. https://doi.org/10.1029/gm040p0067

Bradshaw, J.D., 1989. Cretaceous geotectonic patterns in the New Zealand region. Tectonics 8, 803–820.

Cande, S.C., Stock, J.M., 2006. Constraints on the Timing of Extension in the Northern Basin, Ross Sea. In: Fütterer, D.K., Damaske, D., Kleinschmidt, G., Miller, H., Tessensohn, F. (Eds.), Antarctica. Springer Berlin Heidelberg, Berlin, Heidelberg, 319–326. https://doi.org/10.1007/3-540-32934-x_40

Cande, S.C., Stock, J.M., Müller, R.D., Ishihara, T., 2000. Cenozoic motion between east and west Antarctica. Nature 404, 145–150. https://doi.org/10.1038/35004501

Castillo, P.R., 2015. The recycling of marine carbonates and sources of HIMU and FOZO ocean island basalts. Lithos 216–217, 254–263. https://doi.org/10.1016/j.lithos.2014.12.005

Cawood, P.A., 2005. Terra Australis Orogen: Rodinia breakup and development of the Pacific and Iapetus margins of Gondwana during the Neoproterozoic and Paleozoic. Earth-Science Reviews 69, 249–279. https://doi.org/10.1016/j.earscirev.2004.09.001

Cohen, A.S., Waters, F.G., 1996. Separation of osmium from geological materials by solvent extraction for analysis by thermal ionisation mass spectrometry. Analytica Chimica Acta 332, 269–275.

Davey, F.J., Brancolini, G., 1995. The Late Mesozoic and Cenozoic Structural Setting of the Ross Sea Region. Geology and Seismic Stratigraphy of the Antarctic Margin 68, 167–182. https://doi.org/10.1029/ar068p0167

Davey, F.J., Cande, S.C., Stock, J.M., 2006. Extension in the western Ross Sea region-links between Adare Basin and Victoria Land Basin. Geophysical Research Letters 33, 1–5. https://doi.org/10.1029/2006GL027383

Day, J.M.D., 2013. Hotspot volcanism and highly siderophile elements. Chemical Geology 341, 50–74. https://doi.org/10.1016/j.chemgeo.2012.12.010

Day, J.M.D., Harvey, R.P., Hilton, D.R., 2019. Melt-modified lithosphere beneath Ross Island and its role in the tectono-magmatic evolution of the West Antarctic Rift System. Chemical Geology 518, 45–54. https://doi.org/10.1016/j.chemgeo.2019.04.012

Day, J.M.D., Walker, R.J., Warren, J.M., 2017. 186Os–187Os and highly siderophile element abundance systematics of the mantle revealed by abyssal peridotites and Os-rich alloys. Geochimica et Cosmochimica Acta 200, 232–254. https://doi.org/10.1016/j.gca.2016.12.013

Day, J.M.D., Waters, C.L., Schaefer, B.F., Walker, R.J., Turner, S., 2016. Use of Hydrofluoric Acid Desilicification in the Determination of Highly Siderophile Element Abundances and Re-Pt-Os Isotope Systematics in Mafic-Ultramafic Rocks. Geostandards and Geoanalytical Research 40, 49–65. https://doi.org/10.1111/j.1751-908X.2015.00367.x

Di Vincenzo, G., Horton, F., Palmeri, R., 2016. Protracted (~ 30 Ma) eclogite-facies metamorphism in northern Victoria Land (Antarctica): Implications for the geodynamics of the Ross/Delamerian Orogen. Gondwana Research 40, 91–106. https://doi.org/10.1016/j.gr.2016.08.005

Dickin, A.P., 2005. Radiogenic Isotope Geology, 2nd Editio. ed, CEUR Workshop Proceedings. Cambridge University Press, New York. https://doi.org/10.1017/CBO9781107415324.004

Faure, G., 1986. Principles of Isotope Geology, 2nd Editio. ed. John Wiley & Sons, New York.

Finn, C.A., Müller, R.D., Panter, K.S., 2005. A Cenozoic diffuse alkaline magmatic province (DAMP) in the southwest Pacific without rift or plume origin. Geochemistry, Geophysics, Geosystems 6. https://doi.org/10.1029/2004GC000723

Fitton, J.G., Dunlop, H.M., 1985. The Cameroon line, West Africa, and its bearing on the origin of oceanic and continental alkali basalt. Earth and Planetary Science Letters 72, 23–38. https://doi.org/10.1016/0012-821X(85)90114-1

Gale, A., Dalton, C.A., Langmuir, C.H., Su, Y., Schilling, J.G., 2013. The mean composition of ocean ridge basalts. Geochemistry, Geophysics, Geosystems 14, 489–518. https://doi.org/10.1029/2012GC004334

Gonfiantini, R., Picciotto, E., 1959. Oxygen isotope variations in Antarctic snow samples. Nature 184, 1557–1558.

Granot, R., Cande, S.C., Stock, J.M., Damaske, D., 2013. Revised Eocene-Oligocene kinematics for the West Antarctic rift system. Geophysical Research Letters 40, 279–284. https://doi.org/10.1029/2012GL054181

Granot, R., Cande, S.C., Stock, J.M., Davey, F.J., Clayton, R.W., 2010. Postspreading rifting in the Adare Basin, Antarctica: Regional tectonic consequences. Geochemistry, Geophysics, Geosystems 11, 1–29. https://doi.org/10.1029/2010GC003105

Hart, S.R., Hauri, E.H., Oschman, L.A., Whitehead, J.A., 1992. Mantle plumes and entrainment: the isotopic evidence. Science 256, 517–520.

Hauri, E.H., Whitehead, J.A., Hart, S.R., 1994. Fluid dynamic and geochemical aspects of entrainment in mantle plumes. Journal of Geophysical Research: Solid Earth 99, 24275–24300. https://doi.org/10.1029/94jb01257

Huerta, A.D., Harry, D.L., 2007. The transition from diffuse to focused extension: Modeled evolution of the West Antarctic Rift system. Earth and Planetary Science Letters 255, 133–147. https://doi.org/10.1016/j.epsl.2006.12.011

Jackson, M.G., Hart, S.R., Koppers, A.A.P., Staudigel, H., Konter, J., Blusztajn, J., Kurz, M., Russell, J.A., 2007. The return of subducted continental crust in Samoan lavas. Nature 448, 684–687. https://doi.org/10.1038/nature06048

Janney, P.E., Castillo, P.R., 1996. Basalts from the Central Pacific Basin: evidence for the origin of Cretaceous igneous complexes in the Jurassic western Pacific. Journal of Geophysical Research 101, 2875–2893. https://doi.org/10.1029/95JB03119

Ji, F., Li, F., Gao, J.Y., Zhang, Q., Hao, W.F., 2018. 3-D density structure of the Ross Sea basins, West Antarctica from constrained gravity inversion and their tectonic implications. Geophysical Journal International 215, 1241–1256. https://doi.org/10.1093/GJI/GGY343

King, E.M., Valley, J.W., Davis, D.W., Edwards, G.R., 1998. Oxygen isotope ratios of Archean plutonic zircons from granite-greenstone belts of the Superior Province: Indicator of magmatic source. Precambrian Research 92, 365–387. https://doi.org/10.1016/S0301-9268(98)00082-5

Kyle, P.R., McIntosh, W.C., Schmidt-Thomé, M., Mueller, P., Tessensohn, F., Noll, M.R., Wörner, G., Wörner, G., Viereck, L., Behrendt, J.C., Ellerman, P.J., Wright, A.C., Moore, J.A., Stump, E., Borg, S.G., Sheridan, M.F., 1990. A. McMurdo Volcanic Group Western Ross embayment. In: LeMasurier, W.E., Thomson, J.W., Baker, P.E., Kyle, P.R., Rowley, P.D., Smellie, J.L., Verwoerd, W.J. (Eds.), Volcanoes of the Antarctic Plate and Southern Oceans. 18–145. https://doi.org/10.1029/ar048p0018

Lawrence, J.F., Wiens, D.A., Nyblade, A.A., Anandakrishan, S., Shore, P.J., Voigt, D., 2006. Upper mantle thermal variations beneath the Transantarctic Mountains inferred from teleseismic S-wave attenuation. Geophysical Research Letters 33, 2–5. https://doi.org/10.1029/2005GL024516

Le Bas, M.J., Le Maitre, R.W., Streckeisen, A., Zanettin, B., 1986. A chemical classification of volcanic rocks based on the total alkali silica diagram. Journal of Petrology 27, 745–750. https://doi.org/10.1093/petrology/27.3.745

Li, J., Liang, X.R., Xu, J.F., Suzuki, K., Dong, Y.H., 2010. Simplified technique for the measurements of Re-Os isotope by multicollector inductively coupled plasma mass spectrometry (MC-ICP-MS). Geochemical Journal 44, 73–80. https://doi.org/10.2343/geochemj.1.0044

Luyendyk, B.P., 1995. Hypothesis for Cretaceous rifting of east Gondwana caused by subducted slab capture. Geology 23, 373–376. https://doi.org/10.1130/0091-7613(1995)023<0373:HFCROE>2.3.CO;2

Macdonald, G.A., Katsura, T., 1964. Chemical composition of Hawaiian lavas. Journal of Petrology 5, 82–133. https://doi.org/10.1093/petrology/5.1.82

Martin, A.P., Cooper, A.F., Price, R.C., 2013. Petrogenesis of Cenozoic, alkalic volcanic lineages at Mount Morning, West Antarctica and their entrained lithospheric mantle xenoliths: Lithospheric versus asthenospheric mantle sources. Geochimica et Cosmochimica Acta 122, 127–152. https://doi.org/10.1016/j.gca.2013.08.025

Meisel, T., Walker, R.J., Irving, A.J., Lorand, J.P., 2001. Osmium isotopic compositions of mantle xenoliths: A global perspective. Geochimica et Cosmochimica Acta 65, 1311–1323. https://doi.org/10.1016/S0016-7037(00)00566-4

Molzahn, M., Reisberg, L., Wiirner, G., 1996. OS, Sr, Nd, Pb, 0 isotope and trace element data from the Ferrar flood basalts, Antarctica: evidence for an enriched subcontinental lithospheric source. 144.

Nardini, I., Armienti, P., Rocchi, S., Dallai, L., Harrison, D., 2009. Sr-Nd-Pb-He-O Isotope and Geochemical Constraints on the Genesis of Cenozoic Magmas from the West Antarctic Rift. Journal of Petrology 50, 1359–1375. https://doi.org/10.1093/petrology/egn082

Ngwa, C.N., Hansteen, T.H., Devey, C.W., van der Zwan, F.M., Suh, C.E., 2017. Origin and evolution of primitive melts from the Debunscha Maar, Cameroon: Consequences for mantle source heterogeneity within the Cameroon Volcanic Line. Lithos 288–289, 326–337. https://doi.org/10.1016/j.lithos.2017.06.028

Norman, M.D., Garcia, M.O., 1999. Primitive magmas and source characteristics of the Hawaiian plume: Petrology and geochemistry of shield picrites. Earth and Planetary Science Letters 168, 27–44. https://doi.org/10.1016/S0012-821X(99)00043-6

Panter, K.S., 2006. The Origin of HIMU in the SW Pacific: Evidence from Intraplate Volcanism in Southern New Zealand and Subantarctic Islands. Journal of Petrology 47, 1673–1704. https://doi.org/10.1093/petrology/egl024

Panter, K.S., Castillo, P., Raymond, C. editor, 2007. Petrogenesis and source of lavas from seamounts in the Adare Basin, western Ross Sea; implications for the origin of Cenozoic magmatism in Antarctica. Open-File Report - U. S. Geological Survey Extended Abstract 069.

Panter, K.S., Castillo, P.R., Krans, S., Deering, C., McIntosh, W., Valley, J.W., Kitajima, K., Kyle, P.R., Hart, S.R., Blusztajn, J., 2018. Melt Origin across a Rifted Continental Margin: a Case for Subduction-related Metasomatic Agents in the Lithospheric Source of Alkaline Basalt, NW Ross Sea, Antarctica. Journal of Petrology 59, 517–558. https://doi.org/10.1093/petrology/egy036

Peters, B.J., Day, J.M.D., 2014. Assessment of relative Ti, Ta and Nb (TITAN) enrichments in ocean island basalts. Geochem. Geophys. Geosyst 4424–4444. https://doi.org/10.1002/2014GC005506.Received

Risk, G.F., Hochstein, M.P., 1974. Heat flow at arrival heights, ross island, antarctica. New Zealand Journal of Geology and Geophysics 17, 629–644. https://doi.org/10.1080/00288306.1973.10421586

Rudnick, R.L., 1995. Nature Crust : and Composition of the Continental Perspective. Physics of the Earth and Planetary Interiors 145, 267–309.

Salters, V.J.M., Sachi-Kocher, A., 2010. An ancient metasomatic source for the Walvis Ridge basalts. Chemical Geology 273, 151–167. https://doi.org/10.1016/j.chemgeo.2010.02.010

Salvini, F., Brancolini, G., Busetti, M., Storti, F., Mazzarini, F., Coren, F., 1997. Cenozoic geodynamics of the Ross Sea region, Antarctica: Crustal extension, intraplate strike-slip faulting, and tectonic inheritance. Journal of Geophysical Research: Solid Earth 102, 24669–24696. https://doi.org/10.1029/97jb01643

Stracke, A., Bizimis, M., Salters, V.J.M., 2003. Recycling oceanic crust: Quantitative constraints. Geochemistry, Geophysics, Geosystems 4. https://doi.org/10.1029/2001GC000223

Stracke, A., Hofmann, A.W., Hart, S.R., 2005. FOZO, HIMU, and the rest of the mantle zoo. Geochemistry, Geophysics, Geosystems 6. https://doi.org/10.1029/2004GC000824

Sun, S. -s., McDonough, W.F., 1989. Chemical and isotopic systematics of oceanic basalts: implications for mantle composition and processes. Geological Society, London, Special Publications 42, 313–345. https://doi.org/10.1144/GSL.SP.1989.042.01.19

Thirlwall, M.F., 1995. Generation of the Pb isotopic characteristics of the Iceland plume. Journal

- Geological Society (London) 152, 991–996. https://doi.org/10.1144/GSL.JGS.1995.152.01.19

Wembenyui, E.W., Collerson, K.D., Zhao, J. xin, 2020. Evolution of Mount Cameroon volcanism: Geochemistry, mineral chemistry and radiogenic isotopes (Pb, Sr, Nd). Geoscience Frontiers. https://doi.org/10.1016/j.gsf.2020.03.015

Wilson, M., 1989. Igneous Petrogenesis: A Global Tectonic Approach. Unwin Hyman, London.

Workman, R.K., Hart, S.R., 2005. Major and trace element composition of the depleted MORB mantle (DMM). Earth and Planetary Science Letters 231, 53–72. https://doi.org/10.1016/j.epsl.2004.12.005

Zindler, A., Hart, S.R., 1986. Chemical Geodynamics. Annual Review of Earth and Planetary Sciences 14, 493–571. https://doi.org/10.1146/annurev.earth.14.1.493

Zindler, A., Staudigel, H., Batiza, R., 1984. Isotope and trace element geochemistry of young Pacific seamounts: implications for the scale of upper mantle heterogeneity. Earth and Planetary Science Letters 70, 175–195. https://doi.org/10.1016/0012-821X(84)90004-9

Chapter 5

Conclusions

The geochemistry of mafic lavas illuminates both source and secondary processes that, in turn, give insights into the generation of magmas in different tectonic environments. The principal aim of this thesis is to use unique suites of samples to study the transfer of aqueous fluid-mobile elements or the subduction component in the Izu-Bonin arc system, constrain the origin of geochemical enrichment of the Pacific upper mantle during the Mid-Cretaceous, and investigate the origin of a geochemically related suite of alkalic lavas that crosscut between oceanic and continental lithosphere and overlying crust in the West Antarctic Rift system. Here I will briefly summarize the progress and major findings made and outline potential future work that may be done to further refine our understanding of magma generation in the Izu-Bonin convergent margin, Jurassic to Cretaceous-aged Pacific crust and the WARS.

In Chapter 2, I used Pacific AOC samples to trace the path of the subduction component in the Izu-Bonin arc system. The samples from the along-arc transect revealed several key findings. First, the AOC of the Pacific plate is more heterogeneous than previously estimated. Second, the AOC data showed a geochemical enrichment in both trace elements and Sr-Nd-Pb isotope ratios that progressed from N-MORB values to E-MORB signatures towards the northernmost section of our transect. This is likely the result of the Pacific-Izanagi ridge tapping an enriched upper mantle source coincident with the Mid-Cretaceous Event. An unanticipated finding, however, was that the geochemical signature of Indian-type magmas observed in northern Izu-Bonin arc lavas is not a result of currently subducting materials. While Indian-type crust may have already been previously subducted and could be a source of the Izu-Bonin arc signature, the mantle wedge is the most likely explanation for this mismatch between down-going materials and arc lavas. While the mantle wedge is notoriously depleted in Pb, a substantial partitioning of Pb from the mantle wedge into the subduction component may be accomplished through a “zone-refining” process.

Chapter 3 focused primarily on the origin of the observed geochemical enrichment of the northern Pacific-Izanagi transect samples of Chapter 2. Using Hf isotopes, which are resistant to alteration and, thus, a reliable indicator of source signature, I modeled the relationship between the enriched samples and the contamination effects of LIP production during the Mid-Cretaceous event. I also used data from other (I)ODP and DSDP sites of similar ages in the Pacific basin to better understand the broader evolution of the Pacific upper mantle during this contamination event. Our findings suggest that Pacific-Izanagi crustal basalts that are 127Ma and older represent normal Pacific upper mantle compositions whereas samples that are younger than 127Ma are more enriched in incompatible trace elements and have a more radiogenic isotopic signature. The enriched end-member responsible for the enrichment is likely a mixture of FOZO and up to 20% EMI, which is consistent with the isotopic signatures of the Ontong Java, Manihiki and Hikurangi plateaus that were produced around this time. As a result, I affirm the hypothesis on the origin of the geochemical enrichment of the northern Pacific-Izanagi AOC samples proposed in Chapter 2 as well as the proposed contamination effect on the Pacific upper mantle by a global volcanic pulse by Madrigal et al. (2016). Our results also support previous findings that HIMU is not the predominant mantle end-member signature of the Pacific LIPs produced during the Mid-Cretaceous.

Chapter 4 considers the mantle source and effects of crustal contamination on alkaline magmas generated in the WARS during its second phase of rifting. I used and contributed major and trace element and Sr, Nd and Pb isotope analyses to the dataset used by Panter et al. (2018), though my most critical contribution consisted of HSE and Re-Os isotope measurements. The sensitivity of the HSE and Re-Os system to crustal contamination, in conjunction with O isotope data, shows that the samples from the WARS are variably contaminated, but originate from a common FOZO source best observed in the oceanic ABS samples. In a direct comparison of WARS with both CVL and EARS, it becomes clear that crustal contamination creates compositional heterogeneity in erupted lavas. Results also seem to suggest that both CVL and EARS lavas have a common, FOZO mantle source. However, further work is necessary to categorically affirm this hypothesis.

These chapters represent a small but significant step forward in our understanding of the subtle workings and mechanisms of plate tectonics and show how the chemistry of magmas unravels complex magma geneses in different tectonic settings. Unravelling source signatures from the geochemical influences of contamination, crystal fractionation and partial melting advances our comprehension of the various geologic processes that generate magma at constructive and destructive plate boundaries.

References

Ayers, J., 1998. Trace element modeling of aqueous fluid - peridotite interaction in the mantle wedge of subduction zones. Contributions to Mineralogy and Petrology 132, 390–404. https://doi.org/10.1007/s004100050431

Durkin, K., Castillo, P.R., Straub, S.M., Abe, N., Tamura, Y., 2020. Geoscience Frontiers An origin of the along-arc compositional variation in the Izu-Bonin arc system. Geoscience Frontiers. https://doi.org/10.1016/j.gsf.2019.12.004

Madrigal, P., Gazel, E., Flores, K.E., Bizimis, M., Jicha, B., 2016. Record of massive upwellings from the Pacific large low shear velocity province. 7, 13309.

Panter, K.S., Castillo, P.R., Krans, S., Deering, C., McIntosh, W., Valley, J.W., Kitajima, K., Kyle, P.R., Hart, S.R., Blusztajn, J., 2018. Melt Origin across a Rifted Continental Margin: a Case for Subduction-related Metasomatic Agents in the Lithospheric Source of Alkaline Basalt, NW Ross Sea, Antarctica. Journal of Petrology 59, 517–558. https://doi.org/10.1093/petrology/egy036